Investigation of Conditional Source-Term Estimation Approach for Turbulent Partially Premixed Combustion Modelling

by

Daniele Dovizio

A thesis
presented to the University of Waterloo
in fulfillment of the
thesis requirement for the degree of
Doctor of Philosophy
in
Mechanical Engineering

Waterloo, Ontario, Canada, 2015

I hereby declare that I am the sole author of this thesis. This is a true copy of the thesis, including any required final revisions, as accepted by my examiners.

I understand that my thesis may be made electronically available to the public.

Abstract

Conditional Source-term Estimation (CSE) is a closure technique for modelling turbulent combustion phenomena. CSE uses the Conditional Moment Closure (CMC) hypothesis for closing chemical source terms: conditionally averaged chemical source terms are closed by conditional averaged scalars, which are obtained by inverting an integral equation, instead of solving transport equations (as in CMC). Since CSE has been successfully applied to both premixed and non-premixed configurations, it represents an attractive method for dealing with the more general and complex case of partially premixed combustion.

The objectives of the present study are to (i) consolidate the premixed formulation of CSE through numerical simulations of a turbulent bluff body premixed flame; (ii) formulate, implement and test the Doubly conditional CSE (DCSE) in the context of partially premixed combustion; (iii) compare the DCSE predictions with well documented turbulent partially premixed flames.

The canonical example of partially premixed flames is represented by turbulent lifted flames. A series of lifted turbulent jet flames is investigated in RANS by using DCSE. The DCSE calculations are successful in predicting the lift-off heights at three different conditions and reproducing many aspects of the flame structure in agreement with the experimental observations. The current results show that important aspects of the stabilization mechanism can be reproduced by the DCSE combustion model.

The applicability of DCSE is further evaluated by applying this approach to a series of turbulent V-shaped flames for which experimental data is available. Premixed and stratified conditions are investigated. Overall, the agreement between numerical results and experimental findings is good, demonstrating the capability of DCSE to deal with partially premixed combustion. Future work includes implementation of CSE in LES and investigation of different fuels such as propane and biofuels.

Acknowledgements

I would like to thank all the people who made this possible.
First and foremost I would like to express my gratitude to my advisor, Professor Cecile Devaud. She has been supportive and patient since the first day I arrived in Waterloo. She has assisted and guided me by providing a valuable research assistantship over more than four years. Thanks to her the thesis topic was clearly defined from the beginning of my PhD program and she has constantly helped me staying on track. And during the most difficult times, she gave me the moral support and encouragement I needed to move on. Her attention to details and extensive knowledge in the field are greatly acknowledged.
The financial support of the Natural Sciences and Engineering Research Council of Canada (NSERC), MITACS/MPRIME and Rolls-Royce Canada is gratefully acknowledged.
I also extend my thanks to the committee members for agreeing to be in the present examination: Prof. Kendal Bushe, Prof. Sean Peterson, Prof. Elizabeth Weckman, and Prof. Eric Croiset.
I would like to thank all my colleagues and friends at the Energy Research Centre (ERC) for their valuable support, especially Jeffrey Labahn, Dominic Man Ching Ma, Kevin Lee, Duy Le, Amirali Ashrafizadeh, Andrew Buckrell, Amine Debbagh, and Guillaume Mancini.
I would like to thank the members of the department of Mechanical Engineering of University of British Columbia, in particular Mahdi Salehi for his precious time and support.
I like to give a special thank to my friend and roommate Alessandro Cosentino for being patient, motivating, encouraging and for sharing with me good memories and great food.
I would also like to thank all my friends in Waterloo for their support and the great times that I had with them, in particular Adewunmi Amoye, Kristopher Gutsche, Leighanne Rathwell, Jessica Leavitt, Sophie Hogeveen, Fikayo Odeseye, Matthew Roche, Akilah Sue, Mike Fizesan, Kim and Dan Davis and all the players of the Hopeless Expert soccer team.
I finish with Italy, where the most basic source of my identity resides. Truly I can say I would not have reached this point in my life without the support of my family. I am deeply indebted to my parents, my brother and my sister for their unconditional love and their faith in my endeavours. And talking about Italy, I have special friends to thank: Christian Di Giacomo, Jessica Rocci and Sabrina Starinieri. Your friendship is irreplaceable. I have to especially thank Sara Tuttoilmondo, for being distant-but-close friend and being of great encouragement during these years. I need to thank all of them in Italian ...

Grazie di cuore a voi tutti, che dall'Italia avete fatto sentire forte la vostra presenza nel mio cuore. Parte di questo lavoro è merito anche vostro.

Last but not least, I thank God. He is before all things, and in Him all things hold together.

Dedication

This work is dedicated to ones I love: my family, my close friends and God.

Table of Contents

List of Tables

List of Figures

Nomenclature

$\mathbf{A}$	Kernel of the Fredholm integral equation
$\vec{b}$	Source vector of the linear system representing CSE inversion problem
c	Progress variable
c^*	Sample of the progress variable
$c_{\chi Z}$	Constant for the scalar dissipation rate estimation
c_m	Progress variable characterizing the chemical kinetics
C_{mag}	Eddy Dissipation Concept model constant
$C_\mu, \sigma_k, \sigma_\varepsilon, C_{\varepsilon 1}, C_{\varepsilon 2}$	Standard $k-\varepsilon$ model constants
Da	Damköhler number
F_1, F_2	Blending functions of the $k-\omega$ SST turbulence model
h_t	Total specific enthalpy [$\mathrm{kgm^2/s^2}$]
k	Turbulent kinetic energy [$\mathrm{m^2/s^2}$]
Ka	Karlovitz number
L	Integral length scale [m]
Le	Lewis number
N	Number of species
p	Pressure [Pa]

PDF Probability Density Function

$\tilde{P}_k$ Production of turbulent kinetic energy [kg/(ms^2)]

Re_t Turbulence Reynolds number

S Strain rate [1/s]

s Oxygen-fuel stoichiometric mass ratio

Sc_{kt} Turbulent Schmidt number for species k

S_{ct_1}, S_{ct_2} Turbulent Schmidt numbers appearing in the variance of the progress variable governing equation

s_L Laminar flame speed [m/s]

s_L^0 Unstrained laminar flame speed

T Temperature [K]

T_A Activation temperature [cal/mole]

T_b Adiabatic temperature [K]

t_{chem} Chemical time scale [s]

t_η Kolmogorov time scale [s]

t_L Integral time scale [s]

u' Turbulent velocity [m/s]

u_i i-th component of velocity [m/s]

V_k Diffusion velocity of species k [m/s]

V_{ki} i-component of the diffusion velocity [m/s]

x_i i-th spatial coordinate [m]

y Distance of the first node from the wall [m]

$Y_{i,F}$ Mass fractions of element i in the fuel stream

$Y_{i,O}$	Mass fractions of element i in the oxidizer stream
Y_k	Mass fraction of the species k
Z	Mixture fraction
$\vec{\alpha}$	Solution of the Fredholm integral equation
$\beta^*, a_1, \beta_1, \sigma_{k1}, \sigma_{\omega 1}, a_2, \beta_2, \sigma_{k2}, \sigma_{\omega_2}$	$k-\omega$ SST turbulence model constants
χ_Z	Scalar dissipation rate [1/s]
δ_{ij}	Kronecker symbol
δ	Flame thickness [m]
δ_L^0	Unstrained laminar thermal thickness
ε	Dissipation rate of the turbulent kinetic energy [m^2/s^3]
η_k	Kolmogorov length scale [m]
λ	Thermal conductivity [W/(mK)]
μ	Molecular viscosity [Pas]
μ_t	Turbulent viscosity [Pas]
ν	Kinematic viscosity [m^2/s]
$\dot{\omega}_k$	Species chemical reaction rate [$kg/(m^3s)$]
ω	Specific dissipation rate [1/s]
$\dot{\omega}_c$	Reaction source term of the progress variable
$\overline{\phi}$	Time averaged or filtered value of the quantity ϕ
ϕ''	Fluctuation of the quantity ϕ
ϕ'	Residual value of the quantity ϕ
$\widetilde{\phi}$	Favre averaged or Favre-filtered value of the quantity ϕ
ρ	Density [kg/m^3]
τ_{ij}	Viscous stress tensor [Pa]

Chapter 1

Introduction

The global mean carbon dioxide (CO_2) level in the atmosphere increases each year by about 0.5% [18]. Such a trend has led to severe emission regulations for combustion systems, compelling industries to find solutions to improve the environmental friendliness of these systems. Despite advances in renewable energies, in the foreseeable future the transportation and power generation sectors will continue to rely upon combustion processes. Thus, there is a clear need for the development of fuel-efficient and low-emission industrial combustion devices. For gas turbines, lean premixed combustion appears as one of the most promising approaches to achieve effective reduction in emissions and to increase efficiency simultaneously [19, 20]. This combustion process has already been applied to large-scale natural gas-fired turbines for combined cycle power generation. Research on technologies based on turbulent premixed concepts can also be found for industrial furnaces, aero gas turbines, Homogeneous Charge Compression Ignition (HCCI) and spark-ignition engines. However, the low chemical activity and the consequent low flame speed render this class of flame very susceptible to instability and extinction issues. One solution has been achieved by introducing a spatial variation of the equivalence ratio, leading to the appearance of areas of richer mixtures in the combustion chamber that enhance flame stability, but at the same time keeping the benefits of lean premixed combustion regarding low emissions. Such systems belong to the turbulent partially premixed combustion category and are generally denoted as turbulent stratified flames. Notwithstanding the considerable progress achieved in the last decades in numerical simulations of turbulent combustion phenomena, key issues are still unclear and a theoretical description that is accurate enough to make turbulent combustion models rigorous and quantitative for industrial use is still lacking [21].

Turbulent combustion sits at the interface of two important nonlinear, multiscale phe-

nomena: chemistry and turbulence. These two are strongly coupled leading to typical closure problems in turbulent combustion modelling. Turbulent combustion problems are traditionally divided into two classes: non-premixed and premixed combustion. However, in many applications, the combustion process lies somewhere between these two regimes and partially premixed combustion occurs [22]. A process where the mixing of fuel and oxidizer occurs simultaneously with combustion is called non-premixed combustion. Turbulent non-premixed flames appear in many industrial applications because they are safer and simpler to design than premixed flames. Typical examples are furnaces, diesel engines and gas turbines. Non-premixed flames are also called diffusion flames since diffusion is the rate-controlling process [22]. An important feature regarding these flames is that they do not involve a propagating front and are located where fuel and oxidizer meet. In the case of premixed combustion, the fuel and oxidizer are completely mixed together before combustion takes place. Premixed turbulent combustion applications include homogeneous charge, spark-ignition engines, reheat systems fitted to jet engines for supersonic aircraft and modern industrial gas turbine engines for power generation. Premixed flames are characterized by flame front propagation: they move spontaneously in a direction normal to themselves at a certain flame speed. Premixed and non-premixed turbulent combustion are obtained by assuming either that fuel and oxidizer are fully premixed prior to combustion or that they enter the flame zone separately. However, in real flows, this idealization may not be valid. The burning of liquid fuel sprays, for example, can involve an intermediate regime in which the fuel and oxidizer are partially mixed at the time of combustion, and many practical combustion devices, including reciprocating engines, gas turbines and furnaces, often operate in a partially premixed burning regime [23]. The resulting partially premixed mode of combustion may have a profound impact on the overall burning rate and on pollutant emission levels [22]. Research on turbulent combustion has primarily focused on either premixed or non-premixed regimes, but such an approach has been demonstrated to be inadequate for the description of the more general case of partially premixed combustion. Consequently, accurate modelling of turbulent partially premixed combustion is key to the development and improvement of many engineering combustion devices.

1.1 Motivation

Many combustion models have been investigated to describe either the asymptotic premixed or the asymptotic non-premixed combustion limit, but such an idealization does not represent what is found in practical applications. However, partially premixed regimes

and regimes that involve transitions between premixed and non-premixed behavior, are not very well understood. For these reasons, the development of theoretical models for this type of combustion represents a challenge to model advancement, since these partially premixed and transition processes are very important in realistic combustion devices. Conditional Source-term Estimation (CSE) has been shown to be an interesting combustion model, successfully applied to both premixed and non-premixed conditions, but has never been applied to partially premixed combustion. It does not depend on any combustion regimes and is expected to be a good candidate for partially premixed combustion modelling. In the longer term, the developed model may be used to develop control strategies for pollutant, efficiency and stability in the design of new gas turbines and engines.

1.2 Objectives

The current work aims to improve our understanding of various physical processes involved in partially premixed combustion and thereby to further modelling capabilities in that area. Based on these considerations, the ultimate focus of the present dissertation is to investigate and implement a new partially premixed combustion model based on the CSE approach, called Doubly Conditional Source-term Estimation (DCSE). The objectives can be summarized as

1. **Consolidation of the CSE model for turbulent premixed combustion.** Prior to the current investigation, CSE has been applied to only one turbulent premixed flame characterized by a relatively simple geometry. A further verification of the model for more complex configurations is necessary prior to moving towards the modelling of the more general case of partially premixed combustion.

2. **Formulation, implementation and testing of DCSE for partially premixed turbulent combustion.** More specifically, the CSE method is extended to a partially premixed formulation by the use of a double conditioning operation.

3. **Comparison of DCSE predictions with well documented turbulent partially premixed flames.** First, a series of turbulent lifted flames, considered as the canonical problem for the study of turbulent partially premixed combustion, are examined in terms of flame properties and stabilization mechanism. A series of stratified turbulent V-shaped flames are then simulated with the DCSE approach in order to assess further the capabilities of this combustion model.

1.3 Overview of the study

Following this introductory chapter, some background in turbulent combustion modelling is provided in Chapter 2. Physical description of turbulence, chemistry and their interaction is addressed, as well as the canonical description of premixed, diffusion and partially premixed combustion processes. The governing equations are presented, followed by mathematical and computational strategies for simulating turbulent combustion flows. Chapter 2 concludes with a review of relevant literature about different combustion model approaches for turbulent premixed, non-premixed and partially premixed combustion.

Chapter 3 deals with numerical simulation of a bluff body premixed burner. Turbulence is modelled by the Reynolds-averaged Navier-Stokes (RANS) approach and CSE is the combustion model adopted. The effects of different scalar dissipation rate closures are investigated and results are compared to experimental findings.

Chapter 4 introduces doubly conditioning and the DCSE implementation for turbulent partially premixed combustion. DCSE is then applied to the numerical simulations of a series of turbulent lifted jet flames and numerical results are compared to available experimental data in terms of fuel concentration, stabilization height and stabilization mechanism.

Chapter 5 describes RANS simulations of a series of stratified turbulent V-shaped flames of methane and air. The test case is first investigated in fully premixed conditions and then three different stratified partially premixed cases are considered. An extension of the scalar dissipation closure to the partially premixed formulation is implemented. Comparisons of the numerical results are made with experimental measurements.

1.4 Author's Current Contributions

It is acknowledged that parts of the content presented in Chapter 3-5 are published in the following articles:

- D. Dovizio, M.M. Salehi, and C.B. Devaud. RANS simulation of a turbulent premixed bluff body flame using conditional source-term estimation. *Combustion Theory and Modelling*, 17(5):935–959, 2013.
- D. Dovizio, J.W. Labahn, and C.B. Devaud. RANS simulation of a turbulent lifted jet flame using Conditional Source Estimation. *Proceedings of the Combustion In-*

stitute/Canadian Section Spring Technical Meeting, Université Laval, Québec, May 13-16, 2013.

- D. Dovizio, J.W. Labahn, and C.B. Devaud. Doubly Conditional Source-Term Estimation Applied to a Turbulent Lifted Jet Flame. *Eighth Mediterranean Combustion Symposium,* Çeşme, İzmir, Turkey, September 8-13, 2013.

- D. Dovizio, J.W. Labahn, and C.B. Devaud. Doubly Conditional Source-term Estimation model for the simulation of turbulent lifted jet flames. *Proceedings of the Combustion Institute/Canadian Section Spring Technical Meeting,* University of Windsor, May 12-15, 2014.

- D. Dovizio, J.W. Labahn, and C.B. Devaud. Doubly Conditional Source-term Estimation (DCSE) applied to a series of lifted turbulent jet flames in cold air. *Combustion and Flame*, 162(5):1976–1986, 2015.

- J.W. Labahn, D. Dovizio, and C.B. Devaud. Numerical simulation of the Delft-Jet-in-Hot-Coflow (DJHC) flame using Conditional Source-term Estimation. *Proceedings of the Combustion Institute*, 35(3):3547–3555, 2015.

- D. Dovizio, A. Debbagh and C.B. Devaud. Numerical simulations of turbulent V-shaped flames. *Proceedings of the Combustion Institute/Canadian Section Spring Technical Meeting,* University of Saskatchewan May 11-14, 2015.

- D. Dovizio, A. Debbagh and C.B. Devaud. RANS simulation of a series of turbulent V-shaped flames using Conditional Source-term Estimation. *Proceeding of the 9th Mediterranean combustion symposium,* Rhodes, Greece, June 7-11, 2015.

Chapter 2

Background

In this chapter, background information is provided on different strategies used in turbulent combustion modelling. Turbulent reactive flows are characterized by two interacting phenomena, turbulence and chemistry. The aim of turbulent combustion modelling is to provide an accurate representation of this interaction. Because of its complexity, turbulent combustion is significantly challenging to model, despite the developments in mathematics and computing that have occurred in recent years.

2.1 Governing Equations

The set of instantaneous balance equations involved in the numerical study of turbulent combustion comprises the classical continuity, Navier-Stokes, species and energy transport equations. The continuity equation consists of the mass to be conserved and reads

$$\frac{\partial \rho}{\partial t} + \frac{\partial}{\partial x_i}(\rho u_i) = 0 \ , \tag{2.1}$$

where u_i represents the velocity components for $i = 1$ to 3. The conservation of linear momentum is written

$$\frac{\partial(\rho u_j)}{\partial t} + \frac{\partial}{\partial x_i}(\rho u_i u_j) = -\frac{\partial p}{\partial x_j} + \frac{\partial \tau_{ij}}{\partial x_i} + \rho \sum_{k=1}^{N} Y_k f_{k,j} \ , \tag{2.2}$$

where p is the pressure, Y_k the mass fraction of species k, $f_{k,i}$ the body force along i acting on species k and τ_{ij} the symmetric viscous stress tensor, which for a Newtonian fluid can

be expressed as

$$\tau_{ij} = -\frac{2}{3}\mu\frac{\partial u_k}{\partial x_k}\delta_{ij} + \mu\left(\frac{\partial u_i}{\partial x_j} + \frac{\partial u_j}{\partial x_i}\right) \ , \tag{2.3}$$

where δ_{ij} is the Kronecker's delta and μ the dynamic viscosity. The conservation of species k follows the transport equation

$$\frac{\partial(\rho Y_k)}{\partial t} + \frac{\partial}{\partial x_i}(\rho u_i Y_k) = -\frac{\partial}{\partial x_i}(\rho V_{k,i} Y_k) + \dot{\omega}_k \quad \text{for} \quad k = 1, N \ , \tag{2.4}$$

where $V_{k,i}$ is the i-component of the diffusion velocity V_k of species k and $\dot{\omega}_k$ the reaction rate [24]. The energy equation can be derived following several approaches, depending on the nature of the problem [24]. For combustion problems, the formulation based on the total enthalpy h is preferred and is defined as the sum of the enthalpy of formation and the sensible enthalpy change. The enthalpy of species k is then written as

$$h_k = \int_{T_0}^{T} c_{pk} dT + \Delta h^0_{f,k}, \tag{2.5}$$

where c_{pk} is the specific heat capacity of species k at constant pressure and $\Delta h^0_{f,k}$ the mass enthalpy of formation of species k at the reference temperature T_0. For a mixture of N species, the heat capacity at constant pressure c_p is calculated as a mass-weighted sum of the single specific heat capacities, $c_p = \sum_{k=1}^{N} c_{pk} Y_k$. The same procedure is applied to the enthalpy

$$h = \sum_{k=1}^{N} h_k Y_k = \int_{T_0}^{T} c_{pk} dT + \sum_{k=1}^{N} \Delta h^0_{f,k} Y_k. \tag{2.6}$$

Thus the energy balance equation can be written in terms of total enthalpy as

$$\frac{\partial(\rho h)}{\partial t} + \frac{\partial}{\partial x_i}(\rho u_i h) = \frac{\partial p}{\partial t} + \frac{\partial}{\partial x_i}(u_i \tau_{ij}) - \frac{\partial q_i}{\partial x_i} + \dot{Q}_r + \rho \sum_{k=1}^{N} Y_k f_{k,i} V_{k,i} \ , \tag{2.7}$$

where $\frac{\partial}{\partial x_i}(\rho u_i \tau_{ij})$ is the heating source term due to friction, q_i the energy flux, given by $q_i = -\lambda \frac{\partial T}{\partial x_i} + \rho \sum_{k=1}^{N} Y_k h_k V_{k,i}$ with λ being the thermal conductivity of the mixture, $\rho \sum_{k=1}^{N} Y_k f_{k,i} V_{k,i}$ the power produced by volume forces f_k on species k and $\dot{Q}_r$ the heat source term due to radiation [24].

2.2 Numerical Strategies for Simulating Turbulent Combustion Flows

In principle, Eqs 2.1-2.7 can be discretized in space and time and solved through numerical techniques such as the Finite Element Method (FEM) or the Spectral Element Method (SEM). However, turbulent combustion flows present a wide multi scale complexity deriving from the interaction between combustion and turbulence. A common strategy to solve the turbulent combustion problem consists of the separation of scales [25]. This approach has been successfully applied to an extended class of problems through the use of Computational Fluid Dynamics (CFD) techniques [21]. More specifically, the instantaneous Navier-Stokes equations presented in Section 2.1 are modified to a reduced order or dimension or a statistical form so that ranges of scales are decoupled or eliminated from the solution. Three principal approaches, corresponding to three different levels of computations, have been used to describe turbulent combustion processes: Direct Numerical Simulation (DNS), RANS and Large Eddy Simulation (LES) methods.

2.2.1 Direct Numerical Simulation

In DNS, the instantaneous balance equations are solved without any model for turbulent motions. Meshes in DNS need to be fine enough to resolve the smallest eddies in the flow in both space and time. According to Kolmogorov [26], the size of the eddies spans a wide range of length scales, from a macroscale (integral length scale L) corresponding to the geometrical dimension of the system, to the smallest size of the eddies (Kolmogorov microscale η_k). The energy is supplied to the largest scales of motion through the production mechanism. The large eddies then transfer the energy sequentially to the smaller ones during a process called energy cascade (introduced historically by Richardson [27]). During this energy transfer, the Reynolds number decreases until it becomes equal to unity corresponding to the dissipation scale, where the molecular viscosity converts the turbulent kinetic energy into heat. Kolmogorov also states that since the information of the large scales is lost during the cascade process, the small-scale motions are characterized by a statistically universal characteristic, function of the two parameters controlling the cascade process, i.e. the rate at which the energy is transferred and the viscous dissipation [28]. This property leads to the definition of the Kolmogorov length (η), velocity (u_η) and time (t_η) scale

$$\eta \equiv (\nu^3/\varepsilon)^{1/4} \ , \tag{2.8}$$

$$u_\eta \equiv (\varepsilon\nu)^{1/4} \ , \tag{2.9}$$

$$t_\eta \equiv (\nu/\varepsilon)^{1/2} \ , \tag{2.10}$$

where ν is the kinematic viscosity and ε the dissipation rate of turbulent kinetic energy k. Another important property, summarized by Kolmogorov's second similarity hypothesis, is that, for high Reynolds number turbulent flows, the statistics of the motion of scales larger than η are only dependent on ε. From the combination of this characteristic with Eq. 2.8, the following identity can be written

$$\varepsilon = \frac{u'^3}{L} = \frac{u_\eta^3}{\eta} \ . \tag{2.11}$$

By combining Eq. 2.11 and Eq. 2.8, it can be clearly seen that the Reynolds number calculated at the Kolmogorov scale is

$$Re_\eta = \frac{\eta u_\eta}{\nu} = \frac{\varepsilon^{1/3}\eta^{4/3}}{\nu} = 1 \tag{2.12}$$

In the DNS approach, there is no modelling and the complete range of spatial and temporal scales must be resolved. In practice, solutions of the Navier-Stokes equations for turbulent flows demand a prohibitive amount of computational time. In fact, the ratio between the largest (integral length scale L) and smallest (Kolmogorov η_k) turbulent length scales is [28]

$$\frac{L}{\eta_k} \approx Re_t^{3/4}, \tag{2.13}$$

where Re_t is the turbulent Reynolds number, $Re_t = \frac{u'L}{\nu}$. Considering a three dimensional simulation and estimating that at least 1,000 time steps are needed to mimic a turbulent combustion process, the overall time for the computation increases with the fourth power of the Reynolds number [28]. This analysis is related to a generic turbulent flow. In the case of a reactive flow, the complexity of the system increases even further. First, the number of scalars that needs to be solved is very large. A detailed chemical kinetic system might include tens or hundreds of species and reactions, with a chemical time ranging from 10^{-7} s to 10^{-3} s [29]. Second, the two problems of different nature, turbulence and combustion, cannot be solved separately because of their intrinsic and mutual interaction. It is worth noting that the Navier-Stokes equations are the same with and without combustion, but it is the flow behaviour that changes [24], because of variations in temperature and hence density. This means that, in principle, if one could solve directly the momentum, energy and transport equations of all the species involved in the reaction mechanism, modelling turbulent combustion would not be necessary. However, based on the previous considerations, it is not possible to solve realistic problems through DNS even with the most powerful

available supercomputers. Consequently, DNS is mostly used to analyze turbulent flames in simple configurations such as homogeneous isotropic turbulent flows and mixing layers [30].

2.2.2 Reynolds-averaged Navier-Stokes

RANS computations have historically been the first method because the direct solution of the instantaneous equations was not possible. In this approach, the mean values of the turbulent flow are solved by deriving Reynolds-averaged conservation equations from the Navier-Stokes equations and therefore modelling occurs at each level. In order to apply the time average operation, first the value of any quantity of interest of the flow ϕ is decomposed into its mean (time average) $\overline{\phi}$ and fluctuating part ϕ', through an operation called Reynolds decomposition

$$\phi(\vec{x},t) = \overline{\phi}(\vec{x},t) + \phi'(\vec{x},t) \tag{2.14}$$

and then substituting these quantities in Eqs 2.1-2.4. The averaged continuity and momentum equations result in

$$\frac{\partial \overline{\rho}}{\partial t} + \frac{\partial}{\partial x_i}(\overline{\rho u_i}) = \frac{\partial \overline{\rho}}{\partial t} + \frac{\partial}{\partial x_i}\left(\overline{\rho}\,\overline{u}_i + \overline{\rho' u_i'}\right) = 0\ . \tag{2.15}$$

$$\frac{\partial(\overline{\rho u_j})}{\partial t} + \frac{\partial}{\partial x_i}(\overline{\rho u_i u_j}) = -\frac{\partial \overline{p}}{\partial x_j} + \frac{\partial \overline{\tau}_{ij}}{\partial x_i} - \frac{\partial}{\partial x_i}(\overline{\rho} \overline{u_i' u_j'}) + \overline{\rho} \sum_{k=1}^{N} \overline{Y_k f_{k,j}}\ , \tag{2.16}$$

As shown in Eqs. 2.15-2.16, the averaging process generates additional terms, corresponding to unknown correlation quantities. More specifically, the non-linear terms $\overline{u_i' u_j'}$ represent the components of the Reynolds stress tensor and indicate the momentum of the flow due to turbulent fluctuations (turbulent transport). Equation 2.16 is identical to Eq. 2.2 except for the Reynolds stress term. This difference leads to a large complexity: in fact, while the original system of equations is closed (4 equations and 4 unknowns, u_i and p), in the RANS approach the equations of the mean field are still 4, but against 13 unknowns: u_i, p and the second order tensor $u_i' u_j'$. (Even considering symmetry properties of the tensor, the number of unknowns reduces to 10 and the closure problem remains). This closure problem is known as the turbulent closure problem and is characterized by a number of unknowns always larger than the number of equations.[1] In the case of reactive

[1] In fact, the transport equation for the Reynolds stress presents terms with higher-order correlations, like the triple correlation $\overline{u_i' u_j' u_k'}$.

problems, characterized by large density variations, other unclosed correlations between the density fluctuation and any property f of the flow appear, in the form of $\overline{\rho' f'}$. One method to avoid these terms consists of adopting a density-weighted average (Favre average). In Favre averaging, any dependent variable ϕ can be decomposed into a mean part $\widetilde{\phi}$ and a fluctuating part ϕ'' in the following way

$$\phi \equiv \widetilde{\phi} + \phi'' \equiv \frac{\overline{\rho\phi}}{\overline{\rho}} \ , \tag{2.17}$$

with $\widetilde{\phi''} = 0$. The set of equations, after averaging the instantaneous governing equations, becomes

- Mass conservation (continuity)

$$\frac{\partial \overline{\rho}}{\partial t} + \frac{\partial}{\partial x_i}(\overline{\rho}\widetilde{u}_i) = 0 \ . \tag{2.18}$$

- Momentum

$$\frac{\partial \overline{\rho}\widetilde{u}_i}{\partial t} + \frac{\partial}{\partial x_i}(\overline{\rho}\widetilde{u}_i\widetilde{u}_j) + \frac{\partial \overline{p}}{\partial x_j} = \frac{\partial}{\partial x_i}\left(\overline{\tau}_{ij} - \overline{\rho}\widetilde{u_i'' u_j''}\right) \ . \tag{2.19}$$

- Species

$$\frac{\partial(\overline{\rho}\widetilde{Y}_k)}{\partial t} + \frac{\partial}{\partial x_i}(\overline{\rho}\widetilde{u}_i\widetilde{Y}_k) = -\frac{\partial}{\partial x_i}(\overline{\rho}\overline{V_{k,i}Y_k} + \overline{\rho}\widetilde{u_i'' Y_k''}) + \overline{\rho}\sum_{k=1}^{N}\widetilde{Y_k f_{k,j}} + \overline{\dot{\omega}}_k \ . \tag{2.20}$$

- Energy

$$\begin{aligned}\frac{\partial(\overline{\rho}\widetilde{h}_t)}{\partial t} + \frac{\partial}{\partial x_i}(\overline{\rho}\widetilde{u}_i\widetilde{h}_t) = \frac{\partial \overline{p}}{\partial t} + \frac{\partial}{\partial x_i}\left(\overline{\lambda}\frac{\partial \widetilde{T}}{\partial x_i} - \overline{\rho}\sum_{k=1}^{N}\widetilde{Y_k h_k V_{k,i}} - \overline{\rho u_i'' h_t''}\right) + \\ \overline{\tau_{ij}\frac{\partial u_i}{\partial x_j}} + \widetilde{\dot{Q}_r} + \overline{\rho}\sum_{k=1}^{N}\widetilde{Y_k f_{k,i} V_{k,i}} \ .\end{aligned} \tag{2.21}$$

In Eqs. 2.18-2.21, the Reynolds stresses $\overline{\rho}\widetilde{u_i'' u_j''}$ and fluxes ($\overline{\rho}\widetilde{u_i'' Y_k''}$ and $\overline{\rho}\widetilde{u_i'' h_t''}$) are unclosed terms and are evaluated by either modelling strategies or by deriving balance equations for them.

Reynolds stresses are closed by a turbulence model (such as the $k-\varepsilon$ model [31]) without considering heat release effects. Species $\widetilde{u_i''Y_k''}$ and enthalpy $\widetilde{u_i''h_t''}$ Reynolds fluxes are generally closed using a gradient assumption

$$\widetilde{u_i''Y_k''} = -\frac{\mu_t}{Sc_{kt}}\frac{\partial \widetilde{Y}_k}{\partial x_i} \ , \tag{2.22}$$

where the turbulent viscosity μ_t is calculated by the turbulence model and Sc_{kt} is a turbulent Schmidt number for species k. Laminar diffusive fluxes for species $\overline{V_{k,i}Y_k}$ or enthalpy $\overline{\lambda\frac{\partial T}{\partial x_i}}$ are neglected against turbulent transport in case of large Reynolds number.
The main objective of turbulent combustion modelling consists of the closure of mean species chemical reaction rates $\overline{\dot{\omega}}_k$, which will be discussed in detail in Section 2.3.

Turbulence models for the Reynolds stresses

The most direct way to provide closure for the Reynolds stress tensor consists of solving transport equations for the Reynolds stresses, along with an equation for the dissipation rate. The potential of this method is directly related to its more general formulation, which does not impose the isotropic assumption and is shown to better predict the Reynolds stress anisotropies in turbulent channel flow and homogeneous shear flow [32]. Such a non-linear approach is needed for problems where the contribution of the Reynolds stresses is non negligible, like multiple flows in non-circular ducts, highly swirling flows and flows over a sudden expansion. However, this formulation leads not only to a more complex system (seven additional transport equation are required in the case of 3D flows), but the closure problem still remains challenging due to the presence of new terms in these transport equations that need to be modelled. In particular, the pressure-strain and dissipation-rate terms are not easy to close. In a simpler approach, the turbulent Reynolds stresses $\widetilde{u_i''u_j''}$ are described using the turbulent viscosity hypothesis (introduced by Boussinesq in 1877), which is mathematically analogous to the stress-rate-of-strain for a Newtonian fluid

$$\overline{\rho}\widetilde{u_i''u_j''} = -\mu_t\left(\frac{\partial \widetilde{u}_i}{\partial x_j} + \frac{\partial \widetilde{u}_j}{\partial x_i} - \frac{2}{3}\delta_{ij}\frac{\partial \widetilde{u}_k}{\partial x_k}\right) + \frac{2}{3}\overline{\rho}\delta_{ij}\widetilde{k}, \tag{2.23}$$

where a new quantity, the turbulent viscosity, μ_t, is introduced and δ_{ij} is the Kronecker symbol. The last term in Eq. 2.23 is the turbulent kinetic energy

$$\widetilde{k} = \frac{1}{2}\sum_{k=1}^{3}\widetilde{u_k''u_k''} \ . \tag{2.24}$$

The turbulent viscosity can be obtained from turbulent quantities for which modelled transport equations are solved (such as in the two-equations model). In the present research two different turbulence models are used, the $k-\varepsilon$ approach [31] and the Shear Stress Transport (SST) $k-\omega$ turbulence model [33].

Standard $k-\varepsilon$

In this model [31], the turbulent kinetic energy k and its dissipation rate ε are used to calculate the turbulent viscosity via

$$\mu_t = \overline{\rho} C_\mu \frac{\widetilde{k}^2}{\widetilde{\varepsilon}} \ , \tag{2.25}$$

where k and ε are provided by solving two balance equations

$$\frac{\partial}{\partial t}(\overline{\rho}\widetilde{k}) + \frac{\partial}{\partial x_i}(\overline{\rho}\widetilde{u}_i\widetilde{k}) = \frac{\partial}{\partial x_i}\left[\left(\mu + \frac{\mu_t}{\sigma_k}\right)\frac{\partial \widetilde{k}}{\partial x_i}\right] + \tilde{P}_k - \overline{\rho}\widetilde{\varepsilon} \ , \tag{2.26}$$

$$\frac{\partial}{\partial t}(\overline{\rho}\widetilde{\varepsilon}) + \frac{\partial}{\partial x_i}(\overline{\rho}\widetilde{u}_i\widetilde{\varepsilon}) = \frac{\partial}{\partial x_i}\left[\left(\mu + \frac{\mu_t}{\sigma_\varepsilon}\right)\frac{\partial \widetilde{\varepsilon}}{\partial x_i}\right] + C_{\varepsilon 1}\frac{\widetilde{\varepsilon}}{\widetilde{k}}\tilde{P}_k - C_{\varepsilon 2}\overline{\rho}\frac{\widetilde{\varepsilon}^2}{\widetilde{k}} \ , \tag{2.27}$$

where the source term

$$\tilde{P}_k = -\overline{\rho}\widetilde{u_i'' u_j''}\frac{\partial \widetilde{u}_i}{\partial x_j} \ , \tag{2.28}$$

is called production and determined using Boussinesq expression (see Eq.2.23). The standard values of the model constants given by Launder and Sharma [31] are

$$C_\mu = 0.09 \ ; \ \sigma_k = 1.0 \ ; \ \sigma_\varepsilon = 1.3 \ ; \ C_{\varepsilon 1} = 1.44 \ ; \ C_{\varepsilon 2} = 1.92 \ . \tag{2.29}$$

$k-\omega$ SST

The $k-\omega$ SST formulation [33] has similar transport equations, but with an additional term in the ω (called specific dissipation rate, $\omega \equiv \varepsilon/k$) equation multiplied by a blending function with the capability of switching to the standard ω equation of Wilcox [34] close to walls and to the standard $k-\varepsilon$ model remote from walls

$$\frac{\partial}{\partial t}(\overline{\rho}\widetilde{k}) + \frac{\partial}{\partial x_i}(\overline{\rho}\widetilde{u}_i\widetilde{k}) = \frac{\partial}{\partial x_i}\left[\left(\mu + \sigma_k\frac{\overline{\rho}\widetilde{k}}{\widetilde{\omega}}\right)\frac{\partial \widetilde{k}}{\partial x_i}\right] + \tilde{P}_k - \beta^*\overline{\rho}\widetilde{\omega}\widetilde{k} \ , \tag{2.30}$$

$$\frac{\partial}{\partial t}(\overline{\rho}\widetilde{\omega})+\frac{\partial}{\partial x_i}(\overline{\rho}\widetilde{u}_i\widetilde{\omega}) = \frac{\partial}{\partial x_i}\left[(\mu+\sigma_\omega\mu_t)\frac{\partial\widetilde{\omega}}{\partial x_i}\right]+\overline{\rho}\alpha S^2-\beta\overline{\rho}\widetilde{\omega}^2+2(1-F_1)\frac{\overline{\rho}\sigma_{\omega_2}}{\widetilde{\omega}}\frac{\partial\widetilde{k}}{\partial x_i}\frac{\partial\widetilde{\omega}}{\partial x_i}\ , \quad (2.31)$$

where the blending function F_1 is defined by

$$F_1 = \tanh\left\{\left\{\min\left[\max\left(\frac{\sqrt{\widetilde{k}}}{\beta^*\widetilde{\omega}y},\frac{500\nu}{y^2\widetilde{\omega}}\right),\frac{4\overline{\rho}\sigma_{\omega 2}\widetilde{k}}{CD_{k\omega}y^2}\right]\right\}^4\right\}\ , \quad (2.32)$$

with $CD_{k\omega} = \max\left(2\overline{\rho}\sigma_{\omega_2}\frac{1}{\widetilde{\omega}}\frac{\partial k}{\partial x_i}\frac{\partial\omega}{\partial x_i}, 10^{-10}\right)$ and y is the distance of the first node from the wall. F_1 is equal to zero away from the surface ($k-\varepsilon$ model) and switches over to one inside the boundary layer ($k-\omega$ model). The turbulent eddy viscosity is computed from

$$\mu_t = \frac{\overline{\rho}a_1 k}{\max\left(a_1\widetilde{\omega}, SF_2\right)}\ , \quad (2.33)$$

where S is the invariant measure of the strain rate and F_2 is a second blending function defined by

$$F_2 = \tanh\left[\left[\max\left(\frac{2\sqrt{\widetilde{k}}}{\beta^*\widetilde{\omega}y}\ ,\frac{500\nu}{y^2\widetilde{\omega}}\right)\right]^2\right]\ . \quad (2.34)$$

All constants are computed by a blend from the corresponding constants of the $k-\varepsilon$ and the $k-\omega$ model via $\alpha = \alpha_1F_1+\alpha_2(1-F_1)$ etc. The constants for this model are $\beta^* = 0.09, a_1 = 5/9, \beta_1 = 3/40, \sigma_{k1} = 0.85, \sigma_{\omega 1} = 0.5, a_2 = 0.44, \beta_2 = 0.0828, \sigma_{k2} = 1, \sigma_{\omega_2} = 0.856$.

2.2.3 Large Eddy Simulation

Large Eddy Simulations can be placed between RANS and DNS techniques. In this approach, large structures are simulated, while small scales are modelled. LES is widely used for non-reacting flows [35, 36], but it is still at an early stage for combustion processes. In LES a filter separates the resolved scales from the modelled ones, corresponding to Sub-Filter Scales (SFS). A SFS model is necessary in order to close the unresolved scales and, more specifically, to represent the transfer of energy from large resolved scales to small unresolved scales through the SFS dissipation term. The filtering operation can be done implicitly or can be included explicitly in the numerical scheme. In the former, filtering is obtained directly by two methods, the computational grid (which defines the filter width) and the discretization used in the code (that determines the filter function). In the latter,

the shape of the filtering is explicitly controlled and the filtering procedure is applied separately from the numerical computation. In practice, the governing equations are implicitly filtered [37].

While in DNS the velocity field needs to be resolved for the complete range of length scales, in LES the small scales of the solution are eliminated by applying a low-pass filtering to the Navier-Stokes equations. The solution consists of a filtered velocity field $\overline{U}(\vec{x},t)$ that can be resolved in a coarser grid with respect to the DNS approach [28]. The filtering operation, introduced by Leonard [38], is

$$\overline{U}(\vec{x},t) = \int_D G(\vec{y},\vec{x})\ U(\vec{y},t)d\vec{y}\ , \tag{2.35}$$

where D is the entire flow domain and the filter kernel $G(\vec{y},\vec{x})$ is centered about the point $\vec{y}$. The velocity field U is decomposed into a filtered (resolved) component and a SGS (unresolved) component

$$U(\vec{x},t) = \overline{U}(\vec{x},t) + U'(\vec{x},t)\ , \tag{2.36}$$

corresponding to the fluid motion of the large eddies and the residual field, respectively. Equation 2.36 appears to be similar to the Reynolds decomposition. However, it must be noted here that the filtered residual does not have the property of being null

$$\overline{U'}(\vec{x},t) \neq 0 \tag{2.37}$$

In LES, the filter functions can be defined in either spectral or physical space. The filter size (Δ) is not necessarily uniform, and can vary with spatial location. This leads to commutation errors that must be taken into account.[2] Analogous to the RANS approach, a Favre filter is adopted ($\widetilde{f} = \overline{\rho f}/\overline{\rho}$) for reacting flows and the filtered continuity and Navier-Stokes equations read

$$\frac{\partial\overline{\rho}}{\partial t} + \frac{\partial}{\partial x_i}(\overline{\rho}\widetilde{u}_i) = 0 \tag{2.39}$$

$$\frac{\partial\overline{\rho}\widetilde{u}_i}{\partial t} + \frac{\partial}{\partial x_i}(\overline{\rho}\widetilde{u}_i\widetilde{u}_j) + \frac{\partial\overline{p}}{\partial x_j} = \frac{\partial}{\partial x_i}\left[\overline{\tau}_{ij} - \overline{\rho}\left(\widetilde{u_iu_j} - \widetilde{u}_i\widetilde{u}_j\right)\right]\ , \tag{2.40}$$

[2] In LES the hypothesis of commutation between the derivative and filter operations no longer apply

$$\overline{\frac{\partial f}{\partial x_j}} \neq \frac{\partial\overline{f}}{\partial x_j}\ . \tag{2.38}$$

Ghosal and Moin have determined filters that exhibit the commutation property and for which the commutation error is independent by the form of the filter and scales as Δ^2 [39] .

where $\overline{\tau}_{ij}$ is the filtered viscous stress tensor and $\mathcal{T}_{ij} \equiv (\widetilde{u_i u_j} - \widetilde{u}_i \widetilde{u}_j)$ is the residual stress tensor that requires closure. Eddy viscosity models represent the most popular and simple approaches. For compressible flows, according to the Boussinesq hypothesis, the unresolved momentum fluxes are related to the strain rate by

$$\mathcal{T}_{ij} - \frac{\delta_{ij}}{3}\mathcal{T}_{kk} = -\nu_{t_{SGS}} \left(\frac{\partial \widetilde{u}_i}{\partial x_j} + \frac{\partial \widetilde{u}_j}{\partial x_i} - \frac{2}{3}\delta_{ij}\frac{\partial \widetilde{u}_k}{\partial x_k} \right) = -2\nu_{t_{SGS}} \left(\widetilde{S}_{ij} - \frac{\delta_{ij}}{3}\widetilde{S}_{kk} \right) \ , \tag{2.41}$$

where $\mathcal{T}_{kk}$ is the isotropic contribution of the Reynolds stresses and $\nu_{t_{SGS}}$ is the turbulent SGS viscosity, defined in most cases with an algebraic expression. The first SGS model was proposed by Smagorinsky in 1963 [40]. The SGS viscosity is modelled as

$$\nu_{t_{SGS}} = (C_S \Delta)^2 \sqrt{(2\overline{S}_{ij}\overline{S}_{ij})} \ , \tag{2.42}$$

where Δ is the filter scale [3] and C_S the Smagorinsky coefficient. This latter is zero in laminar flows and $C_S \approx 0.15$ in high-Re free turbulent flows [28] or is estimated as $C_S \approx 0.2$ in homogeneous isotropic turbulence conditions [24]. Therefore one singular value of the Smagorinsky coefficient is not appropriate for different flow conditions. One solution is represented by the dynamic model, where the value of the constant is calculated locally, so that the eddy viscosity magnitude can be reduced in zones of transition between laminar and turbulent regimes or where turbulence is not completely developed. The model was proposed by Germano [41] and the idea is to use the resolved scales for the determination of the small scales dissipation [24]. The advantage of LES against RANS lies in the capability of capturing large scale and unsteady features (flow reverse and recirculation) which are essential to most combustion devices. Finally, it must be noted that even though the RANS and LES balance equations are formally similar, the two approaches are intrinsically different. RANS modelling occurs at all scales, especially at large scales, which are strongly dependent on the boundary conditions and therefore on the specific problem under investigation. In LES, instead, large scales are resolved and the calibration of the model is less restrictive since the behaviour of small scales are expected to be similar for different flow conditions.

2.3 Turbulent combustion modelling

Reacting flows introduce two additional problems. The first is directly related to the chemical nature of the process which involves a large range of time scales, from approximately

[3] The filter scale is usually related to the local cell size. Commonly, for uniform grid $\Delta = 2\Delta x$, while for non uniform grid $\Delta = 2(\prod \Delta x_i)^{1/3}$ for $i = 1, 2, 3$ and Δx_i is the grid size in i-th direction.

10^{-10} s for the fastest reactions, to times of the order of seconds for the slower ones, such as for the formation of thermal nitrogen oxides (NO_x) [21, 24]. The second concerns flame-turbulence interaction and represents the most difficult challenge in numerical simulation, due to the multi-scale and strongly non-linear nature of turbulence and combustion. DNS of turbulent reactive flows of industrial interest is not yet feasible and the recourse to RANS or LES approaches is necessary. The aim of combustion model consists of providing a numerical solution of the thermo-fluid dynamic problem by providing closure to the turbulence and combustion processes and adequately capturing the two-way interaction of chemistry and turbulence. In particular, the most critical challenge in RANS and LES of turbulent combustion is represented by the closure of the reaction source term [21]. The main reason lies in the dependence of this term on the scalar field. If we consider a simple irreversible reaction between fuel (F) and oxidizer (O)

$$F + s\ O \rightarrow (1+s)P\ , \tag{2.43}$$

where s is the oxygen-fuel stoichiometric mass ratio and P denotes the product of the reaction, the fuel mass reaction rate can be expressed from the Arrhenius law as [24]

$$\dot{\omega}_F = -A\rho^2 T^\beta Y_F Y_O\ \exp\left(\frac{-T_A}{T}\right)\ , \tag{2.44}$$

where A is the pre-exponential constant, β the temperature exponent and T_A the activation temperature. As clearly expressed in this equation, the reaction rate is severely non-linear with temperature and the averaged value (resulting for example in the RANS approach) cannot be simply computed from the mean scalars

$$\overline{\dot{\omega}(\rho, Y_k, T)} \neq \dot{\omega}(\overline{\rho}, \overline{Y}_k, \overline{T}) \tag{2.45}$$

A possible solution consists of evaluating the mean reaction rate in terms of the Taylor series of the temperature fluctuation T''. However, this leads to the introduction of new quantities that need to be closed. Further, truncation errors may arise when only few terms of the series are used. Finally, for realistic chemical schemes the formulation (here derived for a simple reaction) is even more complicated. The alternative consists of deriving numerical closures based on physical analysis, as described in the next section. Strategies implemented in the RANS framework have been often adapted and extended to LES approaches. Consequently, the discussion here is focused on the RANS method.

Traditionally, turbulent combustion is classified as non-premixed, premixed or partially premixed, depending on the initial state of the reactants, leading to a different nature of the interaction between chemistry and turbulence. In non-premixed configurations, fuel

and oxidizer are injected through two distinct streams into the combustion chamber and combustion can be considered to occur as the two flows meet. For this reason, the rate of combustion is to a large extent controlled by mixing. Premixed flames occur when the oxidizer has been mixed with the fuel before it reaches the combustor. These two configurations do not represent properly the real behaviour of the flame, which can more likely be in a regime that is in between the two limits and is called partially premixed. This latter has a more general representation of the problem and shows features that can be associated to both premixed and non-premixed regimes. Bilger et al. [25] presented a review on paradigms in turbulent combustion research and found two main approaches, namely the separation of scale and/or the separation of model elements that described the reactive scalars in terms of their distribution function (Probability Density Function (PDF) or Filtered Density Function (FDF)). Commonly-used modelling approaches that belong to the first category are based on the assumption that chemistry is faster than other physical processes and the problem can be considered controlled by mixing (examples are the Eddy Dissipation Model (EDM) and the Eddy Break-Up model (EBU)) and the laminar flamelet model which assumes that chemical reaction is confined to narrow regions (flamelets), whose thickness is small compared to some or all of the characteristic scales of the turbulent flow. In contrast, transported PDF, Conditional Moment Closure (CMC) and CSE models reside in the second group.

2.3.1 Models assuming infinitely fast chemistry

In non-premixed turbulent combustion, the time scale characterizing chemical reactions is often much smaller than that of convection and diffusion. Therefore, it is appropriate to assume infinitely fast chemistry in the study of global properties [42]. This allows the use of combustion models that directly relate the reactive scalars to a conserved scalar. A popular model for non-premixed combustion calculations in the industry is called Eddy Dissipation Concept (EDC), devised by Magnussen [43]. It is based on the assumption that for fast chemistry the reaction rate is proportional to the rate of mixing between reactants and hot products

$$\overline{\dot{\omega}}_F = C_{mag}\ \overline{\rho}\ \frac{\varepsilon}{k}\min\left(\widetilde{Y}_F, \frac{\widetilde{Y}_O}{s}, \beta\frac{\widetilde{Y}_P}{1+s}\right)\ , \tag{2.46}$$

where C_{mag} and β are adjustable parameters. Subscripts F, O and P denote fuel, oxidizer and products respectively. s is the oxygen-fuel stoichiometric mass ratio. This model is simple and requires lower computational cost when compared to other combustion models, but needs to be validated case by case (the two constants have no general validity) and lacks

of prediction capacities when ignition, quenching or stabilization mechanism exist. The origin of EDC is the EBU model of Spalding [44], developed for premixed combustion. In the assumption of fast chemistry the mean reaction rate is controlled by the rate at which turbulence can bring fresh reactants in contact with hot products. The mean production rate of a product species mass fraction Y_P is expressed as

$$\overline{\dot{\omega}}_P = C_{EBU}\ \overline{\rho}\ \frac{\varepsilon}{k}\widetilde{Y''^2_P}^{1/2}\ , \tag{2.47}$$

where C_{EBU} is a constant which must be tuned for each individual case and $\widetilde{Y''^2_P} = \overline{\rho Y''_P Y''_P}$ is the variance of Y_P and quantifies the species mass fraction fluctuation magnitude. A first analysis, assuming that the flame is infinitely thin, leads to

$$\overline{\rho}\widetilde{Y''^2_P} = \overline{\rho\left(Y_P - \widetilde{Y_P}\right)^2} = \overline{\rho}\left(\widetilde{Y_P{}^2} - \widetilde{Y_P}^2\right) = \overline{\rho}\widetilde{Y_P}\left(1 - \widetilde{Y_P}\right)\ . \tag{2.48}$$

EBU-type models are very simple to implement and computationally inexpensive. However, they largely over-predict temperatures and concentrations of products. Another limitation is that they cannot be used for detailed chemistry.

2.3.2 Laminar Flamelet Model

The flamelet concept was independently derived by Peters [45] and Kuznetsov [46]. The Laminar Flamelet model describes the turbulent diffusion flame as an ensemble of laminar flame elements (or flamelets) subjected to strain only [21]. Because a diffusion flame is fully determined by the inter-penetration of the fuel and oxidizer streams, it is convenient to introduce a tracer of the state of the mixture. To track elements, a normalized scalar Z, called mixture fraction, is introduced. Z is taken as unity in the fuel stream and is null in the oxidizer stream. Bilger [42] provided the following definition

$$Z = \frac{Y_i - Y_{i,O}}{Y_{i,F} - Y_{i,O}}, \tag{2.49}$$

where Y_i is the mass fraction of element i in the local mixture and $Y_{i,F}$ and $Y_{i,O}$ are the the mass fractions of element i in the fuel and oxidizer streams, respectively. The mixture fraction is a conserved scalar, i.e. there is no chemical source term and its transport equation is written as

$$\frac{\partial(\rho Z)}{\partial t} + \frac{\partial}{\partial x_i}(\rho u_i Z) = \frac{\partial}{\partial x_i}\left(\rho D \frac{\partial Z}{\partial x_i}\right)\ . \tag{2.50}$$

In the assumption of unity Lewis number, Le, [4] and no heat transfer, the enthalpy (and consequently the temperature) field can also be uniquely described by Z. This implies that for equilibrium ("fast") chemistry, equal diffusivity, $Le = 1$ and no heat loss, all scalars (temperature, mass fraction and density) are functions of the mixture fraction only [3]. The Favre mean mixture fraction transport equation results in

$$\frac{\partial(\overline{\rho}\widetilde{Z})}{\partial t} + \frac{\partial}{\partial x_i}(\overline{\rho}\widetilde{u}_i\widetilde{Z}) = \frac{\partial}{\partial x_i}\left(\overline{\rho D\frac{\partial Z}{\partial x_i}} - \overline{\rho}\widetilde{u_i''Z''}\right) \ . \tag{2.51}$$

In Eq. 2.51 there are several unclosed terms. The Reynolds stresses are closed by the turbulence model and the turbulent flux $\widetilde{u_i''Z''}$ using the gradient assumption (see Eq. 2.22).

The mean of the mixture fraction is not sufficient to calculate averaged values. The variance of Z, $\widetilde{Z''^2}$, can be determined by solving a transport equation given by

$$\begin{aligned}\frac{\partial(\overline{\rho}\widetilde{Z''^2})}{\partial t} + \frac{\partial}{\partial x_i}\left(\overline{\rho}\widetilde{u}_i\widetilde{Z''^2}\right) = &\underbrace{-\frac{\partial}{\partial x_i}\left(\overline{\rho u_i''Z''^2}\right)}_{\text{turbulent transport}} + \underbrace{\frac{\partial}{\partial x_i}\left(\overline{\rho D\frac{\partial Z''^2}{\partial x_i}}\right)}_{\text{molecular diffusion}} \\ &\underbrace{+2\overline{Z''\frac{\partial}{\partial x_i}\left(\rho D\frac{\partial\widetilde{Z}}{\partial x_i}\right)}}_{\text{molecular diffusion}} \underbrace{-2\overline{\rho u_i''Z''}\frac{\partial\widetilde{Z}}{\partial x_i}}_{\text{production}} \underbrace{-2\overline{\rho D\frac{\partial Z''}{\partial x_i}\frac{\partial Z''}{\partial x_i}}}_{\text{dissipation}} ,\end{aligned} \tag{2.52}$$

where the turbulent transport term and the production term are closed by the gradient assumption (see Eq. 2.22). For large Reynolds numbers, molecular diffusion is negligible compared to turbulent transport. The last term on the Right Hand Side (RHS) is the mean scalar dissipation rate $\widetilde{\chi}_Z$ and it dissipates fluctuations of Z in the same way viscous dissipation dissipates fluctuations in velocity. The total scalar dissipation rate $\widetilde{\chi}_{Z_T}$ is defined as [24]

$$\overline{\rho}\widetilde{\chi}_{Z_T} = 2\overline{\rho D\frac{\partial Z}{\partial x_i}\frac{\partial Z}{\partial x_i}} + 2\overline{\rho D\frac{\partial Z''}{\partial x_i}\frac{\partial Z''}{\partial x_i}} \ , \tag{2.53}$$

In the RANS context, the contribution of the gradient of the mean is generally neglected [24]. This assumption has been recently validated by DNS analysis of the scalar dissipation rate for a turbulent hydrogen lifted flame [47], showing that the total scalar dissipation rate is well approximated by the the gradients of fluctuations. This analogy with the dissipation

[4] The Lewis number is defined as the ratio between the thermal diffusivity and the mass diffusivity, $Le \equiv D_{th}/D$.

rate of the kinetic energy, ε and the dimension of the scalar dissipation (inverse of a time) can be used to determine $\widetilde{\chi}_Z$ as

$$\overline{\rho}\widetilde{\chi}_{Z_T} \approx \overline{\rho}\widetilde{\chi}_Z = 2\rho D\overline{\frac{\partial Z''}{\partial x_i}\frac{\partial Z''}{\partial x_i}} = c_{\chi Z}\frac{\widetilde{\varepsilon}}{\widetilde{k}}\widetilde{Z''^2} \ , \tag{2.54}$$

where $c_{\chi Z}$ is a constant often taken as 2 [22]. Once the the mixture fraction and its variance are calculated (Eqs. 2.51-2.52), a PDF of Z can be determined (a presumed form of the PDF is assumed) and the averages are calculated as

$$\widetilde{Y}_i(\vec{x},t) = \int_0^1 \underbrace{Y_i(Z)}_{\text{Flame structure}} \overbrace{\tilde{P}(Z;\vec{x},t)}^{\text{Mixing}} dZ \ , \tag{2.55}$$

where $Y_i(Z)$ is tabulated as a function of Z (flamelet libraries). In the case of finite-rate chemistry (autoignition, extinction, pollutant formation), the fast chemistry idea is not applicable. One additional variable, the scalar dissipation rate χ_Z, can be introduced in the flamelet libraries to characterize departure from chemical equilibrium.

Turbulent non-premixed combustion regimes can be identified by defining relevant quantities that influence the flame structure. Based on dimensional analysis, a chemical time scale, t_{chem} can be defined as the inverse of the scalar dissipation rate for which quenching occurs, χ_q (the heat release from the chemical reaction is not enough to balance the heat loss by diffusion). As for the length scale, it is convenient to define a flame thickness in mixture fraction space. A diffusion length scale can be defined as the ratio between the molecular diffusivity and the strain rate [22]

$$l_D = \sqrt{D/a} \ . \tag{2.56}$$

In mixture fraction space, the flame thickness $(\Delta Z)_F$ can be calculated as

$$(\Delta Z)_F = \left(\frac{dZ}{dx_n}\right)_{st} l_D \ , \tag{2.57}$$

where $(dZ/dx_n)_{st}$ is the mixture fraction gradient at stoichiometric conditions normal to the reaction layer [22]. This latter can be expressed in terms of the scalar dissipation rate conditioned at $Z = Z_{st}$, χ_{st}

$$\chi_{st} = 2D\left(\frac{dZ}{dx_n}\right)^2_{st} \ . \tag{2.58}$$

Combining Eqs. 2.56, 2.57 and 2.58, the following expression for the flame thickness is obtained

$$(\Delta Z)_F = \left(\frac{\chi_{st}}{2a}\right)^{1/2} . \tag{2.59}$$

Peters [22] also defined a reaction zone thickness $(\Delta Z)_R$ as

$$(\Delta Z)_R = \varepsilon(\Delta Z)_F , \tag{2.60}$$

where ε is the oxidation layer thickness (defined in [48] and shown to be proportional to ${\chi_{st}}^{1/4}$) and can be scaled with its value at extinction ε_q

$$\frac{\varepsilon}{\varepsilon_q} = \left(\frac{\chi_{st}}{\chi_q}\right)^{1/4} , \tag{2.61}$$

leading to

$$\frac{(\Delta Z)_R}{(\Delta Z)_F} = \varepsilon_q \left(\frac{\chi_{st}}{\chi_q}\right)^{1/4} . \tag{2.62}$$

$(\Delta Z)_F$ can be compared to the mixture fraction fluctuations at stoichiometric conditions (corresponding by definition to the Root Mean Square (RMS) of the variance, $(\widetilde{Z''^2})_{st}^{1/2}$) to define different regimes in non-premixed combustion. Figure 2.1 presents a log-log diagram of the turbulent non-premixed combustion regimes as a function of the ratio $(\widetilde{Z''^2})_{st}^{1/2}/(\Delta Z)_F$ and the time scale ratio $\chi_q/\widetilde{\chi}_{st}$. For $(\widetilde{Z''^2})_{st}^{1/2} > (\Delta Z)_F$, the fluctuations of the mixture fraction around stoichiometric mixture are not confined close to the reaction zone, leading to the formation of separated diffusion layers (flamelets). On the contrary, when the fluctuations are small (such as in presence of strong mixing or partial premixing), the diffusion layers tend to remain connected. Thus, the criterion $(\widetilde{Z''^2})_{st}^{1/2}/(\Delta\widetilde{Z})_F = 1$ can be used as limit between these two different regimes, separated flamelets and connected flame zones, respectively, as shown in Fig. 2.1. Another quantity that must be taken into account is the scalar dissipation rate. If χ_{st} is too high, quenching occurs, i.e. if $\chi_q/\widetilde{\chi}_{st} < 1$. This regime is denoted as flame extinction in Fig. 2.1. However, it is worth noting that in real burners, the flame structure may depend on the spatial location and different regimes can be encountered by the same flame [24]. This observation is clearly pointed out in Fig. 2.1, where a schematic of a lifted jet flame is included, showing that local conditions on the centerline of the flame (denoted by a dashed-dot line) covers three different regimes. Extinction conditions are found close to the nozzle because the flame is lifted. At the stabilization location (which defines the flame base) the flame approaches the separated flamelets regime. Farther downstream, the variance of the mixture fraction is reduced to values close to $(\Delta\widetilde{Z})_F^2$ and the corresponding regime is the connected flame

zones regime. The slope of the centerline conditions can be approximated with the value of $-1/2$ in the double-logaritimic plot from the consideration that $(\widetilde{Z''^2})_{st}^{1/2}$ scales as x^{-1} and $\widetilde{\chi}_{st}$ as x^{-2} on the centreline in a jet flame [22]. The combustion diagram shown in Fig. 2.1 has only a qualitative meaning about the different regimes that can be found in a non-premixed flame. The accuracy of these regimes is not discussed here and other diagrams can be defined. For example, Poinsot and Veynante presented different regimes for non-premixed turbulent combustion as a function of the Damköhler number and the turbulent Reynolds number [24]. Chapter 4 presents a more detailed description of lifted flames and the stabilization mechanism involved, providing a discussion about the physics and the numerical strategies adopted to simulate this category of flames.

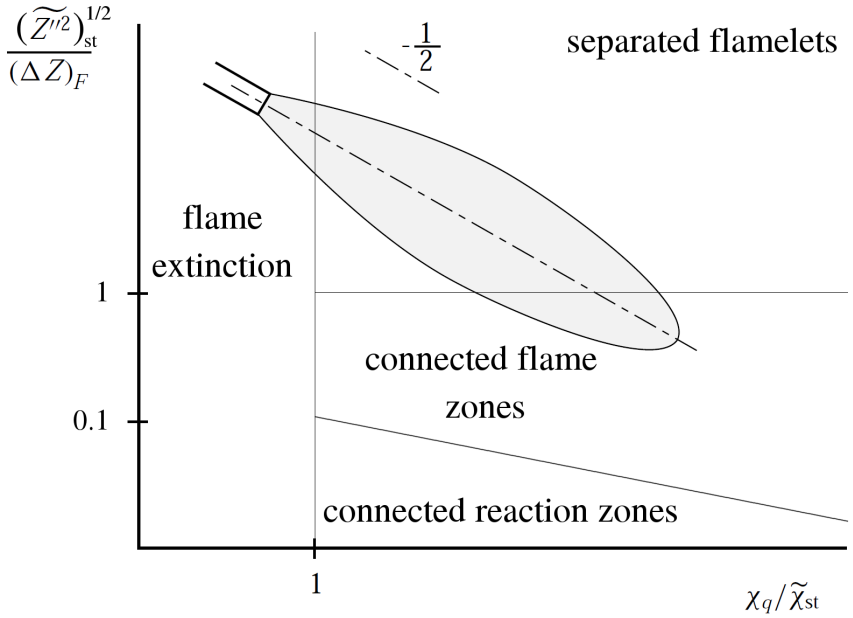

Figure 2.1: Regimes in non-premixed turbulent combustion, scheme extracted from [3].

In the turbulent premixed combustion regime, flame front propagation needs to be accounted for. As a consequence, premixed combustion phenomena have a characteristic velocity scale (the laminar burning velocity) and a characteristic length scale (the flame thickness). These new parameters can be used to characterize the flame/vortex interaction and consequently, the flame structure by defining different regimes in premixed combustion. In the Borghi diagram [49], the turbulence intensity u', normalized by the laminar burning velocity s_L, is plotted versus the ratio between the integral length scale L and the laminar

flame thickness δ (see Fig.2.2). The diagram is divided up into several regions by lines representing values of the Reynolds number, Damköhler number and Karlovitz number. The turbulent Damköhler number is defined as the ratio between the integral time scale and the chemical time scale

$$Da = \frac{t_L}{t_{chem}} = \frac{s_L}{\delta}\frac{L}{u'} \ . \tag{2.63}$$

When the Damköhler number is large, the turbulence is small and does not distort the inner flame structure, i.e. rendering the flame locally laminar. The turbulent Karlovitz number represents the ratio between the chemical time scale and the Kolmogorov time scale

$$Ka = \frac{t_{chem}}{t_\eta} = \frac{\delta}{s_L}\frac{u'}{\eta_k} = \frac{\delta^2}{\eta_k^2} \ . \tag{2.64}$$

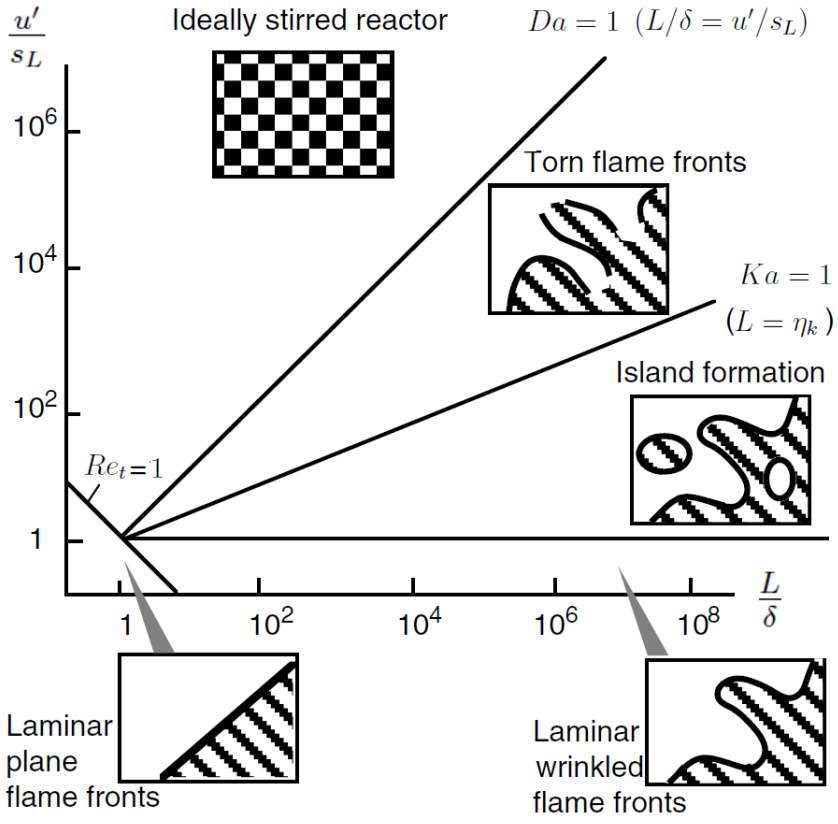

Figure 2.2: Borghi Diagram, extracted from [3].

As shown in Fig.2.2, for $Re_t < 1$ laminar combustion is observed. Below the $Ka = 1$ line ($Ka < 1$), the flame is thin (the flame thickness is smaller than the turbulent length scale) and with a inner structure resembling that of a laminar flame (the chemical time scale is the shortest time scale). For this reason the regime is characterized by island formation and is called flamelet regime. The region above the $Da = 1$ line is characterized by $Da < 1$: the time needed for chemical change is larger than the fluid motion. As a consequence, turbulent eddies penetrate the reaction zones which becomes very broad (fast mixing). This regime is called well-mixed reactor or perfectly stirred reactor regime. In between, is the torn flame front regime. Within this regime, the turbulence interacts with the flame and eddies that have length scale less than δ are embedded in flame front [3].

The flamelet model of premixed flames is analogous to the flamelet model of non-premixed flames. There is a general agreement that the flamelet concept is applicable in the zone of large Damköhler numbers [3]. The model is either implemented using a progress variable approach or a G-equation approach to characterize the extent to which combustion has been completed [24]. In the progress variable approach, a reaction progress variable c is used to describe the progress of combustion and is defined to be zero in unburned reactants and one in fully-burned products. Evolution of the progress variable is described by a transport equation

$$\frac{\partial(\overline{\rho}\widetilde{c})}{\partial t} + \frac{\partial}{\partial x_i}(\overline{\rho}\widetilde{u}_i\widetilde{c}) = -\frac{\partial}{\partial x_i}\left(\overline{\rho}\widetilde{u_i''c''}\right) + \frac{\partial}{\partial x_i}\left(\overline{\rho}D\frac{\partial\widetilde{c}}{\partial x_i}\right) + \overline{\dot{\omega}}_c \ , \tag{2.65}$$

which, contrary to the mixture fraction transport equation (see Eq. 2.51), includes a source term, $\overline{\dot{\omega}}_c$. Equation 2.65 has two unclosed terms: $\overline{\dot{\omega}}_c$ and $\frac{\partial}{\partial x_i}\left(\overline{\rho}\widetilde{u_i''c''}\right)$. The latter is the turbulent scalar flux, which is usually modeled by using a gradient assumption for a passive scalar (see Eq. 2.22). The mean reaction rate can be specified in several ways. In the Bray-Moss-Libby (BML) model [50], an equation can be derived for reaction rates

$$\overline{2\rho D\nabla c \cdot \nabla c} = (2c_m - 1)\overline{\dot{\omega}}_c \ , \tag{2.66}$$

where $c_m = \frac{\int_0^1 c\dot{\omega}\overline{P}(c)dc}{\int_0^1 \dot{\omega}\overline{P}(c)dc}$ is a progress variable characterizing the chemical kinetics ($c_m \approx 3/4$ [51]). The mean reaction rate can be expressed in terms of the scalar dissipation

$$\overline{\dot{\omega}}_c = 2\frac{\overline{\rho\chi_c}}{2c_m - 1} \ . \tag{2.67}$$

The scalar dissipation rate can be evaluated by solving a transport equation or by modelling

$$\overline{\rho\chi_c} = \frac{\overline{\rho}\widetilde{c''^2}}{t_t} \ , \tag{2.68}$$

where t_t is the turbulent time scale and can be estimated from the turbulent kinetic energy $\widetilde{k}$ and its dissipation rate $\widetilde{\varepsilon}$, $t_t = \widetilde{k}/\widetilde{\varepsilon}$. Assuming that the flame front is infinitely thin (i.e. $c = 0$ or $c = 1$), $c^2 = c$ is valid and $\overline{\rho}\widetilde{c''^2}$ is given as

$$\overline{\rho}\widetilde{c''^2} = \overline{\rho\left(c - \widetilde{c}\right)^2} = \overline{\rho}\left(\widetilde{c^2} - \widetilde{c}^2\right) = \overline{\rho}\widetilde{c}\left(1 - \widetilde{c}\right) \ , \tag{2.69}$$

Equation 2.67 becomes

$$\overline{\dot{\omega}}_c = \frac{2}{2c_m - 1}\overline{\rho}\frac{\widetilde{\varepsilon}}{\widetilde{k}}\widetilde{c}\left(1 - \widetilde{c}\right) \ . \tag{2.70}$$

Using the progress variable, the average of any quantity may be evaluated by conditional averaging (see Eq. 2.55).

Another model, also valid under the flamelet assumption, is the Flame Surface Density (FSD) model. In this approach, the mean reaction rate is calculated as the product between the flame surface density (flame area per unit volume) Σ and the flame reaction rate [24]

$$\overline{\dot{\omega}}_c = \rho_u \langle s_c \rangle \Sigma \ , \tag{2.71}$$

where ρ_u is the density of the unburnt mixture, s_c the flame consumption rate and $\langle\rangle$ indicates the average operation along the flame surface. The flame consumption rate can be related to the unstretched laminar flame speed s_L by the introduction of the stretch factor I_0 [52]

$$\langle s_c \rangle = I_0 s_L \ . \tag{2.72}$$

The flame surface density can be approximated through an algebraic model or by solving a transport equation, as described by Poinsot and Veynante [24].

The flamelet model can incorporate realistic chemistry in the framework of a mixture fraction or progress variable approach, namely the use of Eq. 2.55. However, it considers that the flame is thin relative to the Kolmogorov scale ($\delta << \eta_k$). This model yields good results at a small expense, but lacks of generality since the flamelet assumption must be satisfied.

2.3.3 Transported PDF model

A more general approach can be found in the transported PDF method, which is based on the same idea of calculating average quantities through the integration over the joint PDF (see Eq. 2.55), but a transport equation for the joint PDF of velocity, scalar dissipation and composition is derived and solved, instead of assuming a specific form of the PDF.

This model was first proposed by Pope [53] and has the benefit of providing a closed form for the chemical source term and it can be used for both premixed and non-premixed combustion, providing an accurate representation of the joint PDF of several scalar variables [54]. However, the joint PDF transport equation presents an unclosed term that requires modelling, i.e. the mixing term. This is due to the fact that the one-point PDF formalism is assumed to be sufficient to describe the flow. This is true for for the chemical reaction rate since it depends on the local composition, but not for the diffusion spatial gradient terms, for they require spatial informations [22, 24]. Further, transported PDF approaches are characterized by a high dimensionality and finite difference or finite volume methods are not suitable for solving this problem, because the computational cost increases exponentially with the number of scalars [55]. Pope [55, 56] solved the transport equation stochastically using Monte-Carlo simulation techniques, since the memory requirements of such methods depend linearly on the dimensionality of the problem [22]. In this approach, a large number of stochastic particles, subjected to conservation principles, approximate the evolution of the joint PDF. More recently, Valiño [57] and Sabel'nikov and Soulard [58] developed an alternative model independently, which is based on stochastic fields instead of the particle representation. In this method, the PDF of each scalar quantity is represented by an ensemble of N stochastic fields for which a transport equation is solved. The mean quantities are then calculated by doing an ensemble averaging over the fields. Mass conservation and bound properties of the modelled PDF are preserved in the solution of each stochastic field. This approach has the benefits of having no spatially sampling errors, since the stochastic fields are are continuous and differentiable in space, and it generates density and thus pressure fields that are smooth in space [59].

The mathematical robustness and the general validity of PDF methods render such models very attractive in terms of partially premixed flame simulations. However, they are more computationally expensive compared to other turbulent combustion approaches and the closure of the mixing term is not simple.

2.3.4 Conditional Moment Closure

Another approach that is not restricted by the flamelet assumption is the CMC model. CMC methods were first proposed by Bilger [60] and Klimenko [61] independently. The main idea is to use Eq. 2.55, but with the integrand specified in terms of conditional averages, supported by the observation that in non-premixed systems the fluctuations about mean properties are significantly reduced after conditioning on a selected scalar. The conditioning is done on the mixture fraction for non-premixed combustion or progress

variable for premixed combustion. The mean value of the scalar field f is obtained by

$$\widetilde{f} = \int_0^1 \langle f|\eta\rangle \tilde{P}(\eta) d\eta \ . \tag{2.73}$$

The conditional average $Q(\eta)$ of the quantity f conditioned on the mixture fraction Z, subject to the condition of being equal to η, is

$$Q(\eta) = \langle f|Z = \eta\rangle \equiv \langle f|\eta\rangle \ . \tag{2.74}$$

In practice, the mixture fraction dimension is discretized in a determined number of bins and the conditional average is the average value in each bin. The conditional quantities are computed by solving transport equations in sample space. These CMC transport equations present additional unclosed terms, such as conditional velocity, $\langle u_i|\eta\rangle$, conditional turbulent flux, $\langle u_i'' Y_k''|\eta\rangle$ and conditional chemical source term, $\langle \dot{\omega}_k|\eta\rangle$. A key assumption of CMC is that fluctuations about the conditional mean are small. First order CMC hypothesis is often used to close the chemical source term, that is the scalar variance about the conditional average is negligible and the conditional-averaged chemical source terms are closed by conditional-averaged scalars

$$\langle \dot{\omega}_k|\eta\rangle \approx \dot{\omega}(\langle T|\eta\rangle, \langle Y_k|\eta\rangle, \langle \rho|\eta\rangle) \ . \tag{2.75}$$

First order closure may not be appropriate when the effects of conditional fluctuations are expected to be significant, as near flame quenching or extinction [62]. The second order CMC approach may be preferred in these cases, as it provides better predictions for auto igniting cases [63] and in the context of flames characterized by extinction/reignition [64, 65].

The CMC method is well advanced for non-premixed flames, providing good results in terms of finite-rate chemistry effects, ignition and extinction and soot predictions ([66, 67, 68]), but it is in early stages for premixed flames, primarily due to issues related to closure of the conditional scalar dissipation rate and the additional complexity of having a non-conserved conditioning variable [20]. Martin et al. [69] applied this methodology to a lean premixed flame with encouraging results, but a numerical simulation with satisfying results is still lacking. Only recently, some promising CMC results for premixed combustion have been shown by Amzin et al. in numerical simulation of stoichiometric pilot stabilized Bunsen flames [70]. The CMC method can be computationally expensive not only because of the unclosed terms in CMC transport equations, but also because of the need to directly solve CMC equations for each species in space, time and sample space (mixture fraction or progress variable for non-premixed or premixed combustion, respectively).

2.3.5 Multiple Mapping Conditioning

Multiple Mapping Conditioning (MMC), introduced by Klimenko and Pope [71], is derived as a combination of the PDF and the CMC combustion models. It resolves the conditional expectations of all scalars conditioned on a set of reference variables and implicitly provides the joint PDF of the conditioning scalars and the conditioned dissipation rates. By combining the advantages of the PDF and CMC methods, it appears to be the most promising model, in terms of perfect closure and computational efficiency. However, its practical implementation for complex flow geometries is not easy [67]. MMC has been successfully applied to non-premixed flames [72, 73]; however, its extension to premixed combustion has not yet been achieved.

2.3.6 Conditional Source-term Estimation

Another model that uses conditional averages to achieve closure of the chemical reaction source term is the CSE approach. CSE uses the same CMC hypothesis for closing chemical source terms, where the conditional average of the chemical source term is determined by first order averages [60]. An ulterior simplification is made in the CSE approach, i.e. the conditional averages are homogeneous within a known ensemble of points (computational cells). Thus, conditional values are obtained by inverting an integral equation instead of solving transport equation (as in CMC). CSE was originally proposed by Bushe and Steiner for LES of non-premixed turbulent combustion [74]. It has been extended to the RANS framework of non-premixed flames [75, 76] and recently to a premixed configuration [77, 78]. Further details of this model are presented in Chapters 3 to 5.

2.4 Partially premixed combustion models

The main idea of elaborating a partially premixed model is based on a combination of existing models for premixed and non-premixed regimes. The flamelet model has been the main candidate because of its successful applications in both premixed and non-premixed configurations. However this combustion model relies on the limiting assumptions of the flamelet regime. More general methods have been introduced in this direction, such as PDF models, CMC and CSE. The latter has been demonstrated to be competitive in terms of computational cost with the flamelet model for non-premixed flames ([79, 76]) and for premixed flames (see Section 3.3 and [77, 78]).

Partially premixed systems are characterized by variable stoichiometric ratios; for this reason the usual formulation based on either a conserved scalar or a progress variable no longer applies [80]. Furthermore, since different regimes can occur locally, the assumption of fast chemistry associated with large Damköhler numbers may result in inappropriate and finite rate kinetic effects may need to be included. The numerical strategies lie in extending the models described in Section 2.3 to a partially premixed approach. A first approximation consists of considering the premixed/non-premixed domain as a combination of a premixed flame and a diffusion flame. The problem is then divided into premixed and non-premixed parts and an appropriate blending function used to choose the respective model [81]. This non-premixed/premixed blending strategy has been investigated in the context of the flamelet model. Bradley et al. [82] implemented a strained premixed flamelet model constrained within specified flammability limits and the mean heat release rate was calculated by integrating over the PDF of both the reaction progress variable and mixture fraction. The predicted lift-off heights were in reasonable agreement with the experimental data, but the formulation was mostly based on premixed flame propagation. The description was further improved by allowing for premixed flame extinction [83]. Combined with a Reynolds stress turbulence model and second order closure for the temperature, good predictions for the lift-off height and blow-off velocity were shown. Another flamelet model implementation was proposed by Müller et al. [84] and further modified by Chen et al. [85]. Two scalars were considered, mixture fraction to indicate the local equivalence ratio and G to give the location of the premixed flame front. The results for the lift-off height were in good agreement with the experimental values for the flames selected. In these previous studies [85, 84], the main issue was related to the calculation of the turbulent burning velocity needed in the G transport equation [22]. Outside the flamelet model, a complete two-conditional CMC has never been fully implemented in RANS calculations or LES due to the complex closure of many terms in the CMC transport equations. Only a priori tests using DNS can be found where the sensible enthalpy [86] and the scalar dissipation [7] served as a second conditioning variable.

2.5 Summary

This chapter presented relevant background information about turbulent combustion modelling. Traditionally, combustion models are divided into two categories: non-premixed and premixed combustion models. Such a distinction does not apply for partially premixed flames and a combination of the two different approaches characterizes partially premixed combustion modelling. The flamelet model has been successfully applied to partially pre-

mixed flames, due to its feasibility for prediction of both premixed and non-premixed approaches. However, it is limited by the flamelet assumption and such a limitation should be overcome, especially in a partially premixed context. CMC could be a good candidate for modelling of partially premixed combustion, but it is expected to be computationally expensive and has shown some issues for premixed flames. CSE is a simplified version of CMC and has been shown to provide promising results for both premixed and non-premixed flames [77, 75, 78, 76]. Before implementing such a model for partially premixed flames, a verification on turbulent premixed flames is necessary since only one application [78] of this method in a simple configuration has been done so far. In the following chapter, a description of the CSE approach and its application to a bluff body premixed flame are provided.

Chapter 3

CSE for turbulent premixed combustion

CSE has been shown to work well for diffusion flames [87, 79, 76]. Recently Salehi et al. [78] have applied CSE to simulate a turbulent premixed flame with promising results, but applications of this method to complex geometries, such as bluff body configurations, have not yet been performed. In this chapter, a study of a bluff body premixed flame using CSE is presented.

3.1 Formulation

CSE is derived starting from the first order closure of the the conditional average of the chemical source term, as commonly stated in CMC [62]. Thus, the conditional reaction source term can be evaluated using averaged quantities

$$\langle \dot{\omega} | c^* \rangle \approx \dot{\omega}(\langle T | c^* \rangle, \langle Y_i | c^* \rangle, \langle \rho | c^* \rangle) \ , \tag{3.1}$$

where c^* is a conditioning variable and the terms on the RHS are the conditional temperature, mass fraction of species i and density, respectively. In the case of premixed combustion, the normalized mass fraction of a product species, such as CO_2, can be used used as conditioning variable

$$c^* = Y_{CO_2}/Y_{CO_2 eq}, \tag{3.2}$$

where $Y_{CO_2 eq}$ is the mass fraction of CO_2 at chemical equilibrium. c^* has the property of being equal to zero in fresh gases and unity for burnt gases in premixed configurations. In cases far from extinction and reignition, first order closure is justifiable as the fluctuations about the conditional averages are small [88, 89, 62]. For this reason, first order closure is applied for $\langle \dot{\omega} | c^* \rangle$, i.e. the scalar variance about the conditional average is assumed to be negligible. The unconditional mean chemical source term is related to the conditional value via,

$$\overline{\dot{\omega}} = \int_0^1 \langle \dot{\omega} | c^* \rangle (\vec{x}; c^*) P(c^*) dc^*, \tag{3.3}$$

where $P(c^*)$ is a presumed PDF of c^* based on the mean, $\widetilde{c}$, and the variance, $\widetilde{c''^2}$. Different forms of the presumed PDF can be adopted in premixed combustion, such as the β distribution [90], the two Dirac δ functions [91] or the modified laminar flamelet PDF [92]. In the present formulation, the modified laminar flame PDF is used as it is shown to provide a better description of the progress variable statistics compared to the β-PDF [92, 4]. Further details about this approach are presented in Section 3.1.3. In CSE, the conditional averages are assumed to be homogeneous within a known ensemble of points defined using the computational cells in the mesh. The conditional averages have been shown to vary much less in space [93] and this property is commonly used in CMC implementations [94, 95]. In previous CSE simulations for jet flames, the ensemble of points was selected to be either a single centre plane including all the computational cells in the axial and radial directions [78], or a set of planes defined in the axial direction [76]. In the present study, the entire computational domain (one plane) is defined for the ensemble of points. However, several planes are also tested and the present results for the unconditional scalars are shown to be independent of the number of ensembles, consistent with the observation reported in [76]. The conditional values are obtained by inverting an integral equation following

$$\widetilde{f}(\vec{x}_j, t) = \int_0^1 \langle f | c^* \rangle (c^*; t) \tilde{P}(c^*; t, \vec{x}_j) dc^* \qquad j \in J \ , \tag{3.4}$$

where t is the time, $\vec{x}_j$ is the spatial coordinate of the j-th point in the ensemble J and f represents any scalar. On the Left Hand Side (LHS) of Eq. 3.4, the unconditional quantity is known (in the case of species mass fraction a transport equation is solved, following Eq. 2.20), while on the RHS the conditional term inside the integral is unknown. Equation 3.4 is a Fredholm integral equation of the first kind with $\tilde{P}(c^*; \vec{x}, t)$ as the kernel. It can be discretized using M bins for the conditioning variable and in matrix form the system

becomes

$$\vec{b} = \mathbf{A}\vec{\alpha}, \quad A_{j,m} = \int_{c_1}^{c_2} \tilde{P}(c^*; \vec{x}_j, t) dc^*, \tag{3.5}$$

where $b_j = \widetilde{f}(\vec{x}_j, t)$ and $\alpha_m = \langle f | c_m^* \rangle$. The solution for the conditional average $\vec{\alpha}(t) = \mathbf{A}^{-1}\ \vec{b}(t)$ is typically ill-posed, as is often the case with integral equations [96]. A regularization approach is adopted in order to stabilize the ill-posedness. In practice, stability is imposed to the system by specifying some additional information in order to single out a solution which is close to the desired, unknown, exact solution [97].

3.1.1 Regularization methods

In the present work, two different regularization methods are tested, Tikhonov regularization technique [98] and Truncated Singular Value Decomposition (TSVD) [99]. The singular value decomposition of an $n \times M$ matrix $\mathbf{A}$ $(n > M)$ is

$$\mathbf{A} = \mathbf{U} \begin{pmatrix} \sigma_1 & & & & & & \\ & \sigma_2 & & & & & \\ & & \ddots & & & & \\ & & & \sigma_M & & & \\ & & & & 0 & & \\ & & & & & \ddots & \\ & & & & & & 0 \end{pmatrix} \mathbf{V^T}, \tag{3.6}$$

where σ_i are the singular values disposed aligned in decreasing order, while $\mathbf{U}$ and $\mathbf{V}$ have orthogonal columns so that $\mathbf{U}^T\mathbf{U} = 1$ and $\mathbf{V}^T\mathbf{V} = 1$. The solution of Eq. 3.5 can be obtained using

$$\vec{\alpha} = \sum_{i=1}^{m} \frac{U_i^T \cdot b}{\sigma_i} V_i. \tag{3.7}$$

In the case of $\mathbf{A}$ having zero singular values, Eq. 3.7 gives division by zero and an infinite set of solutions exists that satisfy Eq. 3.5 ($\mathbf{A}$ is rank-deficient). This case corresponds to type (ii) ill-posedness, as defined by Hadamard [100], where the solution is not unique. This would typically occur when the flame is in the flamelet regime: the PDF of the reaction progress variable is characterized by two delta functions and as a result, the major part of the integral domain in Eq. 3.5 is equal to zero and the matrix $\mathbf{A}$ is very sparse. In this

particular circumstance, the flamelet solution is sufficient and the integral equation is not required to be inverted [78].

Further, small singular values of $\mathbf{A}$ can amplify any artifact in b in Eq. 3.7 and the solution is unstable to small perturbations, corresponding to type (iii) ill-posedness (according to Hadamard [100]). In this context, a regularization approach to stabilize type (iii) ill-posedness is required. Equation 3.8 shows the regularization approach proposed by Tikhonov and is based on an *a priori* knowledge of the solution [98]. The Tikhonov method consists of solving the augmented minimization problem written as

$$\min \left\{ \left\| \mathbf{A}\vec{\alpha} - \vec{b} \right\|_2^2 + \lambda^2 \left\| \vec{\alpha} - \vec{\alpha}_0 \right\|_2^2 \right\}, \tag{3.8}$$

where the L-2 norm operator, $\|...\|_2$ is introduced. In Eq. 3.8, the second term is the regularization term including $\vec{\alpha}_0$, *a priori* knowledge of the solution and λ, the regularization parameter. Several initial solutions for $\vec{\alpha}_0$ are possible. For example, Grout et al. [101] used the previous time step solution in unsteady RANS. In the present study, the strategy proposed by Jin et al.[92] and implemented in RANS for turbulent premixed combustion by Salehi et al.[78] is adopted: the a-priori solution is a one-dimensional unstrained laminar premixed flame solution.

Another common approach consists of sing the TSVD [99]. In this method, the expansion Eq. 3.7 is simply truncated and written as

$$\vec{\alpha}^* = \sum_{i=1}^{k} \frac{U_i^T \cdot b}{\sigma_i} V_i, \tag{3.9}$$

where $k < m$ corresponds to the regularization parameter in TSVD. If k decreases, small singular values are eliminated resulting in more filtering of the solution. There is an optimum value for the regularization parameter (λ in Tikhonov method and k in TSVD) which can be found by using the L-curve approach [97]. Further discussion on these two regularization methods is presented in Section 3.3.1.

Once the conditional averages are obtained by solving Eq. 3.5, the unconditional mean chemical source term is calculated using Eq. 3.3. The advantages of this method rely on the fact that it does not require the constraining assumptions of the fast chemistry and does not have the necessity of solving conditional average transport equations as in CMC.

3.1.2 Chemistry tabulation

For computational efficiency, the hyper-dimensional manifold based on detailed chemistry is commonly reduced to low-dimensional manifolds in composition space [102]. Huang and

Bushe [87] applied the Trajectory Generated Low-Dimensional Manifold (TGLDM) technique for non-premixed flames using CSE. Autoignition trajectories were used to generate the manifold by solving the following equation for species k

$$\rho \frac{\partial Y_k}{\partial t} = \dot{\omega}_k \ . \tag{3.10}$$

In the context of premixed combustion, Van Oijen and de Goey [103] built a chemistry database by using the Flame-Generated Manifold (FGM) method. This approach is implemented in the present work. Following the methodology proposed by Van Oijen and de Goey [103], the steady-state governing equations of one dimensional laminar unstrained premixed flame are solved to generate different trajectories. The mass fraction transport equation for species k reads

$$\rho_u s_L \frac{\partial Y_k}{\partial x} - \frac{\partial}{\partial x}\left(\rho D_k \frac{\partial Y_k}{\partial x}\right) = \dot{\omega}_k \ , \tag{3.11}$$

where ρ_u is the density of unburned gases, s_L the laminar flame speed and D_k the diffusivity of species k. The effect of mass transport is included in the governing equations and no special treatment is required for the low temperature conditions, compared to the TGLDM technique [102] used by Huang and Bushe [76]. The trajectories are obtained by varying the inlet conditions either doing an element balance for a mixture of the major species or using constrained equilibrium composition. The resulting FGM data base is parametrized as a function of two input variables, CO_2 and H_2O mass fractions. The FGM trajectories applied for methane/air reaction system at an equivalence ratio of 0.75 are shown in Figure 3.1. In practice, a cubic spline interpolation of the points that belong to different trajectories for a given value of CO_2 is performed in order to determine the reaction rates from the table. GRI-MECH 3.0 [104] is adopted as a detailed mechanism for methane-air combustion. As specified in Section 3.1, the progress variable is chosen to be the normalized CO_2 mass fraction, c^*. Thus, the only unknown parameter required to determine the conditional chemical reaction rate is $\langle Y_{H_2O}|c^*\rangle$. This also implies that only one integral equation is solved in CSE for the present case. If the progress variable were not equal to the normalized mass fraction of CO_2, $\langle Y_{CO_2}|c^*\rangle$ would also be needed and would be found by inverting Eq. 3.4.

3.1.3 Presumed PDF

In CSE, the role of the PDF is crucial, since it is used in both the inversion process (Eq. 3.5) and the calculation of the unconditional reaction source term (Eq. 3.3). Thus, a good approximation of the PDF is needed.

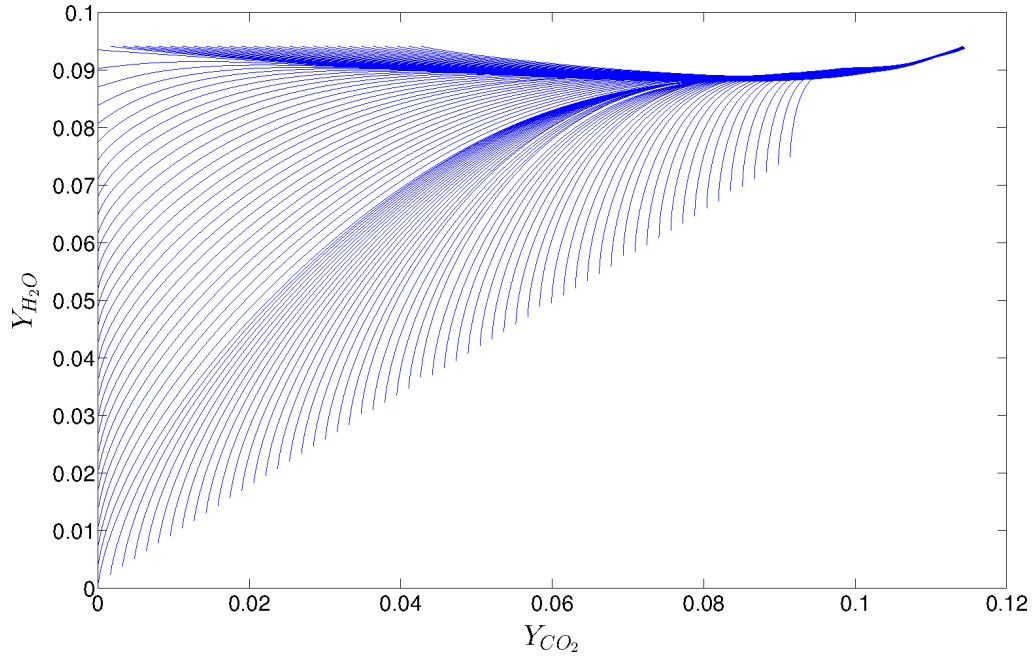

Figure 3.1: Manifold generated by solving Eq. 3.11.

In combustion applications, PDF functions present common features [24] and a fixed shape for the PDF, based on one or two parameters, can be adopted [105]. In particular, the β-functions are able to change continuously from PDF shapes with one or two peaks to gaussian shapes [24]. For this reason, they are usually selected in the case of non-premixed simulations: they approximate well the behaviour of Z ranging from the distribution for unmixed reactants (single or double-delta functions) to that for well-mixed reactants (Gaussian) [90]. In a premixed situation, two main regimes can be defined: one with a large Damköhler number (defined as the ratio between the mixing time-scale to the chemical time-scale, Eq. 2.63) where the variance of the progress variable is high and the PDF becomes two delta functions [91]; the other regime corresponds to a low value of the Damköhler number, denoted by a thick reaction zone and a narrow Gaussian shape PDF. The β-PDF could match these two extremes, but is not able to describe a distribution where the intermediate region (between 0 and 1) is not null, such as in the interior of the flame. Bray et al. [23] proposed an alternative form for the PDF, based on a laminar flamelet shape. It is valid in the flamelet regime and relies on the fact that for a very thin flame, the iso-surfaces of the progress variable turn out to be parallel and the interior part of the PDF distribution is proportional to the gradient of the progress variable. The PDF

of c^* is calculated following

$$\tilde{P}(c^*, x, t) = A\delta(c^*) + Bf(c^*) + C\delta(1 - c^*), \tag{3.12}$$

where $f(c^*)$ is related to the solution of an unstrained laminar premixed flame by

$$f(c^*) = \frac{1}{\nabla c^*}. \tag{3.13}$$

In Eq. 3.12, the three coefficients A, B and C are evaluated by using the first three moment equations of c^*

$$\int_0^1 \tilde{P}(c^*)dc^* = 1 = A + B\int_0^1 f(c^*)dc^* + C \ , \tag{3.14}$$

$$\int_0^1 c^*\tilde{P}(c^*)dc^* = \overline{c} = B\int_0^1 c^* f(c^*)dc^* + C \ , \tag{3.15}$$

$$\int_0^1 c^{*2}\tilde{P}(c^*)dc^* = \overline{c^2} = B\int_0^1 c^{*2} f(c^*)dc^* + C \ . \tag{3.16}$$

It follows that, given the mean of the progress variable, $\overline{c}$, the three coefficients can be calculated as

$$B = \frac{\overline{c} - \overline{c^2}}{I_1 - I_2} \ , \tag{3.17}$$

$$C = \frac{\overline{c^2}I_1 - \overline{c}I_2}{I_1 - I_2} \ , \tag{3.18}$$

$$A = 1 - BI_0 - C \ , \tag{3.19}$$

where $I_0 = \int_0^1 f(c^*)dc^*$, $I_1 = \int_0^1 c^* f(c^*)dc^*$ and $I_2 = \int_0^1 c^{*2} f(c^*)dc^*$. However, the PDF, as shown in Eq. 3.12 can be defined only for a small range of the mean and the variance [4]. Another limitation of Eq. 3.12 is related to the behaviour of the PDF for $c \to 0$ and $c \to 1$, since it rises towards infinity. In order to improve this formulation, Jin et al. [92] proposed a modified version where one or both the δ functions are eliminated and the function $f(c^*)$ is truncated by defining four possible cases: the laminar flamelet PDF (Equation 3.12); the laminar flamelet PDF with only one delta function at $c^* = 0$ and then the same laminar inner distribution until $c^* = c_2 < 1$; the laminar flamelet PDF starting from $c^* = c_1 > 0$ and ending with a delta function at $c^* = 1$; the inner distribution function from $c_1 > 0$ to $c_2 < 1$. These cases are illustrated in Figure 3.2 [4]. In the present study, the modified version [92] is implemented and the value of 0.75 for the equivalence ratio is used to define the shape of $f(c^*)$.

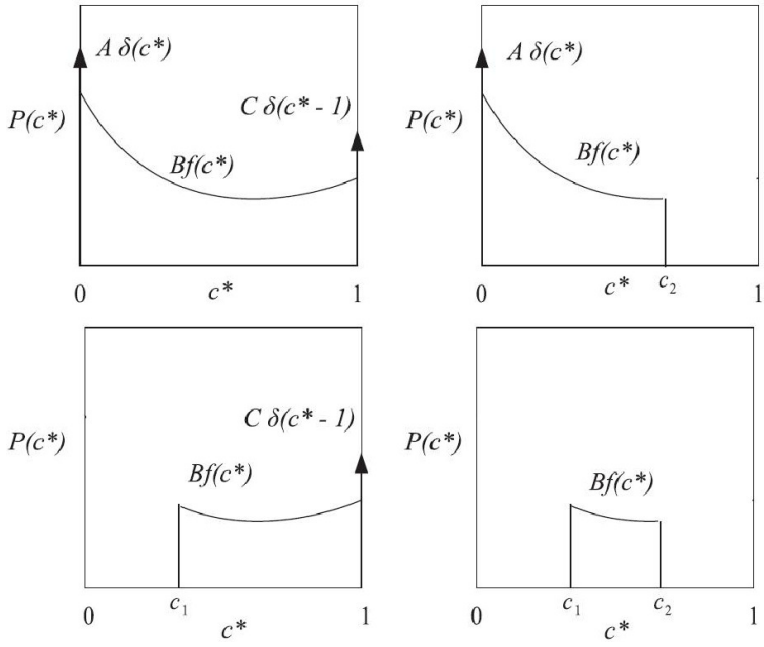

Figure 3.2: Four possible cases of the modified laminar flamelet PDF [4].

3.1.4 CSE method summary

Figure 3.3 shows the interactions between the CSE-FGM combustion model and the CFD code. The CFD section solves the transport equations for the mean flow, turbulence quantities, the unconditional Favre averaged species mass fractions, the progress variable ($\widetilde{c}$) and its variance ($\widetilde{c''^2}$). In particular, the mass fraction of H_2O ($\widetilde{Y}_{H2O}$), $\widetilde{c}$ and $\widetilde{c''^2}$ are supplied to the CSE routine. The PDF is determined using a presumed form based on $\widetilde{c}$ and $\widetilde{c''^2}$ [92, 4] and represents an input for CSE. The PDF sub-model forms the kernel of the inverse problem (matrix $\mathbf{A}$ in Eq. 3.5). The CSE module calculates the conditional averages starting from the unconditional values and the PDF by solving Eq. 3.5. This is the inversion process involving regularization as described in Section 3.1. Chemistry is tabulated as a function of two variables, Y_{CO_2} and Y_{H_2O} using the FGM technique [103]. From the chemistry table, the conditional reaction rates of species are retrieved. The unconditional values are calculated by integrating with the PDF over the entire c^* sample space, as shown in Eq. 3.3 and are returned to the CFD code to update the source terms and solve the unconditional Favre averaged species transport equations until convergence is reached. The procedure adopted is similar to that of Salehi et al. [78].

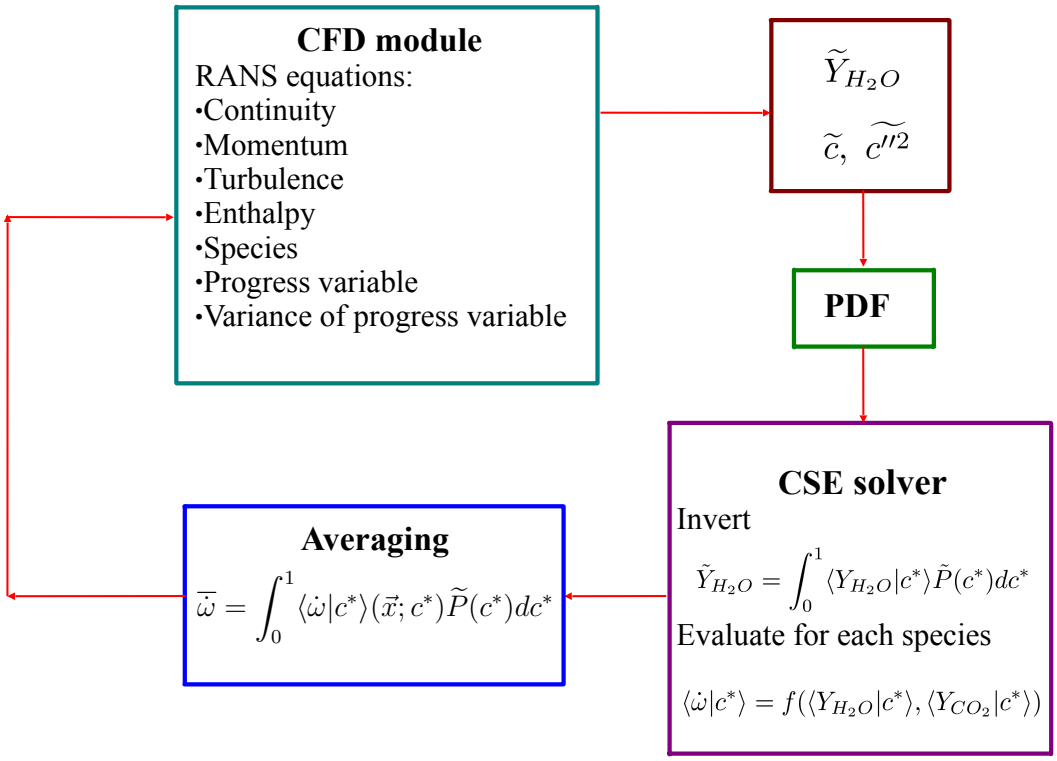

Figure 3.3: CSE-FGM simulation code structure.

The current implementation of CSE-FGM may be compared with that of flamelet models. In contrast to CSE-FGM, flamelet tabulations are only functions of the progress variable (they may be generated for different equivalence ratios [106], radiation losses [107] and strain effects [108]) and do not use any inversion technique. The species mass fractions or reactions rates in the progress variable space are directly retrieved from the chemistry table obtained from the solution of a one-dimensional premixed flame. In contrast to the flamelet model, the conditional averages obtained in CSE are directly evaluated using a regularization technique and may change according to the turbulent flowfield. For each simulation the regularization method provides one unique and stable converged solution for the conditional averages.

3.2 Computational Details

The CSE implementation presented in Section 3.1 is adopted in numerical simulations of a premixed bluff body burner. Computational details are provided in this section.

3.2.1 Experimental conditions

The Cambridge University burner simulated in this work consists of a stainless steel conical bluff body (45° half-angle) with diameter $d = 25$ mm, concentrically fitted within a pipe of diameter $D = 35$ mm [109, 5]. The burner exit is profiled to a knife-edge and is open to atmosphere. The selected flame is unconfined and premixed burning a methane/air mixture at a an equivalence ratio of 0.75 in ambient conditions, far from blow-off. The bulk velocity (axial velocity around the bluff body entering the combustion chamber), U_b, is 21.6 m/s with an uncertainty of 3% (flame noted 'A1' in [5]), corresponding to a Reynolds number of approximately 35,000. This burner is shown schematically in Fig. 3.4.

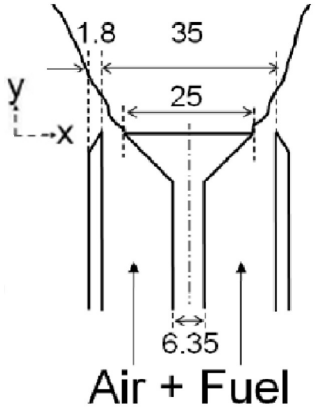

Figure 3.4: Schematic of the bluff body combustor, reproduced from [5]. All dimensions in mm.

3.2.2 CFD calculations

The computational domain is cylindrical with a radius of 140 mm and total length of 450 mm, as presented in Fig. 3.5. The geometry is created as a wedge of a small angle (5°) and 1 cell thick running along the plane of symmetry, thus the simulations are run in two

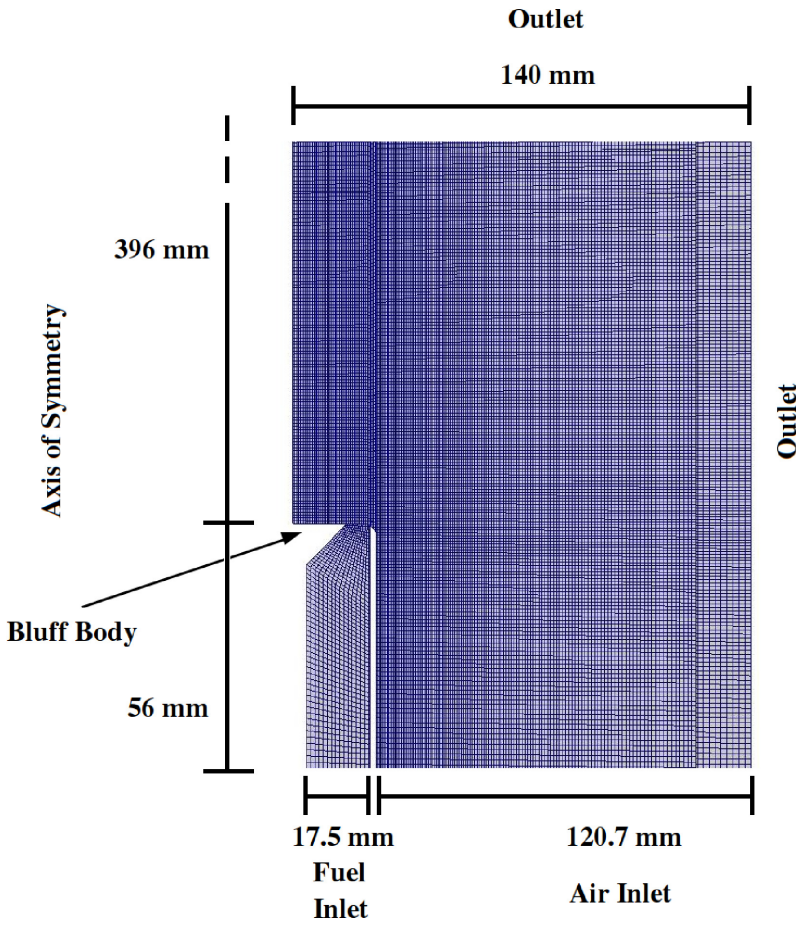

Figure 3.5: Computational domain showing the boundary conditions and dimensions (not to scale).

dimensions. The grid is nonuniform, with high a density of grid points close to the bluff body and between 0 and 25 mm in the radial direction, where the flame is supposed to develop. The current grid consists of 90,240 cells. Further grid refinement was tested and the present results are found to be grid independent. The inlet boundary conditions are placed 56 mm upstream of the burner exit. Premixed fuel and air is supplied at an axial velocity of 10.69 m/s and temperature of 298 K. The inlet turbulence intensity is set equal to 10%, while the integral length scale is equal to 5 mm (radial dimension at the burner exit). Adiabatic and no-slip conditions are applied to the walls. Atmospheric value of the pressure is set at the outlet.

RANS flow equations and continuity are solved by a finite volume low-Mach number pressure based approach using OpenFOAM [110]. Transport equations for the average mass fraction of major species, i.e. methane (CH_4), oxygen (O_2), water (H_2O), carbon dioxide (CO_2) and carbon monoxide (CO) are included. The transport equation for a density-weighted average species, i, mass fraction is given by

$$\frac{\partial(\overline{\rho}\widetilde{Y}_i)}{\partial t} + \frac{\partial}{\partial x_k}(\overline{\rho}\widetilde{u}_k\widetilde{Y}_i) = -\frac{\partial}{\partial x_k}\left(\overline{\rho}\widetilde{u_k''Y_i''}\right) + \frac{\partial}{\partial x_k}\left(\overline{\rho}D\frac{\partial\widetilde{Y}_i}{\partial x_k}\right) + \overline{\dot{\omega}}_i \ . \tag{3.20}$$

In Eq. 3.20, the turbulent scalar flux, $\widetilde{u_k''Y_i''}$is closed by a gradient transport assumption, following Eq. 2.22. This closure neglects counter-gradient diffusion and other models for the turbulent flux may be considered [111]. However, it is also shown that the gradient diffusion occurs when the Bray number is less than unity [111]. The Bray number, B, is defined as

$$B = \frac{\tau s_L}{2\alpha u'} \ , \tag{3.21}$$

where τ is the heat release index, $\tau \equiv (T_b - T_u)/T_u$ where the subscripts b and u refer to burnt and unburnt gas, respectively. s_L is the laminar flame speed, α an empirical constant of order of unity and u' the turbulent velocity fluctuation. For the present case, using the experimental values, the Bray number is found to be smaller than 0.1. The mean chemical source term, $\overline{\dot{\omega}}_i$ is evaluated using CSE-FGM as described in Section 3.1. Further, for comparison purposes, a flamelet model called Presumed Conditional Moments (PCM) [51] is also used. For PCM, a single laminar flame (flamelet) trajectory is considered. In other words, a one-dimensional steady laminar unstrained flame is calculated with detailed chemistry (GRI 3.0 as in FGM). Similar to FGM, the chemical reaction source terms and species mass fractions are tabulated as a function of the progress variable, corresponding to the presumed conditional moments. Thus, in PCM, no inversion is needed and the conditional averages are taken directly from the laminar unstrained flame profiles. To summarize, in PCM, the mean chemical source term is determined by

$$\overline{\dot{\omega}}_i = \int_0^1 \dot{\omega}_i^{flamelet}(c^*)\ P(c^*)\ dc^*, \tag{3.22}$$

and in CSE-FGM

$$\overline{\dot{\omega}}_i = \int_0^1 \dot{\omega}_i^{FGM}(\langle Y_{\mathrm{H_2O}}|c^*\rangle, \langle Y_{\mathrm{CO_2}}|c^*\rangle)\ P(c^*)\ dc^*. \tag{3.23}$$

The presumed form for the PDF of the reaction progress variable (the modified laminar flamelet PDF) is kept the same in both models. In the present work, the integration found

in Eqs. 3.22 and 3.23 is done on the fly, i.e. no look-up table for integrated values is created before the simulations. In the flamelet model, in fact, the integration can be done a priori and an arbitrary number of points for discretization can be used. In the present work, the integration found in Eq. 3.22 is done on the fly (by using M points as in CSE) so that the same integration error is found in both cases. Energy conservation is applied by solving a transport equation for the average total enthalpy. Finally, transport equations for mean and variance of the progress variable, c, are solved in order to determine the presumed PDF model (Eq. 3.3). The transport equation for the mean is given by

$$\frac{\partial(\overline{\rho}\widetilde{c})}{\partial t} + \frac{\partial}{\partial x_i}(\overline{\rho}\widetilde{u}_i\widetilde{c}) = \frac{\partial}{\partial x_i}\left(\frac{\mu_t}{Sc_t}\frac{\partial \widetilde{c}}{\partial x_i}\right) + \overline{\dot{\omega}}_c \ , \tag{3.24}$$

while that for the variance is written as [24]

$$\begin{aligned}\frac{\partial(\overline{\rho}\widetilde{c''^2})}{\partial t} + \frac{\partial}{\partial x_i}\left(\overline{\rho}\widetilde{u}_i\widetilde{c''^2}\right) = &\underbrace{\frac{\partial}{\partial x_i}\left(\overline{\rho D\frac{\partial c''^2}{\partial x_i}}\right) + 2\overline{c''\frac{\partial}{\partial x_i}\left(\rho D\frac{\partial \widetilde{c}}{\partial x_i}\right)}}_{\text{molecular diffusion}} \\ &\underbrace{-\frac{\partial}{\partial x_i}\left(\overline{\rho u_i'' c''^2}\right)}_{\text{turbulent transport}} \underbrace{-2\overline{\rho u_i'' c''}\frac{\partial \widetilde{c}}{\partial x_i}}_{\text{production}} \underbrace{-2\overline{\rho D\frac{\partial c''}{\partial x_i}\frac{\partial c''}{\partial x_i}}}_{\text{dissipation}} + \underbrace{2\overline{c''\dot{\omega}_c}}_{\text{reaction}} \ .\end{aligned} \tag{3.25}$$

This equation can be closed by assuming the following simplifications

- Molecular diffusion terms are negligible compared to turbulent transport, assuming large Reynolds numbers.
- Turbulent transport and production term are closed with gradient assumptions, following Eq. 2.22

$$\overline{\rho u_i'' c''^2} = -\overline{\rho}\frac{\nu_t}{S_{ct_1}}\frac{\partial \widetilde{c''^2}}{\partial x_i} \ , \tag{3.26}$$

$$\overline{\rho u_i'' c''}\frac{\partial \widetilde{c}}{\partial x_i} = -\overline{\rho}\frac{\nu_t}{S_{ct_2}}\frac{\partial \widetilde{c}}{\partial x_i}\frac{\partial \widetilde{c}}{\partial x_i} \ , \tag{3.27}$$

  where S_{ct_1} and S_{ct_2} are two turbulent Schmidt numbers, set to 0.7 for the present case.
- Different closure strategies for the scalar dissipation rate can be found [112, 51]. Historically, the first proposed model is analogous to the closure of the scalar dissipation

of the passive scalar (see Eq. 2.54), sometimes referred as "linear relaxation model" because of the assumption that the scalar fluctuations decay rate is proportional to the turbulent velocity fluctuations decay rate (through the constant c_{χ_c})

$$\overline{\rho}\widetilde{\chi}_c = 2\overline{\rho D\frac{\partial c''}{\partial x_i}\frac{\partial c''}{\partial x_i}} \approx c_{\chi_c}\frac{\widetilde{\varepsilon}}{\widetilde{k}}\widetilde{c''^2} \ , \tag{3.28}$$

where c_χ is a model constant set equal to one. This model, however, is valid for a non reacting diffusive scalar [22] and its use in reactive flow configurations is questionable. Effects of turbulence on scalar interactions such as the heat release should be included in the formulation [113, 114, 115]. Following this observation, several approaches have been suggested and implemented. Swaminathan and Bray [114] derived a balance equation for the scalar dissipation rate. Several terms are unclosed and need to be modelled. Algebraic models for the scalar dissipation rate have also been formulated. Vervisch et al. [51] proposed a method based on the Flame Surface Density (FSD) concept $\Sigma = \Xi|\nabla\overline{c^*}|$. By combining Eq. 2.71 and Eq. 2.67, the scalar dissipation rate can be expressed as

$$\overline{\rho}\widetilde{\chi}_c = \frac{1}{2}(2c_m - 1)\rho_u s_L \Xi|\nabla\overline{c}|\frac{\widetilde{c''^2}}{\widetilde{c}(1-\widetilde{c})} \ , \tag{3.29}$$

where s_L is the laminar flame speed, ρ_u is the density of the unburned gases, and Ξ is a wrinkling factor. The FSD term $\Xi|\nabla\overline{c}| = \Sigma$ must be closed and a transport equation based on the Coherent Flame Model (CFM) [24] is solved

$$\frac{\partial\overline{\Sigma}}{\partial t} + \frac{\partial}{\partial x_i}\left(\widetilde{u}_i\overline{\Sigma}\right) = \frac{\partial}{\partial x_i}\left(\frac{\nu_t}{Sc_{\overline{\Sigma}}}\frac{\partial\overline{\Sigma}}{\partial x_i}\right) + \alpha_0\frac{\widetilde{\varepsilon}}{\widetilde{k}}\overline{\Sigma} - \beta_0 s_L\frac{\overline{\Sigma}^2}{1-\widetilde{c}} \ , \tag{3.30}$$

where $\widetilde{k}$ is the mean turbulent kinetic energy and $\widetilde{\varepsilon}$ is the mean turbulent dissipation rate. α_0 and β_0 are two model parameters and have values equal to 1.7 and 1, respectively, following [116]. $Sc_{\overline{\Sigma}}$ is a turbulent Schmidt number, set to 0.7.

Another algebraic model for the scalar dissipation rate was proposed by Mantel and Borghi [117]

$$\overline{\rho}\widetilde{\chi}_c = \left(1 + \frac{2C_{\varepsilon_c}s_L^0}{3\sqrt{\widetilde{k}}}\right)\left(C_D\frac{\widetilde{\varepsilon}}{\widetilde{k}}\right)\widetilde{c''^2} \ , \quad C_{\varepsilon_c} = 0.1, \quad C_D = 0.21 \ , \tag{3.31}$$

where s_L^0 is the unstrained laminar flame speed. Swaminathan and Bray [114] modified this model by including effects of dilatation due to heat release across the flame

front:

$$\overline{\rho}\widetilde{\chi}_c = \left(1 + \frac{2}{3}C_{\varepsilon_c}\frac{s_L^0}{\sqrt{\widetilde{k}}}\right)\left(C_{D_c}\frac{s_L^0}{\delta_L^0} + C_D\frac{\widetilde{\varepsilon}}{\widetilde{k}}\right)\widetilde{c''^2}\ , \qquad C_{D_c} = 0.24\ , \tag{3.32}$$

where δ_L^0 is the unstrained laminar thermal thickness. Kolla et al. [118] further improved the model and obtained:

$$\overline{\rho}\widetilde{\chi}_c = 2\overline{\rho}\frac{1}{\beta'}\left([2K_c^* - \tau C_4]\frac{s_L^0}{\delta_L^0} + C_3\frac{\widetilde{\varepsilon}}{\widetilde{k}}\right)\widetilde{c''^2}, \tag{3.33}$$

where β' is a model constant equal to 6.7, $K_c^* \equiv \frac{\delta_L^0}{s_L^0}\frac{\int(\rho N_c \nabla\mathbf{u})_L^0 \overline{P}(c)dc}{\int(\rho N_c)_L^0 \overline{P}(c)dc}$ and τ is the heat release index. N_c indicates the instantaneous scalar dissipation rate of c. The model constants are defined as: $C_3 = 1.5/(1+\mathrm{Ka}^{-m})$ and $C_4 = 1.1(1+\mathrm{Ka})^{-0.4}$, where Ka is the Karlovitz number and is defined as the ratio between the chemical time scale to the Kolmogorov length scale, see Eq. 2.64. From experiments [5], it results that $s_L^0 = 23.9$ cm/s and $\delta_L^0 = 0.079$ mm, $\frac{K_c^*}{\tau} = 0.835$ and $\tau = 5.441$ based on laminar flame results for $\phi = 0.75$ as interpolated from Table 1 of [118]. The constant m in the definition of the two model constants is taken to be 0.5 as in [118]. Values for Ka estimated in the experiments range from 1 to 3.5 (Fig. 20 in [5]). A value of Ka equal to 2 is selected in the present study. Other values were tested and negligible differences were found. A spatially variable expression for Ka was also implemented using $\mathrm{Ka} = \{[2(1+\tau)^{0.7}]^{-1}\varepsilon\ \delta_L^0/\ (s_L^0)^3\}^{0.5}$ [114]. However, the simulation results did not show any significant changes in the velocity and progress variable profiles compared to those obtained with Ka equal to 2.

- The last term on the RHS represents the correlation between the fluctuations of the conditioning variable and the reaction rate and can be modeled through the PDF

$$\overline{c''\dot{\omega}_c} = \overline{(c-\widetilde{c})\,\dot{\omega}_c} = \int_0^1 (c^* - \widetilde{c})\,\langle\dot{\omega}_c|c^*\rangle\tilde{P}(c^*)dc^* \tag{3.34}$$

where the conditional reaction rate is provided by the CSE combustion model. In the present case, $\langle\dot{\omega}_c|c^*\rangle$ is equal to the conditional reaction rate of CO_2, $\langle\dot{\omega}_{CO_2}|c^*\rangle$ (obtained from the chemistry tables), divided by the equilibrium value for the mass fraction of CO_2 following Eq. 3.2.

A summary of the governing equations with the corresponding implemented models is given in Table 3.1.

All transport equations are solved using an implicit time integration method, while flux calculations are solved with Total Variation Diminishing (TVD) and the Normalized Variable Diagram (NVD) schemes [110].

Table 3.1: Governing equations

Conservation of mass	$\frac{\partial \overline{\rho}}{\partial t} + \frac{\partial}{\partial x_i}(\overline{\rho}\widetilde{u}_i) = 0$
Conservation of momentum	$\frac{\partial \overline{\rho}\widetilde{u}_i}{\partial t} + \frac{\partial}{\partial x_i}(\overline{\rho}\widetilde{u}_i\widetilde{u}_j) = -\frac{\partial \overline{p}}{\partial x_j} + \frac{\partial}{\partial x_i}\overline{\rho}\widetilde{u_i'' u_j''}$ $\overline{\rho}\widetilde{u_i'' u_j''} = -\mu_t\left(\frac{\partial \widetilde{u}_i}{\partial x_j} + \frac{\partial \widetilde{u}_j}{\partial x_i} - \frac{2}{3}\delta_{ij}\frac{\partial \widetilde{u}_k}{\partial x_k}\right) + \frac{2}{3}\overline{\rho}k$
Conservation of total enthalpy	$\frac{\partial(\overline{\rho}\widetilde{h}_t)}{\partial t} + \frac{\partial}{\partial x_i}(\overline{\rho}\widetilde{u}_i\widetilde{h}_t) = \frac{\partial \overline{p}}{\partial t} + \frac{\partial}{\partial x_i}\left(\frac{\mu_t}{Pr}\frac{\partial \widetilde{h}_t}{\partial x_i}\right)$
Conservation of species	$\frac{\partial(\overline{\rho}\widetilde{Y}_k)}{\partial t} + \frac{\partial}{\partial x_i}(\overline{\rho}\widetilde{u}_i\widetilde{Y}_k) = \frac{\partial}{\partial x_i}\left(\frac{\mu_t}{Sc_t}\frac{\partial \widetilde{Y}_k}{\partial x_i}\right) + \overline{\dot{\omega}}_k$ $\overline{\dot{\omega}_k} = \int_0^1 \dot{\omega}_k^{FGM}\langle Y_{\mathrm{H_2O}}\vert c^*\rangle, \langle Y_{\mathrm{CO_2}}\vert c^*\rangle)\,\tilde{P}(c^*)dc^*$
Progress variable	$\frac{\partial(\overline{\rho}\widetilde{c})}{\partial t} + \frac{\partial}{\partial x_i}(\overline{\rho}\widetilde{u}_i\widetilde{c}) = \frac{\partial}{\partial x_i}\left(\frac{\mu_t}{Sc_t}\frac{\partial \widetilde{c}}{\partial x_i}\right) + \overline{\dot{\omega}}_c$
Variance of progress variable	$\frac{\partial(\overline{\rho}\widetilde{c''^2})}{\partial t} + \frac{\partial}{\partial x_i}\left(\overline{\rho}\widetilde{u}_i\widetilde{c''^2}\right) = \frac{\partial}{\partial x_i}\left(\overline{\rho}\frac{\nu_t}{S_{ct_1}}\frac{\partial \widetilde{c''^2}}{\partial x_i}\right) - 2\overline{\rho}\frac{\nu_t}{S_{ct_2}}\frac{\partial \widetilde{c''}}{\partial x_i}\frac{\partial \widetilde{c''}}{\partial x_i} - 2\overline{\rho}\frac{\varepsilon}{k}\widetilde{c''^2} + 2\overline{c''\dot{\omega}_c}$

3.2.3 Turbulence models

The turbulent flowfield is simulated using a modified $k-\varepsilon$ approach [31]: $C_{\varepsilon 1}$ in Eq. 3.36 is changed from 1.44 to different values (these will be specified in Section 3.3.3). For clarity, the transport equations used in $k-\varepsilon$ (and introduced in Section 2.2.2) are given below.

$$\overline{\rho}\frac{\partial \widetilde{k}}{\partial t} + \overline{\rho}u_i\frac{\partial \widetilde{k}}{\partial x_i} = \frac{\partial}{\partial x_i}\left[\left(\frac{\mu_t}{\sigma_k} + \mu\right)\frac{\partial \widetilde{k}}{\partial x_i}\right] + \tilde{P}_k + \overline{p'\frac{\partial u_k''}{\partial x_k}} - \overline{\rho}\widetilde{\varepsilon}, \tag{3.35}$$

$$\overline{\rho}\frac{\partial\widetilde{\varepsilon}}{\partial t}+\overline{\rho}u_i\frac{\partial\widetilde{\varepsilon}}{\partial x_i}=\frac{\partial}{\partial x_i}\left[\left(\frac{\mu_T}{\sigma_\varepsilon}+\mu\right)\frac{\partial\widetilde{\varepsilon}}{\partial x_i}\right]+C_{\varepsilon 1}\tilde{P}_k\frac{\widetilde{\varepsilon}}{\widetilde{k}}-C_{\varepsilon 2}\overline{\rho}\frac{\widetilde{\varepsilon^2}}{\widetilde{k}}, \tag{3.36}$$

where the $\tilde{P}_k$ is the production term, see Eq. 2.28 and the turbulent viscosity is given by

$$\mu_T=C_\mu\overline{\rho}\frac{\widetilde{k}^2}{\widetilde{\varepsilon}}. \tag{3.37}$$

The standard model constants are given as [31]

$$C_\mu=0.09,\quad C_{\varepsilon 1}=1.44,\quad C_{\varepsilon 2}=1.92,\quad \sigma_k=1.0,\ \text{ and }\ \sigma_\varepsilon=1.3. \tag{3.38}$$

The standard SST $k-\omega$ turbulence model [33] is also used for comparison. It blends the $k-\omega$ formulation in the inner parts of the boundary layer with the free-stream independence of the $k-\varepsilon$ model in the far field. The governing equations of the $k-\omega$ model [34] are

$$\frac{\partial}{\partial t}(\overline{\rho}\widetilde{k})+\frac{\partial}{\partial x_i}(\overline{\rho}\widetilde{u}_i\widetilde{k})=\frac{\partial}{\partial x_i}\left[(\mu+\sigma_{k_1}\mu_t)\frac{\partial\widetilde{k}}{\partial x_i}\right]+\tilde{P}_k+\overline{p'\frac{\partial u_k''}{\partial x_k}}-\beta^*\overline{\rho}\omega\widetilde{k}\ , \tag{3.39}$$

$$\frac{\partial}{\partial t}(\overline{\rho}\widetilde{\omega})+\frac{\partial}{\partial x_i}(\overline{\rho}\widetilde{u}_i\widetilde{\omega})=\frac{\partial}{\partial x_i}\left[(\mu+\sigma_{\omega_1}\mu_t)\frac{\partial\widetilde{\omega}}{\partial x_i}\right]+\overline{\rho}\gamma_1S^2-\beta_1\overline{\rho}\widetilde{\omega^2}\ . \tag{3.40}$$

In Eqs. 3.39 and 3.40, σ_{k_1}, β^*, σ_{ω_1}, γ_1 and β_1 are model constants defined by

$$\begin{aligned}\beta^*=0.09,\quad ,\beta_1=3/40,\quad \sigma_{k_1}=0.85,\\ \sigma_{\omega 1}=0.5,\quad \kappa=0.41,\quad \gamma_1=\beta_1/\beta^*-\sigma_{\omega_1}\kappa^2/\sqrt{\beta^*}.\end{aligned} \tag{3.41}$$

The $k-\varepsilon$ model equations can be transformed into a $k-\omega$ formulation resulting in

$$\frac{\partial}{\partial t}(\overline{\rho}\widetilde{k})+\frac{\partial}{\partial x_i}(\overline{\rho}\widetilde{u}_i\widetilde{k})=\frac{\partial}{\partial x_i}\left[(\mu+\sigma_{k_2}\mu_t)\frac{\partial\widetilde{k}}{\partial x_i}\right]+\tilde{P}_k+\overline{p'\frac{\partial u_k''}{\partial x_k}}-\beta^*\overline{\rho}\omega\widetilde{k}\ , \tag{3.42}$$

$$\begin{aligned}\frac{\partial}{\partial t}(\overline{\rho}\widetilde{\omega})+\frac{\partial}{\partial x_i}(\overline{\rho}\widetilde{u}_i\widetilde{\omega})=\frac{\partial}{\partial x_i}\left[(\mu+\sigma_{\omega_2}\mu_t)\frac{\partial\widetilde{\omega}}{\partial x_i}\right]+\overline{\rho}\gamma_2S^2-\beta_2\overline{\rho}\widetilde{\omega^2}+\\ 2\frac{\overline{\rho}\sigma_{\omega 2}}{\widetilde{\omega}}\frac{\partial\widetilde{k}}{\partial x_i}\frac{\partial\widetilde{\omega}}{\partial x_i}\ .\end{aligned} \tag{3.43}$$

The model constants are given by

$$\begin{aligned}\beta^*=0.09,\quad \beta_2=0.0828,\quad \sigma_{k_2}=1.0,\quad \sigma_{\omega 2}=0.856,\\ \kappa=0.41,\quad \gamma_2=\beta_2/\beta^*-\sigma_{\omega_2}\kappa^2/\sqrt{\beta^*}.\end{aligned} \tag{3.44}$$

The SST $k-\omega$ equations are obtained by multiplying Eq. 3.39 and Eq. 3.40 by F_1 and Eqs. 3.42-3.43 by $(1-F_1)$

$$\frac{\partial}{\partial t}(\overline{\rho}\widetilde{k})+\frac{\partial}{\partial x_i}(\overline{\rho}\widetilde{u}_i\widetilde{k})=\frac{\partial}{\partial x_i}\left[(\mu+\sigma_k\mu_t)\frac{\partial\widetilde{k}}{\partial x_i}\right]+\tilde{P}_k+\overline{p'\frac{\partial u_k''}{\partial x_k}}-\beta^*\overline{\rho}\omega\widetilde{k}\ , \tag{3.45}$$

$$\begin{aligned}\frac{\partial}{\partial t}(\overline{\rho}\widetilde{\omega})+\frac{\partial}{\partial x_i}(\overline{\rho}\widetilde{u}_i\widetilde{\omega})=\frac{\partial}{\partial x_i}\left[(\mu+\sigma_\omega\mu_t)\frac{\partial\widetilde{\omega}}{\partial x_i}\right]+\overline{\rho}\gamma S^2-\beta\overline{\rho}\widetilde{\omega^2}+\\ 2(1-F_1)\frac{\overline{\rho}\sigma_{\omega 2}}{\widetilde{\omega}}\frac{\partial\widetilde{k}}{\partial x_i}\frac{\partial\widetilde{\omega}}{\partial x_i}\ ,\end{aligned} \tag{3.46}$$

where $\tilde{P}_k=\min\left(\mu_t\frac{\partial\widetilde{u}_i}{\partial x_j}\left(\frac{\partial\widetilde{u}_i}{\partial x_j}+\frac{\partial\widetilde{u}_j}{\partial x_i}\right),10\beta^*\widetilde{k}\widetilde{\omega}\right)$ and the blending function F_1 is defined by

$$F_1=\tanh\left\{\left\{\min\left[\max\left(\frac{\sqrt{\widetilde{k}}}{\beta^*\widetilde{\omega}y},\frac{500\nu}{y^2\widetilde{\omega}}\right),\frac{4\sigma_{\omega 2}\widetilde{k}}{CD_{k\omega}y^2}\right],10\right\}^4\right\}\ , \tag{3.47}$$

with $CD_{k\omega}=\max\left(2\overline{\rho}\sigma_{\omega 2}\frac{1}{\widetilde{\omega}}\frac{\partial\widetilde{k}}{\partial x_i}\frac{\partial\widetilde{\omega}}{\partial x_i},10^{-10}\right)$ and y is the distance of the first node from the wall. The turbulent eddy viscosity is computed from

$$\mu_t=\frac{\overline{\rho}a_1\widetilde{k}}{\max\left(a_1\widetilde{\omega},SF_2\right)}\ , \tag{3.48}$$

where $a_1=0.31$, S is the invariant measure of the strain rate and F_2 is a second blending function defined by

$$F_2=\tanh\left[\left[\max\left(\frac{2\sqrt{\widetilde{k}}}{\beta^*\widetilde{\omega}y},\frac{500\nu}{y^2\widetilde{\omega}}\right)\right]^2\right]\ . \tag{3.49}$$

In Eqs. 3.45 and 3.46, the constants ϕ such as σ_k, β^*, σ_ω, γ and β are computed by a blend from the corresponding constants ϕ_1 in Eqs. 3.39 and 3.40 and ϕ_2 in Eqs. 3.42 and 3.43 via $\phi=F_1\phi_1+(1-F_1)\phi_2$ [33]. Equations 3.35, 3.39, 3.42 and 3.45 present an unclosed term that requires modelling, the pressure-dilatation term. It is generally neglected, but is expected to be non-negligible in premixed flames. Numerical simulations including this term are carried out. It is modelled using the expression proposed by Zhang and Rutland [119]

$$\overline{p'\frac{\partial u_k''}{\partial x_k}}=\frac{1}{2}\widetilde{c}\left(\tau s_L^0\right)^2\overline{\dot{\omega}}\ , \tag{3.50}$$

where τ denotes the heat release parameter, that can be related to the density through

$$\frac{\overline{\rho}}{\rho_u} = \frac{1}{1+\tau\widetilde{c}} \,. \tag{3.51}$$

In the present calculations, however, the pressure-dilatation is found to be negligible compared to the other terms in the k equation, consistent with previous findings shown in [20] (see Fig. 2.29 and related comments for a turbulent premixed flame with an expansion ratio approximately equal to 6). The expansion ratio (defined as the ratio of the unburnt mixture density to the burnt gas density - 1) for the selected flame is equal to 6.5.

3.3 Results

CSE is still at an early stage of development, in particular for turbulent premixed combustion. Thus, it is important to investigate the sensitivity of the predictions for the mean progress variable and velocity to different numerical parameters that are included in the present implementation. First, the inversion process needed to determine the conditional species mass fractions (Eq. 3.5) is examined. A regularization technique is required and defining the value of the regularization parameter (noted λ in Eq. 3.8 for the Tikhonov method or k in Eq. 3.9 in TSVD) is crucial.

3.3.1 Regularization Parameter

Figure 3.6 presents the L-curve for the two regularization methods, i.e. the L2 norm of the solution, $\vec{\alpha}$, is plotted versus the L2 norm of the residual for Eq. 3.5 for increasing values of λ in the Tikhonov method and decreasing values of k in TSVD. As shown in Fig. 3.6, both regularization methods give very similar profiles. Thus, in the present case, the solution is not sensitive to the selected method. It should be noted that the L-curve for the TSVD method is discrete as k is an integer varying from 0 to 50. Increasing k decreases the filtering of the solution and decreasing k causes fewer singular values to construct the solution, and hence increases the filtering effect in this regularization method. In contrast, the L-curve for the Tikhonov regularization is continuous and λ can be any real number larger than zero. Due to the continuous L-curve and very small differences between the two methods, in the remaining part of the paper, discussion is focused on the Tikhonov approach and all results are presented including the Tikhonov technique.

In the L-curve two different parts can be distinguished: a flat region (noted (2) in Fig. 3.6) for large residuals and a steep descending section (noted (1) in Fig. 3.6) for small

values of residual. Region (2) corresponds to regularized solutions where the damping is so large that information from b is filtered out and the solution is dominated by regularization errors. In contrast, region (1) is related to regularized solutions where contributions from error dominate because too little damping (less filtering) is introduced. Region (1) is characterized by small values of λ and (2) by large values of λ. Therefore, there is an optimal value for the regularization parameter where a favorable balance between two types of errors can be found: this is the "corner" of the L-curve. For the Tikhonov method, this corresponds to λ on the order of unity, as shown in Fig. 3.6. To generate the L-curve, the flamelet solution is used for $\vec{\alpha}^0$, the a-priori knowledge of the solution (Eq. 3.8). As λ is further increased, the residuals reached a point where they do not increase any more. Thus, it can be concluded the *a priori* knowledge of the solution (flamelet solution) is a good estimate of the solution. In this region, the flamelet model is expected to work well. Similar shape of L-curve was shown in the work of Salehi et al. [78] and similar conclusions were reached. However, the optimal value of λ was different.

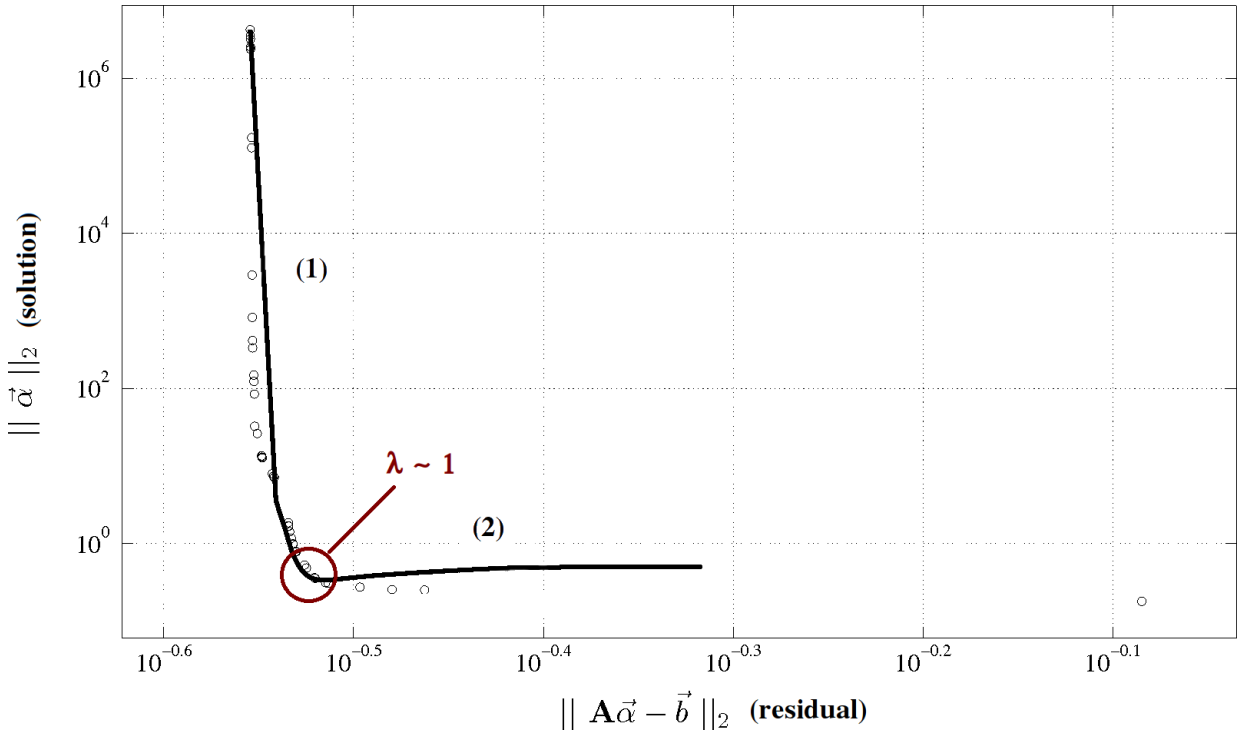

Figure 3.6: L-curve graph for regularization parameters on a log-log scale. The solid line corresponds to Tikhonov regularization and the symbols to TSVD.

It is also important to examine the range of singular values, σ_i, in the matrix system as presented in Eq. 3.6. Figure 3.7 shows the singular values, σ_i, for the initial field (results from unstrained laminar flame solution) and the converged solution achieved with the CSE combustion model using a value of λ equal to 1. The singular values can be seen to be nonzero meaning that a unique solution exists, however they span a wide range of values, approximately ten orders of magnitude. In particular, the small values make the solution unstable if no regularization approach is used. These small values can also lead to numerical problems if λ is too small. It can also be noted that in Fig. 3.7 the two sets of singular values are very close to each other. This may mean that the flame is mostly in the thin reaction regime. Further discussion on this aspect is presented in Section 3.3.4.

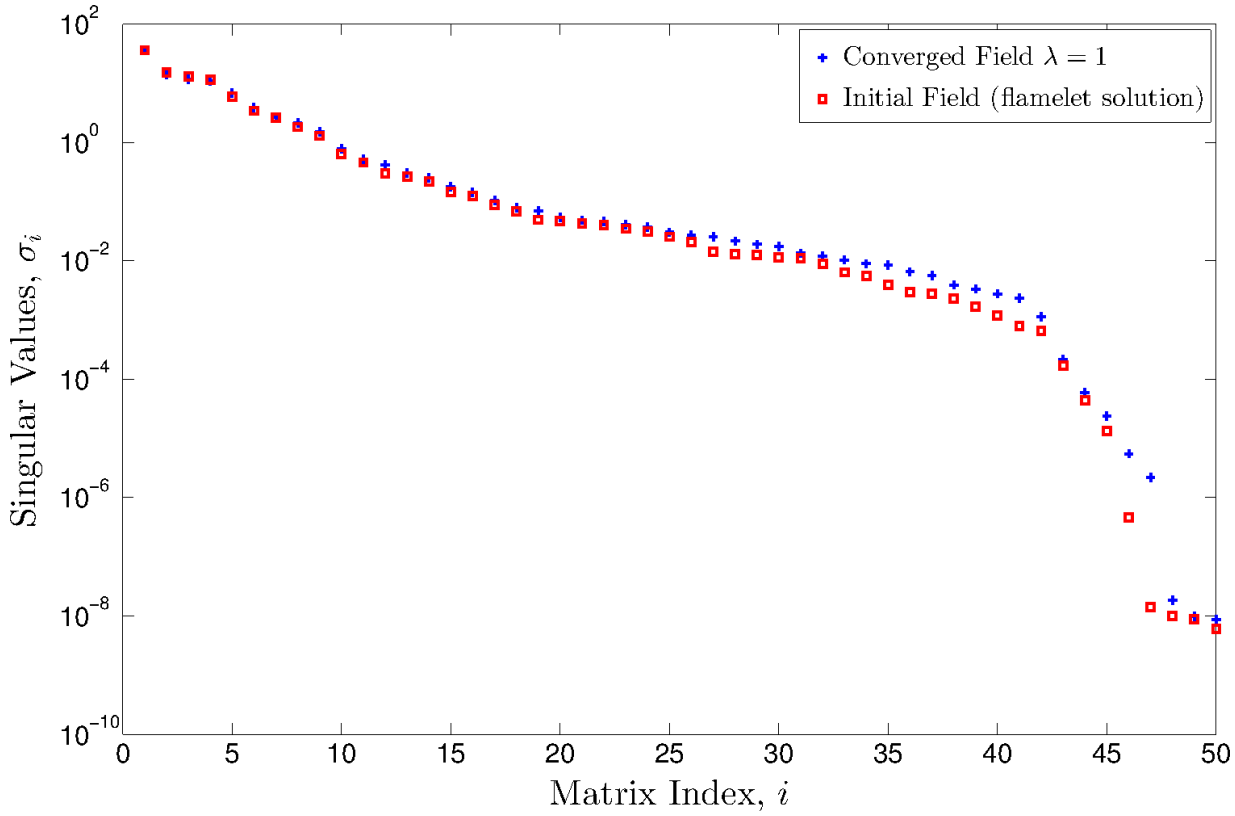

Figure 3.7: Singular Values of the kernel of the inverse problem (Eqs. 3.5, 3.6) for the initial and converged field.

3.3.2 Sensitivity of results to values of λ

In this section, the effect of the regularization parameter on the conditional and unconditional results is investigated. As shown in Section 3.3.1, the optimal value of λ is on the order of one. Values less than one characterize a solution dominated by errors and convergence could not be found. Three values of λ equal to 1, 1.5 and 2 are used. Figure 3.8 shows the estimated $\langle Y_{\mathrm{H_2O}}|c^*\rangle$ for CSE at different values of the regularization parameter λ compared with the flamelet values. In the present case, CSE conditional moments are larger than the laminar flamelet solutions suggesting that the effect of turbulence on the conditional averages (which is neglected in the flamelet profile) plays an important role for the flame under investigation. The effect of the regularization parameter is small for most parts and a noticeable difference is observed only for c^* around 0.5.

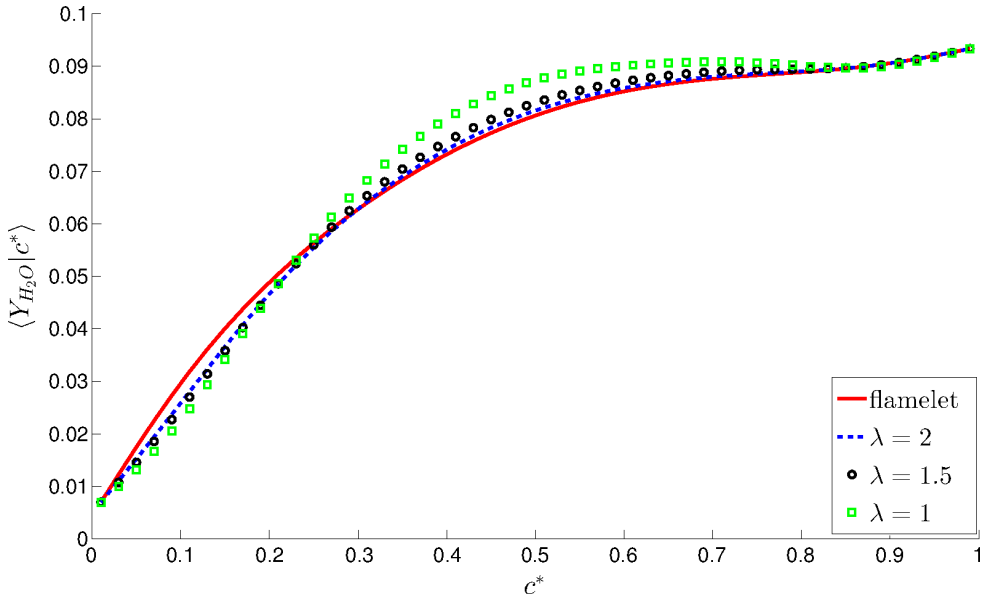

Figure 3.8: Conditional average of water mass fraction of the unstrained laminar flamelet solution and the CSE solution at different values of the regularization parameter λ.

The effect of λ on the progress variable radial profile is presented in Fig. 3.9. For λ equal to 1.5 and 2 the radial profiles are very close to each other, while when λ is set equal to 1 the contour of the progress variable radial profile is slightly different at the last axial location ($y = 40$ mm). Given the small differences in the conditional averages and mean progress variable for the values of λ tested, it is decided to use $\lambda = 2$ for the final CSE

results presented in Section 3.3.4.

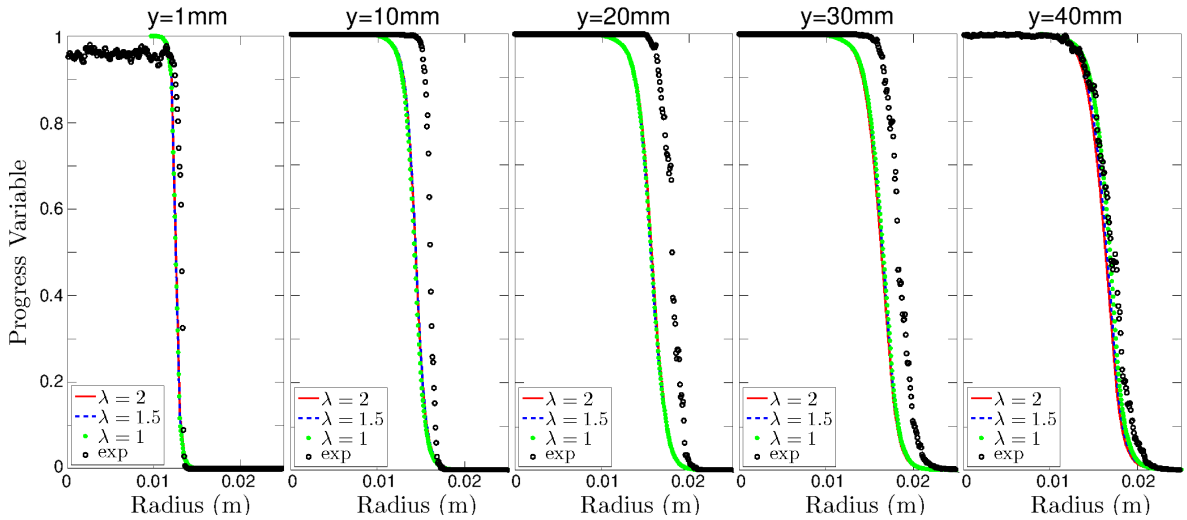

Figure 3.9: Progress variable radial profiles at different values of the regularization parameter λ.

3.3.3 Sensitivity analysis for different turbulence parameters and models

The standard $k-\varepsilon$ turbulence model has well-known deficiencies such as over-prediction of the decay and spreading rate of a round jet flow [120]. Dally et al. [121] implemented different corrections in the k-ε model applied to a non-reacting jet and reached the conclusion that a value of $C_{\varepsilon 1}$ equal to 1.6 was the most appropriate for their selected non-reacting jet and bluff-body flame flowfield predictions. The increase of the empirical constant in the production term in the dissipation transport equation, $C_{\varepsilon 1}$, from 1.44 to 1.6 is a common strategy for bluff body flames [122, 123].

In the present work, different values of C_{ε_1} (see Eq. 3.36) are tested, ranging from the standard value of 1.44 to 1.7. The predictions are compared with the experimental data [5]. Figure 3.10 shows the mean axial velocity radial profiles in the non-reactive case for 4 different values of C_{ε_1}. For all axial locations, the case of $C_{\varepsilon_1} = 1.5$ gives the best agreement with experimental data. Further, the standard value of 1.44 provides poor results,

underestimating the peak of the mean axial velocity with the largest departure from experimental data in the $y = 40$ mm location (differences for the values of C_{ε_1} examined are less than 7 % in the first axial location (contours at $y = 1$ mm)). Thus, the corresponding plots are not shown for clarity.

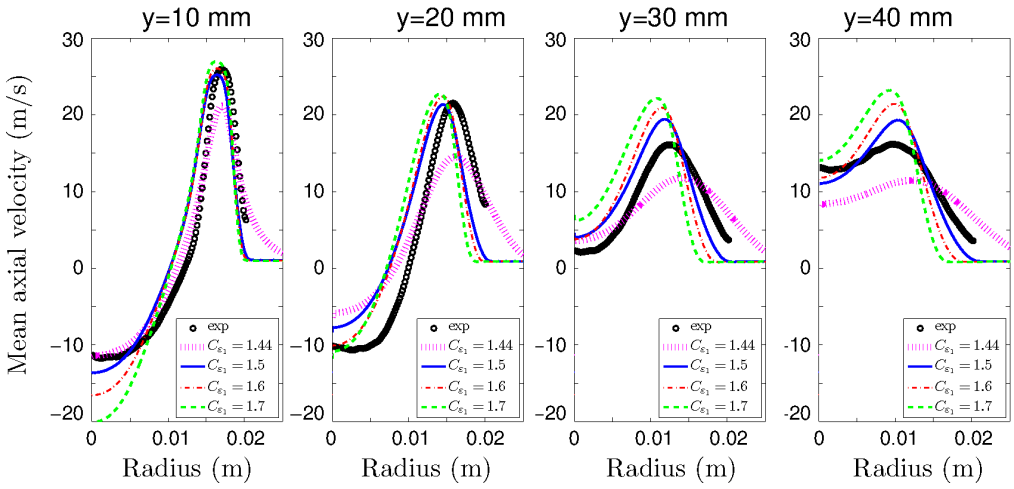

Figure 3.10: Mean axial velocity radial profiles with different values of C_{ε_1} for the modified $k - \varepsilon$ turbulence model in the non-reactive case, symbols denote experimental data [5].

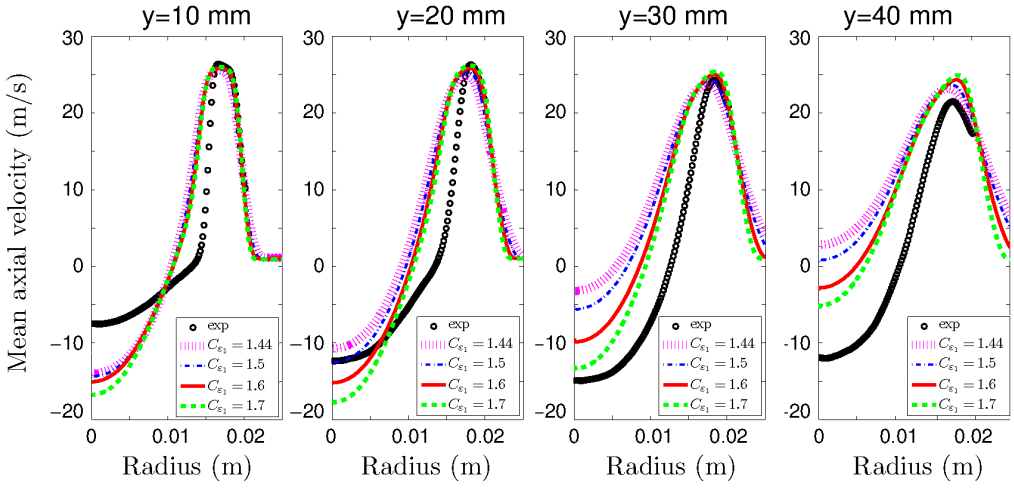

Figure 3.11: Mean axial velocity radial profiles with different values of C_{ε_1} for the modified $k - \varepsilon$ turbulence model in the reactive case, symbols denote experimental data [5].

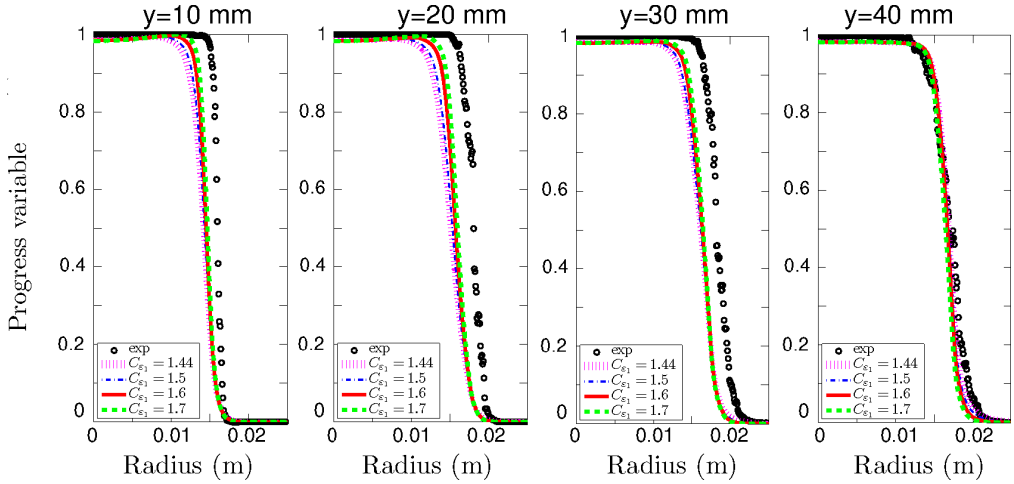

Figure 3.12: Progress variable radial profiles with different values of C_{ε_1} for the modified $k-\varepsilon$ turbulence model in the reactive case, symbols denote experimental data [5].

However, in the reactive case, the trend is different, as can be seen in Figs. 3.11 and 3.12, where the mean axial velocity and progress variable radial profiles are presented, respectively. The value of 1.5 for C_{ε_1} does not give the best prediction, in contrast to the findings for the non-reactive case. The same improvement is not observed in the velocity profiles (see Fig. 3.11): the value of $C_{\varepsilon_1} = 1.7$ provides better results at $y = 30$ mm and $y = 40$ mm for small values of the radial distance, r (see Fig. 3.12) , but for values of r at which the flame is located, i.e. where the progress variable profile is steep, the mean axial velocity is overpredicted as C_{ε_1} increases. At $y = 20$ mm the mean axial velocity obtained with $C_{\varepsilon_1} = 1.7$ is underpredicted close to the centreline. Overall, the contours for the mean velocity and progress variable obtained with $C_{\varepsilon_1} = 1.7$ are the closest to experimental data.

Following the same idea of changing the empirical constant $C_{\varepsilon 1}$ in the production term in the dissipation transport equation, Eq. 3.36, a modified version of the SST $k-\omega$ turbulence model is adopted. In this case, the corresponding constant to be changed is γ_2 in Eq. 3.43, resulting in different values of γ in Eq. 3.46, while γ_1 in Eq. 3.40 remains unchanged. Different values of γ_2 are tested. Figure 3.13 shows the radial profiles of the mean axial velocity in the non-reactive case obtained with three different values of γ_2.

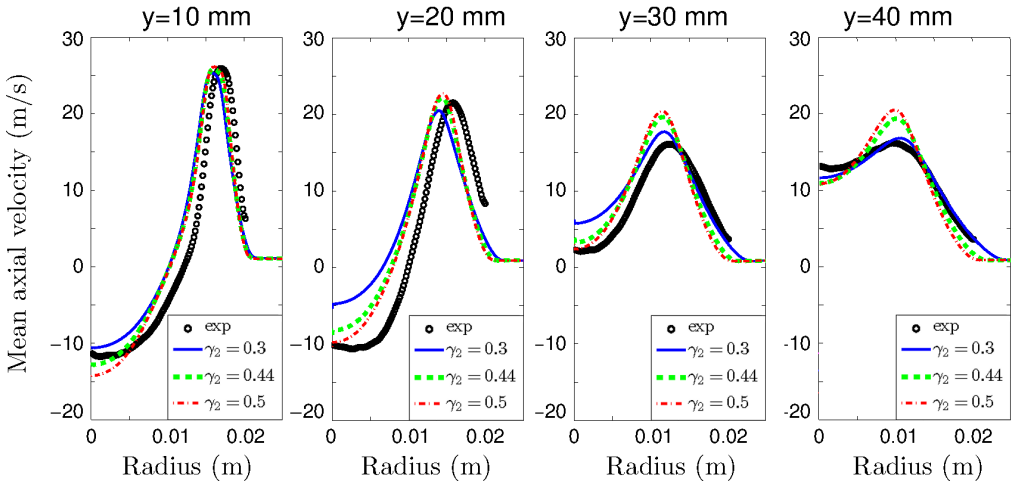

Figure 3.13: Mean axial velocity radial profiles with different values of γ_2 for the modified SST $k-\omega$ turbulence model in the non-reactive case, symbols denote experimental data [5].

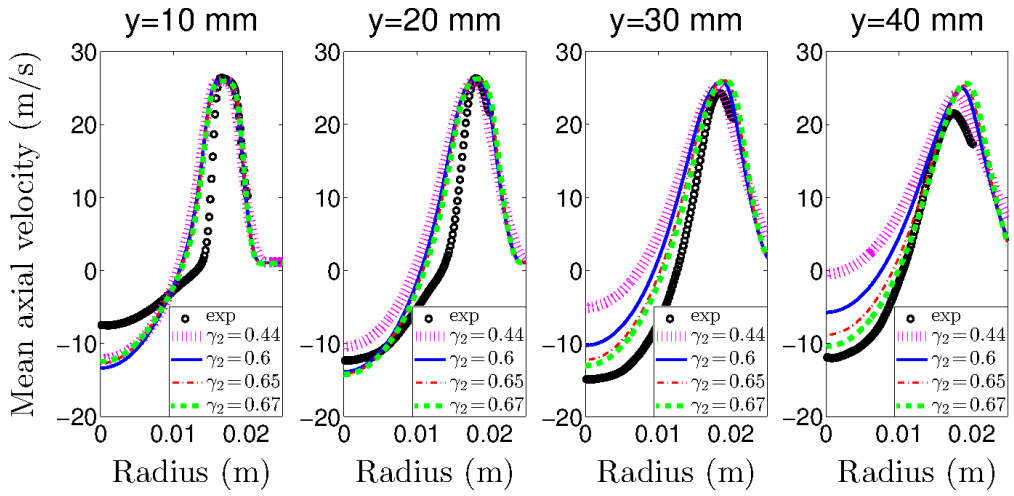

Figure 3.14: Mean axial velocity radial profiles with different values of γ_2 for the modified SST $k-\omega$ turbulence model in the reactive case, symbols denote experimental data [5].

The SST $k-\omega$ model is recommended for accurate boundary layer simulations [124] respect to the $k-\varepsilon$ approach, as can be seen by the improved radial velocity predictions at lower axial locations, close to the bluff body. For $\gamma_2 = 0.5$ the mixing field is well approx-

imated in locations close to the bluff body, while the predictions slightly depart from the experimental data farther downstream, where the maximum velocity is overpredicted. In comparison with the predictions obtained from the modified $k-\varepsilon$ (Fig. 3.10), SST $k-\omega$ appears to provide closer match with the experimental values.

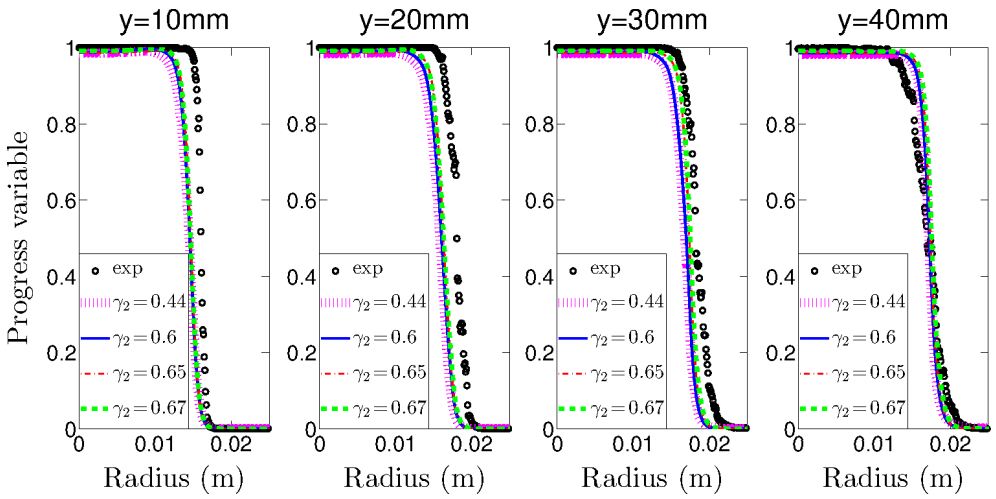

Figure 3.15: Progress variable radial profiles with different values of γ_2 for the modified SST $k-\omega$ turbulence model in the reactive case, symbols denote experimental data [5].

The case with $\gamma_2 = 0.3$ gives better results than the case with $\gamma_2 = 0.5$ only at $y = 40$ mm. The same approach of testing different values of γ_2 is used in the reactive case. Figure 3.14 shows the radial profiles of the mean axial velocity in the reactive case obtained with the modified SST $k-\omega$ turbulence model. As γ_2 increases, the predictions get closer to experimental results. Very good agreement is given by $\gamma_2 = 0.67$ corresponding to the inner region of the flame ($r \leq 18$ mm) for all axial locations. For larger values of r, the velocity is overpredicted at $y = 40$ mm especially for $\gamma_2 = 0.67$, while resulting in good agreement in the three other locations. The radial profiles of the progress variable are shown in Fig. 3.15. The value of the constant γ_2 equal to 0.67 results in better agreement with experimental data for all locations, although no noticeable difference can be found with the case at $\gamma_2 = 0.65$. Further, in the reactive case the SST $k-\omega$ predictions obtained with γ_2 equal to 0.65 provide closer agreement with experimental data than those using the modified $k-\varepsilon$ with $C_{\varepsilon 1}$ equal to 1.7, in particular for the mean velocity. Consequently, the modified SST $k-\omega$ turbulence model with a value for γ_2 of 0.65 is selected for the results presented in Section 3.3.4.

3.3.4 CSE and PCM results

Predictions of mean axial velocity and progress variable obtained with CSE and the flamelet model in the reactive case are presented in Fig. 3.16 and 3.17, respectively. For lower axial locations ($y = 1$ mm, $y = 10$ mm, $y = 20$ mm) the two combustion models provide similar results for the mean axial velocity contours. Farther downstream, CSE gives better results in the inner region of the flame ($r \leq 18$ mm), while both models overpredict the mean axial velocity in the outer region ($r \geq 18$ mm). The progress variable contours (Fig. 3.17) show the same trend of the velocity profiles in the lower locations, while farther downstream ($y = 30$ mm) CSE behaves better than the flamelet model. Finally, similar trends are found at $y = 40$ mm. It should be noted that the experimental values for the mean progress variable are based on OH intensity. In the present simulations, it is not possible to use the same method to determine the progress variable.

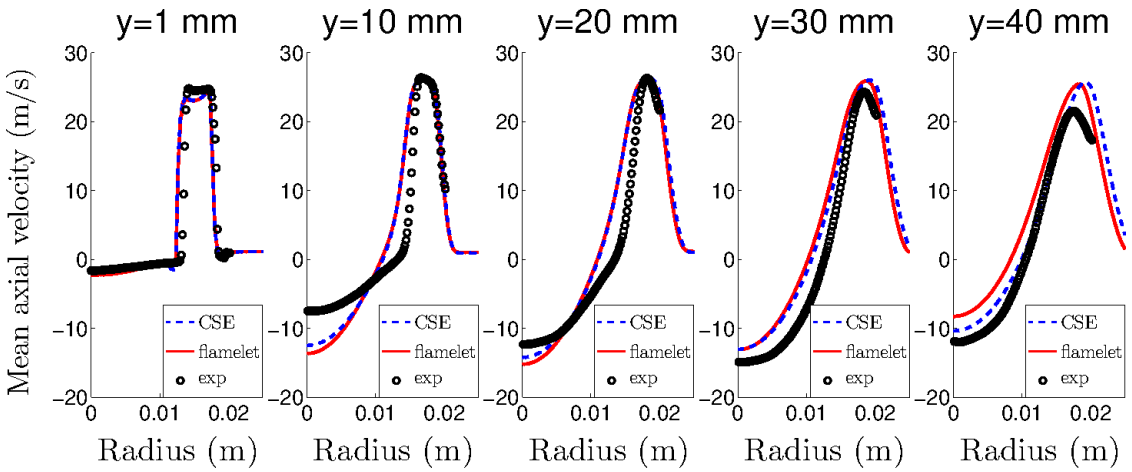

Figure 3.16: Mean axial velocity radial profiles, symbols denote experimental data [5], solid lines and dashed lines are the results of using flamelet and CSE combustion models, respectively.

In Fig. 3.17 the predicted progress variable c is calculated using the normalized mass fraction of CO_2 as defined in Section 3.1 (see Eq. 3.2). Another definition of progress variable based on temperature was also applied using the simulation results. However no significant changes could be noticed between the two sets of calculated progress variable (one based on CO_2 and one on temperature). In the experimental analysis, Kariuki et al.[5] evaluated the values of u'/s_L (velocity root mean square divided by laminar flame speed)

and L_T/δ_L (integral length scale divided by laminar flame thickness) along the $c = 0.2$ contour. Figure 3.18 is reproduced from their work [5] and shows their resulting values in the regime diagram defined by Peters [22]. As can be seen in Fig. 3.18, the measurement values are situated in the Damköhler $Da > 1$ regime (Da is defined as the ratio between the flow time scale and the chemical time scale, see Eq. 2.63), but the downstream flame parts are located closer to the $Da = 1$ boundary. This would explain why the flamelet model and CSE perform equally well for distances less or equal to 20 mm (Fig. 3.17) and larger differences between the two models for predictions of c can be seen farther downstream where the local flame moves away from the flamelet regime. The CSE predictions are slightly in better agreement with the experimental data for distances $y \geq 30$ mm. The flamelet model shows a good representation of turbulence-chemistry interaction in the flamelet regime in the present RANS simulations, while CSE is not limited by this condition.

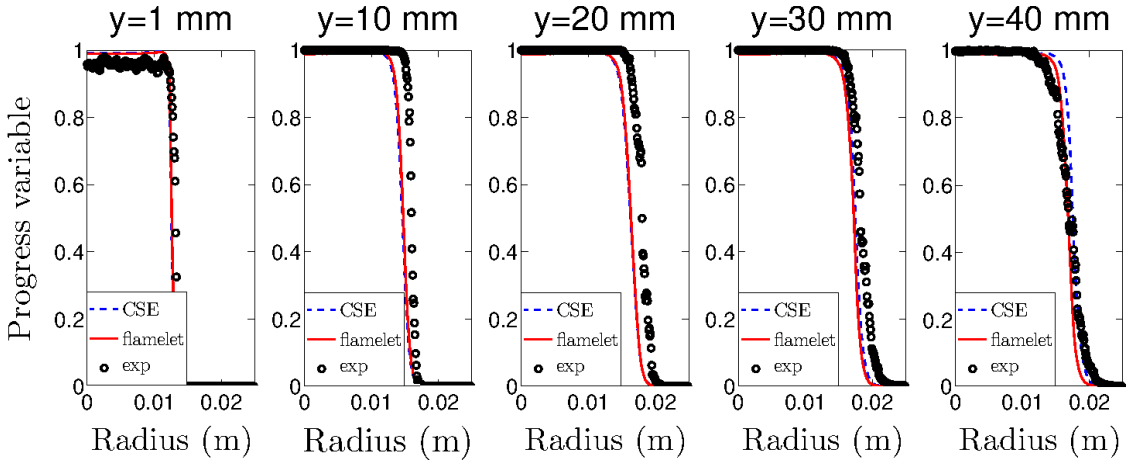

Figure 3.17: Progress variable radial profiles, symbols denote experimental data [5], solid lines and dashed lines are the results of using flamelet and CSE combustion models, respectively.

The mean temperature field is presented in Fig. 3.19. The (averaged) temperature contours from the present simulations (right) are qualitatively in good agreement with the photographs of the flame from the experimental work (left): the anchoring region located right above the bluff body is reproduced as well as the bulge zone observed after the recirculation region. The picture from experiments (left in Fig. 3.19) looks slightly wider in the radial direction, consistent with what is observed for the radial profiles for the mean progress variable (Fig.3.17). The mean reaction rate of CH_4 is presented in Fig. 3.20. In

their experimental results, Kariuki et al. [5] show that the flame brush is located along the shear layer of the annular jet. This feature is confirmed by numerical results, as showed in Fig. 3.20. The maximum value of the mean reaction rate is achieved close to the bluff body and the mean reaction rate profile follows the shear layer curvature. At conditions far from blow-off, the flame brush is primarily located along the shear layer of the annular jet.

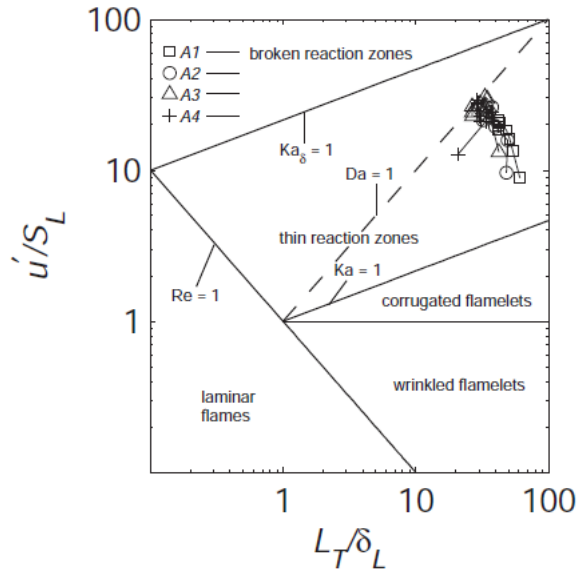

Figure 3.18: Regime diagram for turbulent premixed combustion as defined by Peters [22]. The present simulations are referred to case A1 ($\phi = 0.75, U_b = 21.6m/s$) along contours of $c^* = 0.2$. Figure reproduced from [5].

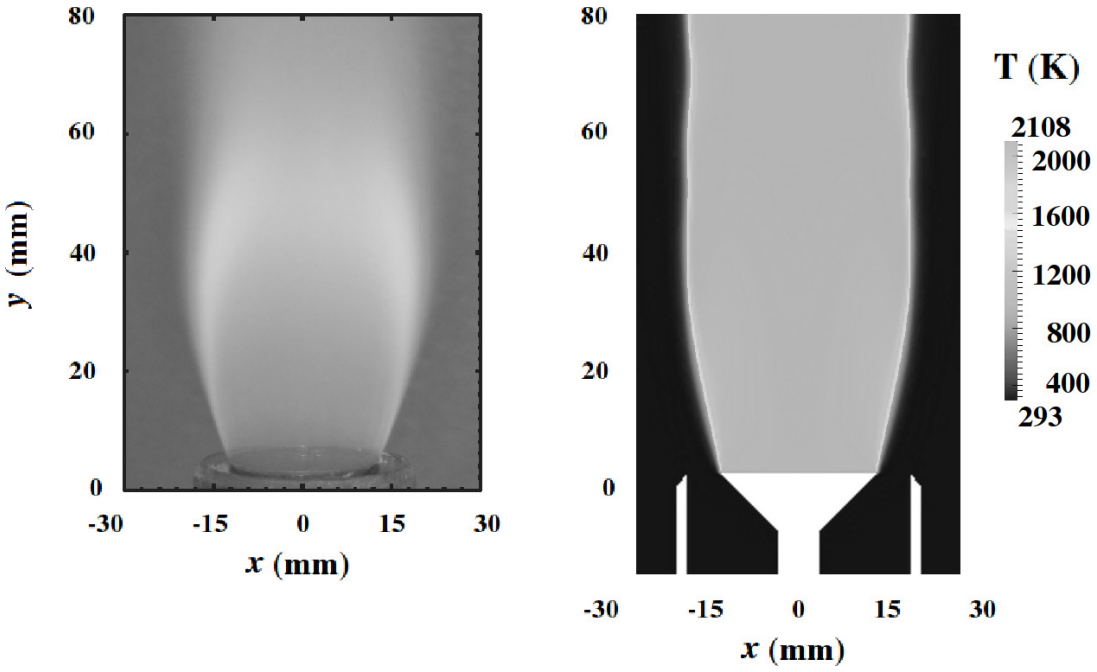

Figure 3.19: Photograph of the flame (taken from Fig. 4a in [5]) (left) and contours of calculated mean temperature field (right).

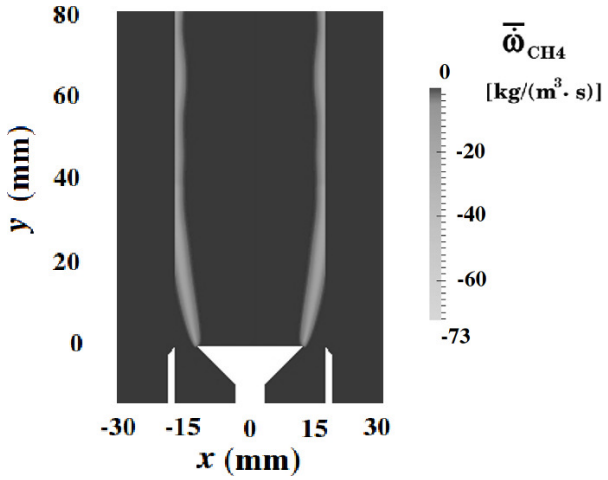

Figure 3.20: Contours of mean reaction rates for CH_4.

3.4 Summary

CSE combustion model in combination with a FGM approach for chemistry reduction is applied to RANS numerical solutions of a turbulent premixed bluff-body for which experimental data are available. A product-based progress variable as a conditioning variable for the CSE model and the modified laminar flamelet PDF as presumed shape of the probability density function are used to calculate the mean reaction rate. Two regularization methods are implemented, Tikhonov technique [98] and TSVD [99]. The optimal regularization parameter is determined using the L-curve and a sensitivity analysis is performed related to the effect of the value of the regularization parameter. In the present study, only small differences in the conditional and unconditional averages are noticed for values of the regularization parameter located in the optimal range determined by the L-curve. Further, CSE is shown to converge to one unique and stable solution which does not depend on the initial solutions or a-priori solution knowledge. Predictions show very good agreement with the available experimental data, in terms of mean axial velocity and progress variable radial profiles. Two different turbulence models are adopted in both reactive and non-reactive cases: the SST $k-\omega$ turbulence model with a modified value the production term constant gives a better solution than the modified $k-\varepsilon$ in both non-reactive and reactive cases for two different values of the constant, $C_{\gamma_2} = 0.3$ and $C_{\gamma_2} = 0.65$, respectively. The results of the CSE combustion model are close to the flamelet approach, and show a slightly better agreement farther downstream, where the flame regime departs from the flamelet region. The numerical temperature contours are in qualitative agreement with the photograph of the flame from the experimental work, not only for the anchoring region located right above the bluff body, but also for the bulge zone observed after the recirculation region. The mean reaction rate of CH_4 profile confirms the location of the flame brush along the shear layer, consistent with the experimental results.

CSE has been demonstrated to provide good results in terms of numerical simulations of both premixed and non-premixed turbulent combustion regimes. The promising results obtained in the current work suggest that CSE is a good candidate for partially premixed turbulent combustion modelling.

Chapter 4

DCSE for turbulent partially premixed combustion

The capability of CSE for dealing with premixed flames characterized by complex geometries, such as bluff body configurations, is attested by the findings presented in Chapter 3. An extension of the CSE combustion model, based on double conditioning using a reaction progress variable and the mixture fraction as the conditioning variables, is presented here to obtain the structure of the CSE approach for partially premixed flames. Such a model is expected to be very general, since it is not limited by any flame regimes, and able to perform adequately for partially premixed turbulent combustion.

4.1 Description of partially premixed turbulent combustion

Turbulent combustion model formulations for partially premixed flames need to include an accurate description of both premixed and diffusion flames occurring simultaneously, in order to incorporate the effects of partially premixed flame propagation. For this reason, the conventional formulations based on either a conserved scalar or a progress variable no longer apply [80]. This is due to the fact that premixed and non-premixed combustion are characterized by fundamentally different properties. The turbulent premixed flame front tends to be thin and can propagate by itself; the turbulent diffusion flame, in contrast, does not show propagation and is strongly controlled by turbulent mixing. Thus, the

main challenge consists of capturing correctly the dual description of diffusion flames and premixed flame fronts (locally defined for a specified equivalence ratio) [125].

4.2 Lifted turbulent flame

A generic configuration for fundamental studies of partially premixed combustion and the development of theoretical models is the lifted turbulent jet flame and it can be considered as the canonical problem for the study of turbulent partially premixed combustion [22]. Lifted turbulent jet flames are observed when the fuel injection or coflow velocity is too high for the flame to stabilize at the burner rim. Further increase in the jet exit or coflow velocity eventually results in flame blowout. The lift-off height is defined as the distance measured between the burner rim and the base of the flame. Many combustion systems include a lifted flame in their operation, for example commercial boilers, flares and diesel engines. The flame configuration is, by itself, simple; however, lifted turbulent flames encompass complex turbulence-chemistry interactions and local ignition/extinction phenomena which have an impact on flame stability and pollutant formation.

Several approaches have been proposed to explain the stabilization mechanism. Detailed reviews can be found in [126, 127] and only a brief summary is given here. The initial classification of stabilization mechanism was mostly polarized between two opposing concepts, the premixed flame propagation [128] versus flamelet quenching [129]. The premixed flame propagation concept assumed that fuel and air are fully premixed prior to ignition and stabilization occurred where the local flow velocity along the stoichiometric contour was equal to the turbulent burning velocity for a premixed, stoichiometric mixture of fuel and air [128]. In contrast, Peters and Williams [129] proposed that diffusion flamelet extinction was responsible for flame stabilization and that lift-off could be explained in terms of the laminar flamelet concept. Other theories have also been suggested such as flame extinction due to large-scale turbulent structures [130] or flame propagation controlled by the turbulence intensity [131]. When a hot coflow is present, autoignition was found to be another important stabilization mechanism in the experiments described by Cabra and co-authors [132, 133] and in DNS [134]. The stabilization mechanisms for hot and cold surroundings were shown to be different [135]. Over the years, numerous experimental and numerical studies have examined the validity of the different competing stabilization theories [136, 127, 22, 137]. Recent experimental investigations pointed towards the idea of flame stabilization through partially premixed flame propagation. For example, Watson et al. [138] investigated the stabilization mechanism of a methane lifted flame and partial premixed flame propagation was concluded to be the governing stabi-

lization mechanism, rather than scalar dissipation rate, consistent with the observations of Stårner et al. [139] and Su et al. [140]. Muniz and Mungal [141] showed that the flame stabilized itself when the local gas velocity was less than or near the premixed laminar flame speed, consistent with more recent measurements [142]. The divergence of the streamlines was observed as the flame was also approached [141, 10]. The scalar dissipation rate at the flame base was also shown to be much lower than the critical flamelet quenching value. These experimental results tended to suggest that partially premixed flame propagation exhibiting the structure of a triple or edge flame existed at the lift-off height. Further, some DNS also supported the existence of a triple flame at the base of a lifted turbulent hydrogen flame [143]. On the numerical side, in order to include the effects of partially premixed flame propagation, the turbulent combustion model formulation needs to include an accurate description of both pure premixed and diffusion flames occurring simultaneously. This non-premixed/premixed blending strategy has been investigated in the context of the flamelet model. Bradley et al. [82] implemented a strained premixed flamelet model constrained within specified flammability limits and the mean heat release rate was calculated by integrating over the PDF of both the reaction progress variable and mixture fraction. The predicted lift-off heights were in reasonable agreement with the experimental data, but the formulation was mostly based on premixed flame propagation. The description was further improved by allowing for premixed flame extinction [83]. Combined with a Reynolds stress turbulence model and second order closure for the temperature, good predictions for the lift-off height and blow-off velocity were shown. Another flamelet model implementation was proposed by Müller et al. [84] and further modified by Chen et al. [85]. Two scalars were considered, mixture fraction to indicate the local equivalence ratio and the level-set of the scalar G to give the location of the premixed flame front. The results for the lift-off height were in good agreement with the experimental values for the flames selected. In these previous studies [85, 84], the main issue was related to the calculation of the turbulent burning velocity needed in the G transport equation [22]. Outside the flamelet model, a complete doubly CMC has never been fully implemented in RANS calculations or LES due to the complex closure of many terms in the CMC transport equations. Only a priori tests using DNS have been performed where the sensible enthalpy [144] and the scalar dissipation [7] served as a second conditioning variable.

In the present work, a different approach is investigated, DCSE. CSE has been successfully applied to both non-premixed [101, 75, 76] and premixed flames [77, 78]. A partially-premixed CSE formulation has the potential of being capable of modelling diverse conditions from fully premixed or non premixed to partially premixed combustion without any combustion regime limitations.

The objective of the present chapter is to evaluate the applicability of DCSE applied to

a series of lifted jet flames experimentally investigated by Schefer and co-authors [11, 9, 10]. The cases simulated are turbulent jet flames burning methane issuing into cold air with very low air coflow. Experimental data is available for methane (CH_4) concentrations and lift-off height, and some information is provided for the flame structure around the flame base such as flammable region width, averaged velocity, instantaneous velocity measurements using Particle Image Velocimetry (PIV) and OH planar images. To the authors' best knowledge, the flames presented by Schefer et al. [11, 9, 10] have never been simulated with a partially-premixed turbulent combustion model. Determination of the joint mixture fraction-progress variable PDF, closure of the progress variable transport equations and numerical implementation will be discussed. The proposed formulation can be applied to LES as well as RANS. As a first investigation, a RANS approach is selected.

4.3 Combustion regimes and PDF shapes

Different regimes in turbulent combustion correspond to different conditions in the mixture fraction space. As a consequence, the corresponding PDF, $P(Z)$, takes different forms, as presented in Fig. 4.1. Premixed flames are characterized by a defined value of of the mixture fraction and the corresponding PDF can be approximated as a Dirac delta function, as represented by the arrow in Fig. 4.1. In the regime of diffusion combustion, mixing occurs in the combustion chamber and the whole range of mixture fraction between 0 and 1 is of interest in the combustion process. Near the leading edge, where combustion barely starts, a bimodal distribution is observed, as shown by the blue solid line in Fig. 4.1. In proximity of the flame, the distribution is monodal (blue solid line in Fig. 4.1), centered on the stoichiometric value of the mixture fraction, where the most intensive reaction takes place. In the more general case of partially premixed combustion, different conditions are observed.

Two different types of partially premixed combustion are generally defined: in the case the flame experiences an equivalence ratio gradient, only fuel-rich or only fuel- lean mixture can exist and diffusion flames will not occur [23]. This particular regime refers to "stratified combustion" or "premixed combustion with variable stoichiometry" and the corresponding $P(Z)$ is constricted to either lean or rich conditions, as represented by the square and cross symbols in Fig. 4.1, for lean and rich mixtures, respectively. In contrast, if both the lean and rich mixtures pockets exist, a combination of premixed and diffusion flame burning takes place. This more general case is sometimes referred to as "partially premixed combustion" and the related mixture fraction can cover a wide range, as denoted by the dotted curve in Fig. 4.1.

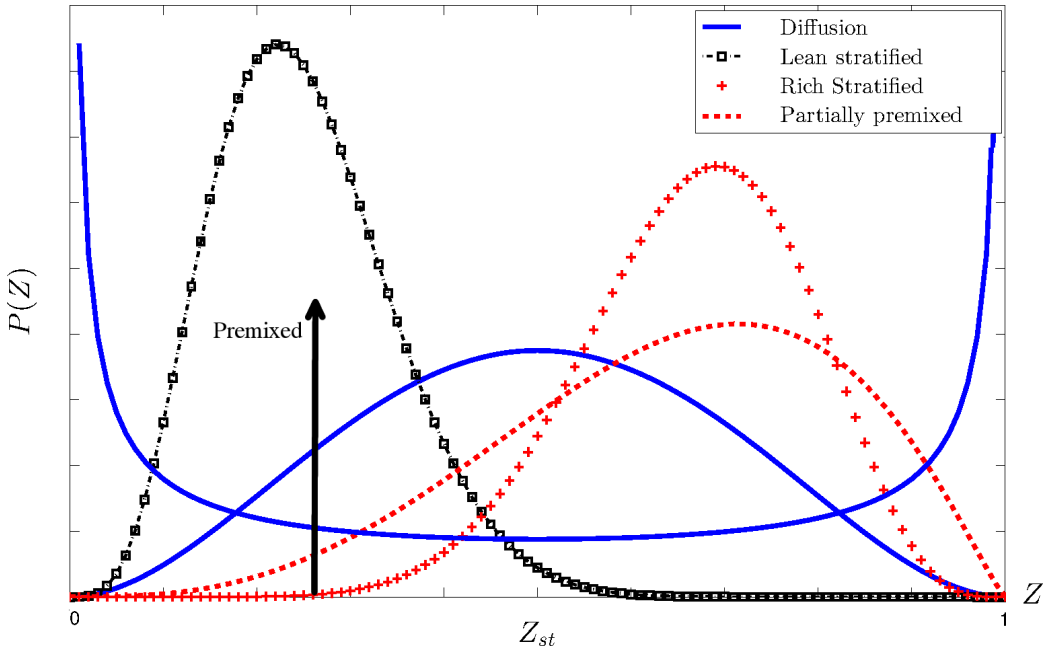

Figure 4.1: Schematic of the shapes of $P(Z)$ or different combustion regimes. Solid blue line: non-premixed; black arrow: premixed; black squares: lean stratified; red crosses: rich stratified; red dotted line: partially premixed.

4.4 Double Conditioning

The idea of introducing an additional conditioning scalar has been proposed in non-premixed combustion modelling, in cases where the mixture fraction alone was not sufficient as conditioning scalar. In the flamelet context, two quantities have been used to parametrize the flow field in turbulent combustion: mixture fraction and scalar dissipation rate [21]. A first attempt of using double conditioning for non-premixed flames can be found in the work of Cha et al. [7], where the scalar dissipation rate served as the second conditioning variable in first-order CMC predictions of turbulent non-premixed combustion characterized by extinction/reignition events. The idea of introducing an additional conditional scalar consisted of reducing the fluctuations about the conditional means so that first-order closure remained a valid approximation. For illustration, experimental

conditional profiles of the reduced temperature $\theta = \frac{T-T_\infty}{T_a-T}$ (where T_a and T_∞ are the adiabatic and reference temperature, respectively) in mixture fraction (η) space of a turbulent methane/air reacting jet [6] with the data taken from an entire planar cross section at 15 diameters downstream the nozzle, are shown in Fig. 4.2. The line shows results of a strained, opposed-flow laminar flame calculation with a strain parameter equal to 50 s^{-1} and is included as a visual guide [6].

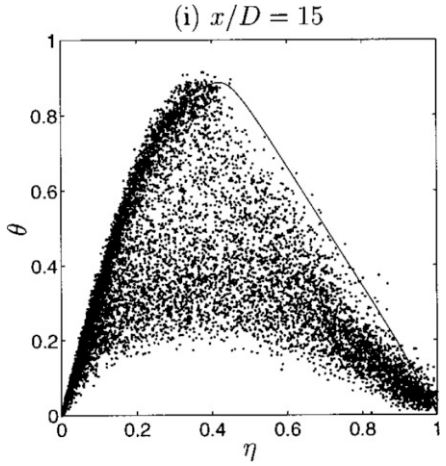

Figure 4.2: Scatter plots of the reduced temperature θ taken from a planar cross section at 15 D from the nozzle of methane/air turbulent reacting jet F of Barlow and Frank [6]. D is the jet nozzle diameter. Reprinted from [7].

The large fluctuations about $\langle\theta|\eta\rangle$ due to extinction/reignition phenomena can be observed in the broad distribution of the scatter plot. Fluctuations can be noticeably reduced if conditioning in an appropriate variable is included. The scalar dissipation rate has been used [7], but lacks a correlation with the chemical source term. A more suitable variable may be preferred, such as fuel and oxidizer mass fractions or temperature [21].

Partially premixed flames represent a case where both the mixing and the reaction progress determine the flame structure and the rate of fuel conversion. Thus, double conditioning in mixture fraction and progress variable appears as an appropriate approach to deal with such flames. Kronenburg [86] presented double conditioning of reactive transport equations on mixture fraction and sensible enthalpy as an attractive extension of singly conditioned CMC for turbulent flames with significant fluctuations of temperature and species about their conditional means. CMC predictions agreed very well with DNS data when a first order closure was used in terms of species mass fractions and chemical reaction

rates and the superiority of double conditioning was clearly evidenced. However, it must be noted that doubly conditioning introduces new issues with respect to the standard singly conditioning that must be addressed. The doubly conditioned dissipation terms and their cross-correlation are not closed and require modelling. As a first attempt, independence of the scalar dissipation of the respective second conditioning scalar can be imposed following Hasse and Peters [145]. This may hold for cases where both the conditioning variables are passive scalars, such as in the case of non-premixed combustion with multiple streams, as implemented by [146] with good results in terms of axial velocity, turbulent kinetic energy, temperature and trend of lift-off height. In more general problems, where progress variable and mixture fraction are correlated, an accurate treatment of the scalar dissipation rate closure is needed. In addition, the joint PDF of the two conditioning variables has to be considered and a careful modelling must be examined. Investigation of DCSE is expected to be the most delicate and crucial step of the present study as no previous work has been done in the context of partially premixed combustion using CSE. In the following sections, DCSE is presented, the implementation in RANS is explained and numerical results are shown and compared with available experimental data.

4.5 DCSE Formulation

Double conditioning in the CSE framework was considered by Bushe and Steiner [74] for non-premixed flames in the presence of local extinction. With the use of a second conditioning variable, reaction rates predictions were significantly improved. The same idea is followed here, but, instead of considering extinction events, a partially premixed combustion model is presented by combining the non-premixed and premixed (see Chapter 3) CSE formulations.

4.5.1 Theory

Similar to the approach described in Chapter 3, first order closure for the conditional chemical source term is applied, neglecting the conditional fluctuations. In the present implementation with doubly conditioning, such an assumption is considered to be even less restrictive compared to a singly conditioning approach. This was also confirmed by Kronenburg's findings in a reactive flow DNS study including incompressible, decaying homogeneous turbulence with a simplified two-step mechanism for hydrocarbon combustion and unity Lewis numbers [86]. The fluctuations about the conditional means were shown to be much smaller than the fluctuations about singly conditioned averages [86]. Further,

CSE assumes statistical homogeneity of the conditional means within a known ensemble of points. This assumption, which is necessary for the CSE approach, is based on the observation that conditional averages vary much less in space than unconditional averages [62, 93]. Knowing the conditional scalars, the unconditional (Favre averaged) quantities are determined by

$$\tilde{f}(\vec{x},t) = \int\int \langle f|Z,c^*\rangle(Z,c^*;\vec{x},t)\tilde{P}(Z,c^*;\vec{x},t)dZdc^*, \tag{4.1}$$

where f may be any scalar such as species concentrations or temperature, t is the time, $\vec{x}$ the vector giving the physical spatial location, and Z and c^* are the sample space variables for the mixture fraction and the progress variable, respectively. The doubly conditional average, $\langle f|Z,c^*\rangle$, and the joint PDF, $\tilde{P}$, are functions of both physical space and time. If the conditional averages are spatially invariant (as it is the case within a specified ensemble), the spatial dependence can be neglected and the conditional values are obtained by inverting the following integral equation

$$\tilde{f}(\vec{x}_j,t) = \int_0^1\int_0^1 \langle f|Z,c^*\rangle(Z,c^*;t)\tilde{P}(Z,c^*;\vec{x}_j,t)\ dZdc^* \quad , \qquad j\in J\ , \tag{4.2}$$

where $\vec{x}_j$ is the spatial coordinate of the j-th point in the ensemble J. Equation (4.2) can be discretized leading to the following equation

$$\vec{b} = \mathbf{A}\vec{\alpha}, \quad A_{j,m} = \int_{Z_1}^{Z_2}\int_{c_1^*}^{c_2^*} \tilde{P}(Z_m,c_m^*;\vec{x}_j,t)\ dZdc^*, \tag{4.3}$$

where $b_j = \tilde{f}(\vec{x}_j,t)$ and $\alpha_m = \langle f|Z,c^*\rangle$. The index m runs from 1 to $M = (n_Z \times n_{c^*})$, where n_Z is the number of points in mixture fraction space and n_{c^*} the number of points in progress variable space. The dimension of A is $N \times M$, where N is the number of points (grid nodes) in a given ensemble. This implies that a much larger matrix needs to be inverted, compared to previous implementations of singly CSE in premixed (Chapter 3, [77, 78]) and non-premixed [101, 75, 76] flames. Consequently, the inversion process becomes much more challenging. The solution for the conditional average $\vec{\alpha}(t) = \mathbf{A}^{-1}\ \vec{b}(t)$ is ill-posed. This means that the solution is sensitive to any small perturbation in the system [97]. A regularization approach is adopted in order to reach a smooth and unique solution.

Several regularization methods can be selected for this operation, including TSVD [99] or Tikhonov regularization methods [98], as presented in Section 3.1.1. It has been shown in Section 3.3.1 that similar results are obtained using both approaches; however,

Tikhonov regularization presents the major advantage over TSVD of being characterized by a continuously-variable degree of regularization. Thus, (zeroth order) Tikhonov regularization has been the preferred method in the different implementations of CSE [77, 78]. Further investigation has also been performed by applying a Bayesian analysis to the inversion process involved in CSE for a non-premixed turbulent methane-air flame [147]. Zeroth (temporal) and first order (spatial) Tikhonov regularization methods were found to perform well. The first order formulation presented the benefit of being independent of the solution time evolution, but zeroth order method was easier to implement than the first order formulation. Thus, zeroth order Tikhonov regularization is selected for the present study. It consists of solving the augmented minimization problem

$$\min \left\{ \left\| \mathbf{A}\vec{\alpha} - \vec{b} \right\|_2^2 + \lambda^2 \left\| \vec{\alpha} - \vec{\alpha}_0 \right\|_2^2 \right\} , \tag{4.4}$$

which has the same form of Eq. 3.8. Several initial solutions for $\vec{\alpha}_0$ are possible and the final solution does not depend on the *a priori* knowledge [77, 78]. In the present study, the strategy proposed by Grout et al. [101] is adopted: the previous time step solution is used for $\vec{\alpha}_0$ and a value of zero is taken as very first value when the simulation starts. The optimum value for the regularization parameter can be found by using the L-curve approach, as described in Section 3.3.1. However, this involves the determination of the norm of the solution and the norm of the residual at each time step, and the determination of the region where these two curves give the minimum error (corresponding to the "corner" of the L-shaped curve). This procedure is not straightforward to implement in an automated manner in DCSE. Thus, the simplified approach proposed by Grout et al. [101] is selected. The regularization parameter is calculated as $\lambda = Tr(\mathbf{A}^T\mathbf{A})/Tr(I)$, where Tr is the trace of the matrix and I the identity matrix. As a postprocess, the values of λ have been compared with those calculated using the L-curve approach and are found to be of the same order of magnitude. The adopted regularization method does not impose the positivity condition on the conditional species mass fractions that must be positive. In the present calculations, very small negative values are observed for very fuel rich conditions. In this region, chemical activity is expected to be negligible and these numerical errors would not have an impact on the overall turbulent combustion modelling. The strategy adopted to circumvent this nonphysical behaviour, consists of setting to zero any negative values for the vector of the solution $\vec{\alpha}$ and rescale it as done by Labahn and Devaud [75]. The scaling process is based on a least-squares approach that defines the scaling factor which minimizes the error. The vector of the solution $\vec{\alpha}$ is multiplied by this

factor and the final value of $\vec{\alpha}$, $\vec{\alpha}_{final}$ is calculated following

$$\vec{\alpha}_{final}(t) = \vec{\alpha}(t)\frac{\sum_j \widetilde{Y}_k(\vec{x}_j,t)\int_0^1\langle Y_k|Z,c^*\rangle(Z,c^*;t)\tilde{P}(Z,c^*;\vec{x}_j,t)}{\sum_j\left(\int_0^1\langle Y_k|Z,c^*\rangle(Z,c^*;t)\tilde{P}(Z,c^*;\vec{x}_j,t)\right)^2} \tag{4.5}$$

Other inversion techniques, such as some described by Twomey [148], could also be investigated in the future.

4.5.2 Joint PDF

As can be seen in Eq. 4.2, the joint PDF is needed for the inversion to obtain the conditional averages. In order to obtain reasonable unconditional quantities from conditional ones, a sufficient approximation of the joint PDF, depending on mixture fraction and reaction progress variable, needs to be generated. The joint PDF can be determined using Bayes theorem, yielding

$$\tilde{P}(Z,c^*) = \tilde{P}(Z)\tilde{P}(c^*|Z)\ . \tag{4.6}$$

The conditional PDF, $\tilde{P}(c^*|Z)$, represents the probability density of the variable being equal to the sample space variable c^* at the condition that Z is satisfied ($c^* = Z$). Vervisch et al. [51] noted that $\tilde{P}(c^*|Z)$ can be well approximated by $\tilde{P}(c^*)$, in particular within the flammability limits, in a DNS of a diffusion flame interacting with freely decaying turbulence. It was shown to be valid if the progress variable corresponded to the product or fuel mass fraction normalized by its chemical equilibrium value. They applied this property in a RANS of the Sandia D Flame and LES of a lifted flame [51]. The statistical independence between the two variables, mixture fraction and progress variable, was commonly applied [149, 150] with good predictions for temperature and species concentration for the Cabra flame [133]. Grout [8] found a weak correlation between the two variables examined here (the correlation coefficient between the two was $R^2 = 0.09$) and compared this approximated statistical independent joint PDF with the PDF using DNS data obtaining good agreement [8], as shown in Fig. 4.3. This definition of the joint PDF is simple, but can lead to some errors especially for values in sample space between 0 and 1. A possible improvement consists of defining the joint PDF following Eq. 4.6. Grout [8] analyzed the the effect of the joint PDF defined in Eq. 4.6 against DNS data. $\tilde{P}(Z)$ was defined by a β function, while two different form for $\tilde{P}(c^*|Z)$ were used: laminar flame derived PDF [92] and a β PDF [90]. Compared to the statistical independent case, Eq. 4.6 resulted in better predictions of the behaviour of the joint PDF. Darbyshire and Swaminathan [151]

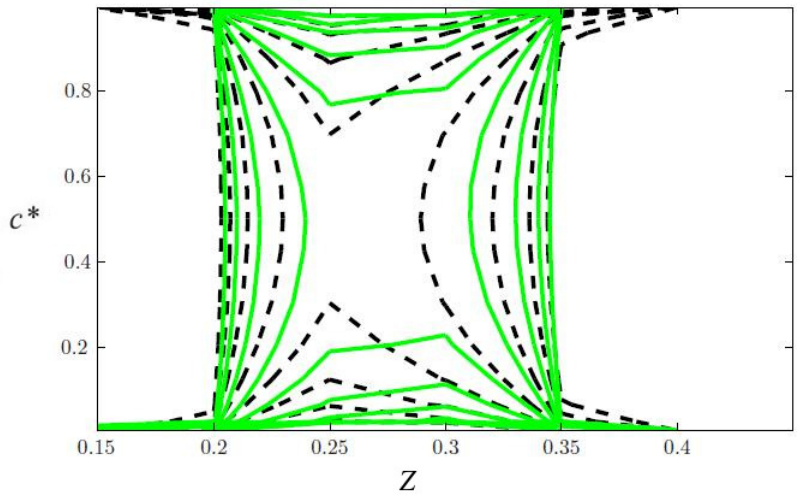

Figure 4.3: Contours of global joint PDF $P(Z, c^*)$ (solid, green) and $P(Z)P(c^*)$ (dashed, black), taken from [8].

have proposed a new model for the joint PDF of the mixture fraction and progress variable based on the use of a copula [1]. The new formulation was shown to give a more accurate description for the joint PDF using DNS, but when implemented in RANS in the context of stratified flames, no significant improvement in temperature, velocity and species concentration was observed compared to the statistically independent PDF formulation. Recently, Ruan et al. [152] have implemented the copula method to determine the joint PDF in a flamelet model approach applied to lifted turbulent hydrogen jet flames in still atmospheric air without coflow. The predicted lift-off heights were shown to be sensitive to the joint PDF definition. The joint PDF copula method resulted in lift-off heights 25-30%, depending on the model formulation used, larger than those obtained assuming statistical independence.

In the present work, the impact of the statistical independence assumption is investigated. First, following [149, 150, 51], statistical independence between mixture fraction and progress variable is assumed and the joint PDF is expressed as

$$\tilde{P}(Z, c^*) = \tilde{P}(Z)\tilde{P}(c^*). \tag{4.7}$$

$\tilde{P}(Z)$ is calculated as a β-PDF distribution [90], while a modified laminar flame PDF is used for $\tilde{P}(c^*)$ as it is shown to provide a better description of the progress variable statistics

[1] In probability theory and statistics a copula is a multivariate probability distribution that is used to describe the dependence between random variables.

compared to the β-PDF [4]. Details of the modified model can be found in Section 3.1.3. In the present study, the stoichiometric value of the equivalence ratio is used to define the shape of $f(c^*)$ (see Eq. 3.13).

Alternatively, using the formulation shown in Eq. 3.12, a joint PDF can be determined relaxing the assumption of statistical independence. For a given equivalence ratio, a defined form of $f(c^*)$ is found. This leads to a clear dependence of $\tilde{P}(c^*)$ to the mixture fraction and the joint PDF can be calculated as Eq. 4.6. The procedure on calculating the joint PDF shown in Eq. 4.6 is as follows: for each sample in mixture fraction space, an equivalence ratio equal to $\frac{Z}{1-Z}\frac{1-Z_{st}}{Z_{st}}$ (where Z_{st} is the stoichiometric value of the mixture fraction) is calculated and a specific form of $f(c^*)$ is obtained, leading to $\tilde{P}(c^*|Z)$. For very fuel lean and very fuel rich conditions, a converged solution for the unstrained laminar premixed flame could not be obtained and instead, a $\beta-$ PDF is used. These regions correspond to values of mixture fraction smaller than 0.0143 and larger than 0.2, far from the flammability limits for methane-air combustion which are approximately equal to 0.0284 and 0.089 (in mixture fraction) at atmospheric conditions [153]. However, the conditional reaction rates are expected to be negligible beyond these limits; consequently, the shape of the PDF should not affect the calculated values of the unconditional reaction rates for conditions outside the flammability region.

4.5.3 Progress variable

As introduced in Section 4.4, two control parameters are used to characterize partially premixed combustion: the distribution of the mixture fraction $Z(x,t)$ and a reaction progress variable $c(Z;x,t)$. The mixture fraction is a passive scalar and is used to define the level of fuel/air mixing in the system. It takes a value of zero in the air stream and unity in the fuel stream. The progress variable is a non-conserved scalar and, as described in Section 3.1, has the property of being equal to zero in fresh gases and unity for burnt gases. The progress variable has found to be a convenient marker for both premixed and nonpremixed reaction zones in partially premixed combustion [23]. Grout [8] explored the effectiveness of the conditioning process through the use of different definitions of the reaction progress variable: a fuel based progress variable and a product based progress variable. The first one had the benefit of being easily defined by the PDF since the chemical source term was confined to a relatively narrow region in space [8]. However, in the case that the fuel was fully consumed and the progress variable did not change, other thermochemical variables varied in space, resulting in a considerable variation of conditional averages. In contrast, the product based progress variable had a non-zero source term in a wider region (wherever reactions took place). Thus, the conditional averages were more homogeneous

in space. This property is essential in the CSE formulation and makes the product based progress variable a suitable candidate for the second conditioning variable definition in DCSE. Because of partial premixing conditions, the progress of reaction is dependent on each possible mixture fraction composition. Thus, a dependence on the mixture fraction is introduced. In the present study, the progress variable is defined as

$$c(Z) = \frac{Y_{\mathrm{CO_2}}}{Y^{Eq}_{\mathrm{CO_2}}(Z)} \ , \tag{4.8}$$

where $Y^{Eq}_{\mathrm{CO_2}}$ is the equilibrium value of the mass fraction of CO_2, when combustion is complete. Equation 4.8 is valid for both premixed and non-premixed combustion. This dependence on mixture fraction leads to a different progress variable transport equation compared to the fully premixed situation (Eq. 3.24) where the progress variable is not function of mixture fraction [23],

$$\frac{\partial(\overline{\rho}\widetilde{c})}{\partial t} + \frac{\partial}{\partial x_i}(\overline{\rho}\widetilde{u}_i\widetilde{c}) = \frac{\partial}{\partial x_i}\left(\overline{\rho D\frac{\partial c}{\partial x_i}} - \overline{\rho}\widetilde{u''_i c''}\right) + \overline{\dot{\omega}}_c + \overline{\rho\frac{1}{Y^{eq}_{\mathrm{CO_2}}}\frac{\partial^2 Y_{\mathrm{CO_2}}}{\partial c^2}\chi_c} + \overline{\rho\frac{1}{Y^{eq}_{\mathrm{CO_2}}}\frac{\partial^2 Y_{\mathrm{CO_2}}}{\partial Z^2}\chi_Z} + 2\overline{\rho\frac{1}{Y^{eq}_{\mathrm{CO_2}}}\frac{\partial^2 Y_{\mathrm{CO_2}}}{\partial Z\partial c}\chi_{cZ}} \ . \tag{4.9}$$

Three additional terms, $\overline{\rho\frac{1}{Y^{eq}_{\mathrm{CO_2}}}\frac{\partial^2 Y_{\mathrm{CO_2}}}{\partial c^2}\chi_c}$, $\overline{\rho\frac{1}{Y^{eq}_{\mathrm{CO_2}}}\frac{\partial^2 Y_{\mathrm{CO_2}}}{\partial Z^2}\chi_Z}$ and $2\overline{\rho\frac{1}{Y^{eq}_{\mathrm{CO_2}}}\frac{\partial^2 Y_{\mathrm{CO_2}}}{\partial Z\partial c}\chi_{cZ}}$ can be found compared to the transport equation in the fully premixed case. Equation 4.9 is valid when all the molecular diffusivities are equal and is applicable to all modes of combustion [23]. The scalar dissipation rates, χ_Z, χ_c and χ_{Zc} are defined as

$$\chi_Z = D\left(\nabla Z \cdot \nabla Z\right), \quad \chi_c = D\left(\nabla c \cdot \nabla c\right) \text{ and } \chi_{Zc} = D\left(\nabla Z \cdot \nabla c\right) \tag{4.10}$$

In Eq. 4.9, the term containing χ_c vanishes because c is defined to be a linear function of $Y_{\mathrm{CO_2}}$, resulting in $\partial^2 Y_{\mathrm{CO_2}}/\partial c^2 = 0$.

The second derivative with respect to Z, $\frac{\partial^2 Y_{\mathrm{CO_2}}}{\partial Z^2}$, is approximately 0 unless $Z \simeq Z_{st}$ [23]. In the present study, this quantity is estimated in a-priori calculations by considering the $Y^{eq}_{\mathrm{CO_2}}(Z)$ profiles from the TGLDM chemistry database and the second derivative calculated through the finite difference method. It is found to be non-zero around stoichiometric conditions, consistent with the findings of [23]. Ruan et al. [47] have investigated different scalar dissipation rates for a lifted flame in DNS. They found that the scalar dissipation rate for mixture fraction, χ_Z, decreased considerably with the axial distance and was shown to have small contributions in the case of a lifted turbulent flame, since no reactions were

expected at locations upstream of the stabilization point. However, the entire term, $\frac{\partial^2 Y_{CO_2}}{\partial Z^2}$ multiplied by χ_z, was shown to have some impact on the lift-off height predictions in a lifted turbulent hydrogen jet flame using RANS and a flamelet model [152]. Improvements in the lift-off height predictions were obtained when this term was included on the order of 13% and 20% depending on the simulations. This aspect needs further investigation in the context of non-flamelet approaches like CSE and hydrocarbon flames displaying different stoichiometric values and flammability limits compared to hydrogen flames. In the present work, the χ_z term is neglected in Eq. 4.9.

As for the last term in Eq. 4.9 containing χ_{Zc}, the cross-scalar dissipation rate χ_{Zc} is challenging to model as both contributions from turbulent diffusive mixing and gradients of the reaction progress variable must be taken into account. To the author's best knowledge, closure strategies of the cross-dissipation term are still an open question [23, 154]. Robin et al. [12] used a more general version of the scalar dissipation model of Mura et al. [155] based on the two limiting behaviours of the scalar dissipation (pure mixing and fully burning) for the numerical simulation of a stratified V-shaped flame [12], obtaining good results. Malkeson and Chakraborty [156] derived a transport equation for the cross-scalar dissipation rate based on the fuel mass fraction and mixture fraction and proposed algebraic models based on DNS results of statistically planar stratified flames. Finally, one simple strategy consists of closing this term by using the classical model based on the inverse of turbulent timescale ε/k [151]

$$\overline{\rho D \frac{\partial c''}{\partial x_i} \frac{\partial Z''}{\partial x_i}} = \widetilde{\chi}_{Z_c} = c_\chi \frac{\widetilde{\varepsilon}}{\widetilde{k}} \widetilde{Z''^2} \widetilde{c''^2} \ . \tag{4.11}$$

However, recent DNS comparisons suggested that the cross-dissipation term in Eq. 4.9 was one order of magnitude smaller than the other two terms [152], consistent with previous conclusions [149]. Thus, $\widetilde{\chi}_{Z_c}$ is neglected in the current study.

4.6 DCSE Implementation

DCSE is implemented in RANS. However, similar implementation is expected in LES where filtered quantities would be considered. The governing equations solved using the CFD code, OpenFoam [110], are: conservation of mass, conservation of momentum, turbulent kinetic energy and its dissipation transport equations, conservation of enthalpy, conservation of species mass fraction, progress variable and its variance transport equations, mixture fraction and its variance transport equations.

The interactions between the CFD code and the different submodels in DCSE follow the same procedure described in Section 3.1.4 and are summarized here. The mean and variance of the progress variable, mixture fraction and mixture fraction variance are needed to calculate the joint PDF (Eq. 4.6 or Eq. 4.7). The PDF module constructs the kernel of the inverse problem (matrix **A** in Eq. 4.3). The DCSE routine calculates the doubly conditional averages, starting from the unconditional values and the kernel by solving Eq. 4.3. Similar to what is commonly done in CMC, the conditional chemical source terms are determined as a function of the conditional chemical species and temperature using first order closure. In the present work, a detailed chemistry mechanism is used [157]. For computational saving, a chemistry tabulation technique, the TGLDM method [102], is adopted. It is important to note that CSE does not require any tabulated chemistry to function properly. The strategy of using tabulated chemistry has also been used by Navarro-Martinez and Rigopoulos [158] to determine the conditional averages in LES of a lifted methane flame in the context of CMC. Further, different chemistry tabulation techniques, other than TGLDM, could have been selected, but have not been investigated within the present framework. In the current study, chemistry is tabulated as a function of two variables, the mass fraction of carbon dioxide (Y_{CO_2}) and the mass fraction of water (Y_{H_2O}). Using the chemistry tables, the conditional reaction rates of species are retrieved and the unconditional values are calculated by integrating with the joint PDF over the entire c^* and Z sample spaces, as shown in Eq. 4.1. Finally, the unconditional mean reaction rates are used as source terms in the unconditionally averaged species transport equations and the loop starts again until convergence is reached.

The resulting TGLDM tables would be four dimensional, functions of c^*, Z, Y_{CO_2} and Y_{H_2O}. However, in the current implementation, the progress variable is selected to be equal to the CO_2 mass fraction normalized by its equilibrium value at a given mixture fraction. Thus, the chemistry table dimensionality is reduced to three dimensions as the conditional mass fraction of CO_2 can be retrieved from the value of the progress variable, knowing the equilibrium value at a given mixture fraction. This also implies that the only unknown parameter required to determine the conditional chemical reaction rates is $\langle Y_{H_2O}|Z, c^*\rangle$, which is obtained by inverting the integral equation as shown in Eq. 4.3. If the progress variable was not equal to the normalized mass fraction of CO_2, $\langle Y_{CO_2}|Z, c^*\rangle$ would also be needed and obtained using Eq. 4.3.

4.7 Computational details

The experimental set-up simulated in the present study consists of a 5.4 mm diameter fuel jet surrounded by ambient air with no coflow (in the experiments, there is a very small air coflow considered to have no effect on the lift-off height), experimentally investigated by Schefer et al. [11, 9]. The jet velocities are equal to 21, 37 and 60 m/s, corresponding to jet exit Reynolds numbers of 7,000, 12,000 and 19,500, respectively. The jet velocities are far below the flame blowout velocity found to be approximately equal to 90 m/s [11]. The computational domain is cylindrical with a radius of 324 mm and total length of 1080 mm. A schematic of the domain is presented in Fig. 4.4. The geometry is created as a wedge of a small angle (5°) and 1 cell thick running along the plane of symmetry. Thus, the simulations are performed in two dimensions. The grid is nonuniform, with high density of grid points close to the central jet and the shear layer, where the flame is supposed to develop. The current grid consists of 22,400 cells. Further grid refinement was tested and the present results are found to be grid independent. The inlet boundary conditions consist of pure methane. The inlet turbulence intensity is set to 10%, consistent with the maximum value of the measured centreline velocity fluctuations for the jet velocity of 21 m/s in non-reacting conditions [159]. The one seventh turbulence power law is applied to the inlet velocity profile. Experimental results showed that the lift-off height increased significantly if the velocity ratio between air and jet was larger than 0.002, while no change in the flame lift-off height was observed for ratios less than 0.002 [11]. In the numerical simulations, this ratio is kept equal to 0.0005, far from the limit value of 0.002, for all the three cases. Atmospheric value of the pressure is set at the outlet (denoted as Pressure Outlet in Fig. 4.4).

The transport equations for the mean mixture fraction, $\widetilde{Z}$ and its variance, $\widetilde{Z''^2}$, as well as those for the mean progress variable, $\widetilde{c}$ and its variance, $\widetilde{c''^2}$, need to be solved. The mixture fraction and its variance transport equations are

$$\frac{\partial(\overline{\rho}\widetilde{Z})}{\partial t} + \frac{\partial}{\partial x_i}(\overline{\rho}\widetilde{u}_i\widetilde{Z}) = \frac{\partial}{\partial x_i}\left(\overline{\rho D\frac{\partial Z}{\partial x_i}} - \overline{\rho}\widetilde{u_i''Z''}\right) \tag{4.12}$$

and

$$\begin{aligned}\frac{\partial(\overline{\rho}\widetilde{Z''^2})}{\partial t} + \frac{\partial}{\partial x_i}\left(\overline{\rho}\widetilde{u}_i\widetilde{Z''^2}\right) = -\frac{\partial}{\partial x_i}\left(\overline{\rho u_i''Z''^2}\right) + \frac{\partial}{\partial x_i}\left(\overline{\rho D\frac{\partial Z''^2}{\partial x_i}}\right) \\ -2\overline{\rho u_i''Z''}\frac{\partial\widetilde{Z}}{\partial x_i} - 2\overline{\rho D\frac{\partial Z''}{\partial x_i}\frac{\partial Z''}{\partial x_i}}\ .\end{aligned} \tag{4.13}$$

The turbulent scalar fluxes are closed by using a gradient assumption (Eq. 2.22) such that

$$\widetilde{u_i'' Z''} = -\frac{\mu_t}{Sc_{kt}} \frac{\partial \widetilde{Z}}{\partial x_i}, \tag{4.14}$$

where the value of Sc_{kt} is 0.7 and μ_t the turbulent viscosity.

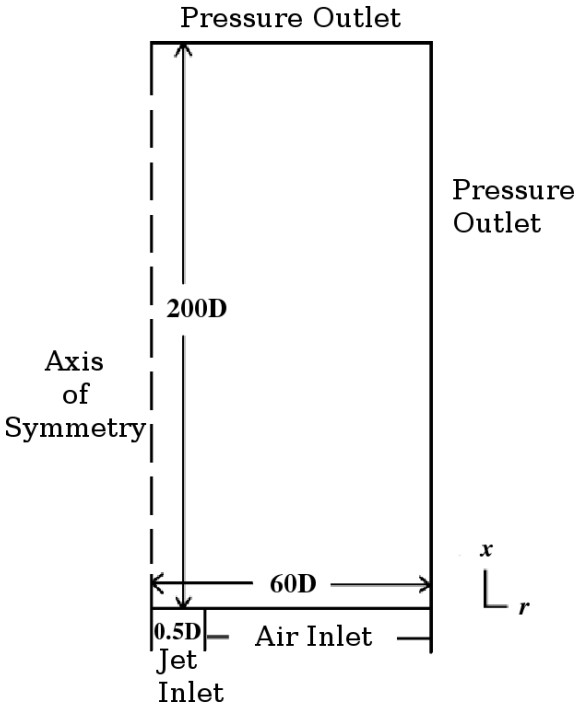

Figure 4.4: Schematic of the computational domain and specification of the adopted boundary conditions.

The last term in Eq. 4.13 represents the scalar dissipation of the mixture fraction fluctuation and a good approximation can be achieved with a linear relaxation model using

$$\overline{\rho D \frac{\partial Z''}{\partial x_i} \frac{\partial Z''}{\partial x_i}} = \widetilde{\chi}_Z = c_\chi \frac{\widetilde{\varepsilon}}{\widetilde{k}} \widetilde{Z''^2} \ , \tag{4.15}$$

where c_χ is a constant assumed equal to 1.

The progress variable is defined as normalized mass fraction of CO_2 (see Eq. 4.8) and its transport equation is given by Eq. 4.9 with the assumptions made in Section 4.5.3. The

transport equation for the variance of the progress variable is given by

$$\frac{\partial(\overline{\rho}\widetilde{c''^2})}{\partial t} + \frac{\partial}{\partial x_i}\left(\overline{\rho}\widetilde{u}_i\widetilde{c''^2}\right) = \frac{\partial}{\partial x_i}\left(\overline{\rho D\frac{\partial c''^2}{\partial x_i}}\right) - \frac{\partial}{\partial x_i}\left(\overline{\rho u_i'' c''^2}\right) \\ -2\overline{\rho u_i'' c''}\frac{\partial \widetilde{c}}{\partial x_i} - 2\overline{\rho D\frac{\partial c''}{\partial x_i}\frac{\partial c''}{\partial x_i}} + 2\overline{c''\dot{\omega}_c}. \tag{4.16}$$

In Eqs. 4.8 and 4.16, the gradient diffusion assumption is used for the turbulent fluxes, similar to the expression shown in Eq. 4.14, neglecting counter-gradient transport. This latter corresponds to situations where the turbulence level is low and the thermal expansion due to heat release is large enough to let the flame impose its own dynamics to the flow field [30]. Several strategies are available to model counter-gradient diffusion [160, 111]. However, as presented in Section 3.2.2, counter-gradient transport is shown to be negligible when the Bray number is smaller than unity [111]. In the lifted turbulent flames presently selected, the experimental investigations did not include any information on counter-gradient diffusion, and the Bray number can only be estimated. Using Eq. 3.21 with the value of the turbulent intensity measured at the base of the flame ($u' = 2.2$ m/s [11]), the laminar flame speed for a stoichiometric methane-air mixture ($S_L = 0.43$ m/s [11]) and the heat release factor based on the stoichiometric adiabatic temperature (2,225 K [161, p. 41]) which yields $\tau = 6.417$, the estimated Bray number is found to be equal to 0.63 for the three flames, which is lower than unity. Thus, the neglect of counter-gradient diffusion is a reasonable assumption in the present simulations. The last two terms in Eq. 4.16 are unclosed. The very last term of Eq. 4.16 is the correlation of the chemical source term and the fluctuations in the progress variable. This term can be computed, knowing the PDF as

$$\overline{c''\dot{\omega}_c} = \overline{(c-\widetilde{c})\,\dot{\omega}_c} = \int_0^1\int_0^1 (c^*-\widetilde{c})\,\langle\dot{\omega}_c|c^*,Z\rangle\tilde{P}(c^*,Z)\;dc^*dZ\;. \tag{4.17}$$

In the present study, $\langle\dot{\omega}_c|c^*,Z\rangle$ is obtained from DCSE and the TGLDM tables: $\langle\dot{\omega}_c|c^*,Z\rangle$ is equal to the conditional source term for CO_2 divided by the equilibrium value of CO_2 mass fraction. The other unclosed term is the Favre-averaged scalar dissipation rate. In turbulent premixed combustion, the scalar dissipation rate is shown to be a significant term and different modelling strategies exist such as using a simple relaxation expression, solving a transport equation or applying an algebraic model [20, p. 74-101]. For example, in Chapter 3, CSE calculations of a premixed bluff body flame successfully implement an algebraic model (Eq. 3.33) proposed by Kolla et al. [118]. In partially premixed combustion, the modelling of the scalar dissipation rate for the progress variable becomes even more complicated due to the dependence on mixture fraction. Models suggested by

Kolla et al. [118] and Mura et al. [155] are among the options and discussed in Section 5.3.1 in the context of stratified flames. In the present framework, keeping in mind that the focus is on the first implementation of DCSE for lifted turbulent flames, a simple algebraic expression, function of the turbulent time scale, similar to Eq. 4.15 is adopted. The choice is also motivated by the fact that the previous CSE predictions for the turbulent premixed flame could be reasonably well reproduced by the simple algebraic model, as presented in Chapter 3.

RANS equations are solved with a finite volume low-Mach number pressure based approach with a PISO algorithm for pressure correction using OpenFOAM [110]. All transport equations are solved using an implicit time integration method, while flux calculations are solved with TVD and NVD schemes. A standard $k-\varepsilon$ approach [31] is adopted.

The chemistry TGLDM tables are generated following Eq. 3.10 using a stiff ODE system solver [162]. The resulting TGLDM database is parametrized as a function of two variables, Y_{CO_2} and Y_{H_2O} for a given mixture fraction. GRI-MECH 2.11 [157] is selected for methane-air combustion and includes 49 species and 277 reactions. 50 different values of mixture fraction Z are considered ranging from 0.0028 to 0.99 with a higher concentration around the stoichiometric value of 0.055. 20 equally spaced bins are used for c^*.

The number of DCSE ensembles in the CFD domain determines the size of the ensemble used for inversion. In practice, the ensemble of points corresponds to a subset of computational grid. To define the DCSE ensembles, the entire computational domain is divided into planes normal to the centreline. The selected strategy takes advantage of the fact that the conditional averages have a weak dependence on the radial direction [62]. There is a small overlap between the ensembles ranging from 3 mm to 5 mm, depending on the total number of ensembles used, to prevent any sharp changes in the conditional values. For points that belong to two consecutive ensembles, the final unconditional mean reaction rate is equal to the simple arithmetic average of the two unconditional values obtained from the two ensembles. The number of points defined in the ensemble (N) must be at least equal to M in order to avoid a rank-deficient condition in the inversion problem. This sets a limit to the choice of the number of DCSE ensembles. However, in the present case, the difference in the predictions of the lift-off height for flame at Re = 7,000 when using 4, 6 or 8 DCSE ensembles is less than 3%. In Section 4.8, the numerical results presented correspond to those with 6 ensembles.

In the progress variable approach, reaction rates are zero for c being zero or one. Thus, the model does not contain a possibility of self-ignition and it is necessary to initiate the combustion process in the computations. Two different strategies are used to achieve ignition of the flow. In the first case, a section of the computational domain is initialized

with a value of CO_2 and H_2O mass fraction close to their respective equilibrium values. Thus, the progress variable has values between zero and unity, and the chemistry tables give non-zero values for the reaction rates. A rectangular box is defined 1 mm downstream from the nozzle exit with one side on the axis, the axial dimension of 100 mm and the radial dimension of 20 mm, where the fields of Y_{CO_2} and Y_{H_2O} are initialized. This region is free to propagate as the simulation proceeds. A second method consists of imposing a preset profile of the conditional values of CO_2 and H_2O mass fraction for a certain number of time steps. Both methods produce the same converged results. In order to save computational time, the simulation is initially advanced with a coarse grid resolution and then mapped onto a finer grid until a converged solution is reached.

4.8 Results

Before examining the predictions obtained with DCSE, it should be noted that the lifted flame corresponding to Re = 7,000 is simulated with singly non premixed CSE, using the same RANS implementation described by Labahn and Devaud [75] and standard $k-\varepsilon$ model. The simulations indicate a severely under-predicted lift-off height, which is less than 5 mm, to be compared to the experimental value of 33 mm. Thus, the resulting flame can be considered attached, as shown in the temperature contour of Fig. 4.5. This significant discrepancy with the experiments (on the order of 85%) clearly demonstrates that an additional conditional variable is needed in the current study. The observation is consistent with previous CMC lift-off predictions using only mixture fraction as conditioning variable [163]. The following results are obtained by using the DCSE method.

4.8.1 Fuel concentration

Due to the axisymmetric properties of the combustion chamber, different values of C_{ε_1} in the k equation of the $k-\varepsilon$ turbulence model are tested, ranging from the standard value of 1.44 to 1.6 in order to resolve the round-jet anomaly, as done in Section 3.3.3. Experimental measurements of the normalized mean CH_4 concentration are available for the flame at Re = 7,000 as centerline variations and radial profiles at four different axial locations for both reacting and non-reacting cases. It should be noted that the methane concentrations, C, provided by Schefer et al. [9], correspond to measured methane number densities divided by the methane number density value for pure methane at standard conditions. The number density is directly related to the molar concentration. The number density (in units of

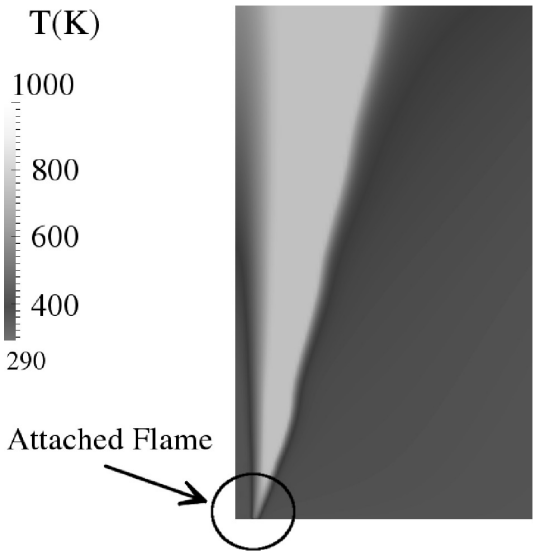

Figure 4.5: Temperature contour obtained with singly non premixed CSE corresponding to Re = 7,000.

m^{-3}) can be expressed in terms of molar concentration c (in units of mol/m^3) of as

$$n = N_A \cdot c \ , \tag{4.18}$$

where N_A is the Avogadro constant $\approx 6.022 \times 10^{23}\ mol^{-1}$. Schefer et al. [9] present the CH_4 concentration C as the measured CH_4 number density normalized by the methane number density for 100% methane at STP conditions (2.5×10^{19} molecules/cm^3)

$$C = \frac{n_{CH_4}}{2.5 \times 10^{19}\ \text{molecules}/cm^3} \ . \tag{4.19}$$

In the numerical simulations, the Favre averaged mass fraction of CH_4, $\widetilde{Y}_{CH_4}$ is solved through a transport equation. This quantity must then be converted in terms of CH_4 number density for direct comparisons with the experimental data. First, the number density is related to the mole fraction through

$$X_{CH_4} = c_{CH_4} \frac{W}{\rho} \ , \tag{4.20}$$

where W and ρ are the average molar mass and the density of the mixture, respectively. The mass fraction in terms of molar fraction is

$$Y_{CH_4} = X_{CH_4} \frac{W_{CH_4}}{W} \ , \tag{4.21}$$

where W_{CH_4} is the atomic weight of CH_4 ($W_{CH_4} = 0.016\ kg/mol$). By combining Eqs. 4.18, 4.20-4.21, Eq. 4.19 can be written as

$$C = \frac{N_A \cdot X_{CH_4} \cdot \frac{\rho}{W}}{2.5 \times 10^{25}\ \text{molecules}/m^3} = \frac{N_A \cdot \rho \frac{Y_{CH_4}}{W_{CH_4}}}{2.5 \times 10^{25}\ \text{molecules}/m^3}\ . \tag{4.22}$$

It is easy to verify that for the pure fuel inlet ($Y_{CH_4} = 1$) and at atmospheric standard conditions ($\rho = 0.66\ kg/m^3$), the equality between the numerator and denominator in Eq. 4.22 is retrieved.

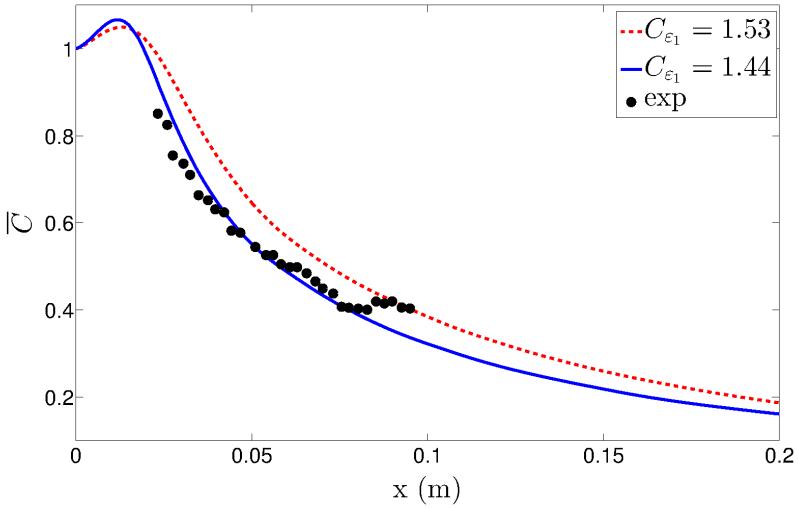

Figure 4.6: Centerline profiles of the mean CH_4 concentration for the lifted turbulent flame at Re = 7,000. Comparison of numerical predictions (lines), obtained with the joint PDF calculated from Eq. 4.6 with two different values of C_{ε_1}, with experimental data (symbols) [9].

The numerical predictions are obtained with the joint PDF shown in Eq. 4.6, without assuming statistical independence between mixture fraction and progress variable and compared with the experimental data [9]. Different values of C_{ε_1} in the dissipation transport equation were tested. Best agreement with the experimental data is provided by $C_{\varepsilon_1} = 1.44$, corresponding to the value included in the standard $k - \varepsilon$ model, as can be seen from Fig. 4.6 where the predicted axial CH_4 concentrations, $\overline{C}$, with the experimental profiles for the lifted flame at Re = 7,000 is presented for two different values of C_{ε_1}, namely 1.44 and 1.53

(other values up to 1.6 have been used and are not shown for brevity). For consistency with the experimental data, the predicted CH_4 mass fractions are converted into number densities expressed in molecules/cm^3 normalized by the value of 2.5×10^{19} molecules/cm^3, through Eq. 4.22. As can be seen in Fig. 4.6, a reasonable agreement with the experimental profile is achieved. There is no experimental measurement available for the other two flames at Re = 12,000 and 19,500. Without any further information, the same value of 1.44 for C_{ε_1} is applied to the simulations of the three flames selected in the presented study.

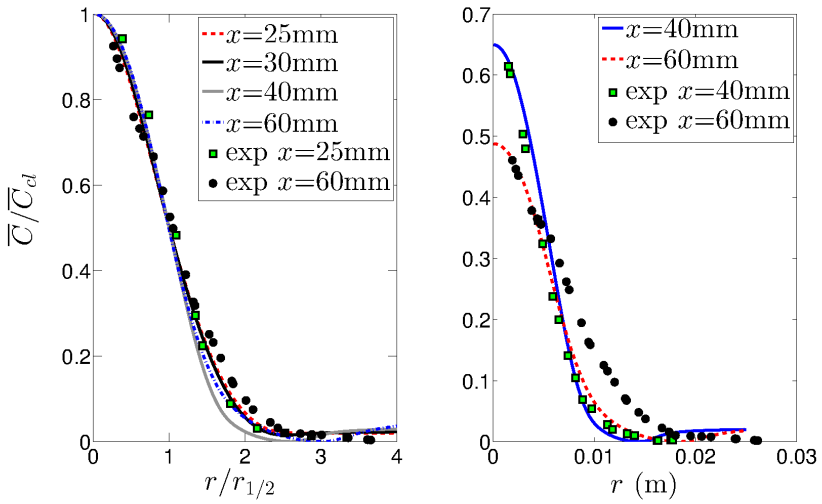

Figure 4.7: Radial profiles of the normalized mean CH_4 concentration in the lifted flame at different axial locations (left) and radial profiles of the non normalized mean CH_4 concentration at x = 40 and 60 mm (right), corresponding to Re = 7,000. The normalized mean concentration corresponds to $\overline{C}$ divided by its centreline value, $\overline{C}_{cl}$. Symbols denote experimental data [9]. The numerical results are obtained with the joint PDF calculated from Eq. 4.6.

Figure 4.7 (left) presents normalized radial contours of the mean CH_4 concentration at different axial locations, x = 25, 30, 40 and 60 mm. The experimental value of the lift-off height is equal to 33 mm. Therefore, some axial positions are upstream and others downstream of the lift-off height. As can be seen in Fig. 4.7 (left), the mean concentrations are normalized by the mean centreline concentration and the radial distance is normalized by the jet half width which is defined as the radial distance at which the concentration has decreased to half the maximum centreline value. The radial profiles collapse onto a single curve as found through self-similarity of round jets, in good agreement with the

experimental analysis. The present flame is characterized by a low lift-off height, leading to a small fraction of reacted CH_4 even at the last axial location ($x = 60$ mm) [9]. For further detail, Fig. 4.7 (right) shows the non normalized radial contours of the mean CH_4 concentration at two axial locations, $x = 40$ mm and $x = 60$ mm. Good agreement is obtained with the experimental data. Very good predictions are obtained for the other available axial locations (25 and 30 mm), as shown in the non normalized radial contours of the mean CH_4 concentration of Fig. 4.8.

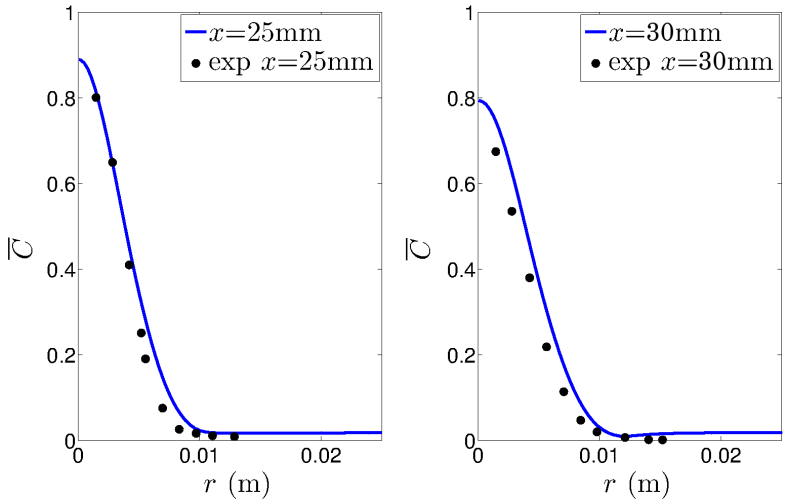

Figure 4.8: Radial profiles of the non normalized mean CH_4 concentration in the lifted flame at $x = 25$ and 30 mm, corresponding to Re = 7,000. Symbols denote experimental data [9]; numerical results are obtained with the joint PDF calculated from Eq. 4.6.

4.8.2 Lift-off height predictions

In the experiments, the lift-off height is generally estimated by visual observation and typically measured from the nozzle exit to the flame leading edge. In the experimental work [11], the stabilization point was defined as the location where OH mass fraction first appeared, but no information was provided for the OH concentrations [11]. The start of the reaction zone marked by a temperature threshold is a common choice in experiments using PIV techniques and it is tracked by the disappearance of the PIV seeding particles [10]. The definition of a temperature threshold is also used in numerical simulations. Up-

atnieks et al. [142] included the 600 K isotherm to outline the hot zone in their examined methane/nitrogen (77%/23% by volume) lifted turbulent jet flames at Re = 4,300. Kim and Mastorakos [164] selected the peak mean temperature of 900 K as lift-off height determination criterion for lifted turbulent jet flames of hydrogen. Devaud et al. [163] used the conditional temperature profile of 1,000 K to determine flame position of a lifted turbulent methane-air flame. Other criteria consisted of defining the flame base as the lowest position of 1% of maximum bound of methane oxidation reaction rate contour [107] or isolines of a reference value of OH radical. In a DNS study of a lifted ethylene jet flame, Yoo et al. [134] defined the flame base as the most upstream location of the $Y_{OH} = 0.004$ isoline. Cabra et al. [132] used a reference value of 0.0006 for the OH mass fraction in a lifted turbulent H_2/N_2 jet flame.

In order to obtain a consistent comparison, the lift-off height is determined from results of the present simulations using these different criteria. The corresponding lift-off height predictions for the three cases are presented in Tables 4.1-4.3. Also shown in Table 4.1, are the values obtained with the two different joint PDF formulations, with and without the statistical independence assumption between mixture fraction and progress variable, Eq. 4.6 and 4.7, respectively. The differences in the predictions are not large: the lift-off heights for the case at Re = 7,000 vary between 31.5 and 37 mm in the first case (when statistical independence is assumed) and between 28.5 and 34.5 mm in the second approach. Consequently, in the present calculations, statistical independence for the joint PDF may be a reasonable assumption. All criteria provide a lift-off height within the experimental range, equal to 26-40 mm [10].

Table 4.1: Lift-off height predictions for the flame at Re = 7,000 based on different criteria with (Eq. 4.7) and without (Eq. 4.6) the statistical independence formulation for the joint PDF.

Criterion	Lift-off height (PDF Eq. 4.7) (mm)	Lift-off height (PDF Eq. 4.6) (mm)	Experimental
$\tilde{Y}_{OH} = 0.0004$ [134]	31.5	28.5	33 ± 7
$\tilde{Y}_{OH} = 0.0006$ [132]	33	29.5	33 ± 7
T = 600 K [142]	35	32.5	33 ± 7
T = 900 K [164]	36.5	34	33 ± 7
T = 1,000 K [163]	37	34.5	33 ± 7
1% of $\dot{\omega}_{CH_4}$ [107]	36	33.5	33 ± 7

Same trends and conclusions are noted for the flames at Re = 12,000 and Re = 19,500 (for brevity shown here only the case with the joint PDF calculated through Eq. 4.6), see Tables 4.2-4.3. In the case at Re = 12,000, the calculated lift-off heights vary between 73 and 83 mm, while in the case at Re = 19,500 they vary between 129 and 137.5 mm. The experimental range was equal to 73-95 mm and 124-146 mm, respectively [10].

Table 4.2: Lift-off height predictions for the flame at Re = 12,000 based on Eq. 4.6 for the joint PDF.

Criterion	Lift-off height (mm)	Experimental
$\tilde{Y}_{OH} = 0.0004$ [134]	73	84 ± 11
$\tilde{Y}_{OH} = 0.0006$ [132]	74.5	84 ± 11
T = 600 K [142]	80.5	84 ± 11
T = 900 K [164]	82	84 ± 11
T = 1,000 K [163]	83	84 ± 11
1% of $\dot{\omega}_{CH_4}$ [107]	81.5	84 ± 11

Best agreement is achieved with the criterion based on the 600 K isotherm, which was previously applied to a methane/nitrogen flame [142]. The lift-off height criteria using a mean OH mass fraction reference value provide lower stabilization distances; however, one OH mass reference value, larger than 0.0006, could be selected to reach a closer agreement with the experimental data. The use of OH would make the lift-off height definition consistent with the experimental analysis, where OH was used to define the flame base.

Table 4.3: Lift-off height predictions for the flame at Re = 19,500 based on Eq. 4.6 for the joint PDF.

Criterion	Lift-off height (mm)	Experimental
$\tilde{Y}_{OH} = 0.0004$ [134]	129	135 ± 11
$\tilde{Y}_{OH} = 0.0006$ [132]	129.5	135 ± 11
T = 600 K [142]	134.5	135 ± 11
T = 900 K [164]	137	135 ± 11
T = 1,000 K [163]	137.5	135 ± 11
1% of $\dot{\omega}_{CH_4}$ [107]	134	135 ± 11

Further, the probability distribution of temperature at the instantaneous flame stabi-

lization point shown in Fig. 6 of [10] indicated that the temperature at the stabilization height was low (around 300 K for the Re = 7,000 case), suggesting that the temperature-based criteria may not be the most appropriate method to determine the lift-off height.

As a compromise between obtaining the best prediction in comparison with the experimental value and maintaining consistency with the experimental method, the OH mass fraction reference value of 0.0006 is selected to determine the lift-off height. Thus, the predicted lift-off height for the case at lowest Re is found to be 33 mm for the statistical independent joint PDF case (Eq. 4.7) and 29.5 mm for the joint PDF calculated from Eq. 4.6, resulting in a difference of approximately 12%. The predictions need to be compared with the experimental value equal to 33 mm with a corresponding Root Mean Square (RMS) of 22% [10]. Figure 4.9 presents the predicted lift-off heights as a function of Re (calculated with the OH mass fraction reference value of 0.0006) for the case with the joint PDF calculated from Eq. 4.6. For all Reynolds number values, the stabilization height is shown to be in very good agreement with the experimental data. The largest discrepancy between the predicted and measured lift-off heights is equal to 11% for Re = 12,000.

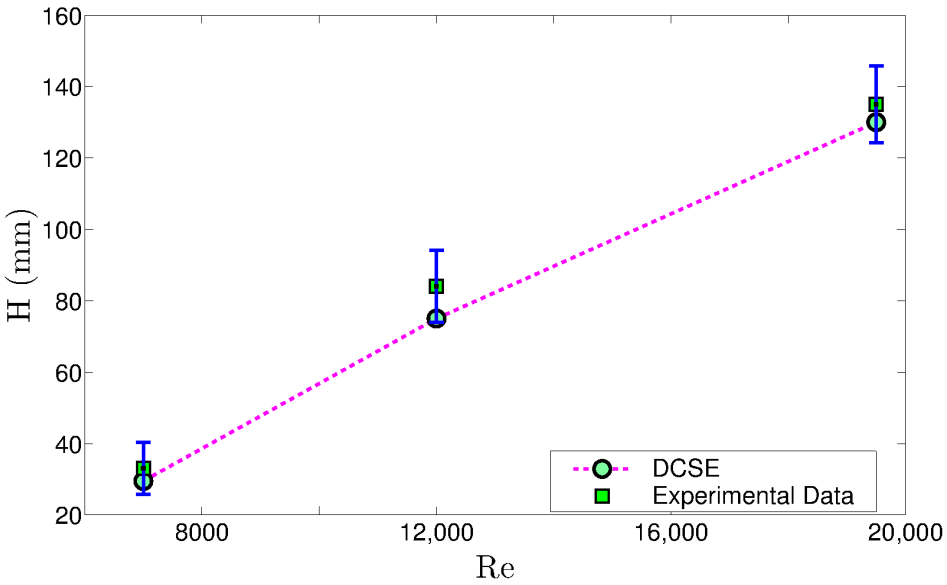

Figure 4.9: Mean lift-off heights at different Reynolds numbers with the joint PDF calculated from Eq. 4.6. Comparison of numerical predictions (circles) with experimental data (squares) [10]. The bars indicate the RMS of fluctuations of the mean lift-off height [10].

Both approaches for the joint PDF provide similar results and the values obtained with Eq. 4.7 are not presented for brevity. Some comparison can also be made for the radial position where the flame is found to stabilize. The predicted radial stabilization locations are 11.5 mm and 18 mm for the Re equal to 7,000 and 12,000 (no direct comparison for the flame at Re = 19,500 is made as no experimental value was given for the radial location), respectively. These positions are also close to the experimental value of 10 and 14 mm [10] for the same flames. Thus, the predicted radial and axial locations of the flame stabilization are in good agreement with the experimental observations. Further, for the present lifted turbulent flames, statistical independence for the determination of the joint PDF is found to be a reasonable approximation with the laminar premixed flame solution determined at the stoichiometric mixture fraction (Eq. 3.13). It must be noted though that when statistical independence is assumed in the formulation of the PDF (Eq. 3.12), the choice of the equivalence ratio or mixture fraction at which $f(c^*)$ is determined, may affect the predictions more significantly compared with what is currently observed.

4.8.3 Flame structure

Beyond the lift-off height predictions, it is also important to examine the current predictions in further detail in order to establish which aspects of flame stabilization mechanism the present DCSE calculations can or cannot reproduce. In the present section, a more direct comparison will be made with the observations reported in the experimental studies of the same flames [11, 9, 10]. Further analysis will also be included using additional published experimental and numerical work.

Figure 4.10 presents the OH mass fraction contours from the numerical simulations with the mean mixture fraction isolines superimposed for the three flames under consideration. The experimental measurements [10] showed that the fuel and air were premixed near stoichiometric conditions immediately upstream of the flame base, with the mixture exceeding the fuel-rich flammability limit towards the central jet and the fuel-lean limit toward the ambient air. This aspect is observed in the numerical predictions and the stabilization point is located on the lean side (on the right side of the stoichiometric isoline of $\tilde{Z} = 0.055$). As shown in Fig. 4.10, the mixture fraction isolines are deflected at the flame base due to expansion at the flame front.

These observations are consistent with the numerical results of Chen et al. [85]. It must also be noted that the stabilization region is characterized by a fuel concentration gradient (as can be seen in Fig. 4.10), a condition that is required for the realization of a triple flame structure [141].

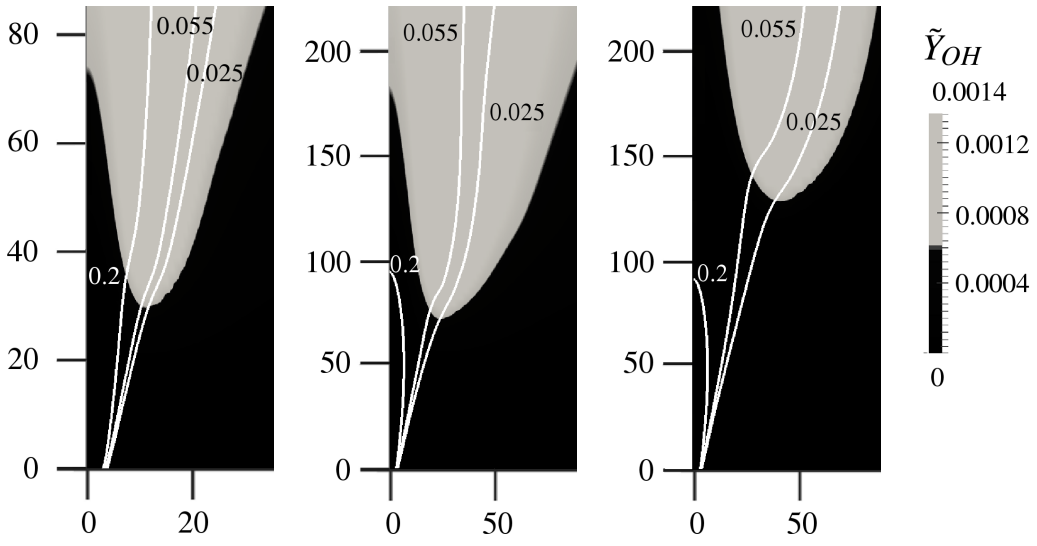

(a) Re = 7,000 (b) Re = 12,000 (c) Re=19,500

Figure 4.10: Mean OH mass fraction contour showing the value of the predicted lift-off height with the mean mixture fraction isolines superimposed, for the three flames under investigation and the joint PDF calculated from Eq. 4.6.

Figure 4.11 displays the velocity vectors and the mean temperature field around the flame base for the same three flames. Significant entrainment of air by the fuel jet upstream of the flame stabilization point is indicated by the inward direction of the velocity vectors. This would be in agreement with the stabilization mechanism proposed by Broadwell et al. [130].

Another interesting feature is the shape of the flame zone. Two types of flame were observed in the experimental work: one characterized by a curvature that is convex to the outer flow near the upstream stabilization point (indicating strong interaction between the large-scale jet structure and the flame zone) and a second in which the flame zone was relatively straight (parallel to the axis) and continuous along the axial direction [10]. Such a pattern can also be seen in the numerical predictions of the mean OH mass fraction, as shown in Fig. 4.10.

The measurements presented in Table 1 of [11] indicated that the flame zone increased in size with the Reynolds number. The flame width was determined by the width of the flammable region [11] and the same procedure is applied to the present calculations to compare the numerical results with the experimental findings. Figure 4.12 shows the variation in width of the flammable region with the Reynolds number. The width is

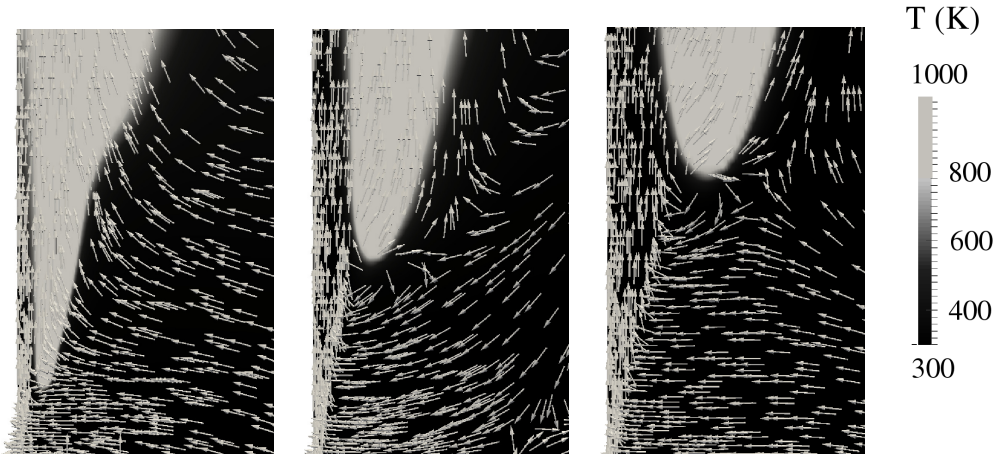

(a) Re = 7,000 (b) Re = 12,000 (c) Re=19,500

Figure 4.11: Velocity vector fields (unscaled) in the region of the flame stabilization point superimposed on mean temperature field for the three flames under investigation using the joint PDF calculated from Eq. 4.6.

determined at the stabilization heights presented in Fig. 4.9 and very good agreement with the experimental values is obtained for the three flames. Similar to what is seen in Fig. 4.9 for the predicted lift-off heights, the largest discrepancy between the numerical results and mean experimental values is found for Re = 12,000 on the order of 40 %, but the predictions are all within the range of experimental RMS fluctuations.

Finally, the triple flame structure is examined in the context of the present reacting flow conditions. In lifted turbulent flames, a triple flame may be evidenced through different characteristics such as the presence of a fuel concentration gradient at the flame base [141], deceleration of the flow at the stabilization height [11], and the observation of the lean and the reach branches on the sides of the diffusion tail. As shown in Fig. 4.10, a range of $\widetilde{Z}$ can be observed at the flame base, demonstrating the presence of a premixed region. Also seen in Fig. 4.10, is the divergence of the mean mixture fraction isolines in correspondence of the flame base, consistent with the deceleration of the flow at the stabilization height, observed in the numerical simulations and shown in Figure 4.14.

Further, the radial profiles of the OH reaction rate at axial locations slightly above the lift-off height are presented in Fig. 4.13 for the three flames under investigation. The values shown in Fig. 4.13 are obtained using the joint PDF given by Eq. 4.6. For the first axial location shown in Fig. 4.13(a)-4.13(c), a single peak can be seen in proximity of the flame

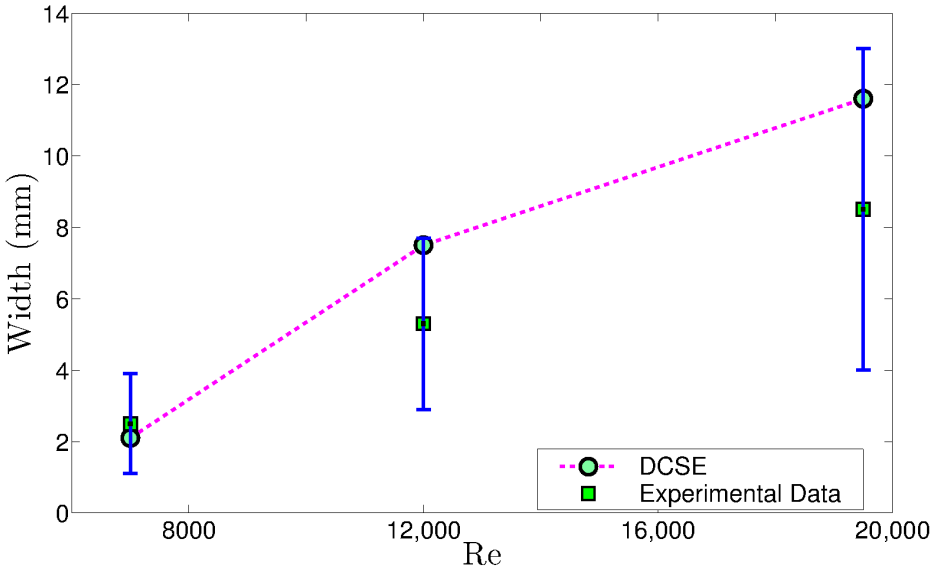

Figure 4.12: Variation of the flammable region with the Reynolds number (numerical predictions are obtained with the joint PDF calculated from Eq. 4.6). The bars indicate the RMS of fluctuations of the flame width [11].

base, which could indicate the presence of the triple point. Farther downstream, three different peaks are visible. The central peak could correspond to the diffusion tail and the other two wings on the fuel rich and lean sides, could represent the premixed branches. It must be noted that the central peak is not at stoichiometric conditions: the mean mixture fraction is equal to 0.035, 0.035 and 0.028 for Re = 7,000, 12,000 and 19,500, respectively, whereas the stoichiometric value is 0.055. Further, as can be seen in Fig. 4.13(b) and 4.13(c), there is no fuel rich premixed branch at the flame base for Re = 12,500 and 19,500. There is a third branch, but it is on the fuel lean side. These characteristics can be explained by the fact that the flame is stabilized in fuel lean mixtures, as seen in Fig. 4.10. The current reaction rate distribution resembles that of Kioni et al. in a laminar triple flame [165]. However, in [165], the highest value for the reaction rate was obtained at the triple point and decreased slightly downstream, while in the present case an opposite trend is observed.

Mansour [166] used a combined Rayleigh scattering, Laser-Induced Predissociative Fluorescence (LIPF) of OH, and Laser-Induced Fluorescence (LIF) of C2Hx to study the triple flame structure of partially premixed lifted flames. The lean and the reach branches were

captured by the LIF of C_2H_x signal, while the diffusion zone by the LIPF-OH signal. The triple point was found as the intersection of the 3 reaction zones. In the present study, the C_2H_x fields are not resolved; in the future, it would be interesting to investigate this aspect further. In the current work, it is important to reinforce that presently observed characteristics are consistent with the triple flame theory; however, the triple flame structure cannot be unambiguously detected in the present case. Triple flames are also expected to be a transient phenomenon which cannot be easily captured using RANS and will also be significantly distorted by the turbulent velocity field.

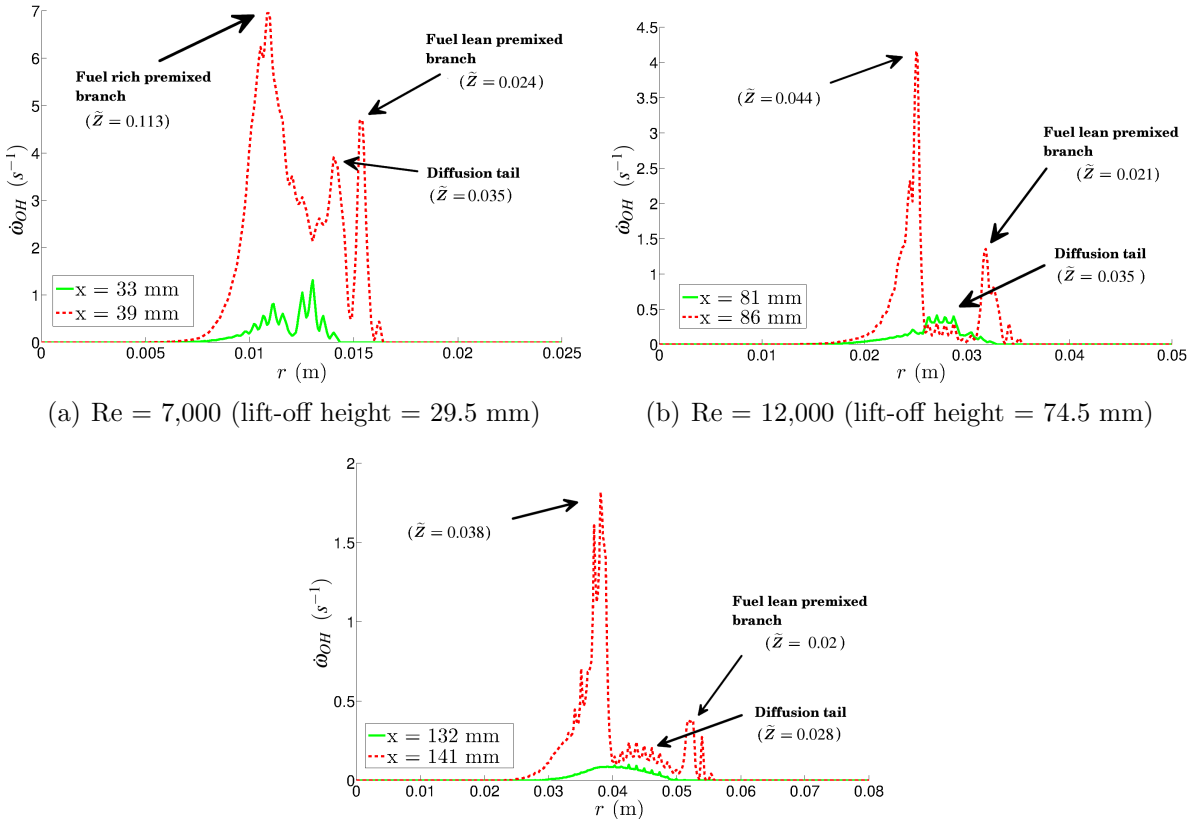

(a) Re = 7,000 (lift-off height = 29.5 mm)

(b) Re = 12,000 (lift-off height = 74.5 mm)

(c) Re=19,500 (lift-off height = 129.5 mm)

Figure 4.13: Mean OH reaction rates in the radial direction at two axial locations around the flame base at different Reynolds numbers with the joint PDF calculated from Eq. 4.6.

Finally, Schefer and Goix [9] provided some instantaneous profiles of the axial velocity as function of the axial distance at the radial location corresponding to the flame base for

Re = 7,000 and 12,000 as well as some averaged velocities calculated from 50 images at the base of flame for the three flames. Similar trends are observed in the present numerical results, as presented in Fig. 4.14: low values are found upstream of the stabilization point, smaller than the laminar burning velocity, $S_L = 0.43$ m/s, for Re = 7,000, followed by a sudden acceleration in correspondence of the reacting zone. In the other two flames (Re = 12,500 and Re = 19,500), the velocity at the flame base was measured to be on the same order of magnitude than S_L [9], whereas the present simulations give much lower velocities close to 0 m/s. Due to limited number of velocity measurements, no further quantitative comparison can be made.

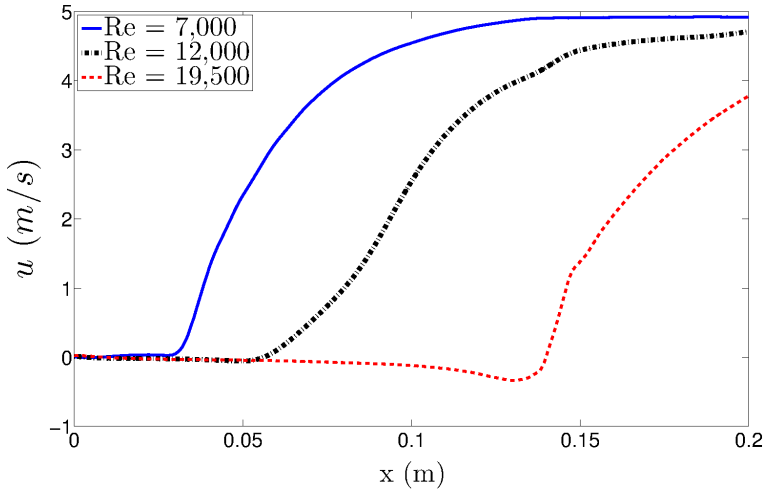

Figure 4.14: Mean axial velocity profiles passing through the stabilization point at different Reynolds numbers with the joint PDF calculated from Eq. 4.6.

Doubly conditional averages of water, $\langle Y_{\mathrm{H2O}} | Z, c^* \rangle$, obtained from the inversion of Eq. 4.2 are presented as functions of mixture fraction and progress variable in Fig. 4.15 corresponding to two ensembles, one located close to the inlet (Fig. 4.15(a)) and one at the top of the computational domain (Fig. 4.15(b)). These contours refer to the flame at Re = 7,000 and the joint PDF calculated from Eq. 4.6. In both regions, the peak of the conditional mass fraction is reached for values of mixture fraction close to the stoichiometric level (0.055 for methane/air). The region close to the nozzle extends for an axial distance starting from the inlet and ending at $x = 200$ mm, well above the stabilization height. Thus, the progress variable profile is varying from null values to values close to unity (inside the flame). This particular condition is reflected in the profile of $\langle Y_{\mathrm{H2O}} | Z, c^* \rangle$, which is very broad (Fig. 4.15(a)).

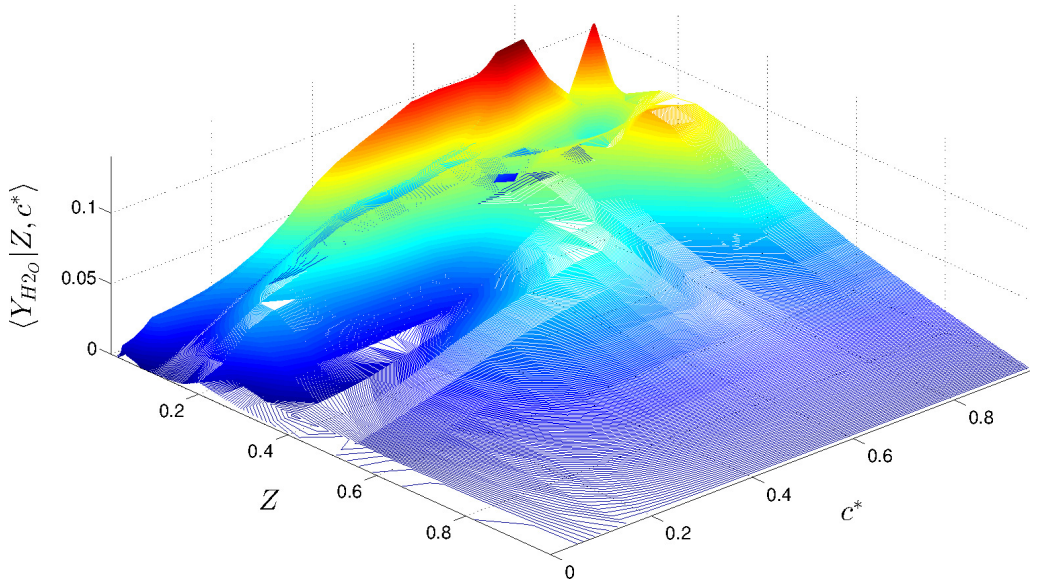

(a) Ensemble close to the nozzle

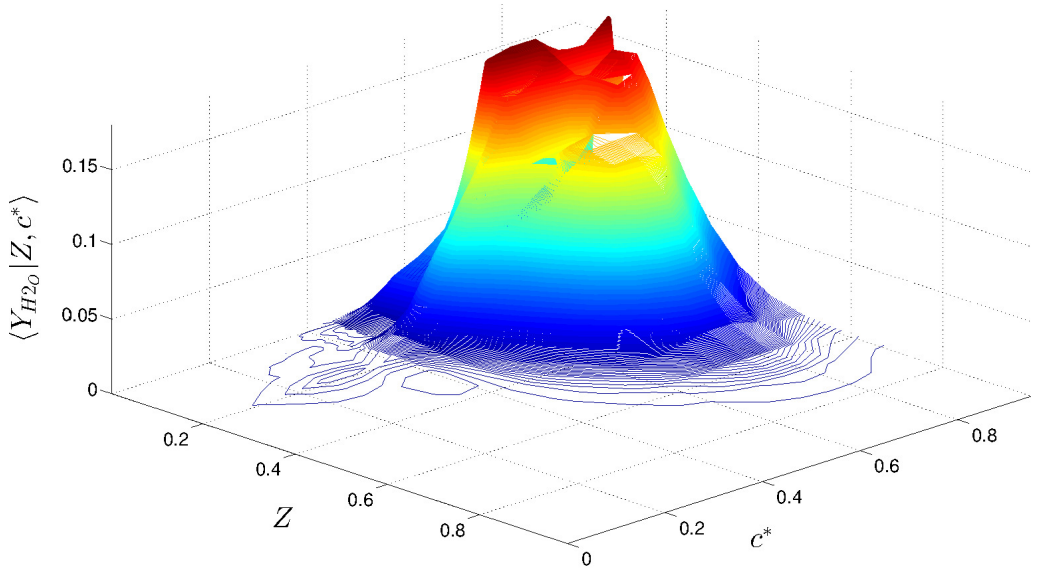

(b) Ensemble at the top of the computational domain

Figure 4.15: Doubly conditional values of water, $\langle Y_{\mathrm{H2_O}}|Z,c^*\rangle$, as functions of Z and c^* for the flame at Re = 7,000 and the joint PDF calculated from Eq. 4.6.

In contrast, farther downstream, the mixture fraction values are very small and the progress variable is more uniform. As a consequence, the doubly conditional values of water are confined in a narrower region, where the mixture fraction is around the stoichiometric value and the progress variable close to unity, as presented in Fig. 4.15(b). Similar trends are observed for the other flames and not shown for brevity.

4.9 Summary

In this chapter, RANS-based numerical simulations of a series of lifted turbulent jet flames have been presented by using a partially premixed formulation of CSE based on double conditioning, namely DCSE. The main outcome of this chapter is that this new combustion model is able to predict very well the lift-off heights of the three flames under investigation and proves to be superior to the singly CSE approach in terms of partially premixed combustion simulations. This important result allows to open up the CSE framework to new horizons and new frontiers such as the numerical simulations of partially premixed configurations.

Chapter 5

DCSE applied to a series of turbulent V-shaped flames

The capability of DCSE in predicting important characteristics of partially premixed combustion has been discussed in Chapter 4 in the context of turbulent lifted jet flame simulations. In the present chapter, stratified turbulent combustion is investigated in the DCSE framework. In particular, a series of stratified turbulent V-shaped methane/air flames is selected due to available experimental data for a range of conditions.

5.1 Introduction

In the context of power generation, lean premixed combustion has the potential of providing low emissions and high efficiency, and is extensively applied to large-scale natural gas-fired turbines for combined cycle power generation. In recent years, the general interest is moving towards stratified flames as a possible way to achieve stable lean combustion. In stratified combustion, the flame is ignited in a rich mixture and propagates through non-uniform reactants towards lean mixture to reduce CO and NO_x formation [167]. One example is found in Direct Injection Spark Ignition (DISI) engines, where direct injection of the fuel in the combustion chamber is followed by ignition during the mixing of the fuel and oxidizer. This leads to the reduction of pollutant emissions and fuel consumption due to the spatial stratification of the equivalence ratio [168, 169]. Cho and Santavicca [170] investigated stratified combustion in terms of the effect of reactant heterogeneity on flame properties and found that local flame characteristics were affected by the the interaction

of pockets of regions at different equivalence ratio. This observation may invalidate the flamelet assumption, for which the turbulent flame can be described globally by knowing turbulent and scalar reactant characteristics (such as temperature, species, reaction rates), without considering the interaction between different flame regions [1]. The introduction of a strong spatial or temporal variation of the equivalence ratio has several effects on the flame structure. The three generally accepted and most observed are: (1) variation of the flame speed and extension of the flammability limit, (2) change in the inner structure of the flame, (3) dependence of the reaction rate on turbulence and reactive scales. Flame front propagation is higher by 20-30% in the case of turbulent flame with large-scale stratification of the equivalence ratio, compared to the corresponding homogeneous mixture at the same mean equivalence ratio [171, 168]. This aspect can be related to the fact that heat and radicals flux from the richer products supports the leaner flame region, enhancing its resistance to extinction and is known as "back support" and "memory effect" [171]. Jiménez et al. [172] found that, for lean conditions, the increased flame speed may be associated to the increased wrinkling of the stratified flame. Modification of the inner structure of the flame such as wrinkling, curvature and rate of strain is another aspect to be considered in the stratified combustion. In particular, wrinkling is due to differential propagation speeds and is enhanced in the stratified case [173], especially if the turbulence is not strong enough to affect completely the flame structure, i.e. the turbulence intensity is comparable with the laminar flame speed: $u'/s_L \approx 1$. Finally, the effect of stratification on combustion and heat release efficiency has been investigated [170, 172] without reaching a definitive conclusion, for the intensity of combustion resulted to be either enhanced or reduced compared to the homogenous case in stratified flames. On the numerical side, several models for turbulent stratified flames have been proposed that are based on premixed approach [174, 175, 176, 177], which are expected to be valid as long as no diffusion flame occurs. However, a more rigorous approach based on partially premixed combustion is preferred so that the formulation would consider the physics of the problem as realistic as possible.

The DCSE combustion model presented in Chapter 4 is applied to a series of stratified turbulent V-shaped flames. The case of pure premixed combustion is considered first, by the use of the CSE combustion model described in Chapter 3. A sensitivity analysis on the regularization parameter value and the number of CSE ensembles is presented. Three different models for the scalar dissipation rate are included for the homogeneous mixture case. This analysis is followed by a second step where the partially premixed

[1] In the flamelet assumption, the flame is considered as an ensemble of thin laminar flamelets that are stretched and strained by the turbulent structures in a flow field and hence the behaviour of premixed flames can be determined by turbulence and scalar reactant properties.

implementation of CSE, DCSE, is applied to the study of stratified turbulent V- shaped flames at three different stratification conditions. These are characterized by an equivalence ratio gradient, ranging from a maximum value at the center of the combustion chamber to a value equal to 0 at the periphery of the domain [13].

5.2 Fully premixed combustion

The premixed implementation of CSE, presented in Chapter 3 is adopted for the study of the fully premixed case for which experimental data are available in terms of axial velocity, transverse velocity and progress variable profiles. As described in Chapter 3, the conditional mass fractions $\langle Y_k|c^*\rangle$ are not obtained through the solution of transport equations, but they are calculated by inverting the following integral equation

$$\tilde{Y_k}(\vec{x},t) = \int_0^1 \langle \tilde{Y_k}|c^*\rangle(\vec{x},t;c^*)\tilde{P}(\vec{x},t;c^*)dc^* \tag{5.1}$$

A modified laminar flame PDF is used for the presumed density-weighted PDF of c^*, following the observations made in Section 3.1.3. Since the inversion problem is equivalent to the solution of transport equations for the conditional mass fractions in CMC, the number of inversions is equal to the number of species involved in the reaction mechanism. For a detailed chemical mechanism (such as GRI-MECH 3.0 [104] adopted in the premixed case or GRI-MECH 2.11 [157] for the stratified case) it would be extremely computationally expensive to invert Eq. 3.3 for each species. A possible solution is to reduce the full kinetic mechanism to a small manifold in a small number of dimensions. Thus, the FGM method, introduced in Section 3.1.2 is used and allows the solution of only one integral equation. Transport equations for mean and variance of the progress variable are solved in order to determine the presumed PDF model needed in Eq. 3.3. For clarity, Eq. 3.25 for variance is given to provide further discussion on the modelling of the scalar dissipation rate

$$\frac{\partial(\overline{\rho}\widetilde{c''^2})}{\partial t} + \frac{\partial}{\partial x_i}\left(\overline{\rho}\widetilde{u}_i\widetilde{c''^2}\right) = \frac{\partial}{\partial x_i}\left(\overline{\rho}\frac{\nu_t}{S_{ct_1}}\frac{\partial\widetilde{c''^2}}{\partial x_i}\right) + 2\overline{\rho}\frac{\nu_t}{S_{ct_2}}\frac{\partial\widetilde{c}}{\partial x_i}\frac{\partial\widetilde{c}}{\partial x_i} - \overline{2\rho D\frac{\partial c''}{\partial x_i}\frac{\partial c''}{\partial x_i}} + 2\overline{c''\dot{\omega}_c}. \tag{5.2}$$

The Schmidt numbers, S_{ct_1} and S_{ct_2}, are set to 0.7. The last term on the RHS of Eq. 5.2 represents the correlation between the fluctuations of the conditioning variable and the reaction rate and can be modelled as $\overline{c''\dot{\omega}_c} = \overline{(c-\widetilde{c})\,\dot{\omega}_c} = \int_0^1 (c^*-\widetilde{c})\,\langle\dot{\omega}_c|c^*\rangle P(c^*)dc^*$, where the conditional reaction rate, $\langle\overline{\dot{\omega}}_c|c^*\rangle$ is provided by the CSE combustion model. The other unclosed term is the scalar dissipation rate, $\widetilde{\chi}_c$, which gives an indication of local mixing

and plays an important role in turbulent premixed combustion. Different closure strategies for this term can be found [20]. In the present study, three different models are investigated and the predictions are discussed in Section 5.2.6. The first formulation consists of a linear relaxation assumption based on the eddy-breakup-type hypothesis: the Favre-averaged scalar dissipation rate is considered proportional to a turbulent mixing time [24] such that

$$\overline{\rho D \frac{\partial c''}{\partial x_i} \frac{\partial c''}{\partial x_i}} = \overline{\rho} c_\chi \frac{\varepsilon}{k} \widetilde{c''^2} \ , \tag{5.3}$$

where c_χ is a model constant equal to one. The second model is based on the concept of Flame Surface Density (FSD), $\Sigma = \Xi |\nabla \overline{c^*}|$ [51], Ξ being the wrinkling factor and is calculated as

$$\widetilde{\chi}_c = \frac{1}{2}(2c_m - 1)\rho_u s_L \Xi |\nabla \overline{c^*}| \frac{\widetilde{c''^2}}{\widetilde{c}(1-\widetilde{c})} \ , \tag{5.4}$$

where s_L is the laminar flame speed (equal to 0.111 m/s for the present case [12]), ρ_u is the density of the unburned gases, c_m is assumed equal to 3/4 as in [51]. The FSD term must be closed and a transport equation based on the Coherent Flame Model (CFM) [24] is solved

$$\frac{\partial \overline{\Sigma}}{\partial t} + \frac{\partial}{\partial x_i}\left(\widetilde{u}_i \overline{\Sigma}\right) = \frac{\partial}{\partial x_i}\left(\frac{\nu_t}{Sc_{\overline{\Sigma}}} \frac{\partial \overline{\Sigma}}{\partial x_i}\right) + \alpha_0 \frac{\widetilde{\varepsilon}}{\widetilde{k}} \overline{\Sigma} - \beta_0 s_L \frac{\overline{\Sigma}^2}{1-\widetilde{c}} \ , \tag{5.5}$$

where α_0 and β_0 are two model parameters (set to 1.7 and 1, respectively, as done in Section 3.2.2), $\widetilde{k}$ is the mean turbulent kinetic energy and $\widetilde{\varepsilon}$ is the mean turbulent dissipation rate.

Finally, the algebraic model of Kolla et al. [118] is applied to the Favre-averaged scalar dissipation rate

$$\widetilde{\chi}_c = 2\overline{\rho} \frac{1}{\beta'} \left([2K_c^* - \tau C_4] \frac{s_L}{\delta_L} + C_3 \frac{\widetilde{\varepsilon}}{\widetilde{k}} \right) \widetilde{c''^2}, \tag{5.6}$$

where δ_L is the unstrained laminar thermal thickness ($\delta_L = 0.62$ mm from experiments [12]), β' is a model constant equal to 6.7, $K_c^* \equiv \frac{\delta_L}{s_L} \frac{\int \rho N (\nabla \mathbf{u})_L^0 f(c) dc}{\int \rho N_L^0 f(c) dc}$ ($\frac{K_c^*}{\tau} = 0.82$ and $\tau = 4.58$ based on laminar flame results for $\phi = 0.6$ as found in Table 1 of [118]), $C_3 = 1.5/(1+\mathrm{Ka}^{-m})$ (m taken to be 0.5 as in [118]) and $C_4 = 1.1(1+\mathrm{Ka})^{-0.4}$. The Karlovitz number Ka (defined in Eq. 2.64) is taken equal to 1.22 as in [12].

Numerical results obtained with these three different models (Eqs. 5.3, 5.4, 5.6) are presented in Section 5.2.6.

5.2.1 Numerical details

The experimental setup consists of a vertical wind tunnel where a methane-air turbulent premixed flame is spark-ignited in the center of a combustion chamber ($x = 0$ mm, $z = 0$ mm) with an 80×80 mm square section using a 0.8-mm-diameter heated rod [12], as shown in Fig. 5.1. Metrological air is injected into an upstream mixing chamber constituted by nine parallel compartments. Fuel injectors are connected to those compartments so that an upstream stratified flow with a transverse gradient of equivalence ratio can be obtained. The mixture of air and fuel is then homogenized while passing through small glass marbles. The flow reaches the honeycomb structure where it is laminarized and is conducted to a convergent channel. A turbulence grid is added 70 mm upstream of the stabilizing rod. Two different grids are studied, called "B" and "E" [12]. The methane-air mixture is convected vertically, passes through the turbulence grid and then propagates downstream in the study zone (between $z = 20$ to $z = 1{,}000$ mm) in a decaying isotropic turbulent flow at atmospheric pressure, as presented in Fig. 5.1.

Mean flow conditions calculated in the study zone (shown in Fig. 5.1) corresponding to the two grids are summarized in Table 5.1.

Table 5.1: Mean flow conditions in the study zone [1, 2]

	Grid B	Grid E
$U\ (m/s)$	3.75	3.14
$u'\ (m/s)$	0.139	0.237
$L\ (mm)$	5.5	6.1
Re_t	53	101
$k\ (m^2/s^2)$	0.029	0.061
$\varepsilon\ (m^2/s^3)$	0.49	2.18

The computational domain is two dimensional and axisymmetric with a width of 40 mm and total length of 85 mm, as shown in Fig. 5.2. The grid is nonuniform in the x direction, with high density of grid points close to the rod (as clearly shown in the enlargement at the bottom of Fig. 5.2), where the flame is expected to develop and represents half of the physical domain. Numerical simulations on the entire domain have been performed and no noticeable differences with the half domain case were observed. From a numerical point of view, the combustion stabilizes by the recirculation produced by the half-rod, consistent with the numerical analysis of Robin et al. [12]. The current grid consists of 56,119 cells.

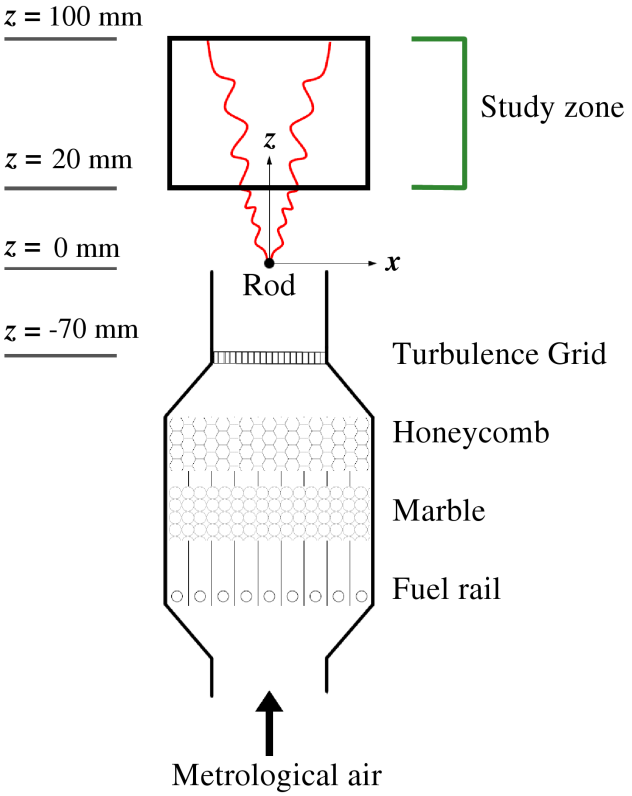

Figure 5.1: Schematic of the experimental setup [12].

Further grid refinement was tested and the present results are found to be grid independent, as presented in Section 5.2.2. The inlet boundary conditions are placed 5 mm upstream of the stabilization rod (z = -5 mm), following [12]. Premixed fuel and air is supplied at an axial velocity based on the profiles measured in experiment [1] and temperature of 300 K. The initialization of the reactive problem consists of setting the progress variable of unity value at the rod which is consistent with the experimental configuration [12]. Atmospheric value of the pressure is set at the outlet and zero-gradient is used for the velocity. On the RHS of the domain, a wall is used for z $<$ 0, along the convergent exit of the channel. For z $>$ 0, an inlet-outlet boundary condition is used for the velocity. This condition is equivalent to zero-gradient when the flow is heading outwards the domain, and can be set to act as a wall when the flow is heading inwards.

RANS flow equations are solved by a finite volume low-Mach number pressure based approach using OpenFOAM [110]. Transport equations for the average mass fraction of

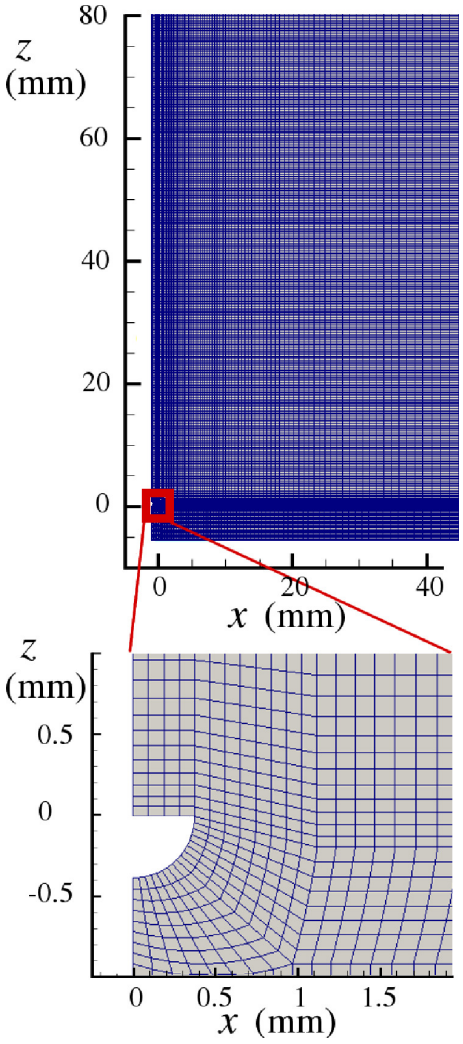

Figure 5.2: Schematic of the grid used for numerical simulation.

major species, i.e. methane (CH_4), oxygen (O_2), water (H_2O), carbon dioxide (CO_2), hydroxyl (OH) and carbon monoxide (CO) are included. The turbulent scalar flux is closed by a gradient transport assumption (Eq. 2.22). This closure neglects counter-gradient diffusion, which is a reasonable assumption in the present turbulent premixed flame with the Bray number (see Eq. 3.21) being less than unity. Energy conservation is applied by solving a transport equation for the average total enthalpy. All transport equations are solved using an implicit time integration method, while flux calculations are solved with

TVD and NVD schemes [110]. Two different turbulence models are used and compared in the present study for the fully premixed case: the $k-\varepsilon$ approach [31] and the standard SST $k-\omega$ turbulence model [33]. As noted by Robin et al. [12], inlet boundary conditions for the present case may have a strong influence in the numerical analysis and therefore require special treatment. For example, the inlet velocity profiles for the different turbulent grids presented different results depending on how it was measured (with Laser Doppler Anemometry (LDA) or PIV) [2]. Renou et al. [1] performed experimental measurements of a propane-air premixed flame by using the same apparatus investigated in this work. They presented mean and fluctuating velocity profiles corresponding to the turbulence grid E at the electrode location for the non-reacting case. This profile is selected in the present numerical calculations. It is also compared to the different profiles obtained by Samson [2] in order to have a consistent profile for the B turbulence grid case as well, since it was not provided by Renou et al [1]. The turbulent quantities such as the turbulent kinetic energy and its dissipation rate need also to be defined at the inlet of the computational domain. Experimental data provides values of the turbulent kinetic energy at the inlet locations (z = -5 mm) for the two different grids: $k = 0.058\ m^2/s^2$ for grid B and $k = 0.15\ m^2/s^2$ for grid E [12] in the non-reacting case.

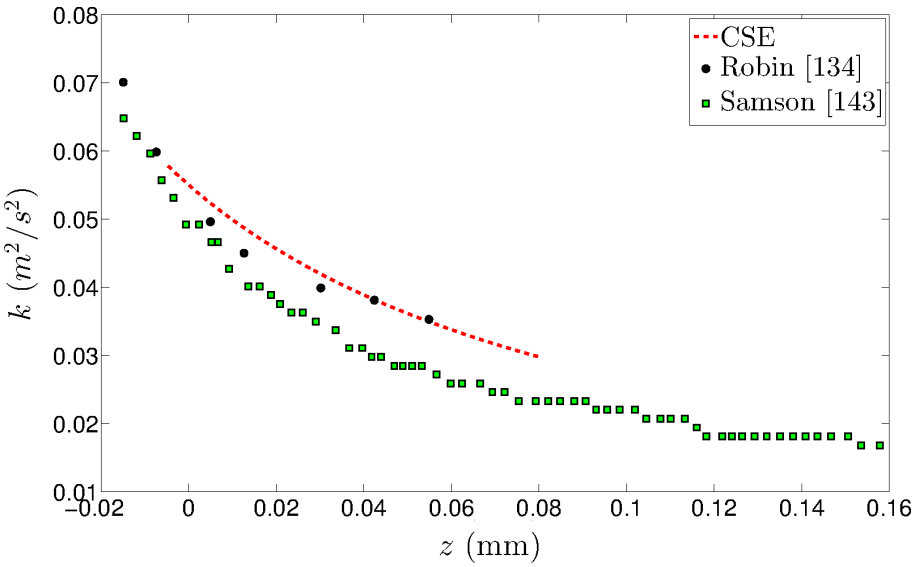

Figure 5.3: Axial centreline profiles of the turbulent kinetic energy as a function of the axial coordinate z for the turbulent grid B. Comparison of numerical predictions (dotted line) with experimental data (circles for [13] and squares for [2]).

Axial centreline profiles of the decay of turbulent kinetic energy are also available for the grid B [13, 2] and E [13, 12, 2] and used to define the scalar dissipation rate of the turbulent kinetic energy at the inlet. Comparisons between the numerical simulations and the two sets of experimental data for the decay of k are presented in Figs. 5.3 and 5.4 for the grid B and E, respectively.

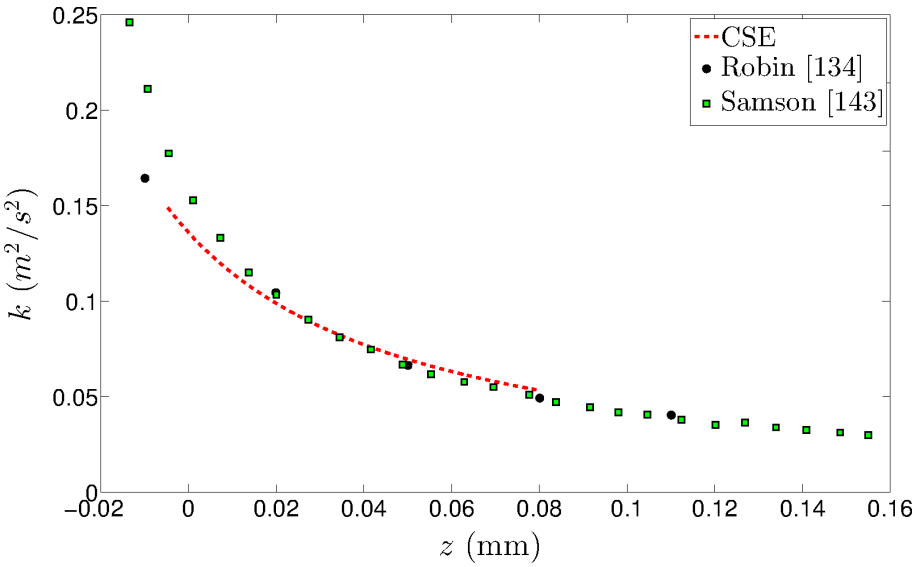

Figure 5.4: Axial centreline profiles of the turbulent kinetic energy as a function of the axial coordinate z for the turbulent grid E. Comparison of numerical predictions (dotted line) with experimental data (circles for [12] and squares for [2]).

It is worth noting that for the grid E the experimental data from Robin et al. [12] and Samson [2] are very similar, as shown in Fig. 5.4, but for the grid B the decay of k provided by Robin et al. is less steep, as presented in Fig. 5.3. The profiles of Robin et al. are considered in the present work in order to be as consistent as possible with the experiments, since the stratified conditions presented in Section 5.3 have been studied only by Robin et al. [12] through both numerical and experimental analysis.

The fully premixed case is considered first and the correspondent numerical results are presented in this section. The equivalence ratio is $\Phi = 0.6$ (flame noted 'HE06' in [12], where H stands for homogeneous, E denotes the type of turbulence grid and the number corresponds to the value of the equivalence ratio). Mean axial and transverse velocity profiles at three distinct locations and mean progress variable profiles at two different locations are provided by the experimental data and compared with the numerical results.

5.2.2 Grid Independence - Premixed Case

Three different meshes are tested for the fully premixed case. Mesh 1 has 87×413 cells, Mesh 2 and Mesh 3 have higher refinement, i.e. 109×516 (1.25 times finer than mesh 1) and 122×578 (1.12 times finer than mesh 2) cells, respectively. Differences between Mesh 1 and 2 are equal to 4.5%, while Mesh 2 and Mesh 3 result in differences smaller than 1% for the mean axial velocity profile calculated with the simple algebraic model for scalar dissipation rate (Eq. 5.3), as shown in Fig. 5.5. Similar trends are observed for the transverse mean velocity profiles and are not shown for brevity, while no noticeable differences can be found in the progress variable profiles for the three different grids. Based on these observations, Mesh 2 is considered to be sufficiently fine to produce acceptable grid independent solutions and is used for the present work. Difference in the axial mean velocity profiles between Mesh 2 and Mesh 3 for the FSD algebraic model (Eq. 5.4) is less than 0.8 %.

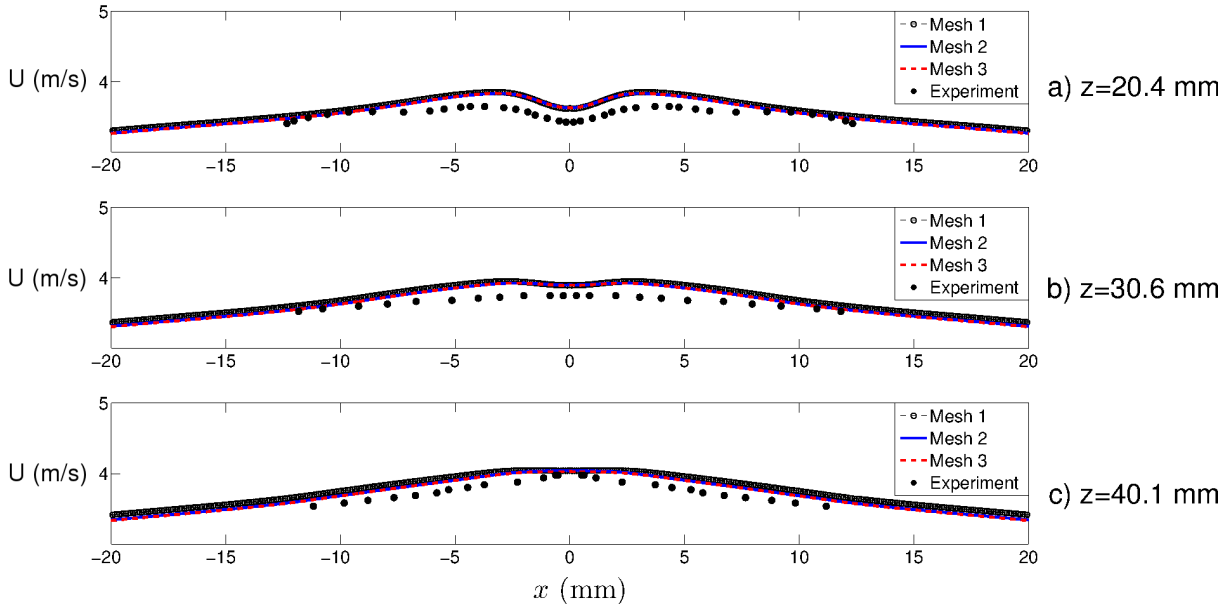

Figure 5.5: Mean axial velocity at different locations with three different meshes and simple algebraic model for scalar dissipation rate (Eq. 5.3).

5.2.3 Sensitivity analysis for different turbulence parameters and models - Premixed Case

The standard $k-\varepsilon$ turbulence model is widely used and provides reasonable predictions for fully developed and non-separated turbulent flows, but performs poorly for complex flows involving severe pressure gradient, separation and strong streamline curvature [33]. An alternative to this approach is represented by the $k-\omega$ turbulence model of Wilcox [34], which results to a more accurate near wall treatment. In the present analysis, the stabilization of the flame occurs around a heated rod, treated in the numerical simulations as a wall. Therefore, the choice of the turbulence model is not straightforward . Two different approaches, namely the standard $k-\varepsilon$ turbulence model and the standard SST $k-\omega$ turbulence model [33] are compared in order to define which approach is more suitable for the flames under investigation. Details of the two models have been presented in Section 3.2.3.

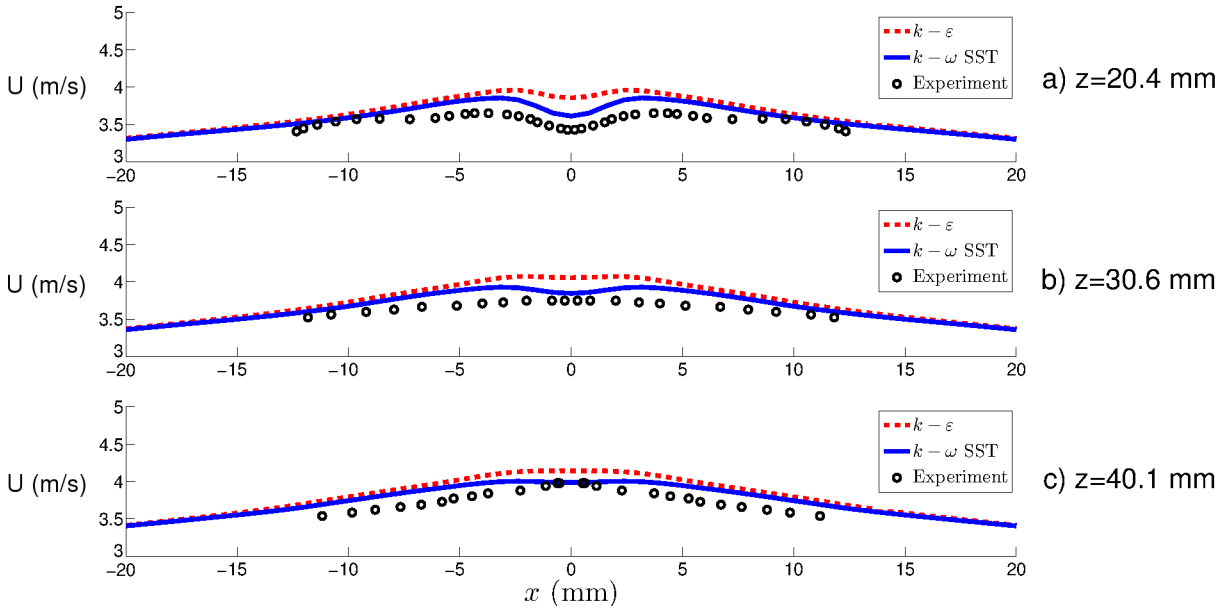

Figure 5.6: Mean axial velocity at different locations with two different turbulence models and simple algebraic model for scalar dissipation rate (Eq. 5.3).

Figure 5.6 shows the mean axial velocity profiles at three different axial locations obtained with the two distinct turbulence models, compared with experimental data. Both

approaches give good results, but the SST model is closer to experimental data, in particular close to the stabilization rod, i.e. for the location $z = 20.4$ mm and close to the centreline ($x = 0$), as expected by considering the better performance of SST close to walls. Mean transverse velocity profiles are also plotted at the same three axial locations,

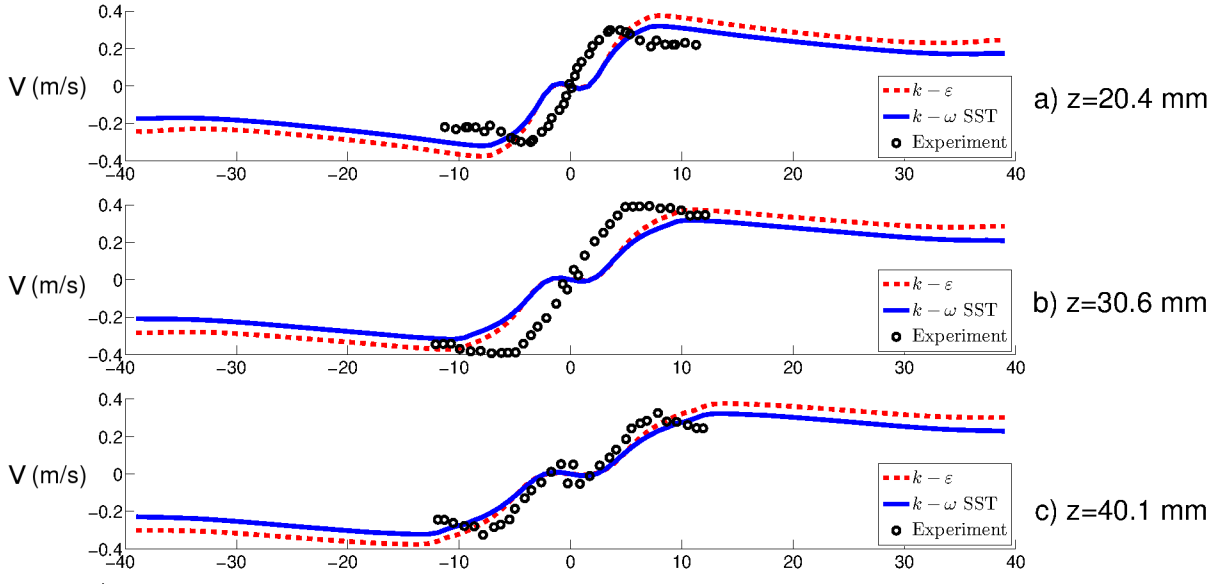

Figure 5.7: Mean transverse velocity at different locations with two different turbulence models and simple algebraic model for scalar dissipation rate (Eq. 5.3).

as reported in Fig. 5.7. Both models provide very similar results, with the SST performing slightly better at the first and last axial location ($z = 20.4$ mm and 40.1 mm, respectively) in terms of recovery velocity far from the centreline, while $k - \varepsilon$ has a recovery velocity closer to the experimental findings for the intermediate location ($z = 30.6$ mm). It must be noted that discrepancies between numerical simulations and experimental data that appear large close to the centreline, are amplified in the plot by the fact that the transverse component is small, much smaller than the axial component (maximum $|0.4|$ m/s). This means that such discrepancies are not expected to have a significant effect on the overall numerical simulation due to their small values compared to the axial component of the velocity profile. Similar differences have been obtained in the numerical study carried out by Robin et al. [12] for the transverse velocity profiles. Based on these considerations, the standard SST $k-\omega$ turbulence model [33] is selected in the present study and the following results refer to numerical simulations performed by using such a turbulence model.

5.2.4 Sensitivity of results to values of λ - Premixed Case

In this section, the effect of the regularization parameter (see Section 3.3.1) on the velocity and progress variable results is investigated in the case of premixed combustion. In the present study, the optimal value of λ based on the L-curve approach (see Fig. 3.6) is on the order of one. Values of λ ranging from 1 to 20 were tested. In the present case, values less than 3 characterize an unstable solution dominated by errors and convergence could not be found. Comparisons are presented for λ equal to 3, 5 and 10.

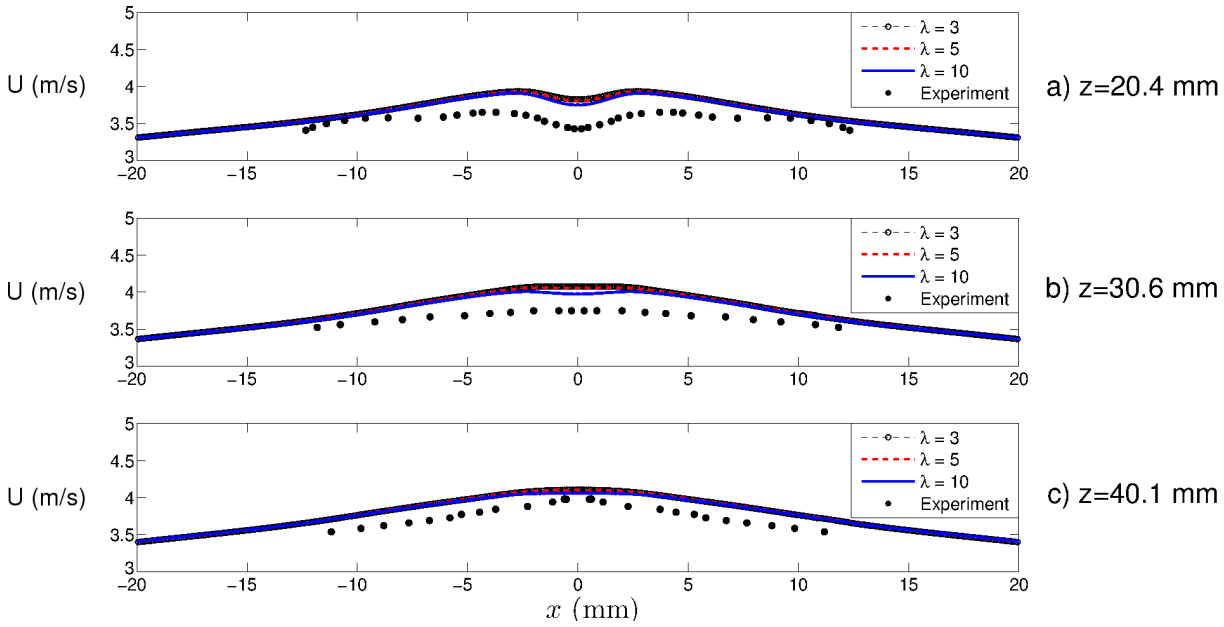

Figure 5.8: Mean axial velocity at different locations for different values of λ and simple algebraic model for scalar dissipation rate (Eq. 5.3).

Figures 5.8 and 5.9 show the predicted axial velocity and progress variable profiles for different values of the regularization parameter λ, respectively. Experimental data is provided in terms of Reynolds mean values, while the numerical simulation deals with Favre averages quantities (see Section 2.2.2). The conversion from Favre averages to Reynolds averages for the progress variable is done by following [14]

$$\overline{c} = 1 - \frac{\overline{\rho}}{\rho_u}\left(1 - \widetilde{c}\,\right) \ , \tag{5.7}$$

where $\overline{\rho}$ is the density of the mixture and ρ_u the density of the unburnt mixture. The simple algebraic model given in Eq. 5.3 is used for the scalar dissipation rate closure.

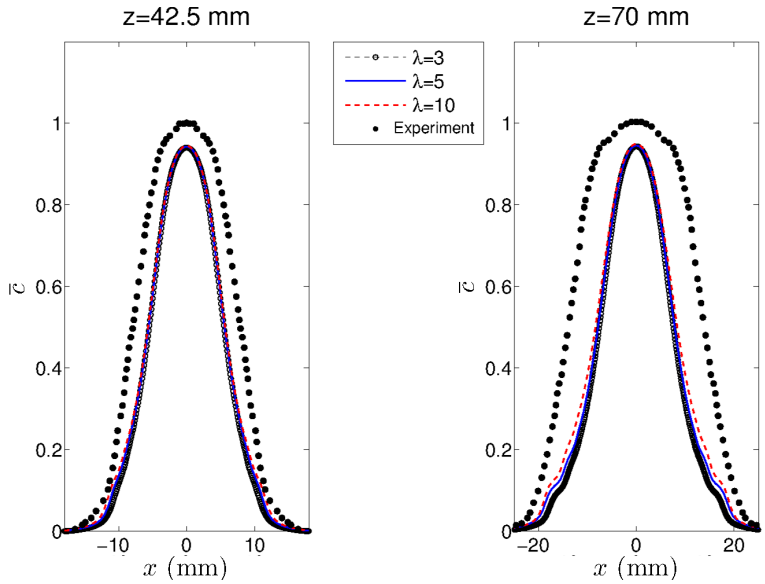

Figure 5.9: Progress variable at different locations for different values of λ and simple algebraic model for scalar dissipation rate (Eq. 5.3).

No significant differences can be observed for the different cases, suggesting that the conditional values corresponding to the flamelet solution (obtained for large values of λ as demonstrated in [78]) is a good estimate of the solution of the inversion problem (Eq. 3.5). This result is consistent with the fact that the present flame belongs to the flamelet regime [12]. Given the small differences for the values of λ tested, it is decided to use $\lambda = 3$ for the final CSE results, so that effects of the flamelet solution are filtered out and the CSE approach is retained.

5.2.5 Sensitivity analysis to CSE ensemble number - Premixed Case

In previous non-premixed CSE simulations, Labahn and Devaud [75] have shown that the predictions obtained using CSE can be affected by the size and location of the ensembles used for the inversion process. Since each ensemble is solved independently, increasing

the number of ensembles results in approaching a CMC-like method, with the benefits of a better justification of the first order closure assumption, as the variations in the conditional averages through the computational domain can be better captured. A larger ensemble also provides more information in the regularization process, resulting in a more stable solution. In the current study, five simulations using 2, 4, 8, 10 and 16 CSE ensembles have been tested to determine the sensitivity of the CSE predictions to the ensemble selection in the fully premixed case with the simple algebraic model for scalar dissipation rate (Eq. 5.3). The CSE ensembles are created over the same computational grid in the axial direction, keeping the entire transverse distance. All other computational and modelling parameters are kept the same.

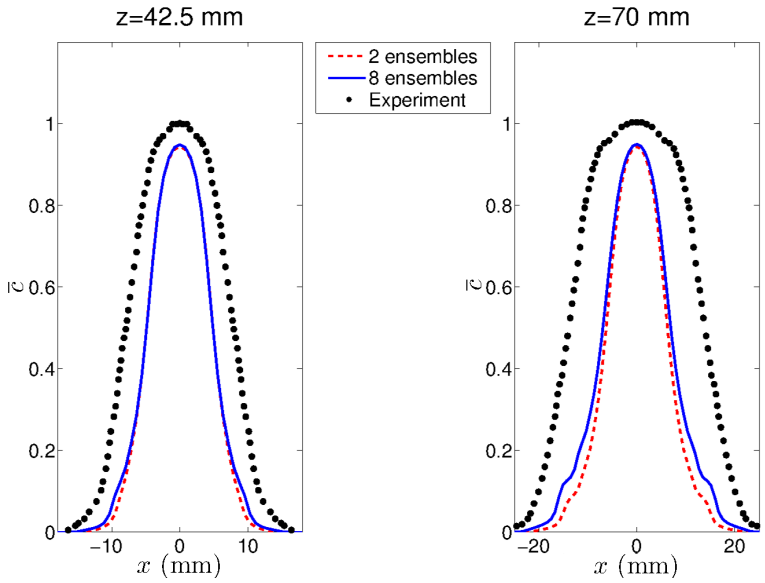

Figure 5.10: Progress variable at different locations with 2 and 8 CSE ensembles and simple algebraic model for scalar dissipation rate (Eq. 5.3).

The cases with 8 and 10 ensembles provide the same profiles for velocity and progress variable. The same trend is obtained between the case with 2 and 4 ensembles. The case with 16 ensembles presents some instabilities in the velocity profiles, confirming that increasing the number of ensembles will eventually lead to numerical instabilities. The largest difference is observed when using 2 and 8 ensembles. For this reason, Figs. 5.10 and 5.11 compare the numerical predictions of progress variable and axial velocity profiles using 2 and 8 ensembles with experimental data. The progress variable is underpredicted

in the case of 2 ensembles, while the predictions are improved using 8 ensembles, especially in locations farther downstream, where the differences in the conditional averages are expected to be larger. Figure 5.11 presents the axial velocity profiles at three axial locations. The case using 8 ensembles gives more accurate predictions compared to the experimental data at all locations. Thus, 8 ensembles are selected for the results presented in Section 5.2.6 for the final CSE results.

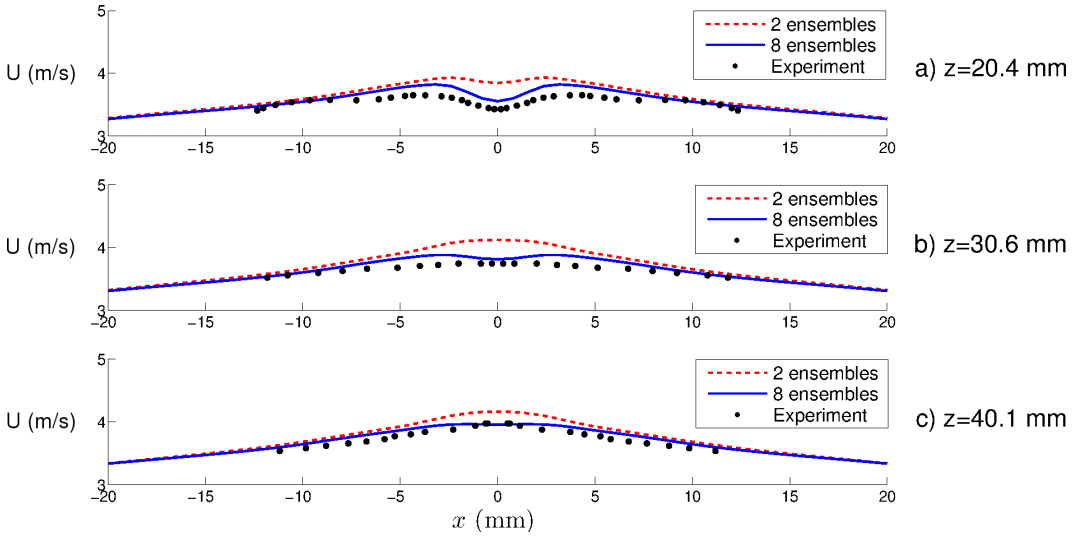

Figure 5.11: Mean axial velocity at different locations with 2 and 8 CSE ensembles and simple algebraic model for scalar dissipation rate (Eq. 5.3).

5.2.6 Sensitivity analysis to the scalar dissipation rate model - Premixed Case

Different scalar dissipation rate models are considered in the present work. The three different models calculated through Eqs. 5.3, 5.4 and 5.6 are compared with experimental data in terms of progress variable and velocity profiles.

Figure 5.12 shows the mean progress variable profiles at different axial locations with the three scalar dissipation rate models. The simple algebraic model (Eq. 5.3) and the FSD model (Eq. 5.4) severely underpredict the progress variable at the two locations of interest, while the algebraic method of Kolla et al. [118] (Eq. 5.6) provides very good

agreement with the experimental data.

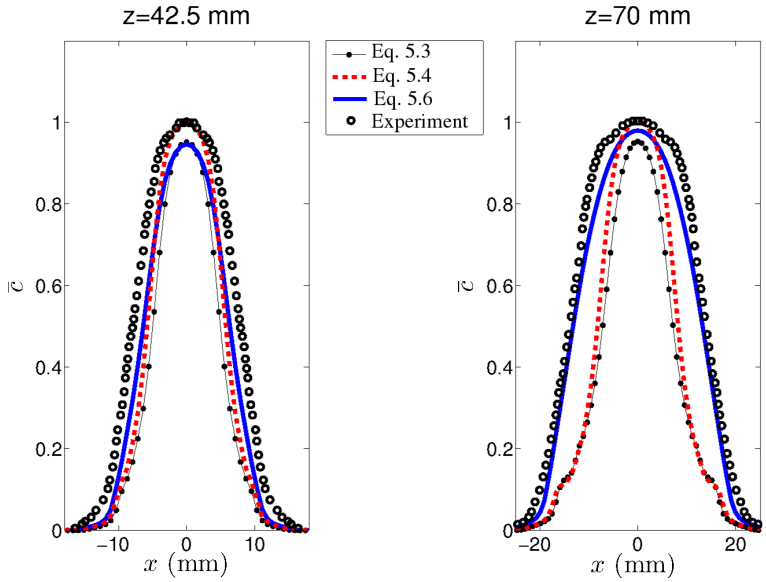

Figure 5.12: Progress variable at z=42.5 and 70 mm for different scalar dissipation rate models (Eqs. 5.3, 5.4, 5.6).

The axial velocity profiles do not follow the same trend, as shown in Fig. 5.13. The velocity field calculated with the algebraic model of Kolla et al. [118] (Eq. 5.6) for the scalar dissipation rate underpredicts the axial velocity at the central location, while following the experimental values very well far from the centerline. A similar observation can be made for the FSD model (Eq. 5.4): it is very close to the experimental data for transverse location far from the centerline, but overpredicts the velocity when the transverse coordinate approaches to zero. Finally, the simple algebraic model predicts accurately the mean axial velocity at each location. The three models perform similarly in terms of the transverse velocity profiles, as presented in Fig. 5.14. The algebraic model of Kolla et al. [118] (Eq. 5.6) provides better results close to the centreline, especially for the first two axial locations ($z = 20.4$ and $z = 30.6$ mm), while the simple algebraic model (Eq. 5.3) is able to capture the recovery velocity far from the centreline, in particular in the location farthest downstream ($z = 40.1$ mm).

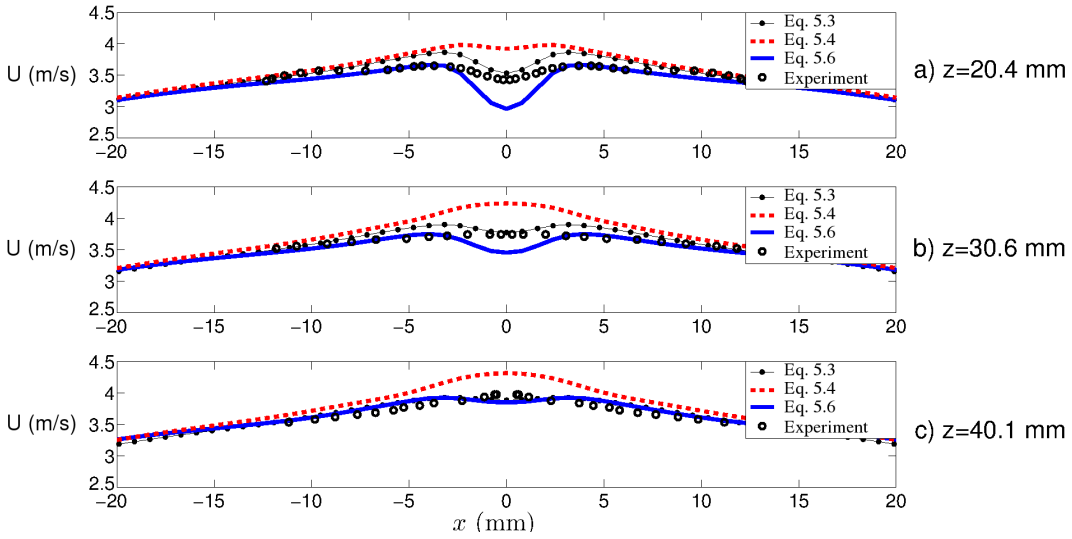

Figure 5.13: Mean axial velocity profiles at three locations, z=20.4, 30.6 and 40.1 mm for different scalar dissipation rate models (Eqs. 5.3, 5.4, 5.6).

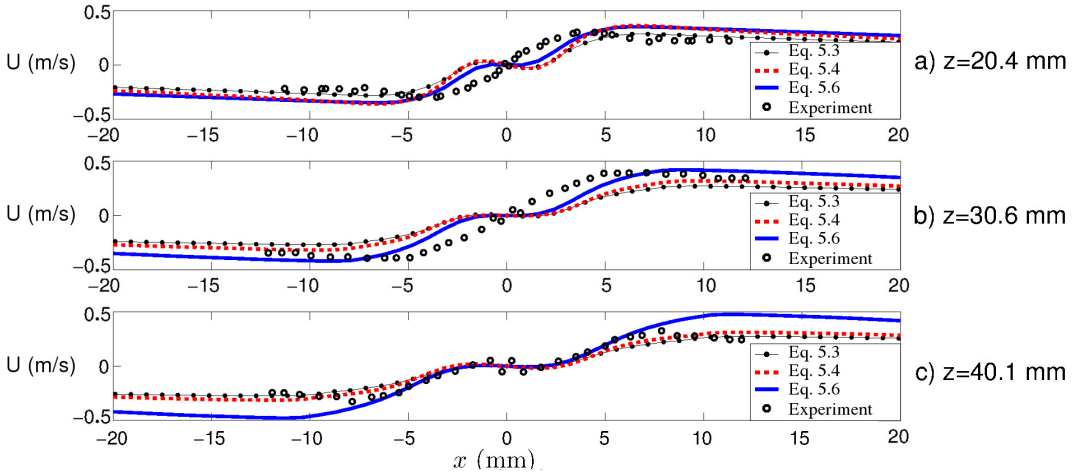

Figure 5.14: Mean transverse velocity profiles at three locations, z=20.4, 30.6 and 40.1 mm for different scalar dissipation rate models (Eqs. 5.3, 5.4, 5.6).

Due to the large discrepancies in the progress variable profiles for the results obtained with the simple algebraic model (Eq. 5.3), the method of Kolla et al. [118] (Eq. 5.6) is

considered for the present case and the corresponding numerical results are compared to the ones obtained by Robin et al. [12] through a flamelet approach denoted as the Libby-Williams-Poitiers (LW-P) model. The progress variable profiles corresponding to the CSE and LW-P approaches are presented in Fig. 5.15.

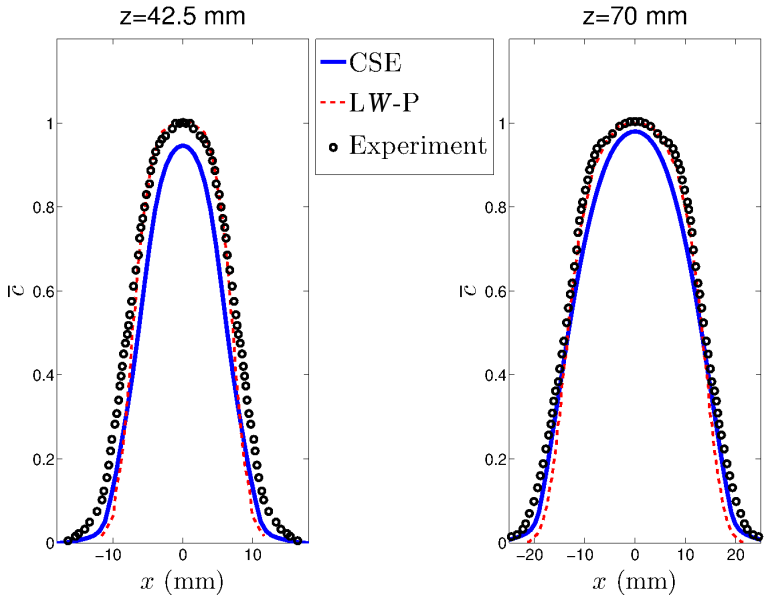

Figure 5.15: Progress variable at z=42.5 and 70 mm for different combustion models. Solid line refers to CSE and dotted line to LW-P [12].

The peak at the centreline is well approximated by the LW-P model, while it is underpredicted by the CSE formulation, in particular at the lower axial location ($z = 42.5$ mm). However, the CSE model is found to better predict the profiles for higher transverse distances at both axial locations. Similar observations can be made about the mean axial velocity profiles, measured at three distinct axial locations, as shown in Fig. 5.16. For the first location ($z = 20.4$) both methods provide very good predictions far from the center, but underpredict the centreline velocity, which corresponds to the recirculation caused by the stabilization rod. The underestimation is slightly more pronounced in the CSE case. Farther downstream, at the second axial location ($z = 42.15$ mm) the two methods provid similar results, while in the last axial location ($z = 40.1$ mm), CSE provides better agreement for the centreline location. Finally, mean transverse velocity profiles are presented in Fig. 5.17.

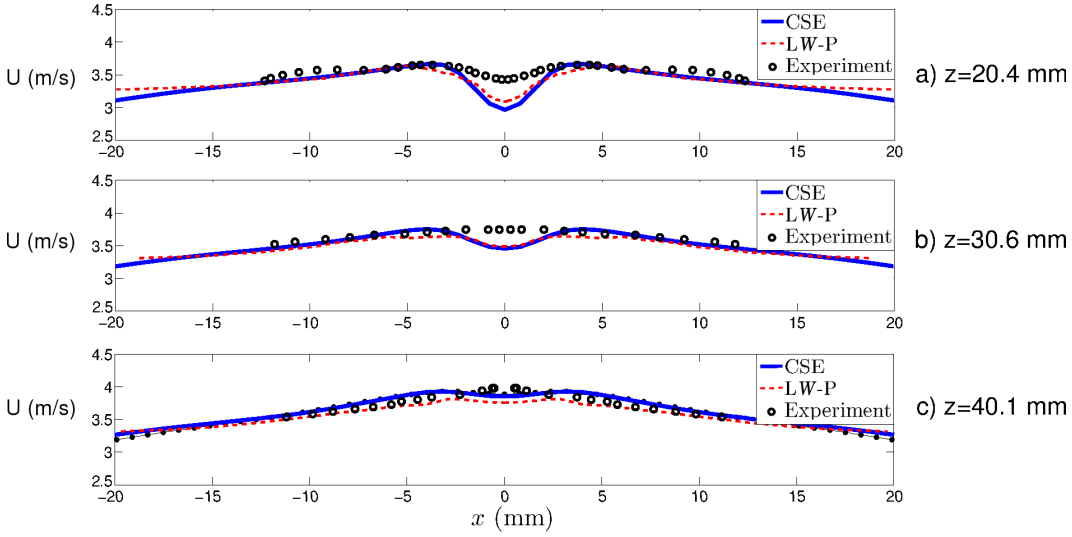

Figure 5.16: Mean axial velocity profiles at three locations, z=20.4, 30.6 and 40.1 mm for different combustion models. Solid line refers to CSE and dotted line to LW-P [12].

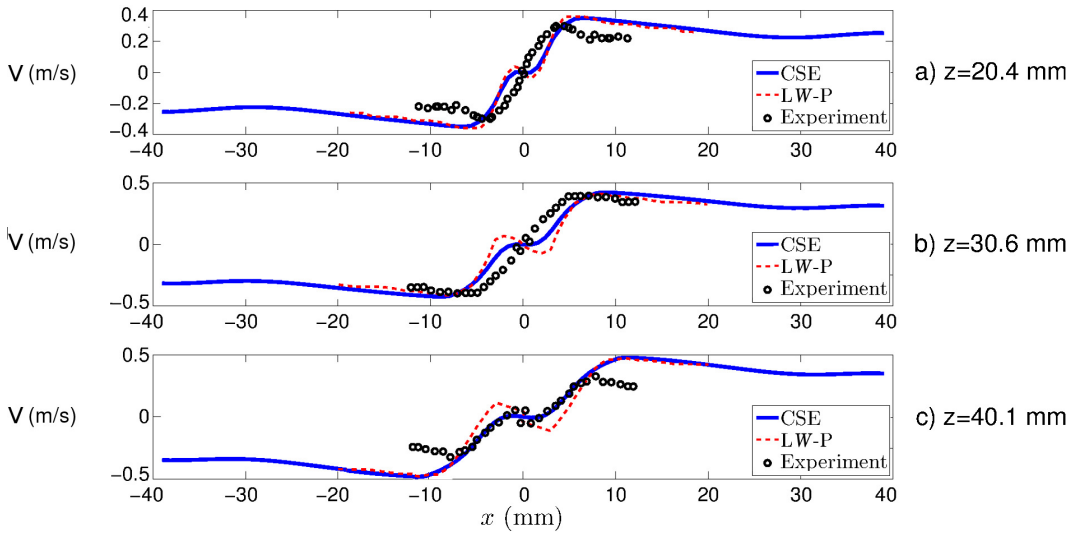

Figure 5.17: Mean transverse velocity profiles at three locations, z=20.4, 30.6 and 40.1 mm for different combustion models. Solid line refers to CSE and dotted line to LW-P [12].

Best agreement with experimental data is found for the CSE results at the centreline locations, especially for higher distances downstream the stabilization rod. One plausible

reason is the turbulence model adopted in the current simulations, consisting of the standard SST $k-\omega$ turbulence model [33], while in [12], the standard $k-\varepsilon$ turbulence model is used. Overall, both combustion models perform reasonably well. The next step consists of extending the study to the more general case of stratified combustion.

5.3 DCSE for Stratified Combustion

In the case of partially premixed flames, the CSE formulation entails the use of both the mixture fraction and reaction progress variable and is called DCSE. The idea is to calculate doubly conditionally averaged quantities by using the mixture fraction, Z, and the reaction progress variable, c as the conditioning variables (see Chapter 4). Equation 3.3 in the DCSE formulation can be written as Eq. 4.2. The same procedure described in Section 4.6 is used as implementation of DCSE for stratified combustion. However, it must be noted here that the upper bound for the mixture fraction, Z_2 in Eq. 4.2, is reduced due to the particular configuration of these flames. The number of points in mixture fraction space, n_Z, is limited to 35, since very rich conditions are not encountered in any of the three cases [2]. This choice leads to two simultaneous benefits: computational time is reduced for the size of the inversion matrix (the index m runs from 1 to $M = n_Z \times n_{c^*}$, see Eq. 4.3) is reduced from 1,000 to 700 (n_{c^*} is kept equal to 20) and, at the same time, stability in the regularization process is enhanced since many zeros and hence lack of information, corresponding to points in mixture fraction space $n_Z > 35$, are avoided. The same considerations made in Section 4.5.3 are applied here regarding the progress variable definition for partially premixed combustion. For simplicity and consistency with the partially premixed formulation presented in Chapter 4, the regularization parameter and the *a priori* knowledge of the solution are calculated in the same way as in Section 4.5.1, $\lambda = Tr(\mathbf{A}^T\mathbf{A})/Tr(I)$, where Tr is the trace of the matrix and I the identity matrix and the previous time step solution is used for $\vec{\alpha}_0$, respectively. Chemistry tabulation follows the same strategy presented in 4.7 for partially premixed combustion.

Experimental analysis is conducted in the case of stratified flames with the same burner presented in Section 5.2.1. In the stratified regime, the equivalence ratio varies between a maximum value at the central axis and 0 at the periphery. Three different conditions are carried out based on the profile of the equivalence ratio at the inlet and correspond to SE1.0-0, SB0.8-0 and SB1.2-0, respectively, following [12], where S stands for stratified, E

[2] The 35^{th} point in mixture fraction space corresponds to $Z = 0.1$, which is larger than the maximum value of the mixture fraction obtained in the rich case, SB12 (see Fig. 5.20).

and B denote the type of turbulence grid used, while the numbers specify the equivalence ratio gradient, namely from the value at the center of the combustion number (1.0, 0.8 and 1.2, respectively) to a value equal of 0 at the periphery. The first step consists of defining the equivalence ratio profiles at the inlet of the computational domain. Experimental data provided mean and RMS mixture fraction profiles for the non-reacting case at a distance of 20 mm downstream from the rod ($z = 20$ mm), for cases SE1.0-0 [14] SB0.8-0 and SB1.2-0 [14, 12]. Numerical simulations without combustion are carried out with different inlet profiles for the equivalence ratio to recover the right profile at $z = 20$ mm, as shown in Figs. 5.18-5.20.

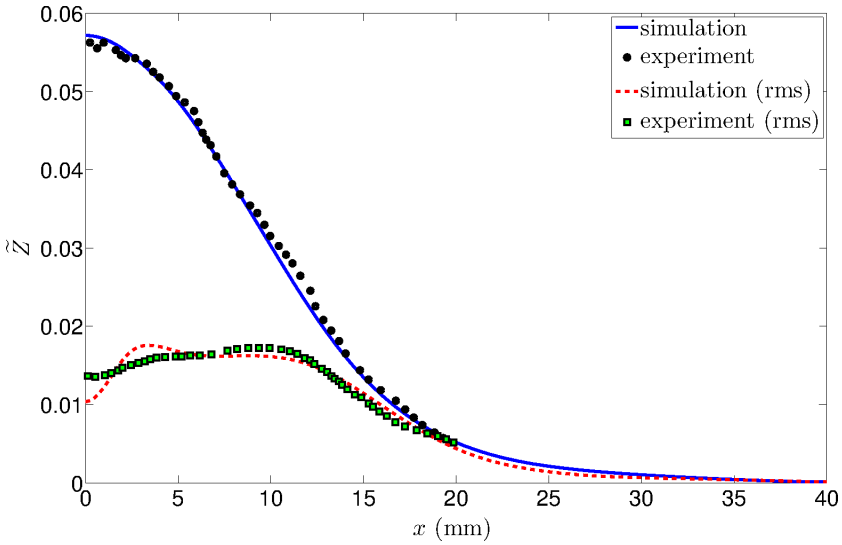

Figure 5.18: Mean and RMS mixture fraction profiles at $z = 20$ mm in the non-reacting case for the case SE1.0-0. Symbols denote experimental data [14, 12], lines refer to numerical simulations.

The mean mixture fraction is well approximated by the numerical simulations, while some discrepancies have been found in the RMS profiles, in particular near the centre of the combustion chamber. It must be noted that the experimental profiles in terms of mixture fraction can be easily converted in terms of equivalence ratio through

$$Z = \frac{\phi}{\phi + s} \,, \tag{5.8}$$

where the stoichiometric air-fuel ratio of methane, s, is 17.15 [14].

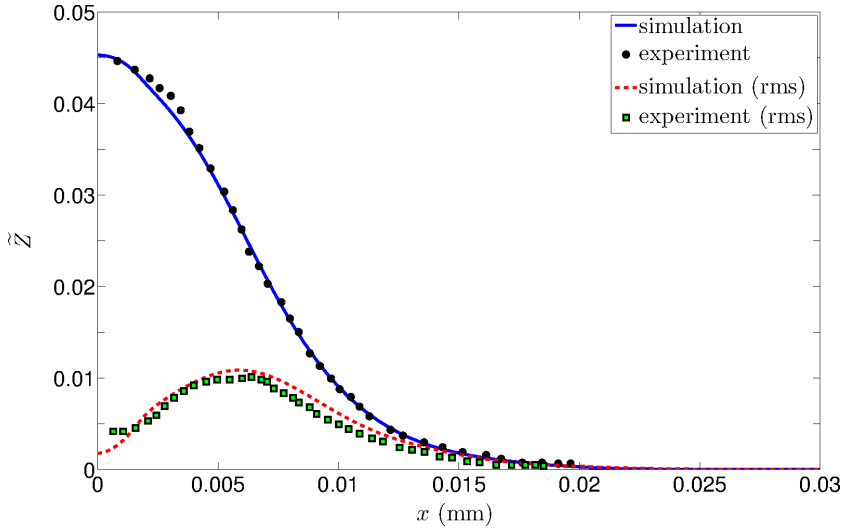

Figure 5.19: Mean and RMS mixture fraction profiles at $z = 20$ mm in the non-reacting case for the case SB0.8-0. Symbols denote experimental data [14, 12], lines refer to numerical simulations.

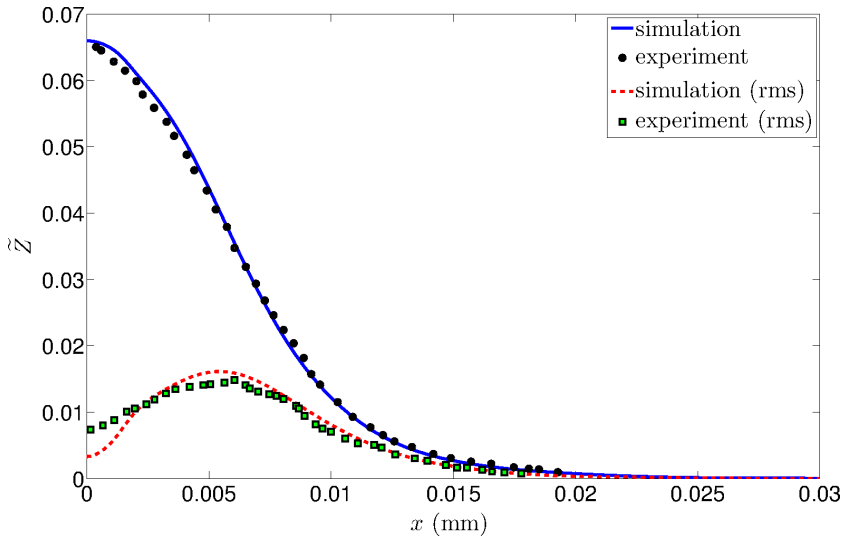

Figure 5.20: Mean and RMS mixture fraction profiles at $z = 20$ mm in the non-reacting case for the case SB1.2-0. Symbols denote experimental data [14, 12], lines refer to numerical simulations.

Experimental findings [13, 12] are available for the non-reactive case at two axial locations downstream of the stabilizing rod, z = 40 and 70 mm, respectively. Comparisons of the numerical simulations with experiments are presented in Figs. 5.21-5.23 and Figs. 5.24-5.26 in terms of equivalence ratio and its variance profiles, respectively.

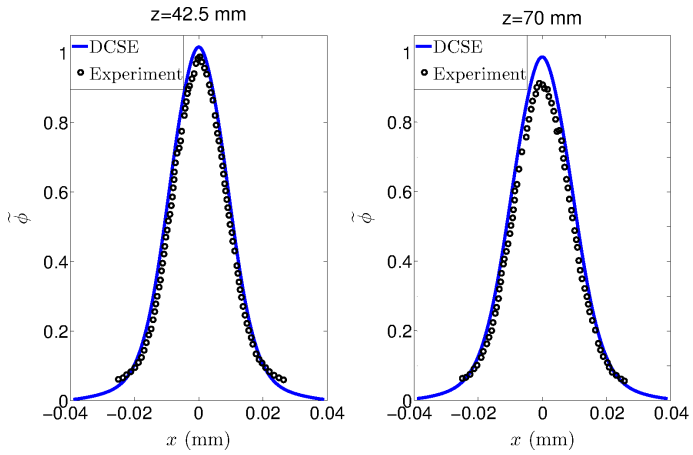

Figure 5.21: Mean equivalence ratio profiles at $z = 42.5$ mm (left) and $z = 70$ mm (right) in the non-reacting case for the case SE1.0-0. Symbols denote experimental data [13, 12], lines refer to numerical simulations.

The mean equivalence ratio follows the experimental findings very well for the case SE1.0-0 at the axial location $z = 42.5$ mm (Fig. 5.21 left). Farther downstream, at $z = 70$ mm, the centreline peak is overpredicted by 8% (Fig. 5.21 right). Because of the non-reacting nature of the presented simulation, this discrepancy can be attributed solely to the mixing field and, in particular, to the turbulence model adopted, which is the standard SST $k - \omega$ [33]. However, Robin et al. [12] obtained a very similar trend for the SE1.0-0 case by using the standard $k - \varepsilon$ model . A slightly larger disagreement is observed in the variance of progress variable profiles, as can be seen in Fig. 5.24, in both axial locations. Figures 5.22 and 5.23 show the equivalence ratio profiles for the cases SB0.8-0 and SB1.2-0, corresponding to the different turbulence grid (B). The agreement is not as good as what observed in the SE1.0-0 case. Discrepancies are found in both axial locations, consistent with the findings of [13]. Further, the rich case, SB1.2-0, shows larger discrepancies at the lower axial location, i.e. the peak is underpredicted by 5% for the lean case (see Fig. 5.22) and by 10% for the rich case (see Fig. 5.23). One possible explanation can be related to the two different turbulence grids, characterized by different values of turbulent properties (see Table 5.1).

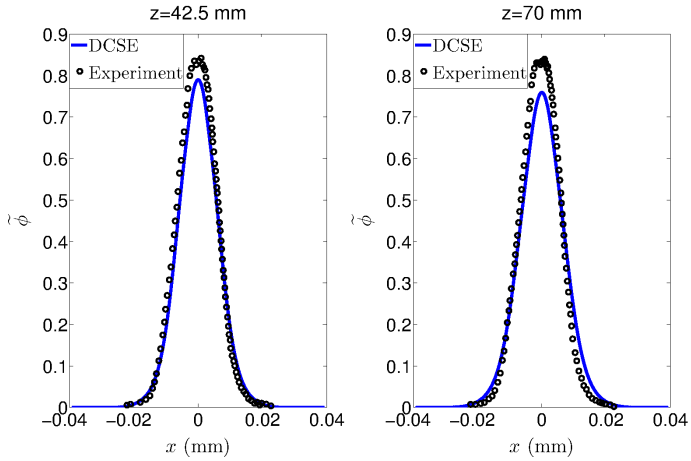

Figure 5.22: Mean equivalence ratio profiles at $z = 42.5$ mm (left) and $z = 70$ mm (right) in the non-reacting case for the case SB0.8-0. Symbols denote experimental data [13, 12], lines refer to numerical simulations.

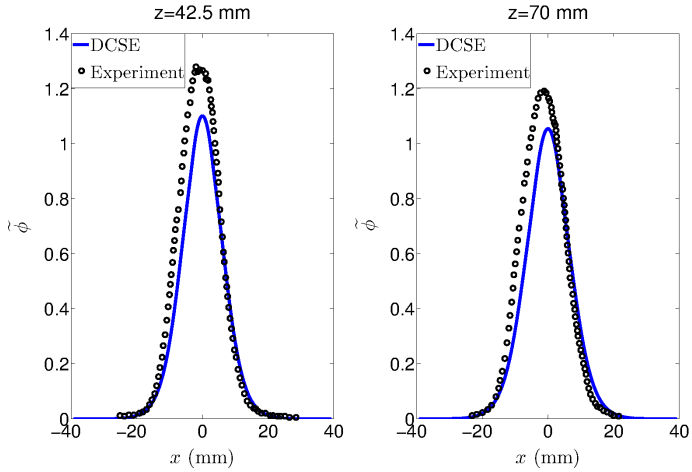

Figure 5.23: Mean equivalence ratio profiles at $z = 42.5$ mm (left) and $z = 70$ mm (right) in the non-reacting case for the case SB1.2-0. Symbols denote experimental data [13, 12], lines refer to numerical simulations.

The turbulence model adopted in the numerical simulations has not been tested for both of them, but the conclusions presented in Section 5.2.3 about the fully premixed case for the grid "E" are kept here for consistency.

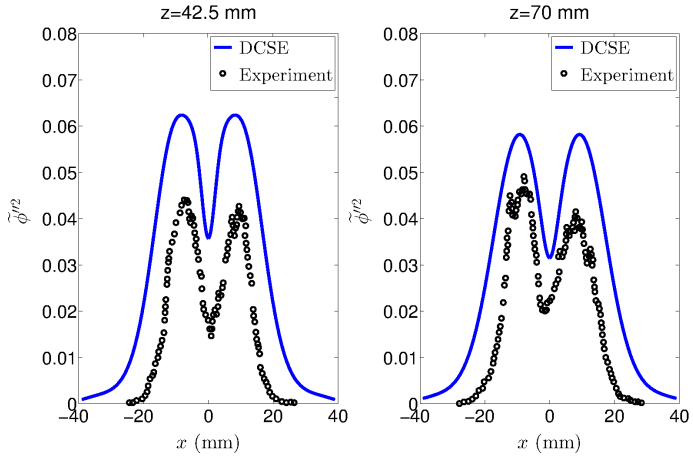

Figure 5.24: Variance of equivalence ratio profiles at $z = 42.5$ mm (left) and $z = 70$ mm (right) in the non-reacting case for the case SE1.0-0. Symbols denote experimental data [14, 12], lines refer to numerical simulations.

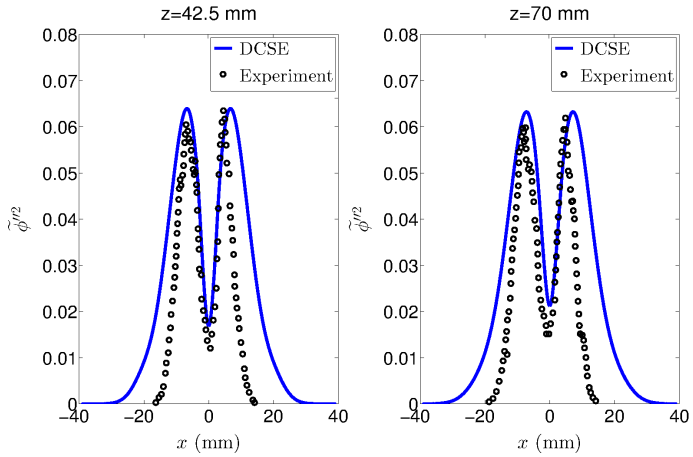

Figure 5.26: Variance of equivalence ratio profiles at $z = 42.5$ mm (left) and $z = 70$ mm (right) in the non-reacting case for the case SB1.2-0. Symbols denote experimental data [14, 12], lines refer to numerical simulations.

However, experimental uncertainties should be considered too: the peaks of the equivalence ratio are higher than the inlet values (0.8 for SB0.8-0 and 1.2 for SB1.2-0) at $z = 42.5$ mm and for lean conditions the centreline peak does not decrease in the $z = 70$ mm location, as expected and observed in the other two cases. It must be noted that the ex-

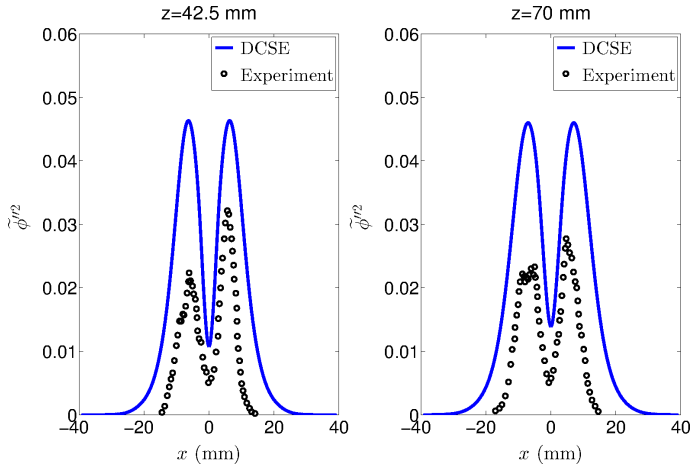

Figure 5.25: Variance of equivalence ratio profiles at $z = 42.5$ mm (left) and $z = 70$ mm (right) in the non-reacting case for the case SB0.8-0. Symbols denote experimental data [14, 12], lines refer to numerical simulations.

perimental results for the B grid are taken from a PhD dissertation [13] and no explanation was provided for these discrepancies. Finally, the variance of progress variable is overpredicted for the lean case (see Fig. 5.25), consistent with [13] and follows the experimental findings very well for the rich case, as reported in Fig. 5.26.

5.3.1 Scalar dissipation rate for partially premixed combustion

The numerical simulations of the the fully premixed case are carried out with three distinct models for the scalar dissipation rate (see Section 5.2.6). The simple algebraic model (Eq. 5.3) shows some weakness in describing the reactive scale fluctuations decay adequately. The model proposed by Kolla et al. [118] (Eq. 5.6) provides very good results, in particular in terms of the mean progress variable. Thus, its use in the stratified combustion case might be the logical step. However, in its original form, it presents several terms that are functions of the stoichiometry of the specific turbulent premixed flame. This means that for partially premixed combustion, characterized by a range of different values of the equivalence ratio, the dependence on the equivalence ratio must be included in the formulation. Darbyshire et al. [178] extended Eq. 5.6 to the partially premixed case by including a dependence on the equivalence ratio and obtained improved results with respect to the simple algebraic model case (Eq. 5.3) in terms of mean velocities, species mass fraction, and temperature. They introduced the dependence on the local equivalence ratio level in the expression for the

adiabatic flame temperature T_b by using the procedure of Fernandez-Tarrazo [15], which was used in the calculation of the heat release index (normalized temperature rise)

$$\tau(Z) = \frac{T_b(Z) - T_u}{T_u} \ . \tag{5.9}$$

The values of $s_L(Z)$ and $\delta_L(Z)$ were retrieved from analytical expressions of Gottgens et al. [16]. However these were defined for lean conditions ($\phi < 1$) and did not describe the dependence of s_L and δ_L on the equivalence ratio adequately for rich conditions, as presented in Fig. 5.28. Further, K_c^*/τ was assumed to be constant in [178], even though a dependence on the equivalence ratio existed [179].

In the present work, an extension of the closure proposed by Kolla et al. [118] (Eq. 5.6) for the scalar dissipation rate is presented by following a more rigorous approach, where all the terms in Eq. 5.6 are expressed as functions of the local equivalence ratio value. In DCSE, both progress variable and mixture fraction are used as conditioning variables. The mixture fraction can be easily converted to the equivalence ratio through Eq. 5.8. For convenience, the implementation of the closure for $\widetilde{\chi}_c(Z)$ is expressed in terms of mixture fraction since this quantity is directly available in the simulations. Therefore, the quantities that are given as functions of ϕ are converted in mixture fraction space first. Figure 1 of [15] shows the variation with equivalence ratio of the adiabatic flame temperature T_b for methane-air flames in a range of equivalence ratios between 0.6 (Z = 0.034) and 1.5 (Z = 0.080). This profile is numerically interpolated through polynomial interpolation for a range of mixture fraction values between 0.0006 and 0.15. For $Z < 0.0006$ and $Z > 0.15$, T_b is assumed to be equal to 301 K. Figure 5.27 presents the resulting profile of the calculated $T_b(Z)$ compared to the experimental values given in [15]. Since no experimental data is given for $\phi > 1.5$, an additional point is included in the experimental profile in order to confine the interpolating curve, which corresponds to $T_b = 685$ K for $\phi = 3$. The accuracy of this last point is not expected to have a considerable impact in the formulation since it is outside the flammability region and the corresponding value of τ is very low ($\tau = 1.28$). Once the dependence of T_b on Z is determined, the local value of the heat release index is retrieved from Eq. 5.9. The next step consists of calculating the local value of K_c^*/τ. Table 2b of [179] summarizes the values of K_c^*/τ for methane-air flames with $T_u = 300$ K in a range of equivalence ratios between 0.6 and 1.4. This profile is interpolated and the value of K_c^* that appears in Eq. 5.6 can be estimated by knowing the local value of Z by simply multiplying the interpolated value of $K_c^*(Z)/\tau(Z)$ with the corresponding value of $\tau(Z)$, which is dependent on T_b, see Eq. 5.9. At this point, the dependence of s_L and δ_L on the mixture fraction needs to be provided. Instead of using analytical expression as done by Darbyshire et al. [178], numerical interpolation is

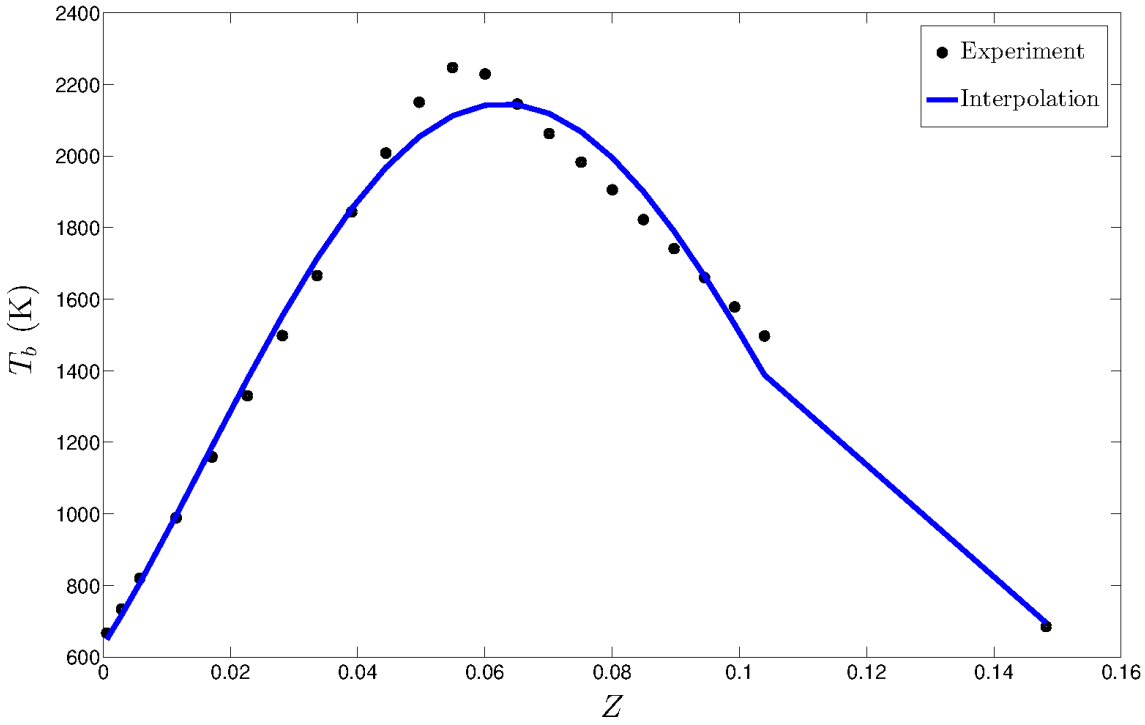

Figure 5.27: Variation of the adiabatic flame temperature T_b as a function of the mixture fraction for methane-air flames. Symbols denote experimental measurements [15], lines refer to numerical interpolations.

applied directly to experimental data. Degardin [14] presented the distribution of s_L as a function of the equivalence ratio (the lean and rich limit being $\phi = 0.6$ and $\phi = 1.6$, respectively) for methane air combustion at atmospheric conditions and compared it with previous experimental works ([180, 181, 182]), resulting in a very good correlation. The same interpolation procedure used for the determination of T_b and K_c^* is applied to this set of data. Outside the flammability limits (which are approximately equal to 0.0284 and 0.089 in mixture fraction at atmospheric conditions for methane-air combustion [153]), the value of s_L is set equal to a small value (0.1 cm/s) in order to avoid interpolation errors. Figure 5.28 presents the interpolated profile in comparison with the experimental data and numerical calculations from the analytical expression of Gottgens et al. [16], used by Darbyshire et al. [178]. The analytical formulation [16] predicts the laminar flame speed very well for lean conditions, but considerably overpredicts s_L for rich mixtures, as shown in Fig. 5.28. On the contrary, the interpolated values follow the experimental findings very well for both lean and rich conditions. The same interpolation method is applied

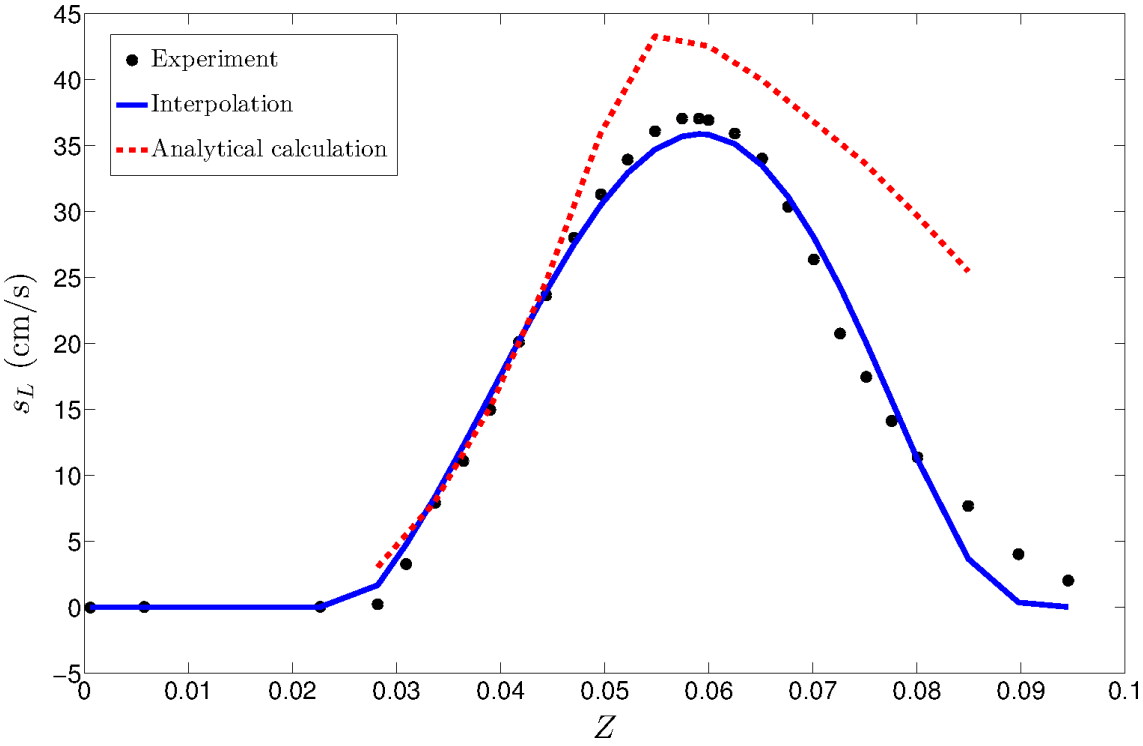

Figure 5.28: Variation of the flame speed s_L as a function of the mixture fraction for methane-air flames. Symbols denote experimental measurements [14], solid lines refer to numerical interpolations and dotted lines correspond to analytical expressions of Gottgens et al. [16].

to δ_L. Experimental data of $\delta_L(\phi)$ is taken from [17] and comparison with the numerical interpolation is presented in Fig. 5.29. Since no experimental data is given for lean and rich conditions, a constant value of 0.1 m for δ_L is used in the numerical implementation for the range of mixture fraction values outside the flammability region. As can be observed in Figs. 5.27-5.29, an error is introduced in the interpolation process. Ideally, the best approach would be to use experimental profiles. However, this is not possible and different strategies can be adopted. The use of analytical expressions could also be considered, but in this work their validity has been questioned, due to the lack of ability on describing adequately rich mixture conditions, as clearly shown in Fig. 5.28. Thus, the polynomial interpolation seems to be a better strategy, for it is simple to implement numerically (all the profiles depend on just one variable, i.e. Z) and represents experimental profiles with good accuracy. It must be noted that the higher the degree of the polynomial, the

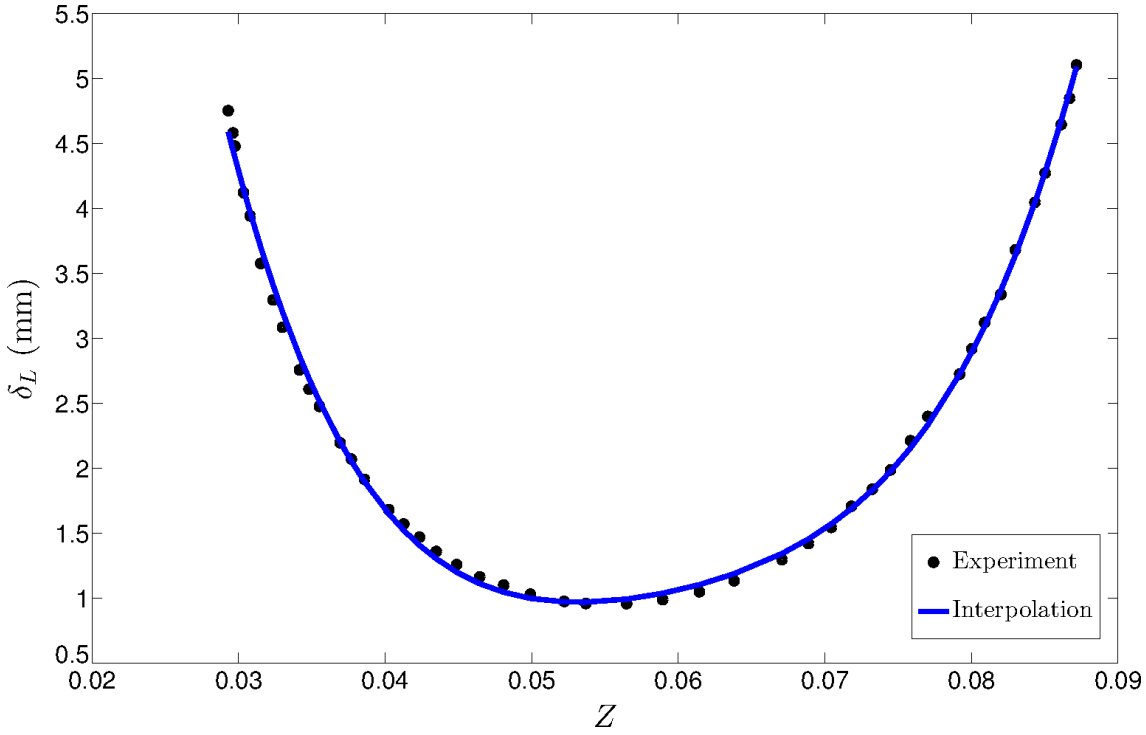

Figure 5.29: Variation of the flame thickness δ_L as a function of the mixture fraction for methane-air flames. Symbols denote experimental measurements [17], lines refer to numerical interpolations.

better the approximation, but this corresponds to higher risk of divergence in particular at the boundary of the realization domain. This aspect has been avoided in the current implementation by truncating the interpolation outside the flammability limits for s_L and δ_L. In this way, the physics of the problem is retained, and at the same time, the method is expected to be sufficiently robust. Finally, the local value of the Karlovitz number is needed to estimate the values of $C_3(Z)$ and $C_4(Z)$ in Eq. 5.6. The Karlovitz number, Ka, can be expressed as

$$\mathrm{Ka}(Z) = \frac{t_{chem}(Z)}{t_\eta} = \frac{\delta(Z)/s_L(Z)}{\sqrt{\nu/\varepsilon}} \ , \tag{5.10}$$

where the Zeldovich thickness $\delta(Z)$ is related to the thermal thickness $\delta_L(Z)$ by $\delta(Z) = \frac{\delta_L(Z)}{2(1+\tau(Z))^{0.7}}$ [24]. As can be seen in Eq. 5.10, s_L is in the denominator and hence is set to a nonzero value outside the flammability limits to avoid divergence in the numerical simulations, as mentioned earlier. The final expression of the scalar dissipation rate model

of Kolla et al. [118] extended to partially premixed configurations reads

$$\widetilde{\chi}_c(Z) = 2\overline{\rho}\frac{1}{\beta'}\left([2K_c^*(Z) - \tau(Z)C_4(Z)]\frac{s_L(Z)}{\delta_L(Z)} + C_3(Z)\frac{\widetilde{\varepsilon}}{\widetilde{k}}\right)\widetilde{c''^2}, \tag{5.11}$$

where there is a clear dependence on Z in several terms. In Eq. 5.11, three main contributions can be considered. The first term, denoted as I represents the correlation between dissipation and dilatation rates [118], $\mathrm{I} \equiv 2K_c^*(Z)\frac{s_L(Z)}{\delta_L(Z)}$. The second term corresponds to the strain due to heat release [118], $\mathrm{II} \equiv -\tau(Z)C_4(Z)\frac{s_L(Z)}{\delta_L(Z)}$. The last term indicates the turbulent strain rate and is proportional to the turbulent time scale, $\mathrm{III} \equiv C_3(Z)\frac{\widetilde{\varepsilon}}{\widetilde{k}}$. Thus, Eq. 5.11 can be written as

$$\widetilde{\chi}_c(Z) = 2\overline{\rho}\frac{1}{\beta'}\left(\mathrm{I} + \mathrm{II} + \mathrm{III}\right)\widetilde{c''^2}, \tag{5.12}$$

The contribution of each term is calculated in the numerical simulations and presented in Fig. 5.30 corresponding to the SE1.0-0 case at two axial locations, z=42.5 and 70 mm, respectively. For comparison, the corresponding contributions in the premixed formulation (Eq. 5.6) are presented by the dashed lines. In both locations the contribution from III is negligible, while the first two terms are dominant. I is larger than II, leading to a positive scalar dissipation rate. Similar observations can be made in the fully premixed case, but clearly, in the latter, the three terms have constant values. The dependence of the scalar dissipation formulation on the local value of the mixture fraction is reflected in the fact that the curves I and II approach the x-axis at a larger value of the transverse coordinate as the axial location increases (x = 15 mm at z = 42.5 mm and x = 20 mm at z = 70 mm), resembling the shape of the turbulent V-flame, which gets wider as the distance from the igniting rod increases. Figure 5.30 demonstrates that the premixed formulation is not suitable in this case since is not able to represent the stratification conditions.

5.4 Numerical Results for the stratified conditions

Numerical results obtained for the more general case of stratified turbulent combustion are presented here. The first flame corresponds to SE1.0-0, which is characterized by the same turbulence grid (and inlet velocity conditions) of the fully premixed case described in Section 5.2, but with a non homogeneous equivalence ratio inlet profile, as shown in Fig. 5.18. The same computational domain introduced in Section 5.2.1 is adopted. Similar to what is presented in Section 4.5.2, two distinct approaches for the presumed form of the

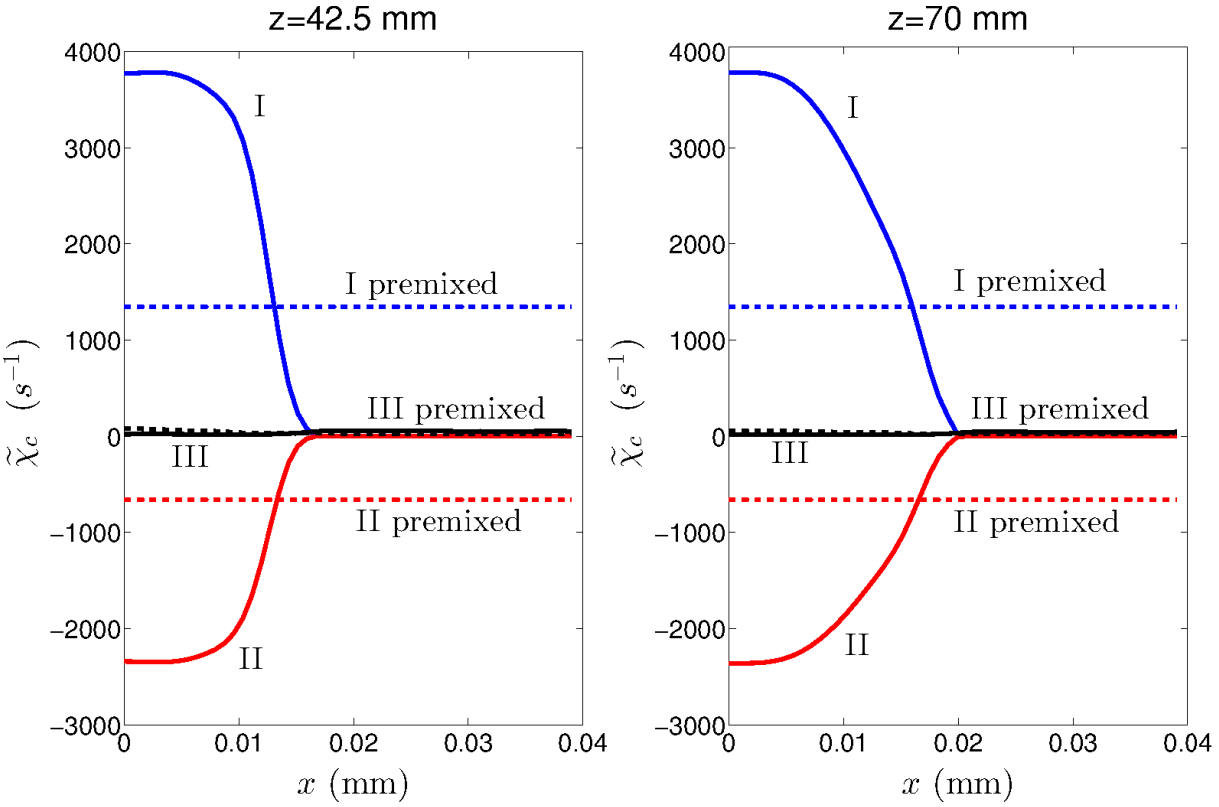

Figure 5.30: Contributions of the different terms of the scalar dissipation rate (Eq. 5.12) at z=42.5 and 70 mm. Solid lines refer to the partially premixed implementation (Eq. 5.11) and dotted lines correspond to the premixed formulation (Eq. 5.6).

joint PDF are used. A statistical independence between the two variables, mixture fraction and progress variable, is first assumed (see Eq. 4.7) and the value of the equivalence ratio given at the centreline (stoichiometric for the SE1.0-0 case) is used to define the shape of $f(c^*)$. Then, the more general approach, introduced in Section 4.5.2 (Eq. 4.6), for which the assumption of statistical independence is relaxed, is selected. The same presumed forms of the PDF introduced in Chapter 4 are used here: β-PDF for the mixture fraction and modified laminar flamelet PDF [4] for the progress variable. Numerical results performed with the two forms of the joint PDF are compared to experimental data [12]. Figure 5.31 shows the mean progress variable profiles at two different axial locations for the flame SE1.0-0 obtained with the two approaches for the joint PDF. Very good agreement is obtained in both axial locations, especially far from the centreline. The two formulations for the joint PDF provide very similar results, suggesting that statistical independence

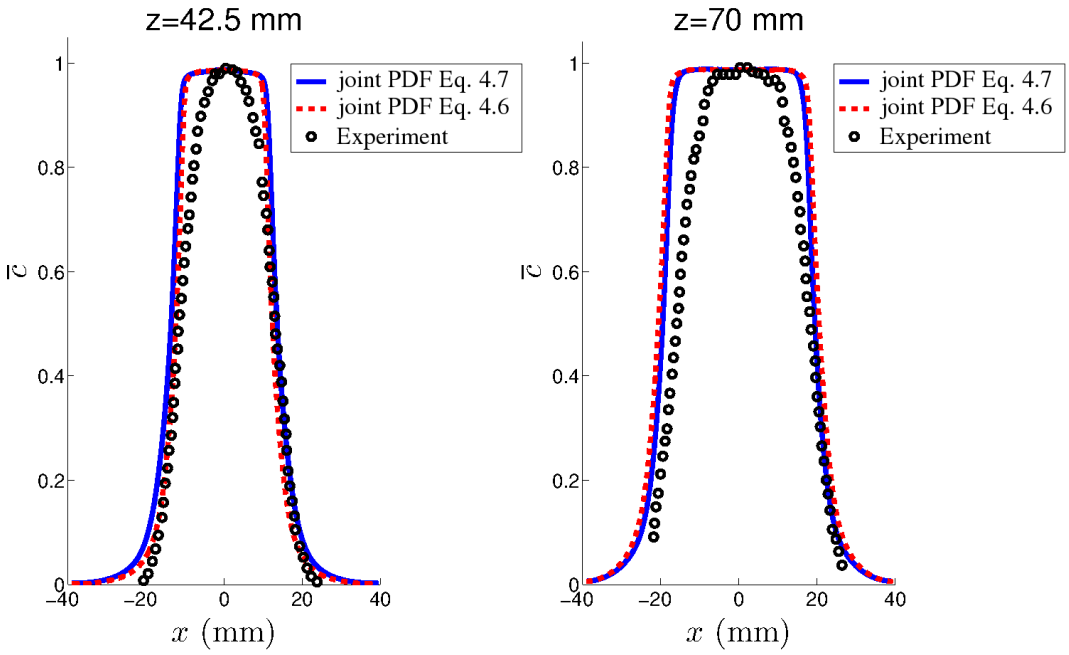

Figure 5.31: Progress variable at z=42.5 and 70 mm for different joint PDF approaches for stratified conditions SE1.0-0.

is a good assumption for the present case. Slight improvement of the progress variable profile obtained with the joint PDF calculated through Eq. 4.6 is observed, especially at the second location, z = 70 mm. Similar to the fully premixed case, mean axial velocity profiles are given at three axial locations in the experimental work for the flame SE1.0-0. Figure 5.32 presents the mean axial velocity profiles obtained with the DCSE model and the two approaches for the joint PDF (using Eq. 4.6 and Eq. 4.7) compared to experimental findings. Very good agreement is found in both cases. In particular, the numerical results obtained with the statistical independent joint PDF (see Eq. 4.7) follow very well the experimental values in all three locations, while an overprediction in the centreline value is observed for the joint PDF case calculated through Eq. 4.6 in the last axial location, z = 40.1 mm. Mean transverse velocity profiles calculated at the same three axial locations are included in Fig. 5.33. In the first two axial locations, the joint PDF calculated through Eq. 4.6 is found to follow very accurately the experiments, while the statistical independent approach tends to overpredict the recovery velocity far from the centreline. In the last axial location, the statistical independent approach follows very well the experimental profiles, while the joint PDF calculated from Eq. 4.6 provides a less satisfactory agreement.

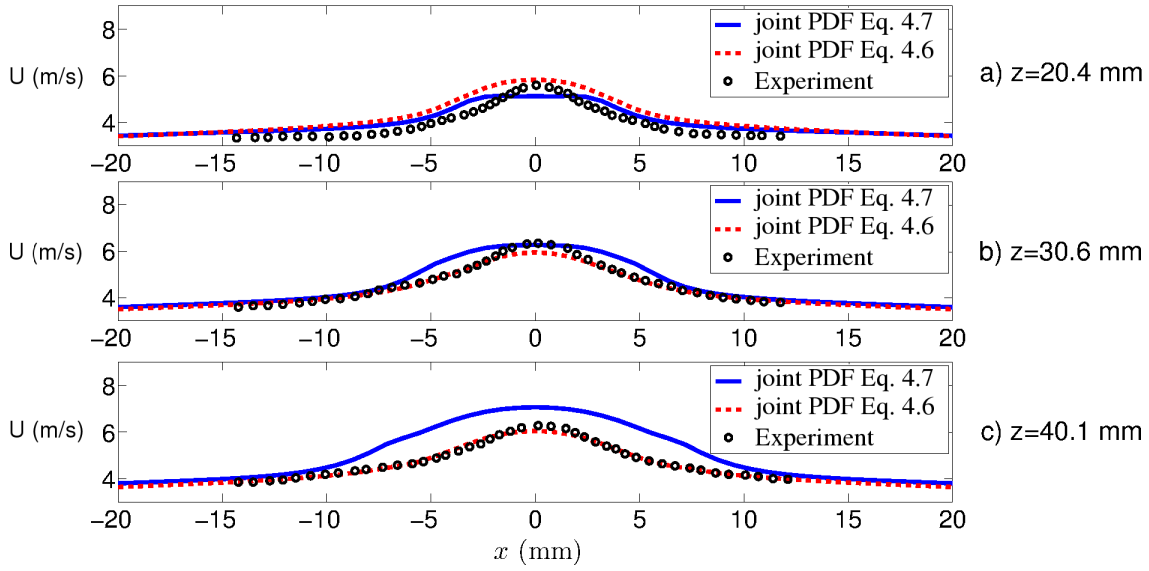

Figure 5.32: Mean axial velocity profiles at three locations, z = 20.4, 30.6 and 40.1 mm for different joint PDF approaches for stratified conditions SE1.0-0.

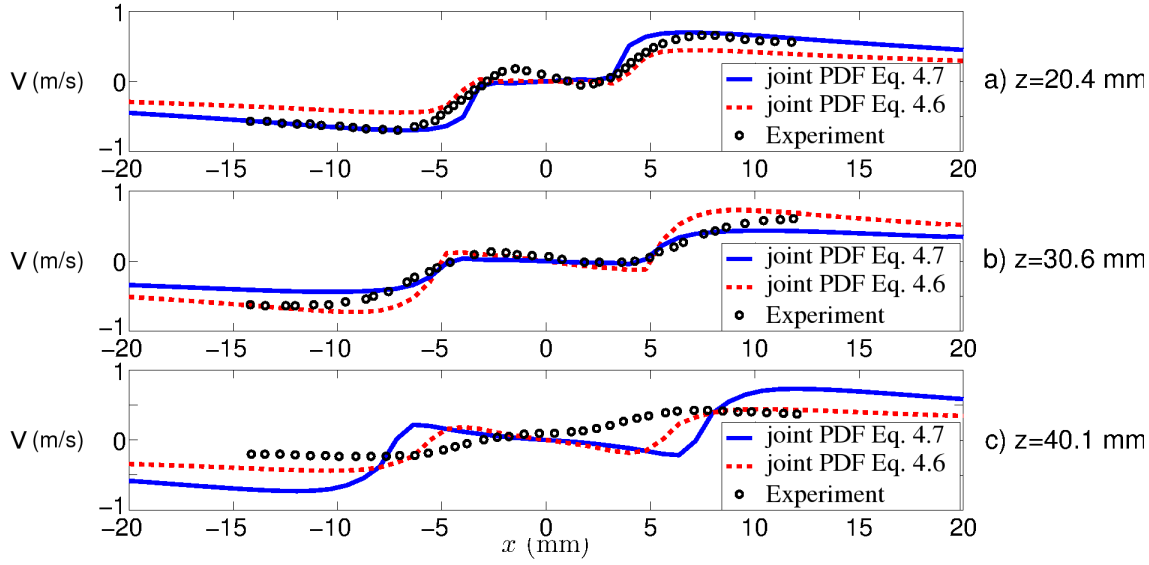

Figure 5.33: Mean transverse velocity profiles at three locations, z = 20.4, 30.6 and 40.1 mm for different joint PDF approaches for stratified conditions SE1.0-0.

Experimental analysis provides mean progress variable profiles at three axial locations for two additional stratified cases corresponding to a different turbulence grid, i.e. SB0.8-0 and SB1.2-0. These conditions lead to situations of only lean (SB0.8) and rich to lean (SB1.2) mixtures. Numerical results for the flame SB0.8-0 are presented in Fig. 5.34. Both approaches for the joint PDF definition yield profiles very close to each other. Very good predictions are found in the first location (z = 42.5 mm), while farther downstream the simulated flame results narrower than the experimental one. A similar behaviour is observed in the numerical work of Robin et al. [12].

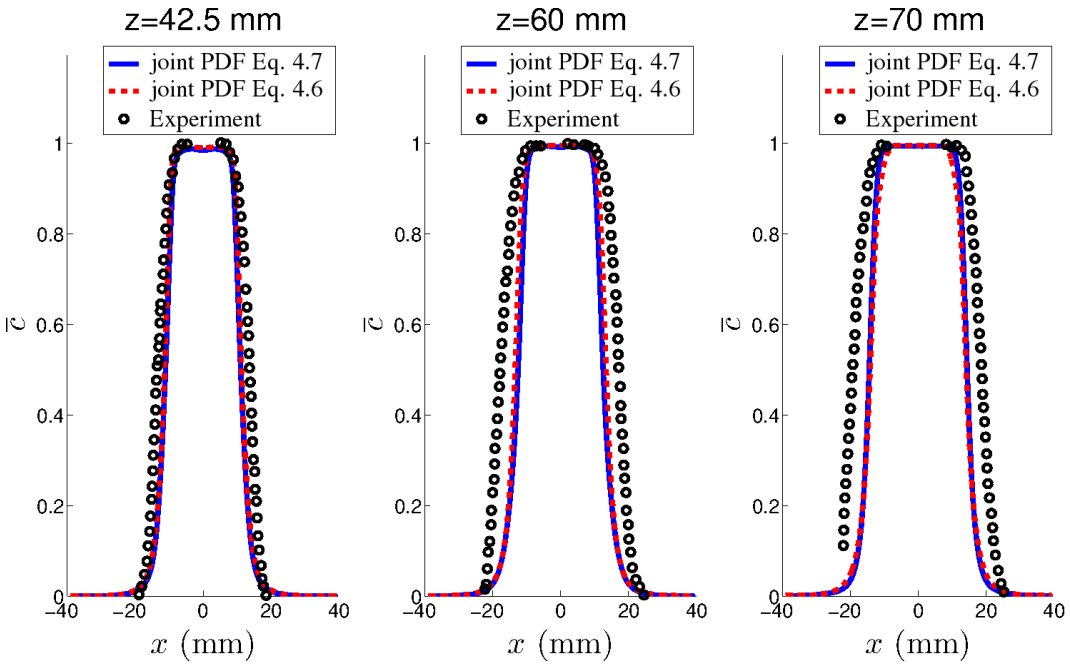

Figure 5.34: Progress variable at z=42.5, 60 and 70 mm for different joint PDF approaches for stratified conditions SB0.8-0.

Figure 5.35 presents the numerical predictions, compared to experimental findings, for the rich case, SB1.2-0. The flame width is underpredicted in both approaches. The joint PDF calculated through Eq. 4.6 is in better agreement than the statistical independent approach, especially when moving downstream. However, it must be noted that the present flame is better predicted by DCSE than by LW-P of Robin et al. [12]. This result is not very surprising if one considers that in [12] a single-step global chemistry is used in the calculation of the mean chemical source term and that such a mechanism provides poor

results for rich conditions [12].

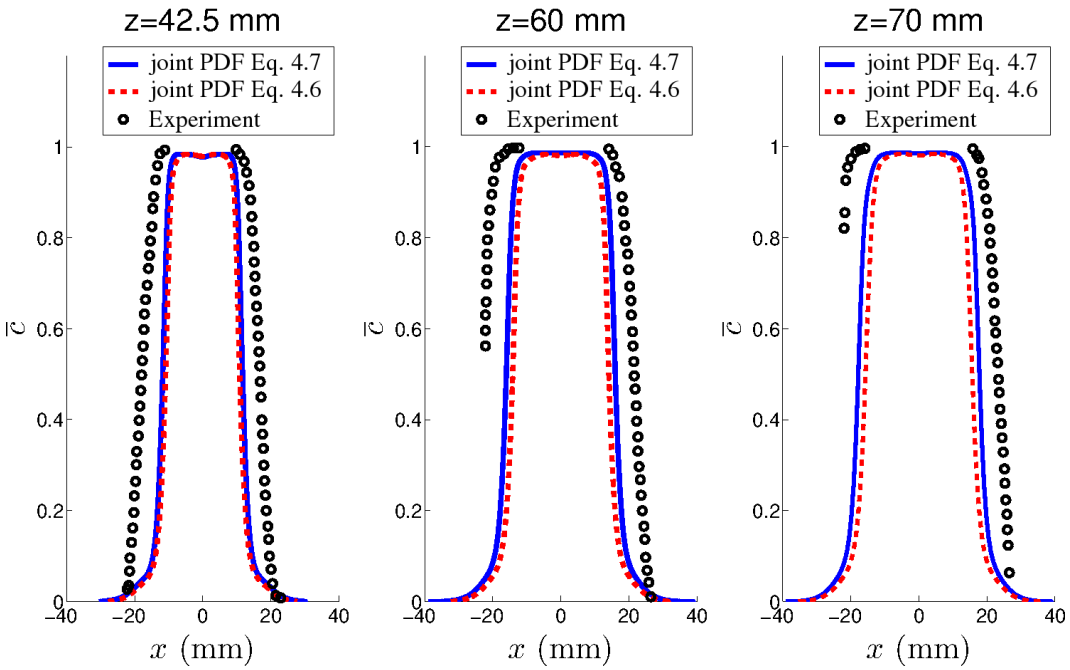

Figure 5.35: Progress variable at z=42.5, 60 and 70 mm for different joint PDF approaches for stratified conditions SB1.2-0.

Overall, the agreement between numerical results and experimental findings is good, proving the ability of DCSE to deal with partially premixed combustion.

5.5 Summary

In this Chapter, the CSE combustion model is applied to RANS numerical solutions of a series of turbulent V-shaped flames for which experimental data is available. Premixed and stratified conditions are investigated. In the premixed case, predictions show very good agreement with the available experimental data, in terms of mean axial velocity and progress variable radial profiles. Different values of the regularization parameter are used and the predictions result to be independent on this parameter. A sensitivity analysis on the number of ensembles used in the inversion process is performed for the fully premixed configuration. The number of CSE ensembles is shown to have a significant impact on

the results if not selected appropriately. For the present case, the suitable number of CSE ensembles results to be equal to 8. Three different models for the scalar dissipation closure are compared in the case of premixed combustion. Very good predictions are obtained for the velocity field in the case of the simple linear relaxation model, while the algebraic model of Kolla et al. [118] performs better in terms of progress variable predictions. A partially premixed formulation of CSE, DCSE, based on doubly conditioning in progress variable and mixture fraction space, is also presented, following the description introduced in Chapter 4 and applied to a series of stratified turbulent flames. An extension of the scalar dissipation model of Kolla et al. is presented for the partially premixed case and the contribution of the different terms in both premixed and partially premixed approaches is investigated. Two formulations of the joint PDF are used, based on Eq. 4.7 and Eq. 4.6. Good predictions compared to experimental data are obtained, in particular for the lean and stoichiometric cases. The joint PDF formulation, for which the statistical independence assumption is relaxed, is found to provide better agreements, in particular for the stoichiometric case. Reasonable agreement is observed for the rich case, consistent with previous numerical studies.

Chapter 6

Conclusions

The primary aim of the present dissertation is to develop and implement the CSE combustion model to provide simulations for the general case of turbulent partially premixed combustion. The major findings and conclusions are summarized here, followed by recommendations for future work.

6.1 Summary of main findings

In Chapter 3, the CSE combustion model in combination with a FGM approach for chemistry reduction is applied to RANS numerical solutions of a turbulent premixed bluff-body for which experimental data is available. A product-based progress variable as a conditioning variable for the CSE model and the modified laminar flamelet PDF as presumed shape of the probability density function are used to calculate the mean reaction rate. The optimal regularization parameter is determined using the L-curve and a sensitivity analysis is performed related to the effect of the value of the regularization parameter. Only small differences in the conditional and unconditional averages are noticed for values of the regularization parameter located in the optimal range determined by the L-curve. Further, CSE is shown to converge to one unique and stable solution which does not depend on the initial solutions or a priori solution knowledge. Predictions show very good agreement with the available experimental data, in terms of mean axial velocity and progress variable radial profiles. Two different turbulence models are adopted in both reactive and non-reactive cases: the SST $k-\omega$ turbulence model with a modified value the production term constant gives a better solution than the modified $k-\varepsilon$ in both non-reactive and reactive cases for two different values of the constant, $\gamma_2 = 0.3$ and $\gamma_2 = 0.65$, respectively. The

results of the CSE combustion model are close to those of the flamelet approach, and show a slightly better agreement farther downstream, where the flame regime departs from the flamelet region. The numerical temperature contours are in qualitative agreement with the photograph of the flame from the experimental work, not only for the anchoring region located right above the bluff body, but also for the bulge zone observed after the recirculation region. The mean reaction rate of the CH4 profile confirms the location of the flame brush along the shear layer, consistent with the experimental results.

Chapter 4 investigates a series of lifted turbulent jet flames in RANS by using a partially premixed formulation of CSE, namely DCSE. The mean centerline and radial profiles of CH_4 are in good agreement with the experimental results. The predicted lift-off heights and radial locations of flame stabilization are in very good agreement with the experimental values. The validity of the statistical independence assumption between mixture fraction and progress variable is studied by using two forms of the joint PDF. For the series of flames under investigation, the statistical independence assumption between mixture fraction and progress variable is found to be reasonable as it provides similar results in terms of axial and radial CH4 concentration profiles and lift-off height predictions, as long as the laminar flame used to determine the PDF is for stoichiometric conditions. The stabilization point is located on the fuel lean side and the mixture fraction isolines are deflected around the flame base. Significant entrainment of air by the fuel jet upstream of the flame stabilization point is observed which is consistent with the experimental results. The shape of the flame zone obtained in the numerical simulations reflects the experimental observations, showing a curvature that is convex to the outer flow near the upstream stabilization point and a relatively straight region continuous along the axial direction. The flame width is calculated with the width of the flammable region and becomes larger with increasing Reynolds number, in very good agreement with the experimental findings. Several features of triple flame structure are observed, such as the presence of a fuel concentration gradient at the flame base, deceleration and divergence of the flow at the stabilization height, and the observation of the lean and the reach branches on the sides of the diffusion tail. However, some differences are noted, in particular for the location of the central branch which is off stoichiometry, on the fuel lean side and magnitude of the OH chemical source term. The DCSE calculations are successful in predicting the lift-off heights and reproducing many aspects of the flame structure in agreement with the experimental observations. The current results show that important aspects of the stabilization mechanism can be reproduced by the DCSE partially premixed combustion model.

In Chapter 5, the CSE combustion model is applied to RANS numerical solutions of a series of turbulent V-shaped flames for which experimental data is available. Premixed and stratified conditions are investigated. A product-based progress variable and the mix-

ture fraction as conditioning variables for the doubly conditioned DCSE model and the modified laminar flamelet PDF as presumed shape of the probability density function of the progress variable are used to calculate the mean reaction rates. In the premixed case, predictions show very good agreement with the available experimental data, in terms of mean axial velocity and progress variable radial profiles. Different values of the regularization parameter are used and the predictions result to be independent on this parameter. A sensitivity analysis on the number of ensembles used in the inversion process is performed for the fully premixed configuration. The number of CSE ensembles is shown to have a significant impact on the results if not selected appropriately. For the present case, the suitable number of CSE ensembles results to be equal to 8. Three different models for the scalar dissipation closure are compared in the case of premixed combustion: the linear relaxation assumption based on the eddy-breakup-type hypothesis (Eq. 5.3), the flame surface density model (Eq. 3.29)) and the algebraic model of Kolla et al. (Eq. 3.33). Very good predictions are obtained for the axial velocity field in the case of the simple linear relaxation model, while the algebraic model of Kolla et al. [118] performs better in terms of progress variable predictions and transverse velocity field. A partially premixed formulation of CSE, DCSE, is also presented and applied to a series of stratified turbulent flames. An extension of the scalar dissipation model of Kolla et al. is presented for the partially premixed case and the contribution of the different terms in both premixed and partially premixed approaches is investigated. Two formulations of the joint PDF are used, based on Eq. 4.7 and Eq. 4.6. Good predictions compared to experimental data are obtained, in particular for the lean and stoichiometric cases. The joint PDF formulation, for which the statistical independence assumption is relaxed, is found to provide better agreements, in particular for the stoichiometric case. Reasonable agreement is observed for the rich case, consistent with previous numerical studies.

6.2 Summary of Accomplishments

A list of the main outcomes is presented here:

- The CSE premixed approach is used for the numerical simulations of a bluff-body flame. Consolidation of the CSE model for turbulent premixed combustion is achieved. In particular, CSE provides promising results in regions where the flame regime departs from the flamelet region (Fig. 3.18).
- The doubly conditioned CSE formulation, DCSE is implemented and applied to a series of turbulent lifted flames. DCSE proves to be able to predict well the stabilization

heights and the stabilization mechanism of lifted flames.

- DCSE is applied to turbulent stratified flames, demonstrating the capability of DCSE to deal with partially premixed combustion.

6.3 Future Work

One limitation in the CSE approach is that the conditional averages need to be smooth. In the present work, the inversion of the integral equation is obtained by using Tikhonov regularization method. Some smoothness is introduced in the inversion process and can lead to some sort of numerical errors. However, the numerical errors introduced by the regularization method are considered to be minimal, if considering the adequate level of numerical predictions obtained for different configurations (premixed bluff-body flame, turbulent lifted jet flames and stratified turbulent V-shaped flames, respectively). However, other inversion techniques can be found in literature, some of them are summarized by Twomey [148]. The use of an alternative method for the inversion would provide some insights regarding the impact of numerical errors in the final solution.

DCSE is implemented in RANS as first application. Further investigation using LES is required to obtain a better solution of the flow field. LES is more computationally expensive, but not complicated in terms of implementation in the CSE framework, as demonstrated by previous investigations using LES and singly CSE.

The present work uses methane as fuel. However, the CSE approach is not limited to specific fuels and its implementation with different fuels such as propane and biofuels is not expected to raise further issues. The extension of CSE to different fuels would verify its range of applicability.

Similar to CMC, CSE does not require any tabulated chemistry to function properly as it provides closure for the reaction source for arbitrarily complex chemical kinetic mechanisms. In the current work, FGM and TGLDM are used as chemistry tabulation techniques for computational saving. Other approaches have been proposed in literature and can be adopted in order to show that CSE is not dependent on any particular techniques for chemistry tabulation.

References

[1] B. Renou, E. Samson, and A. Boukhalfa, "An experimental study of freely propagating turbulent propane/air flames in stratified inhomogeneous mixtures," *Combus. Sci. Technol.*, vol. 176, no. 11, pp. 1867–1890, 2004.

[2] E. Samson, *Etude expérimentale de la propagation de flammes en expansion dans un milieu à richesse stratifiée*. PhD thesis, Institut National des Sciences Appliquées de Rouen, 2002.

[3] J. Warnatz, U. Maas, and R. Dibble, *Combustion*. Springer, 2006.

[4] M. Salehi and W. Bushe, "Presumed PDF modeling for RANS simulation of turbulent premixed flames," *Combust. Theor. Model.*, vol. 14, no. 3, pp. 381–403, 2010.

[5] J. Kariuki, J. Dawson, and E. Mastorakos, "Measurements in turbulent premixed bluff body flames close to blow-off," *Combust. Flame*, vol. 159, pp. 2589–2607, 2012.

[6] R. Barlow and J. Frank, "Effects of turbulence on species mass fractions in methane/air jet flames," *Proc. Combust. Inst.*, vol. 27, pp. 1087–1095, 1998.

[7] C. Cha, G. Kosály, and H. Pitsch, "Modeling extinction and reignition in turbulent nonpremixed combustion using a doubly-conditional moment closure approach," *Phys. Fluids*, vol. 13, pp. 3824–3834, 2001.

[8] R. Grout, *DNS supported modelling for lean and stratified premixed flames*. PhD thesis, Department of Engineering University of Cambridge, 2007.

[9] R. Schefer, M. Namazian, and J. Kelly, "Structural characteristics of lifted turbulent-jet flames," *Proc. Combust. Inst.*, vol. 22, no. 1, pp. 833–842, 1989.

[10] R. Schefer, M. Namazian, and J. Kelly, "Stabilization of lifted turbulent-jet flames," *Combust. Flame*, vol. 99, no. 1, pp. 75–86, 1994.

[11] R. Schefer and P. Goix, "Mechanism of flame stabilization in turbulent, lifted-jet flames," *Combust. Flame*, vol. 112, pp. 559–574, 1998.

[12] V. Robin, A. Mura, M. Champion, O. Degardin, B. Renou, and M. Boukhalfa, "Experimental and numerical analysis of stratified turbulent V-shaped flames," *Combust. Flame*, vol. 153, no. 1–2, pp. 288–315, 2008.

[13] V. Robin, *Contribution à la modélisation des écoulements turbulents réactifs partiellement pré-mélangés*. PhD thesis, ISAE-ENSMA Ecole Nationale Supérieure de Mécanique et d'Aérotechique, 2007.

[14] O. Degardin, *Effets des Hétérogénéités de Richesse sur la Structure Locale des Flammes Turbulentes*. PhD thesis, L'Institut National des Sciences Aqppliquees de Rouen, 2006.

[15] E. Fernández-Tarrazo, A. Sánchez, A. Liñán, and F. Williams, "A simple one-step chemistry model for partially premixed hydrocarbon combustion," *Combust. Flame*, vol. 147, no. 1–2, pp. 32–38, 2006.

[16] J. Göttgens, F. Mauss, and N. Peters, "Analytic approximations of burning velocities and flame thicknesses of lean hydrogen, methane, ethylene, ethane, acetylene, and propane flames," *Proc. Combust. Inst.*, vol. 24, no. 1, pp. 129–135, 1992.

[17] I. Yamaoka and H. Tsuji, "Determination of burning velocity using couterflow flames," *Proc. Combust. Inst.*, vol. 20, no. 1, pp. 1883–1892, 1985.

[18] U. D. of Commerce, "National Oceanic and Atmospheric Administration, Earth System Research Laboratory, Global Monitoring Division," *http://www.esrl.noaa.gov/gmd/ccgg/trends/global.html*, 2012.

[19] J. Heywood, "Pollutant formation and control in spark ignition engines," *Prog. Energy Comb. Sci*, vol. 15, pp. 1191–1211, 1975.

[20] N. Swaminathan and K. Bray, *Turbulent Premixed Flames*. Cambridge University Press, 2011.

[21] T. Echekki and E. Mastorakos, *Turbulent Combustion Modeling: Advances, New Trends and Perspectives*. Springer, 2011.

[22] N. Peters, *Turbulent Combustion*. Cambridge University Press, 2000.

[23] K. Bray, P. Domingo, and L. Vervisch, "Role of the progress variable in models for partially premixed turbulent combustion," *Combust. Flame*, vol. 141, no. 4, pp. 431–437, 2005.

[24] T. Poinsot and D. Veynante, *Theoretical and numerical combustion*. Edwards, 2005.

[25] R. Bilger, S. Pope, K. Bray, and J. Driscoll, "Paradigms in turbulent combustion research," *Proc. Combust. Inst.*, vol. 30, pp. 21–42, 2005.

[26] A. Kolmogorov, "The local structure of turbulence in incompressible viscous fluid for very large Reynolds numbers," *C. R. Acad. Sci. USSR*, vol. 30, pp. 301–305, 1941.

[27] L. Richardson, *Weather Prediction by Numerical Process*. Cambridge University Press, 1922.

[28] S. Pope, *Turbulent Flows*. Cambridge University Press, 2000.

[29] J. Griffiths and J. Barnard, *Flame and Combustion*. Blackie Academic & Professional, 1995.

[30] D. Veynante and L. Vervisch, "Turbulent combustion modeling," *Prog. in Energ. Combust. Sci.*, vol. 28, pp. 193–266, 2002.

[31] B. Launder and B. Sharma, "Application of the energy-dissipation model of turbulence to the calculation of flow near a spinning disc," *Letters In Heat And Mass Transfer*, vol. 1, pp. 131–138, 1974.

[32] C. Speziale and N. Mhuiris, "Scaling laws for homogeneous turbulent shear flows in a rotating frame," *Phys. Fluids A*, vol. 1, pp. 294–301, 1989.

[33] F. Menter, "Two-equation eddy-viscosity turbulence models for engineering applications," *AIAA J.*, vol. 32, pp. 1598–1605, 1994.

[34] D. Wilcox, "Reassessment of the scale-determining equation for advanced turbulence models," *AIAA J.*, vol. 26, pp. 1299–1310, 1988.

[35] M. Lesieur, "New Trends in Large-Eddy simulations of turbulence," *Annu. Rev. Fluid Mech. Mech.*, vol. 28, pp. 45–82, 1996.

[36] U. Piomelli and J. Chasnov, "Large-Eddy Simulations: Theory and Applications," in *Turbulence and Transition Modelling* (H. Hallbäck, D. S. Henningson, A. V. Johansson, and P. H. Alfredsson, eds.), vol. 2 of *ERCOFTAC Series*, pp. 269–336, Springer Netherlands, 1996.

[37] J. Blazek, *Computational Fluid Dynamics: Principles and Applications*. Elsevier, 2006.

[38] A. Leonard, "Energy cascade in Large Eddy Simulation of turbulent fluid flow," *Adv. Geophys.*, vol. 18A, pp. 237–248, 1974.

[39] S. Ghosal and P. Moin, "The basic equations for the Large Eddy Simulation of turbulent flows in complex geometry," *J. Comput. Phys.*, vol. 118, pp. 24–37, 1995.

[40] J. Smagorinsky, "General circulation experiments with the primitive equations," *Monthly Weather Review*, vol. 91, pp. 99–164, 1963.

[41] M. Germano, U. Piomelli, P. Moin, and W. Cabot, "A dynamic sub-grid scale eddy viscosit model," *Phys. Fluids*, vol. A 3, pp. 1760–1765, 1991.

[42] R. Bilger, "Turbulent flows with nonpremixed reactants," in *Turbulent Reacting Flows* (P. Libby and F. Williams, eds.), Top. Appl. Phys., pp. 65–113, Springer Berlin / Heidelberg, 1980.

[43] B. Magnussen and B. Hjertager, "On mathematical modeling of turbulent combustion with special emphasis on soot formation and combustion," *Proc. Combust. Inst.*, vol. 16, pp. 719–729, 1977.

[44] D. Spalding, "Mixing and chemical reaction in steady confined turbulent flames," *Proc. Combust. Inst.*, vol. 13, pp. 649–657, 1971.

[45] N. Peters, "Laminar diffusion flamelet models," *Prog. Energy Combust. Sci.*, vol. 10, no. 3, pp. 319–339, 1984.

[46] V. Kuznetsov, "Effect of turbulence on the formation of large superequilbrium concentration of atoms and free radicals in diffusion flames," *Mehan. Zhidkosti Gasa*, vol. 6, pp. 3–9, 1982.

[47] S. Ruan, N. Swaminathan, K. Bray, Y. Mizobuchi, and T. Takeno, "Scalar and its dissipation in the near field of turbulent lifted jet flame," *Combust. Flame*, vol. 159, pp. 591–608, 2012.

[48] K. Seshadri and N. Peters, "Asymptotic structure and exctinction of methane-air diffusion flames," *Combust. Flame*, vol. 73, pp. 23–44, 1988.

[49] R. Borghi, "On the structure and morphology of turbulent premixed flames," in *Recent Advances in the Aerospace Sciences* (C. Casci and C. Bruno, eds.), pp. 117–138, Springer US, 1985.

[50] K. Bray and J. Moss, "A unified statistical model of the premixed turbulent flame," *Acta Astronautica*, vol. 4, no. 291–319, 1977.

[51] L. Vervisch, R. Hauguel, P. Domingo, and M. Rullaud, "Three facets of turbulent combustion modelling: Dns of premixed v-flame, les of lifted non-premixed flame and rans of jet-flame," *J. Turbulence*, vol. 5, pp. 1–36, 2004.

[52] K. Bray, "Studies of the turbulent burning velocity," *Proc. R. Soc. Lond. A*, vol. 431, pp. 315–335, 1990.

[53] S. Pope, "Lagrangian PDF methods for turbulent flows," *Annu. Rev. Fluid Mech.*, vol. 26, pp. 23–63, 1994.

[54] S. Pope and W. Cheng, "The stochastic flamelet model of turbulent premixed combustion," *Proc. Combust. Inst.*, vol. 22, pp. 781–789, 1989.

[55] S. Pope, "A Monte Carlo method for the PDF equation of turbulent reacting flow," *Combust. Sci. Technol.*, vol. 25, pp. 159–174, 1981.

[56] S. Pope, "PDF methods for turbulent reactive flows," *Prog. in Energ. Combust. Sci.*, vol. 11, pp. 119–192, 1985.

[57] L. Valiño, "A field Monte carlo formulation for calculating the probability density function of a single scalar in a turbulent flow," *Flow Turbul. Combust.*, vol. 60, pp. 157–172, 1998.

[58] V. Sabel'nikov and O. Soulard, "Rapidly decorrelating velocity-field model as a tool for solving one-point fokker-planck equations for probability density functions of turbulent reactive scalars," *Phys. Rev. E*, vol. 72, pp. 16301–163022, 2005.

[59] W. Jones, A. Marquis, and V. Prasad, "LES of a turbulent premixed swirl burner using the Eulerian stochastic field method," *Combust. Flame*, vol. 159, pp. 3079–3095, 2012.

[60] R. W. Bilger, "Conditional moment closure for turbulent reacting flow," *Phys. Fluid A: Fluid Dynam.*, vol. 5, pp. 436–444, 1993.

[61] A. Y. Klimenko, "Multicomponent diffusion of various admixtures in turbulent flow," *Fluid Dynam.*, vol. 25, pp. 327–334, 1990.

[62] A. Klimenko and R. Bilger, "Conditional moment closure for turbulent combustion," *Prog. Energy Combust. Sci.*, vol. 25, no. 6, pp. 595–687, 1999.

[63] E. Mastorakos and R. Bilger, "Second-order conditional moment closure for the autoignition of turbulent flows.," *Phys. Fluids*, vol. 31, no. 6, pp. 1246–1248, 1998.

[64] M. Fairweather and R. Woolley, "First- and second-order elliptic conditional moment closure calculations of piloted methane diffusion flames," *Combust. Flame*, vol. 150, no. 1-2, pp. 92–107, 2007.

[65] S. Sreedhara and K. Huh, "Modeling of turbulent, two-dimensional nonpremixed CH_4/H_2 flame over a bluffbody using first- and second-order elliptic conditional moment closures," *Combust. Flame*, vol. 143, pp. 119–134, 2005.

[66] A. Kronenburg, R. Bilger, and J. Kent, "Modeling soot formation in turbulent methane air jet diffusion flames," *Combust. Flame*, vol. 121, pp. 24–40, 2000.

[67] A. Kronenburg and E. Mastorakos, "The conditional moment closure model," in *Turbulent Combustion Modeling*, vol. 95, pp. 91–117, Springer Netherlands, 2011.

[68] R. Woolley, M. Fairweather, and Y. Yunardi, "Conditional moment closure modelling of soot formation in turbulent non-premixed methane and propane flames," *Fuel*, vol. 8, no. 3, pp. 393–407, 2009.

[69] S. Martin, J. Kramlich, G. Kosaly, and J. Riley, "The premixed Conditional Moment Closure method applied to idealized lean premixed gas turbine combustors," *J. Eng. Gas Turb. Power*, vol. 125, no. 4, pp. 895–900, 2003.

[70] S. Amzin, N. Swaminathan, J. Rogerson, and J. Kent, "Conditional moment closure for turbulent premixed flames," *Combust. Sci. Technol.*, vol. 184, pp. 1743–1767, 2012.

[71] A. Klimenko and S. Pope, "The modeling of turbulent reactive flows based on multiple mapping conditioning.," *Phys. Fluids*, vol. 15, pp. 1907–1925, 2003.

[72] M. Cleary, A. Klimenko, J. Janicka, and M. Pfitzner, "A sparse-lagrangian multiple mapping conditioning model for turbulent diffusion flames," *Proc. Combust. Inst.*, vol. 32, no. 1, pp. 1499–1507, 2009.

[73] K. Vogiatzaki, A. Kronenburg, M. Cleary, and J. Kent, "Multiple mapping conditioning of turbulent jet diffusion flames," *Proc. Combust. Inst.*, vol. 32, no. 2, pp. 1679–1685, 2009.

[74] W. Bushe and H. Steiner, "Conditional moment closure for large eddy simulation of nonpremixed turbulent reacting flows," *Phys. Fluids*, vol. 11, pp. 1896–1906, 1999.

[75] J. Labahn and C. Devaud, "Investigation of conditional source-term estimation applied to a non-premixed turbulent flame," *Combust. Theory Model.*, vol. 17, no. 5, pp. 960–982, 2013.

[76] M. Wang, J. Huang, and W. Bushe, "Simulation of a turbulent non-premixed flame using conditional source-term estimation with trajectory generated low-dimensional manifold," *Proc. Combust. Inst.*, vol. 31, no. 2, pp. 1701–1709, 2007.

[77] D. Dovizio, M. Salehi, and C. Devaud, "RANS simulation of a turbulent premixed bluff body flame using conditional source-term estimation," *Combust. Theory Model.*, vol. 17, no. 5, pp. 935–959, 2013.

[78] M. Salehi, W. Bushe, and K. Daun, "Application of Conditional Source-term Estimation model for Turbulence-Chemistry Interactions in a Premixed Flame," *Combust. Theory Model.*, vol. 16, pp. 301–320, 2012.

[79] H. Steiner and W. Bushe, "Large eddy simulation of a turbulent reacting jet with conditional source-term estimation," *Phys. Fluids*, vol. 13, no. 3, pp. 754–769, 2001.

[80] P. Libby and F. Williams, "A presumed PDF analysis of partially premixed turbulent combustion," *Combust. Sci. Technol.*, vol. 161, no. 1, pp. 351–390, 2000.

[81] D. Haworth, B. Cuenot, T. Poinsot, and R. Blint, "Numerical simulation of turbulent propane–air combustion with nonhomogeneous reactants," *Combust. Flame*, vol. 121, pp. 395–417, 2000.

[82] D. Bradley, P. Gaskell, and A. Lau, "A mixedness-reactedness flamelet model for turbulent diffusion flames," *Proc. Combust. Inst.*, vol. 23, pp. 685–692, 1990.

[83] D. Bradley, P. Gaskell, and X. Gu, "The mathematical modeling of liftoff and blowoff of turbulent non-premixed methane jet flames at high strain rates," *Proc. Combust. Inst.*, vol. 27, pp. 1199–1206, 1998.

[84] C. Müller, H. Breitbach, and N. Peters, "Partially premixed turbulent flame propagation in jet flames," *Proc. Combust. Inst.*, vol. 25, pp. 1099–1106, 1994.

[85] M. Chen, M. Herrmann, and N. Peters, "Flamelet modeling of lifted turbulent methane/air and propane/air jet diffusion flames," *Proc. Combust. Inst.*, vol. 28, no. 1, pp. 167–174, 2000.

[86] A. Kronenburg, "Double conditioning of reactive scalar transport equations in turbulent nonpremixed flames," *Phys. Fluids*, vol. 16, no. 7, pp. 2640–2648, 2004.

[87] J. Huang and W. Bushe, "Simulation of transient turbulent methane jet ignition and combustion under engine-relevant conditions using conditional source-term estimation with detailed chemistry," *Combust. Theor. Model.*, vol. 11, no. 6, pp. 977–1008, 2007.

[88] R. Barlow, N. Smith, J.-Y. Chen, and R. Bilger, "Nitric oxide formation in dilute hydrogen jet flames: isolation of the effects of radiation and turbulence-chemistry submodels," *Combust. Flame*, vol. 117, no. 1–2, pp. 4–31, 1999.

[89] M. Fairweather and R. Woolley, "First-order conditional moment closure modeling of turbulent, nonpremixed methane flames.," *Combust. Flame*, vol. 138, no. 1–2, pp. 3–19, 2004.

[90] A. Cook and J. Riley, "A subgrid model for equilibrium chemistry in turbulent flows," *Phys. Fluids*, vol. 6, no. 8, pp. 2868–2870, 1994.

[91] G. Ribert, M. Champion, O. Gicquel, N. Darabiha, and D. Veynante, "Modelling nonadiabatic turbulent premixed reactive flows including tabulated chemistry," *Combust. Flame*, vol. 141, no. 3, pp. 271–280, 2004.

[92] B. Jin, R. Grout, and W. Bushe, "Conditional source-term estimation as a method for chemical closure in premixed turbulent reacting flow," *Flow Turbul. Combust.*, vol. 81, pp. 563–582, 2008.

[93] S. Stårner, R. Bilger, K. Lyons, J. Frank, and M. Long, "Conserved scalar measurements in turbulent diffusion flames by a Raman and Rayleigh ribbon imaging method," *Combust. Flame*, vol. 99, no. 2, pp. 347–354, 1994.

[94] C. Markides, G. De Paola, and E. Mastorakos, "Measurements and simulations of mixing and autoignition of an n-heptane plume in a turbulent flow of heated air.," *Exp. Therm. Fluid Sci.*, vol. 31, no. 5, pp. 393–401, 2007.

[95] A. Milford and C. Devaud, "Investigation of an inhomogeneous turbulent mixing model for conditional moment closure applied to autoignition," *Combust. Flame*, vol. 157, no. 8, pp. 1467–1483, 2010.

[96] W. Press, S. Teukolsky, W. Vetterling, and B. Flannery, *Numerical Recipes: The Art of Scientific Computing*, vol. 29. Cambridge University Press, 2007.

[97] P. Hansen, "Numerical tools for analysis and solution of Fredholm integral equations of the first kind," *Inverse Probl.*, vol. 8, no. 6, pp. 849–872, 1992.

[98] A. Tikhonov and V. Arsenin, *Solutions of ill-posed problems / Andrey N. Tikhonov and Vasiliy Y. Arsenin ; translation editor, Fritz John*. Distributed solely by Halsted Press, Washington, 1977.

[99] P. Hansen, "The truncated SVD as a method for regularization," *BIT*, vol. 27, pp. 534–553, 1987.

[100] J. Hadamard, *Lectures on Cauchy's problem in linear partial differential equations*. Yale University Press, 1923.

[101] R. Grout, W. Bushe, and C. Blair, "Predicting the ignition delay of turbulent methane jet using Conditional Source-term Estimation," *Combust. Theor. Model.*, vol. 11, pp. 1009–1028, 2007.

[102] S. Pope and U. Maas, "Simplifying chemical kinetics: Trajectory-Generated Low-Dimensional Manifolds," *Cornell Report FDA*, vol. 93–11, 1993.

[103] J. Van Oijen and L. De Goey, "Modelling of premixed counterflow flames using the flamelet-generated manifold method," *Combust. Theor. Model.*, vol. 6, pp. 463–478, 2002.

[104] G. Smith, D. Golden, M. Frenklach, B. Eiteener, M. Goldenberg, C. T. Bowman, R. Hanson, W. Gardiner, V. Lissianski, and Z. Qin, "Gri-mech 3.0," 2000.

[105] F. Williams, *Combustion theory*. Benjamin Cummings, Menlo Park, CA, 1985.

[106] O. Gicquel, N. Darabiha, and D. Thevenin, "Laminar premixed hydrogen/air counterflow flame simulations using flame prolongation of ILDM with differential diffusion," *Proc. Combust. Inst.*, vol. 28, pp. 1901–1908, 2000.

[107] K. Wang, G. Ribert, P. Domingo, and L. Vervisch, "Self-similar behavior and chemistry tabulation of burnt-gas diluted premixed flamelets including heat-loss," *Combust. Theor. Model.*, vol. 14, no. 4, pp. 541–570, 2010.

[108] H. Kolla and N. Swaminathan, "Strained flamelets for turbulent premixed flames, I: Formulation and planar flame results," *Combust. Flame*, vol. 157, no. 5, pp. 943–954, 2010.

[109] R. Balachandran, B. Ayoola, C. Kaminski, A. Dowling, and E. Mastorakos, "Experimental investigation of the nonlinear response of turbulent premixed flames to imposed inlet velocity oscillations," *Combust. Flame*, vol. 143, pp. 37–55, 2005.

[110] OpenFOAM, "The open source CFD toolbox." Software available at http://www.openfoam.org.

[111] D. Veynante, A. Trouvre, K. Bray, and T. Mantel, "Gradient and counter gradient scalar transport in turbulent premixed flames," *Fluid Mech.*, vol. 332, pp. 263–293, 1997.

[112] K. Bray, M. Champion, P. Libby, and N. Swaminathan, "Scalar dissipation and mean reaction rates in premixed turbulent combustion," *Combust. Flame*, vol. 158, pp. 2017–2022, 2011.

[113] N. Chakraborty and N. Swaminathan, "Influence of the Damköhler number on turbulence-scalar interaction in premixed flames. I. physical insight," *Phys. Fluids*, vol. 19, p. 045103, 2007.

[114] N. Swaminathan and K. Bray, "Effect of dilatation on scalar dissipation in turbulent premixed flames," *Combust. Flame*, vol. 143, pp. 549–565, 2005.

[115] N. Swaminathan and R. Grout, "Interaction of turbulence and scalar fields in premixed flames," *Phys. Fluids*, vol. 18, p. 045102, 2006.

[116] R. Prasad and J. Gore, "An evaluation of flame surface density models for turbulent premixed jet flames," *Combust. Flame*, vol. 116, no. 1–2, pp. 1–14, 1999.

[117] T. Mantel and R. Borghi, "A new model of premixed wrinkled flame propagation based on a scalar dissipation equation," *Combust. Flame*, vol. 96, pp. 443–457, 1994.

[118] H. Kolla, J. Rogerson, N. Chakraborty, and N. Swaminathan, "Scalar dissipation rate modeling and its validation," *Combust. Sci. Tech.*, vol. 181, no. 3, pp. 518–535, 2009.

[119] S. Zhang and C. Rutland, "Premixed flames effects on turbulence and pressure-related terms," *Combust. Flame*, vol. 102, pp. 447–461, 1995.

[120] S. Pope, "An explanation of the turbulent round-jet/plane-jet anomaly," *AIAA J.*, vol. 16, pp. 279–281, 1978.

[121] B. Dally, D. Fletcher, and A. Masri, "Flow and mixing fields of turbulent bluff-body jets and flames," *Combust. Theor. Model.*, vol. 2, pp. 193–219, 1998.

[122] M. Hossain and M. Malalasekera, "A combustion model sensitivity study for CH_4/H_2 bluff-body stabilised flame," *Proc. IME C J. Mech. Eng. Sci.*, vol. 221(11), pp. 1377–1390, 2007.

[123] S. Kim and K. Huh, "Use of the conditional moment closure model to predict no formation in a turbulent CH_4/H_2 flame over a bluff-body," *Combust. Flame*, vol. 130, pp. 94–111, 2002.

[124] S. Sklavounos and F. Rigas, "Validation of turbulence models in heavy gas dispersion over obstacles," *J. Hazard. Mater.*, vol. 108, pp. 9–20, 2004.

[125] P. Domingo, L. Vervisch, and K. Bray, "Partially premixed flamelets in LES of nonpremixed turbulent combustion," *Combust. Theor. Model.*, vol. 6, pp. 529–551, 2002.

[126] C. Lawn, "Lifted flames on fuel jets in co-flowing air," *Prog. Energy Combust. Sci.*, vol. 35, pp. 1–30, 2009.

[127] K. Lyons, "Toward an understanding of the stabilization mechanisms of lifted turbulent jet flames: Experiments," *Prog. Energ. Combust.*, vol. 33, no. 2, pp. 211–231, 2007.

[128] L. Vanquickenborne and A. v. Tiggelen, "The stabilization mechanism of lifted diffusion flames," *Combust. Flame*, vol. 10, no. 1, pp. 59–69, 1966.

[129] N. Peters and F. Williams, "Lift-off characteristics of turbulent jet diffusion flames," *AIAA J.*, vol. 21, pp. 423–429, 1983.

[130] J. Broadwell, W. Dahm, and M. Mungal, "Blowout of turbulent diffusion flames," *Proc. Combust. Inst.*, vol. 20, pp. 303–310, 1984.

[131] T. Gautam, "Liftoff heights and visible lengths of vertical turbulent jet diffusion flames in still air," *Combust. Sci. Technol.*, vol. 41, no. 1–2, pp. 17–29, 1984.

[132] R. Cabra, T. Myhrvold, J. Chen, R. Dibble, A. Karpetis, and R. Barlow, "Simultaneous laser Raman-Rayleigh-LIF measurements and numerical modeling results of a lifted turbulent H_2/N_2 jet flame in a vitiated coflow," *Proc. Combust. Inst.*, vol. 29, no. 2, pp. 1881–1888, 2002.

[133] R. Cabra, J. Chen, R. Dibble, A. Karpetis, and R. Barlow, "Lifted methane-air jet flames in a vitiated coflow," *Combust. Flame*, vol. 143, no. 4, pp. 491–506, 2005.

[134] C. Yoo, E. Richardson, R. Sankaran, and J. Chen, "A DNS study on the stabilization mechanism of a turbulent lifted ethylene jet flame in highly-heated coflow," *Proc. Combust. Inst.*, vol. 33, no. 1, pp. 1619–1627, 2011.

[135] L. Gordon, A. Masri, S. Pope, and G. Goldin, "A numerical study of auto-ignition in turbulent lifted flames issuing into a vitiated co-flow," *Combust. Theory Model.*, vol. 11, no. 3, pp. 351–376, 2007.

[136] C. Burgess and C. Lawn, "The premixture model of turbulent burning to describe lifted jet flames," *Combust. Flame*, vol. 119, no. 1–2, pp. 95–108, 1999.

[137] W. Pitt, "Assessment of theories for the behavior and blowout of lifted turbulent jet diffusion flames," *Proc. Combust. Inst.*, vol. 22, no. 1, pp. 809–816, 1988.

[138] A. Watson, C. Lyons, K.M. Carter, and J. Donbar, "On scalar dissipation and partially premixed flame propagation," *Combust. Sci. Technol.*, vol. 175, no. 4, pp. 649–664, 2003.

[139] S. Stårner, R. Bilger, J. Frank, D. Marran, and M. Long, "Mixture fraction imaging in a lifted methane jet flame," *Combust. Flame*, vol. 107, pp. 307–313, 1996.

[140] K. Su, O. Sun, and M. Mungal, "Experimental investigation of stabilization mechanisms in turbulent, lifted jet diffusion flames," *Combust. Flame*, vol. 144, pp. 494–512, 2006.

[141] L. Muñiz and M. Mungal, "Instantaneous flame-stabilization velocities in lifted-jet diffusion flames," *Combust. Flame*, vol. 111, pp. 16–31, 1997.

[142] A. Upatnieks, J. Driscoll, C. Rasmussen, and S. Ceccio, "Liftoff of turbulent jet flames-assessment of edge flame and other concepts using cinema-piv," *Combust. Flame*, vol. 138, pp. 259–272, 2004.

[143] Y. Mizobuchi, S. Tachibana, J. Shinjo, S. Ogawa, and T. Takeno, "A numerical analysis of the structure of a turbulent hydrogen jet lifted flame," *Proc. Combust. Inst.*, vol. 29, pp. 2009–2015, 2002.

[144] A. Kronenburg and M. Kostka, "Modeling extinction and reignition in turbulent flames," *Combust. Flame*, vol. 143, no. 4, pp. 342 – 356, 2005.

[145] C. Hasse and N. Peters, "A two mixture fraction flamelet model applied to split injections in a DI Diesel engine," *Proc. Combust. Inst.*, vol. 30, pp. 2755–2762, 2005.

[146] J. Labahn, D. Dovizio, and C. Devaud, "Numerical simulation of the Delft-Jet-in-Hot-Coflow (DJHC) flame using Conditional Source-term Estimation," *Proc. Combust. Inst.*, vol. 35, no. 3, pp. 3547–3555, 2015.

[147] J. Labahn, C. Devaud, T. Sipkens, and K. Daun, "Inverse analysis and regularisation in conditional source-term estimation modelling," *Combust. Theory Model.*, vol. 18, pp. 474–499, 2014.

[148] S. Twomey, *Introduction to the mathematics of inversion in remote sensing and indirect measurements*. Dover Publications, 1997.

[149] P. Domingo, L. Vervisch, and D. Veynante, "Large-eddy simulation of a lifted methane jet flame in a vitiated coflow," *Combust. Flame*, vol. 152, no. 3, pp. 415–432, 2008.

[150] M. Ihme and Y. See, "Prediction of autoignition in a lifted methane/air flame using an unsteady flamelet/progress variable model," *Combust. Flame*, vol. 157, no. 10, pp. 1850–1862, 2010.

[151] O. Darbyshire and N. Swaminathan, "A presumed joint PDF model for turbulent combustion with varying equivalence ratio," *Combust. Sci. Technol.*, vol. 184, pp. 2036–2067, 2012.

[152] S. Ruan, N. Swaminathan, and O. Darbyshire, "Modelling of turbulent lifted jet flames using flamelets: A priori assessment and a posteriori validation," *Combust. Theory Model.*, vol. 18, pp. 295–329, 2014.

[153] B. Vanderstraeten, D. Tuerlinckx, J. Berghmans, S. Vliegen, E. V. Oost, and B. Smit, "Experimental study of the pressure and temperature dependence on the upper flammability limit of methane/air mixtures," *J. Hazard. Materials*, vol. 56, pp. 237–246, 1997.

[154] P. Domingo, L. Vervisch, and Réveillon, "DNS analysis of partially premixed combustion in spray and gaseous turbulent flame-bases stabilized in hot air," *Combust. Flame*, vol. 140, no. 3, pp. 172–195, 2005.

[155] A. Mura, V. Robin, and M. Champion, "Modelling of scalar dissipation in partially premixed flames," *Combust. Flame*, vol. 149, pp. 217–224, 2007.

[156] S. Malkeson and N. Chakraborty, "Statistical analysis of cross scalar dissipation rate transport in turbulent partially premixed flames: A direct numerical simulation study," *Flow Turbul. Combust.*, vol. 83, no. 2-3, pp. 313–349, 2011.

[157] C. T. Bowman, D. F. Hanson, D. F. Davidson, W. C. J. Gardiner, V. Lissianski, G. P. Smith, D. M. Golden, M. Frenklach, and M. Goldenberg, "GRI-Mech 2.11," 1995.

[158] S. Navarro-Martinez and S. Rigopoulos, "Large eddy simulation of a turbulent lifted flame using conditional moment closure and rate-controlled constrained equilibrium," *Flow Turbul. Combust.*, vol. 87, pp. 407–423, 2011.

[159] M. Namazian, R. M. Schefer, and J. Kelly, "Scalar dissipation measurements in the developing region of a jet," *Combust. Flame*, vol. 74, no. 2, pp. 147–160, 1988.

[160] V. Robin, A. Mura, M. Champion, and T. Hasegawa, "Modeling the effects of thermal expansion on scalar turbulent fluxes in turbulent premixed flames," *Combust. Sci. Technol.*, vol. 182, no. 4-6, pp. 449–464, 2010.

[161] C. Law, *Combustion Physics*. Cambridge University Press, 2006.

[162] A. Hindmarsh, "ODEPACK, A Systematized Collection of ODE Solvers," *Sci. Comput.*, vol. 1, pp. 55–64, 1983.

[163] C. Devaud, J. Kent, and R. Bilger, "Conditional moment closure applied to a lifted turbulent methane-air flame," *Proc. of the 3rd Mediterranean combustion symposium, Marrakech*, pp. 972–981, 2003.

[164] I. Kim and E. Mastorakos, "Simulations of turbulent lifted jet flames with two-dimensional conditional moment closure," *Proc. Combust. Inst.*, vol. 30, no. 1, pp. 911–918, 2005.

[165] P. Kioni, B. Rogg, and K. Bray, "Flame spread in laminar mixing layers: the triple flame," *Combust. Flame*, vol. 95, pp. 276–290, 1993.

[166] M. Mansour, "Stability characteristics of lifted turbulent partially premixed jet flames," *Combust. Flame*, vol. 133, pp. 263–274, 2003.

[167] N. Miyamoto, H. Ogawa, T. Shudo, and F. Takeyama, "Combustion and emissions in a new concept DI stratified charge engine with two-stage fuel injection," *SAE Tech. Ser. Paper 940675*, 1994.

[168] N. Pasquier, B. Lecordier, M. Trinité, and A. Cessou, "An experimental investigation of flame propagation through a turbulent stratified mixture," *Proc. Combust. Inst.*, vol. 31, no. 1, pp. 1567–1574, 2007.

[169] S. Shiga, S. Ozone, H. Machacon, T. Karasawa, H. Nakamura, T. Ueda, N. Jingu, Z. Huang, M. Tsue, and M. Kono, "A study of the combustion and emission characteristics of compressed-natural-gas direct-injection stratified combustion using a rapid-compression-machine," *Combust. Flame*, vol. 129, no. 1–2, pp. 1–10, 2002.

[170] Y. Cho and D. Santavicca, "The effect of incomplete fuel-air mixing on spark-ignited flame kernel growth," *SAE Tech. Ser.*, vol. Paper 932715, 1993.

[171] T. Kang and C. Kyritsis, "Departure from quasi-homogeneity during laminar flame propagation in lean, compositionally stratified methane–air mixtures," *Proc. Combust. Inst.*, vol. 31, no. 1, pp. 1075–1083, 2007.

[172] C. Jiménez, B. Cuenot, T. Poinsot, and D. Haworth, "Numerical simulation and modeling for lean stratified propane-air flames," *Combust. Flame*, vol. 128, pp. 1–21, 2002.

[173] A. Mura, F. Galzin, and R. Borghi, "A unified PDF-flamelet model for turbulent premixed combustion," *Combus. Sci. Technol.*, vol. 175, no. 9, pp. 1573–1609, 2003.

[174] S. Bondi and W. Jones, "A combustion model for premixed flames with varying stoichiometry," *Proc. Combust. Inst.*, vol. 29, pp. 2123–2129, 2002.

[175] J. Hélie and A. Trouvé, "A modified coherent flame model to describe turbulent flame propagation in mixtures with variable composition," *Proc. Combust. Inst.*, vol. 28, no. 193–201, 2000.

[176] W. Polifke, P. Flohr, and M. Brandt, "Modeling of inhomogeneously premixed combustion with an extended TFC model," *J. Eng. Gas Turb. Power*, vol. 124, no. 1, pp. 58–65, 2002.

[177] V. Robin, A. Mura, M. Champion, and P. Pilon, "A multi-Dirac presumed PDF model for turbulent reactive flows with variable equivalence ratio," *Combus. Sci. Technol.*, vol. 178, pp. 1843–1870, 2006.

[178] O. Darbyshire, N. Swaminathan, and S. Hochgreb, "The effects of small-scale mixing models on the prediction of turbulent premixed and stratified combustion," *Combust. Sci. Technol.*, vol. 182, pp. 1141–1170, 2010.

[179] J. Rogerson and N. Swaminathan, "Correlation between dilatation and scalar dissipation in turbulent premixed flames," *Proc. European Combustion Meeting*, 2007.

[180] X. Gu, M. Haq, M. Lawes, and R. Woolley, "Laminar burning velocity and Markstein lengths of methane–air mixtures," *Combust. Flame*, vol. 121, no. 1-2, pp. 41–58, 2000.

[181] C. Vagelopoulos and F. Egolfopoulos, "Direct experimental determination of laminar flame speeds," *Proc. Combust. Inst.*, vol. 27, pp. 513–519, 1998.

[182] A. Van Maaren, D. Thung, and L. De Goey, "Measurement of flame temperature and adiabatic burning velocity of methane/air mixtures," *Combus. Sci. Technol.*, vol. 96, no. 4-6, pp. 327–344, 1994.